

**DEVELOPMENT OF METAL-BASED  
(RADIO)PHARMACEUTICALS FOR IMAGING AND THERAPY**

by

Thomas Isaac N. Kostelnik

B.Sc (Hons.), Mount Allison University, 2015

A THESIS SUBMITTED IN PARTIAL FULFILLMENT OF  
THE REQUIREMENTS FOR THE DEGREE OF

DOCTOR OF PHILOSOPHY

in

THE FACULTY OF GRADUATE AND POSTDOCTORAL STUDIES

(Chemistry)

THE UNIVERSITY OF BRITISH COLUMBIA

(Vancouver)

December 2020

© Thomas Isaac N. Kostelnik, 2020

The following individuals certify that they have read, and recommend to the Faculty of Graduate and Postdoctoral Studies for acceptance, the dissertation entitled:

Development of Metal-Based (Radio)pharmaceuticals for Imaging and Therapy

submitted by Thomas Kostelnik in partial fulfillment of the requirements for

the degree of DOCTOR OF PHILOSOPHY

in Chemistry

**Examining Committee:**

Chris Orvig, Professor, Department of Chemistry, UBC  
Supervisor

Michael O Wolf, Professor, Department of Chemistry, UBC  
Supervisory Committee Member

Harry Brumer, Professor, Department of Chemistry, UBC  
University Examiner

Thomas Chang, Professor, Department of Pharmaceutical Sciences, UBC  
University Examiner

**Additional Supervisory Committee Members:**

Pierre Kennepohl, Associate Professor, Department of Chemistry, University of Calgary  
Supervisory Committee Member

Lawrence McIntosh, Professor, Department of Biochemistry and Molecular Biology, UBC  
Supervisory Committee Member

## Abstract

Contemporary metalloradiopharmaceuticals are usually comprised of four components; radionuclide, bifunctional chelator, linker and targeting vector. Physical decay of the radionuclide is responsible for the diagnostic or therapeutic effect of the drug, and the bifunctional chelator simultaneously binds the radiometal ion to prevent release *in vivo* and provides a handle for covalent linkage to the other component of the molecule. Optimal performance of these components is essential for effective radiopharmaceuticals, and have been the focus of this thesis. Antimony-119 is considered one of the most promising radionuclides for Auger electron therapy; however, few studies exploring separation and radiolabeling of radioantimony exist in the literature. Bombardment of  $^{nat}\text{Sn}$  with 12.8 MeV protons achieved production of primarily  $^{120m}\text{Sb}$ , as well as  $^{117m}\text{Sn}$ . These species were then used to monitor separation radiochemistry and the purified  $^{120m}\text{Sb}$  was successfully radiolabeled. Non-bifunctional chelators **H<sub>6</sub>phospa**, **H<sub>6</sub>dipedpa**, and **H<sub>6</sub>eppy** were synthesized and studied with  $\text{In}^{3+}$ ,  $\text{Lu}^{3+}$ ,  $\text{Y}^{3+}$ ,  $\text{Sc}^{3+}$ , and  $\text{La}^{3+}$  via NMR and thermodynamic solution studies. Results showed that **H<sub>6</sub>phospa** formed the most thermodynamically stable complexes. As a result, **H<sub>6</sub>dappa** was synthesized as a bifunctional analogue. While thermodynamic results were encouraging, serum stability studies revealed complex lability, which was further supported by DFT calculations. Inspired by interest in  $^{203/212}\text{Pb}] \text{Pb}^{2+}$ , **DTPAm** was synthesized and studied. NMR spectra and preliminary radiolabeling studies with  $^{203}\text{Pb}] \text{Pb}^{2+}$  were encouraging; however, thermodynamic parameters and serum stability studies (with  $^{203}\text{Pb}$ ) pointed towards complex lability, likely as a result of the lack of ionisable protons of **DTPAm**. Lastly, interest in phosphonate-bearing ligands resulted in studies exploring their use in delivering oral  $\text{La}^{3+}$  for bone-resorption disorders. Working closely with Dr. David Weekes, large scale batches of

**La(XT)** were synthesized. Following animal studies, the lanthanum content of animal tissue (healthy Sprague Dawley rats) was analyzed by ICP-MS. Short-term studies (4 weeks) pointed towards dose-dependent lanthanum concentrations in bone (femur) and no observable toxicity. Long-term studies (3 months) showed no kidney or liver toxicity, however minimal mechanical advantage of  $\text{La}^{3+}$  incorporation into bone was noted. Synthesis and NMR studies were also carried out on **dppa** and **DEDA-(PO)** to investigate their stability with  $\text{La}^{3+}$ , among other metal ions.

## **Lay Summary**

Nuclear medicine is a field that uses radioactive atoms for medical purposes. A fundamental aspect of this field is the development of radioactive drugs. There are four components of state-of-the-art “radiopharmaceuticals,” with this thesis focusing on the radioactive atom, or “radionuclide,” and “chelator”, which binds to the radionuclide to prevent its release in the human body. Since the radioactive decay of the radionuclide is what is responsible for the drug’s effectiveness, choosing radionuclides with ideal decay properties will lead to better drugs. Part of this thesis investigates how to purify a new therapeutic radionuclide ( $^{119}\text{Sb}$ ). The other aspect of this thesis explores how to better secure these radionuclides by developing new chelators. This includes making the molecules and studying how strongly it can bind the desired metal ion. Several chelators can be found in this thesis, each aiming to gain deeper understanding of how to improve clinically used chelators.

## Preface

**Chapter 1** is an adaptation of published work and is reproduced in part from T. I. Kostelnik and C. Orvig; Radioactive main group and transition metals for imaging and therapy, *Chem. Rev.* **2019**, *119*, 902-956, Copyright 2019 The American Chemical Society. I researched and wrote the review article, with input and editing from Dr. Orvig.

**Chapter 2** is a manuscript in preparation. I am the first author of the article, as I spearheaded the majority of tin irradiations, and subsequent purification and radiolabeling studies at TRIUMF, as well as wrote the majority of the manuscript. Victoria Brown (co-op student) and Jenasee Mynerich (co-op student) helped establish liquid-liquid extraction, solid-phase purification and radiolabeling protocols, as well as ran some of the gamma-spectroscopy samples required for quantification. Dr. Valery Radchenko facilitated this work by helping to set up irradiations and provide working space at TRIUMF, as well as gave scientific input throughout the process. Collaborators at University of Wisconsin (Dr. Jonathan Engle, Aeli Olson, Paul Ellison) also provided valuable input.

**Chapter 3** is an adaptation of a manuscript in preparation. I am the first author on the article as I made the three ligands under investigation (**H<sub>6</sub>phospa**, **H<sub>6</sub>dipedpa** and **H<sub>6</sub>eppy**), carried out all NMR studies and wrote the majority of the manuscript. Felix Lindheimer assisted with the early stages of **H<sub>6</sub>eppy** synthesis. Dr. Guadalupe Jaraquemada-Peláez (with help from Rosita Cappai) was responsible for calculating thermodynamic stability constants via potentiometric and spectrophotometric titrations for the aforementioned ligands, as well as for each ligand with the five metal ions under investigation. Dr. Jaraquemada-Peláez wrote the corresponding section of the manuscript. Neha Choudhary is a graduate student in the Orvig group, and solved the crystal structures of **H<sub>6</sub>phospa** and **H<sub>6</sub>dipedpa**. Ms. Choudhary also

provided experimental details, which I adapted for the manuscript in preparation. Dr. Guadalupe Jaraquemada-Peláez and Hayden Scheiber collaborated on DFT calculations and theoretical NMR generation. Dr. Orvig gave input throughout the process and edited several versions of the manuscript.

**Chapter 4** is an adaptation of published work and is reproduced in part by T. I. Kostelnik, X. Wang, L. Southcott, H. K. Wagner, M. Kubeil, H. Stephan, M. de G. Jaraquemada-Peláez and C. Orvig; Rapid and thermodynamically stable complex formation of  $[\text{nat}/^{111}\text{In}]\text{In}^{3+}$ ,  $[\text{nat}/^{90}\text{Y}]\text{Y}^{3+}$  and  $[\text{nat}/^{177}\text{Lu}]\text{Lu}^{3+}$  with **H<sub>6</sub>dappa**, *Inorg. Chem.*, **2020**, *59*, 7238-7251, Copyright 2020 The American Chemical Society. I am the first author on the article, as I made and fully characterized the ligand (**H<sub>6</sub>dappa**), executed and analyzed all NMR data, performed radiolabeling studies at Helmholtz-Zentrum Dresden-Rossendorf (HZDR) under the supervision of Dr. Kubeil and Dr. Stephan, and wrote the majority of the manuscript. Dr. Wang calculated DFT structures found in the article and supporting information. Lily Southcott is a graduate student in the Orvig group and completed final radiolabeling studies, also under the supervision of Dr. Kubeil and Dr. Stephan at HZDR. Hannah Wagner was a six-week visiting student and helped with the synthesis of **H<sub>6</sub>dappa**. Dr. Jaraquemada-Peláez and I executed the potentiometric and spectrophotometric studies together; all fitting of corresponding data was done by Dr. Jaraquemada-Peláez. Dr. Orvig gave input throughout the process and edited several versions of the manuscript leading to the published article.

**Chapter 5** is a manuscript in preparation. I am the first author as I synthesized **DTPAm**, conducted NMR studies, and assisted in further experiments where collaboration was necessary. Neha Choudhary and Dr. Brian Patrick solved the crystal structure after I provided them with X-ray quality crystals. Dr. Jaraquemada-Peláez conducted solution studies to

calculate ligand  $pK_a$  values and the lead(II) complex stability constant and  $pM$  values. Andrew Robertson (TRIUMF) and Winnie Fu (TRIUMF) produced and purified the  $^{203}\text{Pb}$ , and Winnie Fu assisted with radiolabeling and serum stability studies. Dr. Orvig gave input throughout the process and edited the manuscript.

**Chapter 6** is an adaptation of published works and has been reproduced in part from D. M. Weekes, C. Ramogida, M. de G. Jaraquemada-Peláez, B. O. Patrick, C. Apte, T. I. Kostelnik, J. F. Cawthray, L. Murphy and C. Orvig; Dipicolinate complexes of gallium(III) and lanthanum(III), *Inorg. Chem.*, **2016**, *55*, 12544–12558, Copyright 2016 The American Chemical Society. Additionally, from D. M. Weekes, J. F. Cawthray, M. Rieder, J. Syeda, M. Ali, E. Wasan, T. I. Kostelnik, B. O. Patrick, A. Panahifar, A. Al-Dissi, D. Cooper, K. M. Wasan and C. Orvig; La(III) biodistribution profiles from intravenous and oral dosing of two lanthanum complexes, La(dpp)<sub>3</sub> and La(XT), and evaluation as treatment for bone resorption disorders, *Metallomics*, **2017**, *9*, 902–909, Copyright 2017 The Royal Society of Chemistry; and D. M. Weekes, M. de G. Jaraquemada-Peláez, T. I. Kostelnik, B. O. Patrick and C. Orvig; Di- and trivalent metal-ion solution studies with the phosphinate-containing heterocycle DEDA-(PO), *Inorg. Chem.* **2017**, *56*, 10155–10161, Copyright 2017 The American Chemical Society. Each of the above articles were primarily written by the first author, Dr. Weekes. However, I did play a role in each project, and as the unifying theme of the three articles is the development of chelators for bone resorption disorders, here they are presented together. For Weekes *et al.* *Inorg. Chem.* **2016**, I resynthesized the ligand **H<sub>4</sub>dppa** and helped study its protonation constants and stability constant with La<sup>3+</sup> via <sup>1</sup>H and <sup>31</sup>P{<sup>1</sup>H} NMR spectroscopy, along with Dr. Jaraquemada-Peláez and a very talented undergraduate student, Chirag Apte. For Weekes *et al.* *Metallomics* **2017**, I analyzed La content of animals (healthy Sprague Dawley

rats) via ICP-MS and analysed resulting data, along with Dr. Weekes. For Weekes *et al. Inorg. Chem.* **2017**, I carried out  $^1\text{H}$  NMR studies to distinguish between 1:1 and 1:2 (L:M) complex formation between the ligand of interest [DEDA-(PO)] and  $\text{La}^{3+}$ .

The animal studies presented in Section 6.2.3 have been published (Weekes *et al. Metallomics* **2017**). These studies were carried out primarily at the University of Saskatchewan (U.Sask), and the protocols were approved by the University Animal Care Committee (UACC) Animal Research Ethics Board (approval certificate # 20150060) and performed in accordance with the guidelines outlined in by the CCAC. The short-term oral and IV studies were coordinated and executed by Dr. Jacqueline Cawthray. Drug candidates were synthesized by Dr. Weekes, and formulations of  $\text{La}(\text{dpp})_3$  were made by Dr. Ellen Wasan (U.Sask). Soft-tissue organs were harvested, homogenized, and prepared for ICP-MS under the direction of Dr. Cawthray, and sent to UBC for analysis, which was undertaken by myself and Dr. Weekes. Bones were harvested by Dr. Cawthray and sent to UBC, where Dr. Weekes and I were responsible for cleaning and preparation for ICP-MS. All results were interpreted by myself, Drs. Weekes and Cawthray, with input from Drs. Chris Orvig and Kishor Wasan.

## Table of Contents

<b>Abstract .....</b>	<b>iii</b>
<b>Lay Summary.....</b>	<b>v</b>
<b>Preface .....</b>	<b>vi</b>
<b>Table of Contents.....</b>	<b>x</b>
<b>List of Tables.....</b>	<b>xvi</b>
<b>List of Figures .....</b>	<b>xviii</b>
<b>List of Charts .....</b>	<b>xxvi</b>
<b>List of Symbols.....</b>	<b>xxvii</b>
<b>List of Abbreviations.....</b>	<b>xxviii</b>
<b>List of Schemes.....</b>	<b>xxxii</b>
<b>List of Equations.....</b>	<b>xxxiii</b>
<b>Acknowledgements .....</b>	<b>xxxiv</b>
<b>Chapter 1. Introduction .....</b>	<b>1</b>
1.1 Nuclear Medicine and Radiopharmaceuticals .....	1
1.2 Metal-Based Radiopharmaceutical Drug Design .....	1
1.3 Importance of Radiometal Decay for Drug Function.....	4
1.3.1 Principles of Diagnostic Radiometals.....	6
1.3.2 Principles of Therapeutic Radiometals.....	7
1.3.3 Theranostic Isotopes .....	9
1.4 Production and Purity of Radionuclides.....	9
1.4.1 Radionuclide Production .....	9
1.4.2 Nomenclature of Radioactive Purity .....	12

1.5	The Chemistry of Radiopharmaceuticals .....	13
1.5.1	Fundamentals of Chelators and Metal Complexation .....	14
1.5.2	Chelator Evaluation .....	18
1.5.3	Bifunctional Chelators and Linkers.....	22
1.6	Bioconjugates .....	23
1.7	Thesis Overview .....	26
<b>Chapter 2. Production and Radiochemistry of Antimony-120m: Efforts Toward Auger Electron Therapy.....</b>		<b>28</b>
2.1	Introduction .....	28
2.1.1	Therapeutic Radionuclides and Auger Electron Therapy.....	28
2.1.2	Radionuclides for Auger Electron Therapy.....	30
2.2	Results and Discussion .....	31
2.2.1	Target Irradiation.....	31
2.2.2	Purification of <sup>120m</sup> Sb by Liquid-Liquid Extraction .....	33
2.2.3	Purification of <sup>120m</sup> Sb by Solid-Phase Chromatography .....	36
2.2.4	Preliminary Radiolabeling Studies .....	38
2.3	Conclusions .....	40
2.4	Experimental.....	41
2.4.1	Materials and Methods .....	41
2.4.2	Irradiation and Handling of Tin Target .....	42
2.4.3	Liquid-Liquid Extraction.....	42
2.4.4	Cation-Exchange Chromatography .....	43
2.4.5	Radiolabeling.....	44

<b>Chapter 3. Phosphonate Chelators for Medicinal Metal Ions</b> .....	<b>46</b>
3.1 Introduction .....	46
3.1.1 Medicinal Applications of Chelators.....	46
3.1.2 Development of Chelators.....	48
3.1.3 Phosphonate- and Picolate-Bearing Chelators .....	49
3.2 Results and Discussion .....	51
3.2.1 Ligand Synthesis and Characterization .....	51
3.2.2 X-ray Crystal Structures .....	55
3.2.3 Metal Complexation Studies .....	56
3.2.4 Solution Thermodynamics of H <sub>6</sub> phospa, H <sub>6</sub> dipedpa and H <sub>6</sub> eppy .....	60
3.2.5 Complex Formation Equilibria of H <sub>6</sub> phospa, H <sub>6</sub> dipedpa and H <sub>6</sub> eppy with In <sup>3+</sup> , Lu <sup>3+</sup> , Y <sup>3+</sup> , Sc <sup>3+</sup> , La <sup>3+</sup> .....	64
3.2.6 Density Functional Theory Calculations .....	67
3.3 Conclusions .....	70
3.4 Experimental.....	71
3.4.1 Materials and Methods .....	71
3.4.2 Synthesis and Characterization.....	72
3.4.3 Metal Complexation .....	77
3.4.4 X-ray Crystallography .....	77
3.4.5 Solution Thermodynamics.....	78
3.4.6 DFT Calculations.....	80

**Chapter 4. Investigation of Bifunctional Phosphonate-Bearing Chelator for Trivalent Radiometals.....83**

4.1	Introduction .....	83
4.1.1	Rational Design of H <sub>6</sub> dappa .....	83
4.1.2	Selection of Metal Ions for Study with H <sub>6</sub> dappa.....	84
4.2	Results and Discussion .....	85
4.2.1	Ligand Synthesis and Characterization .....	85
4.2.2	NMR Studies on Metal Complexation .....	87
4.2.3	Ligand Solution Thermodynamics .....	90
4.2.4	In <sup>3+</sup> , Lu <sup>3+</sup> , Sc <sup>3+</sup> and Y <sup>3+</sup> Complex Formation Equilibria .....	91
4.2.5	Radiolabeling and Serum Stability Experiments.....	94
4.2.6	Density Functional Theory Calculations of H <sub>6</sub> dappa Complexes .....	97
4.3	Conclusions .....	101
4.4	Experimental.....	102
4.4.1	Materials and Methods .....	102
4.4.2	Synthesis and Characterization.....	103
4.4.3	Metal Complexation .....	106
4.4.4	Solution Thermodynamics.....	107
4.4.5	Radiolabeling and Human Serum Challenge Experiments .....	108
4.4.6	Density Functional Theory Calculations .....	109

**Chapter 5. Amide-Dominant Chelator for Lead(II) Radiopharmaceuticals .....110**

5.1	Introduction .....	110
5.1.1	Radioactive Lead as a Therapeutic.....	110

5.1.2	Lead Chelation and Project Rationale .....	112
5.2	Results and Discussion .....	114
5.2.1	Ligand Synthesis and Characterization .....	114
5.2.2	NMR Complexation Studies with [ <sup>nat</sup> Pb]Pb <sup>2+</sup> .....	115
5.2.3	X-ray Crystal Structure of [Pb(DTPAm)] <sup>2+</sup> .....	116
5.2.4	Solution Thermodynamics of DTPAm and Complex Formation Equilibria with Pb <sup>2+</sup> .....	118
5.2.5	Radiolabeling and Serum Stability Assay with [ <sup>203</sup> Pb]Pb <sup>2+</sup> .....	123
5.3	Conclusions .....	126
5.4	Experimental.....	128
5.4.1	Materials and Methods .....	128
5.4.2	Synthesis and Characterization.....	128
5.4.3	Metal Complexation .....	129
5.4.4	X-ray Crystallography .....	129
5.4.5	Solution Studies.....	130
5.4.6	Radiolabeling and Serum Stability Studies .....	130

**Chapter 6. Phosphonate- and Phosphinate-Containing Ligands for Bone Resorption**

**Disorders.....132**

6.1	Introduction .....	132
6.1.1	Dipicolinate Ligands.....	133
6.1.2	Previous Work with La(XT).....	133
6.1.3	Previous Work with TETA-(PO) <sub>2</sub> .....	135
6.2	Results and Discussion .....	136

6.2.1	Synthesis and H <sub>4</sub> dppa, LaXT and DEDA-(PO) .....	136
6.2.2	<sup>1</sup> H and <sup>31</sup> P{ <sup>1</sup> H} NMR Titrations of H <sub>4</sub> dppa and [La(H <sub>x</sub> dppa)] <sup>x-1</sup> (x = 1, 0, -1).....	138
6.2.3	ICP-MS of Animal Tissues to Determine La Content Following La(dpp) <sub>3</sub> and La(XT) Dosing .....	143
6.2.4	NMR Studies with DEDA-(PO) and La <sup>3+</sup> .....	146
6.3	Conclusions .....	149
6.4	Experimental.....	150
6.4.1	Materials and Reagents.....	150
6.4.2	Instruments .....	151
6.4.3	Synthesis and Characterization.....	151
6.4.4	<sup>1</sup> H and <sup>31</sup> P{ <sup>1</sup> H} NMR Titrations of H <sub>4</sub> dppa, DEDA-(PO) and Their La <sup>3+</sup> Complexes .....	153
<b>Chapter 7. Ongoing Work and Future Studies.....</b>		<b>154</b>
7.1	Ongoing Work .....	154
7.2	Future Studies .....	156
<b>References.....</b>		<b>159</b>
<b>Appendices .....</b>		<b>188</b>
Appendix A. Supplementary Data for Chapter 2 .....		188
Appendix B. Supplementary Data for Chapter 3.....		189
Appendix C: Supplementary Data for Chapter 5.....		220

## List of Tables

<b>Table 1.1</b> Popular subject radiometals with relevant production routes, decay parameters and applications .....	5
<b>Table 1.2</b> Relevant chemical parameters of discussed metal cations .....	16
<b>Table 2.1</b> Abundance of natural tin isotopes and their produced (p,n) radionuclides .....	33
<b>Table 3.1</b> Protonation constants ( $\log K_a$ ) of discussed ligands .....	61
<b>Table 3.2</b> Stability constants ( $\log K_{ML}$ ) and the corresponding stepwise protonation constants $\log K_{1n1}(MH_nL)$ of $H_6\text{phospa}$ , $H_6\text{dipedpa}$ and $H_6\text{eppy}$ with metals of interest ( $T = 25^\circ\text{C}$ , $I = 0.16\text{ M NaCl}$ ).....	66
<b>Table 3.3</b> Comparison of DFT calculated metal coordination bond lengths of $\text{La}^{3+}$ and $\text{Sc}^{3+}$ phospa complexes.....	69
<b>Table 4.1</b> Protonation constants of $H_6\text{dappa}$ .....	91
<b>Table 4.2</b> Stepwise stability constants ( $\log K$ ) of $H_6\text{dappa}$ with $\text{In}^{3+}$ , $\text{Lu}^{3+}$ , $\text{Sc}^{3+}$ and $\text{Y}^{3+}$ .....	92
<b>Table 4.3</b> Serum stability of $^{111}\text{In}[\text{In}(\text{dappa})]^{3-}$ .....	97
<b>Table 4.4</b> Comparison of DFT calculated In-O and In-N bond lengths in In-octapa and In-dappa complexes.....	99
<b>Table 5.1</b> List of selected $[\text{Pb}(\text{DTPAm})]^{2+}$ bond lengths .....	117
<b>Table 5.2</b> Protonation constants of selected ligands .....	118
<b>Table 5.3</b> Stepwise stability constants ( $\log K$ ) of DTPAm with $\text{Pb}^{2+}$ .....	121
<b>Table 5.4</b> Formation constants, pPb values and basicity of selected ligands .....	123
<b>Table 5.5</b> Concentration-dependent labeling of $^{203}\text{Pb}[\text{Pb}^{2+}$ with DTPAm and TCMC .....	125
<b>Table 5.6</b> Serum stability of $^{203}\text{Pb}[\text{Pb}(\text{DTPAm})]^{2+}$ .....	126

<b>Table 6.1</b> Comparison of the stepwise protonation constants for dppa obtained by NMR titrations and potentiometry .....	139
<b>Table 6.2</b> Lanthanum complex formation constants for dppa .....	141
<b>Table A.1</b> Total activities of $^{120\text{m}}\text{Sb}$ and $^{117\text{m}}\text{Sn}$ measured from target solution.....	188
<b>Table A.2</b> Activities following liquid-liquid extraction of tin target.....	188
<b>Table A.3</b> Activities of $^{120\text{m}}\text{Sb}$ and $^{117\text{m}}\text{Sn}$ expressed as a fraction over total target solution activity .....	188
<b>Table A.4</b> Crystallographic information for $\text{H}_6\text{phospa}$ and $\text{H}_6\text{dipedpa}$ .....	189
<b>Table A.5</b> HR-ESI-MS data for $\text{H}_6\text{phospa}$ , $\text{H}_6\text{dipedpa}$ and $\text{H}_6\text{eppy}$ with $\text{In}^{3+}$ , $\text{Sc}^{3+}$ , $\text{Lu}^{3+}$ , $\text{Y}^{3+}$ , $\text{La}^{3+}$ .....	216
<b>Table A.6</b> Selected bond lengths from the crystal structure of $\text{H}_6\text{phospa}$ .....	217
<b>Table A.7</b> Selected bond angles from the crystal structure of $\text{H}_6\text{phospa}$ .....	217
<b>Table A.8</b> Selected bond lengths from the crystal structure of $\text{H}_6\text{dipedpa}$ .....	218
<b>Table A.9</b> Selected bond angles from the crystal structure of $\text{H}_6\text{dipedpa}$ .....	219
<b>Table A.10</b> Crystallographic information for $[\text{Pb}(\text{DTPAm})(\text{NO}_3)_2]$ .....	220

## List of Figures

<b>Figure 1.1</b> Colour coded Periodic Table with current or potential applications of each element in diagnostic and/or therapeutic radiopharmaceuticals .....	2
<b>Figure 1.2</b> Standard, four-component radiopharmaceutical design.....	3
<b>Figure 1.3</b> Radiometal decay types, and their corresponding applications in nuclear medicine.....	4
<b>Figure 1.4</b> Selected macrocyclic chelators and their respective BFC .....	19
<b>Figure 1.5</b> Selected acyclic chelators and their respective BFC.....	20
<b>Figure 1.6</b> Simplified illustration of radiopharmaceutical targeting .....	24
<b>Figure 2.1</b> Natural tin target (99.9%, 3.0 cm diameter, 0.127 mm thick) used for production of radioantimony .....	32
<b>Figure 2.2</b> Visual representation of radioantimony purification. Wash ether with equal volume 10 M HCl (x2) prior to back extraction.....	35
<b>Figure 2.3</b> $\gamma$ -ray spectra of a) target solution b) extracted target solution c) back extracted solution .....	36
<b>Figure 2.4</b> Cation-exchange chromatography system for $\text{Sn}^{4+}/\text{Sb}^{5+}$ separation.....	37
<b>Figure 2.5</b> Elution profile of $[\text{}^{117\text{m}}\text{Sn}]\text{Sn}^{4+}$ and $[\text{}^{120\text{m}}\text{Sb}]\text{Sb}^{5+}$ during cation-exchange chromatography.....	37
<b>Figure 2.6</b> a) Schematic of radiolabeling method for $^{120\text{m}}\text{Sb}$ ; b) Radio-TLC data for radiolabeling of $^{120\text{m}}\text{Sb}$ .....	40
<b>Figure 3.1</b> ORTEP diagrams of $\text{H}_6\text{phospa}$ (left) and $\text{H}_6\text{dipedpa}$ (right).....	55

**Figure 3.2**  $^1\text{H}$  NMR spectra of a)  $\text{H}_6\text{phospa}$ , b)  $\text{H}_6\text{dipedpa}$  and c)  $\text{H}_6\text{eppy}$  and their corresponding  $\text{La}^{3+}$  and  $\text{Sc}^{3+}$  complexes. Stars in  $[\text{Sc}(\text{dipedpa})]^{3-}$  spectrum represent neighboring ethylene protons of the asymmetric complex.....59

**Figure 3.3** Speciation plot of  $\text{H}_6\text{phospa}$ ,  $\text{H}_6\text{dipedpa}$  and  $\text{H}_6\text{eppy}$ .  $^{31}\text{P}$  chemical shift dependence on pH of  $\text{H}_6\text{phospa}$  and HypNMR2008 fitting overlaps the speciation plot.....63

**Figure 3.4** pM values ( $\text{M}^{3+} = \text{Sc}^{3+}, \text{In}^{3+}, \text{Y}^{3+}, \text{Lu}^{3+}, \text{La}^{3+}$ ) versus ionic radii (CN=8) for discussed chelating ligands (left) and  $\text{Sc}^{3+}$  scavenging ability of discussed ligands with pH (right).....67

**Figure 3.5** DFT calculated structures of  $[\text{La}(\text{H}_2\text{phospa})(\text{H}_2\text{O})]^-$  (left) and  $[\text{Sc}(\text{H}_2\text{phospa})]^-$  (right). Ligand hydrogens omitted for clarity.....68

**Figure 3.6** Experimental and DFT calculated  $^1\text{H}$  NMR spectra of  $[\text{La}(\text{H}_2\text{phospa})]^-$ . Molecule structure and corresponding peak assignments shown .....70

**Figure 4.1** (a)  $^1\text{H}$  NMR spectra of  $\text{H}_6\text{dappa}$ ,  $[\text{La}(\text{H}_x\text{dappa})]^{x-3}$ ,  $[\text{In}(\text{H}_2\text{dappa})]^-$  and  $[\text{Bi}(\text{H}_x\text{dappa})]^{x-3}$  (top-bottom) ( $\text{D}_2\text{O}$ , 400 MHz, 298 K). (b)  $^{31}\text{P}\{^1\text{H}\}$  NMR spectra of  $\text{H}_6\text{dappa}$ ,  $[\text{La}(\text{H}_x\text{dappa})]^{x-3}$ ,  $[\text{In}(\text{H}_2\text{dappa})]^-$  and  $[\text{Bi}(\text{H}_x\text{dappa})]^{x-3}$  (top-bottom) ( $\text{D}_2\text{O}$ , 162 MHz, 298 K). (c)  $^1\text{H}$ - $^1\text{H}$  COSY-45 NMR spectrum of  $[\text{La}(\text{H}_x\text{dappa})]^{x-3}$  ( $x = \text{not determined}$ ). Ligand/ $\text{La}^{3+}$  spectra pD 7,  $\text{In}^{3+}/\text{Bi}^{3+}$  spectra pD 1 .....89

**Figure 4.2** Speciation diagrams for  $\text{H}_6\text{dappa}$  complexes calculated from values in Table 4.2 (298 K,  $I = 0.16 \text{ M NaCl}$ ); dashed lines indicate physiological pH (7.4) (conditions simulated with HySS:  $[\text{H}_6\text{dappa}] = 1 \text{ mM}$ ,  $[\text{M}^{3+}] = 1 \text{ mM}$ ).....93

**Figure 4.3** pM values versus ionic radii for  $[\text{M}(\text{dappa})]^{3-}$  complexes (CN = 8).....93

**Figure 4.4** Concentration- and pH-dependent radiolabeling of  $\text{H}_6\text{dappa}$  (10 min, RT) in  $\text{NH}_4\text{OAc}$  solution (0.1 M) with (A)  $^{111}\text{In}]/\text{In}^{3+}$ , (B)  $^{177}\text{Lu}]/\text{Lu}^{3+}$  and (C)  $^{90}\text{Y}]/\text{Y}^{3+}$ . (D) Time-

and temperature-dependent radiolabeling of H <sub>6</sub> dappa (10 <sup>-5</sup> M) in NH <sub>4</sub> OAc solution (0.1 M, pH 5.5) with [ <sup>177</sup> Lu]Lu <sup>3+</sup> .....	95
<b>Figure 4.5</b> Structures of selected DFT calculated metal complexes.....	98
<b>Figure 4.6</b> DFT simulated structures of In <sup>3+</sup> -dappa complexes. Energies referenced to In-dappa structure in Figure 4.5 (set to zero).....	100
<b>Figure 5.1</b> Thorium-228 decay chain.....	111
<b>Figure 5.2</b> Design principle behind DTPAm .....	113
<b>Figure 5.3</b> <sup>1</sup> H NMR spectra of DTPAm (top) and [Pb(DTPAm)] <sup>2+</sup> (bottom) (D <sub>2</sub> O, pD = 7, 300 MHz).....	115
<b>Figure 5.4</b> ORTEP diagrams of the cation in [Pb(DTPAm)](NO <sub>3</sub> ) <sub>2</sub> .....	116
<b>Figure 5.5</b> Experimental (blue) and calculated (red) titration curves for DTPAm; a) calculated curve does not include pK <sub>a</sub> values; b) calculated curve includes three pK <sub>a</sub> values (9.37, 5.99, 2.33).....	120
<b>Figure 5.6</b> Speciation diagram of DTPAm calculated from values shown in Table 5.2 using HySS software .....	120
<b>Figure 5.7</b> Speciation diagram of the Pb <sup>2+</sup> -DTPAm complex .....	121
<b>Figure 5.8</b> HPLC radiochromatograms of free [ <sup>203</sup> Pb]Pb <sup>2+</sup> (top) and [ <sup>203</sup> Pb][Pb(DTPAm)] <sup>2+</sup> (bottom) .....	124
<b>Figure 6.1</b> Plot of pH dependent <sup>31</sup> P chemical shift applied to calculate pK <sub>a</sub> values of H <sub>4</sub> dppa using the HypNMR2008 software .....	140
<b>Figure 6.2</b> Speciation diagram for the La <sup>3+</sup> -dppa system derived from Table 6.2 (298 K, I = 0.16 M NaCl). [La <sup>3+</sup> ] = 6.64 × 10 <sup>-4</sup> M; [dppa] = 6.55 × 10 <sup>-4</sup> M .....	140

**Figure 6.3** (left) Portion of the  $^1\text{H}$  NMR spectra for the  $\text{La}^{3+}$ -dppa system at various pH levels (400 MHz, 298 K);  $[\text{La}^{3+}] = 0.010 \text{ M}$ ;  $[\text{dppa}] = 0.015 \text{ M}$ . (right)  $^{31}\text{P}\{^1\text{H}\}$  NMR chemical shift dependence on pH of the  $\text{La}^{3+}$ -dppa system ( $[\text{La}^{3+}] = 0.010 \text{ M}$ ;  $[\text{dppa}] = 0.015 \text{ M}$ ) at 298 K .....142

**Figure 6.4** (left)  $\text{La}^{3+}$  tissue distribution from the oral administration of  $\text{La}(\text{dpp})_3$  (two formulations) or  $\text{La}(\text{XT})$  (50 mg/kg/day) in healthy SD rats ( $n = 4$ ; mean std. dev.). The control group (no drug given) is also included; (right)  $\text{La}^{3+}$  distribution within the femurs of SD rats ( $n = 4$ ) in hip, mid, and knee sections from the oral administration of  $\text{La}(\text{dpp})_3$  (two formulations) or  $\text{La}(\text{XT})$  (50 mg/kg/day) for 4-weeks, relative to a control (no drug) group .....143

**Figure 6.5** (left)  $\text{La}^{3+}$  distribution in tissue resulting from 3 different dosing levels of  $\text{La}(\text{XT})$  (50, 100, and 200 mg/kg/day) and compared to a control group (no drug) in SD rats ( $n = 4$ ; mean std. dev.). \* $p < 0.05$  versus previous treatment group. (right)  $\text{La}^{3+}$  distribution in femurs of SD rats ( $n = 4$ ) following oral administration of  $\text{La}(\text{XT})$  (50, 100, or 200 mg/kg/day) for 4-weeks relative to a control (no drug). \* $p < 0.05$  versus previous treatment group .....145

**Figure 6.6** Speciation diagram of the  $\text{La}^{3+}$ -DEDA-(PO) system from potentiometric titrations. (25 °C,  $I = 0.16 \text{ M}$ ). a)  $[\text{L}] = 8.11 \times 10^{-4} \text{ M}$ ;  $[\text{La}^{3+}] = 7.70 \times 10^{-4} \text{ M}$ . b)  $[\text{L}] = 9.52 \times 10^{-4} \text{ M}$ ;  $[\text{La}^{3+}] = 4.67 \times 10^{-4} \text{ M}$  .....147

**Figure 6.7** Portions of the  $^1\text{H}$  NMR spectra of the  $\text{La}^{3+}$ -DEDA-(PO) system (400 MHz, 298 K): (left) 1:1 M/L molar ratio and  $[\text{L}] = 0.008 \text{ M}$ ; (right) 1:2 M/L molar ratio and  $[\text{L}] = 0.008 \text{ M}$ . A:  $\text{La}(\text{DEDA}-(\text{PO}))$ . B:  $\text{La}(\text{DEDA}-(\text{PO}))_2^{3-}$  .....148

**Figure 6.8** Portions of the  $^{31}\text{P}$  NMR spectra of the  $\text{La}^{3+}$ -DEDA-(PO) system (162 MHz, 298 K): (left) 1:1 M/L molar ratio and  $[\text{L}] = 0.008 \text{ M}$ ; (right) 1:2 M/L molar ratio and  $[\text{L}] = 0.008 \text{ M}$ . A:  $\text{La}(\text{DEDA}-(\text{PO}))$ . B:  $\text{La}(\text{DEDA}-(\text{PO}))_2^{3-}$  .....148

<b>Figure A.1</b> ORTEP diagrams of H <sub>6</sub> dipedpa with water H-bonding .....	190
<b>Figure A.2</b> <sup>1</sup> H NMR spectrum of the In <sup>3+</sup> -H <sub>6</sub> dipedpa complex (400 MHz, 298 K, D <sub>2</sub> O, pD = 7).....	190
<b>Figure A.3</b> <sup>31</sup> P{ <sup>1</sup> H} NMR spectrum (bottom) of the In <sup>3+</sup> -H <sub>6</sub> dipedpa complex (162 MHz, 298 K, D <sub>2</sub> O, pD = 7).....	191
<b>Figure A.4</b> <sup>1</sup> H- <sup>1</sup> H COSY spectrum of the In <sup>3+</sup> -H <sub>6</sub> dipedpa complex (400 MHz, 298 K, D <sub>2</sub> O, pD = 7).....	191
<b>Figure A.5</b> <sup>31</sup> P{ <sup>1</sup> H} NMR spectrum of the La <sup>3+</sup> -H <sub>6</sub> dipedpa complex (162 MHz, 298 K, D <sub>2</sub> O, pD = 7).....	192
<b>Figure A.6</b> <sup>1</sup> H- <sup>1</sup> H COSY spectrum of the La <sup>3+</sup> -H <sub>6</sub> dipedpa complex (400 MHz, 298 K, D <sub>2</sub> O, pD = 7).....	192
<b>Figure A.7</b> <sup>31</sup> P{ <sup>1</sup> H} NMR spectrum of the Sc <sup>3+</sup> -H <sub>6</sub> dipedpa complex (162 MHz, 298 K, D <sub>2</sub> O, pD = 7).....	193
<b>Figure A.8</b> <sup>1</sup> H- <sup>1</sup> H COSY spectrum of the Sc <sup>3+</sup> -H <sub>6</sub> dipedpa complex (400 MHz, 298 K, D <sub>2</sub> O, pD = 7).....	193
<b>Figure A.9</b> <sup>1</sup> H NMR spectrum (top) of the Y <sup>3+</sup> -H <sub>6</sub> dipedpa complex (400 MHz, 298 K, D <sub>2</sub> O, pD = 7); <sup>31</sup> P{ <sup>1</sup> H} NMR spectrum (bottom) of the Y <sup>3+</sup> -H <sub>6</sub> dipedpa complex (162 MHz, 298 K, D <sub>2</sub> O, pD = 7).....	194
<b>Figure A.10.</b> <sup>1</sup> H NMR spectrum (top) of the In <sup>3+</sup> -H <sub>6</sub> eppy complex (400 MHz, 298 K, D <sub>2</sub> O, pD = 7); <sup>31</sup> P{ <sup>1</sup> H} NMR spectrum (bottom) of the In <sup>3+</sup> -H <sub>6</sub> eppy complex (162 MHz, 298 K, D <sub>2</sub> O, pD = 7).....	195
<b>Figure A.11</b> <sup>1</sup> H- <sup>1</sup> H COSY spectrum of the In <sup>3+</sup> -H <sub>6</sub> eppy complex (400 MHz, 298 K, D <sub>2</sub> O, pD = 7).....	196

<b>Figure A.12</b> $^{31}\text{P}\{^1\text{H}\}$ NMR spectrum of the $\text{La}^{3+}$ - $\text{H}_6\text{eppy}$ complex (162 MHz, 298 K, $\text{D}_2\text{O}$ , pD = 4).....	196
<b>Figure A.13</b> $^1\text{H}$ NMR spectrum (top) of the $\text{Lu}^{3+}$ - $\text{H}_6\text{eppy}$ complex (400 MHz, 298 K, $\text{D}_2\text{O}$ , pD = 4); $^{31}\text{P}\{^1\text{H}\}$ NMR spectrum (bottom) of the $\text{Lu}^{3+}$ - $\text{H}_6\text{eppy}$ complex (162 MHz, 298 K, $\text{D}_2\text{O}$ , pD = 4).....	197
<b>Figure A.14</b> $^1\text{H}$ - $^1\text{H}$ COSY spectrum of the $\text{Lu}^{3+}$ - $\text{H}_6\text{eppy}$ complex (400 MHz, 298 K, $\text{D}_2\text{O}$ , pD = 4).....	198
<b>Figure A.15</b> $^{31}\text{P}\{^1\text{H}\}$ NMR spectrum of the $\text{Sc}^{3+}$ - $\text{H}_6\text{eppy}$ complex (162 MHz, 298 K, $\text{D}_2\text{O}$ , pD = 4).....	198
<b>Figure A.16</b> $^1\text{H}$ - $^1\text{H}$ COSY spectrum of the $\text{Sc}^{3+}$ - $\text{H}_6\text{eppy}$ complex (400 MHz, 298 K, $\text{D}_2\text{O}$ , pD = 4).....	199
<b>Figure A.17</b> $^1\text{H}$ NMR spectrum (top) of the $\text{Y}^{3+}$ - $\text{H}_6\text{eppy}$ complex (400 MHz, 298 K, $\text{D}_2\text{O}$ , pD = 4); $^{31}\text{P}\{^1\text{H}\}$ NMR spectrum (bottom) of the $\text{Y}^{3+}$ - $\text{H}_6\text{eppy}$ complex (162 MHz, 298 K, $\text{D}_2\text{O}$ , pD = 4).....	200
<b>Figure A.18</b> $^1\text{H}$ - $^1\text{H}$ COSY spectrum of the $\text{Y}^{3+}$ - $\text{H}_6\text{eppy}$ complex (400 MHz, 298 K, $\text{D}_2\text{O}$ , pD = 4).....	201
<b>Figure A.19</b> $^1\text{H}$ NMR spectrum (top) of the $\text{In}^{3+}$ - $\text{H}_6\text{phospa}$ complex (400 MHz, 298 K, $\text{D}_2\text{O}$ , pD = 7); $^{31}\text{P}\{^1\text{H}\}$ NMR spectrum (bottom) of the $\text{In}^{3+}$ - $\text{H}_6\text{phospa}$ complex (162 MHz, 298 K, $\text{D}_2\text{O}$ , pD = 7).....	202
<b>Figure A.20</b> $^{31}\text{P}\{^1\text{H}\}$ NMR spectrum of the $\text{La}^{3+}$ - $\text{H}_6\text{phospa}$ complex (162 MHz, 298 K, $\text{D}_2\text{O}$ , pD = 7).....	202
<b>Figure A.21</b> $^1\text{H}$ - $^1\text{H}$ COSY spectrum of the $\text{La}^{3+}$ - $\text{H}_6\text{phospa}$ complex (400 MHz, 298 K, $\text{D}_2\text{O}$ , pD = 7).....	203

<b>Figure A.22</b> $^1\text{H}$ NMR spectrum (top) of the $\text{Lu}^{3+}$ - $\text{H}_6\text{phospa}$ complex (400 MHz, 298 K, $\text{D}_2\text{O}$ , pD = 7); $^{31}\text{P}\{^1\text{H}\}$ NMR spectrum (bottom) of the $\text{Lu}^{3+}$ - $\text{H}_6\text{phospa}$ complex (162 MHz, 298 K, $\text{D}_2\text{O}$ , pD = 7).....	204
<b>Figure A.23</b> $^1\text{H}$ - $^1\text{H}$ COSY spectrum of the $\text{Lu}^{3+}$ - $\text{H}_6\text{phospa}$ complex (400 MHz, 298 K, $\text{D}_2\text{O}$ , pD = 7).....	205
<b>Figure A.24</b> $^{31}\text{P}\{^1\text{H}\}$ NMR spectrum of the $\text{Sc}^{3+}$ - $\text{H}_6\text{phospa}$ complex (162 MHz, 298 K, $\text{D}_2\text{O}$ , pD = 4).....	205
<b>Figure A.25</b> $^1\text{H}$ - $^1\text{H}$ COSY spectrum of the $\text{Sc}^{3+}$ - $\text{H}_6\text{phospa}$ complex (400 MHz, 298 K, $\text{D}_2\text{O}$ , pD = 4).....	206
<b>Figure A.26</b> $^1\text{H}$ NMR spectrum (top) of the $\text{Y}^{3+}$ - $\text{H}_6\text{phospa}$ complex (400 MHz, 298 K, $\text{D}_2\text{O}$ , pD = 7); $^{31}\text{P}\{^1\text{H}\}$ NMR spectrum (bottom) of the $\text{Y}^{3+}$ - $\text{H}_6\text{phospa}$ complex (162 MHz, 298 K, $\text{D}_2\text{O}$ , pD = 7).....	207
<b>Figure A.27</b> Normalized $^{31}\text{P}\{^1\text{H}\}$ NMR chemical shift dependence on pH overlaid to speciation plot calculated with protonation constants from Table X, a); Normalized $^1\text{H}$ NMR methylene chemical shift dependence on pH (H1, H2, H3) overlaid to $\text{H}_6\text{phospa}$ speciation plot, b, c and d). $[\text{H}_6\text{phospa}] = \text{M}$ , $T = 298 \text{ K}$ .....	208–210
<b>Figure A.28</b> Representative spectra of $\text{H}_6\text{phospa}$ during (a/b) acidic in-batch UV spectrophotometric titration $[\text{L}] = 7.77 \times 10^{-5} \text{ M}$ , $T = 298 \text{ K}$ , $l = 1 \text{ cm}$ , $I = 0.16 \text{ M NaCl}$ when possible; (c/d) combined UV-potentiometric titration $[\text{L}] = 4.84 \times 10^{-4} \text{ M}$ , $T = 298 \text{ K}$ , $l = 0.2 \text{ cm}$ , $I = 0.16 \text{ M NaCl}$ .....	211
<b>Figure A.29</b> Representative spectra of $\text{H}_6\text{dipedpa}$ during (a/b) acidic in-batch UV spectrophotometric titration $[\text{L}] = 7.11 \times 10^{-5} \text{ M}$ , $T = 298 \text{ K}$ , $l = 1 \text{ cm}$ , $I = 0.16 \text{ M NaCl}$ when possible; (c/d) combined UV-potentiometric titration $[\text{L}] = 6.76 \times 10^{-4} \text{ M}$ , $T = 298 \text{ K}$ , $l = 0.2$	

cm,  $I = 0.16$  M NaCl; (f) speciation plot of  $H_6dipedpa$  calculated with stability constants in Table 3.1,  $[H_6dipedpa] = 0.001$  M; dashed line indicates  $pH = 7.4$  .....212–213

**Figure A.30** Representative spectra of  $H_6eppy$  during (a/b) acidic in-batch UV spectrophotometric titration  $[L] = 7.25 \times 10^{-5}$  M,  $T = 298$  K,  $l = 1$  cm,  $I = 0.16$  M NaCl when possible; (c/h) combined UV-potentiometric titration  $[L] = 7.15 \times 10^{-4}$  M,  $T = 298$  K,  $l = 0.2$  cm,  $I = 0.16$  M NaCl.....214–215

## List of Charts

<b>Chart 3.1</b> Medicinal applications and corresponding examples of chelating ligands .....	47
<b>Chart 3.2</b> Phosphonate-bearing picolinic acid-based chelators. Top: previously reported (not described); Bottom: under investigation in this work .....	51
<b>Chart 6.1</b> Structures of ligands discussed throughout Chapter 6 .....	132
<b>Chart 6.2</b> Structures of the two lanthanum-based lead compounds discussed in this section .....	134
<b>Chart 7.1</b> Comparison of DTPAm and suggested ligands for future lead-based radiopharmaceuticals .....	155
<b>Chart 7.2</b> Phosphonate-bearing ligands of potential future interest .....	157

## List of Symbols

$^{\circ}$	degrees
$^{\circ}\text{C}$	degrees Celsius
$\text{\AA}$	angstrom $1 \times 10^{-10}$ m
$\sim$	approximate
$\alpha$	alpha; representative of helium nucleus
$\beta^{+}$	positron; representative of an anti-electron
$\beta$	beta; representative of an electron
$\gamma$	gamma
$\delta$	delta of chemical shift in parts per million
$\Delta$	heat or reflux
$\sigma$	cross-section
$C_A$	covalent contribution to hardness parameter ( $I_A$ )
$E_A$	electrostatic contribution to hardness parameter ( $I_A$ )
$I$	ionic strength
$I_A$	hardness parameter, $I_A = E_A/C_A$
$K_{ML}$	formation constant
$p/e$	photon-to-electron ratio
$pK_a$	protonation constant; $pK_a = -\log K_a$
$pM$	$p\text{Metal} = -\log[\text{metal}]$
$t_{1/2}$	half-life
$T_m$	melting temperature
$t_R$	retention time (HPLC)

## List of Abbreviations

AA	atomic absorption
AAS	atomic absorption standard
ACN	acetonitrile
b	barn, $1\text{b} = 10^{-24}\text{ cm}^2$
BBN	bombesin
BFC	bifunctional chelator
Bn	benzyl
Bq	becquerel, SI unit of radioactivity ( $\text{s}^{-1}$ )
Bq/g	becquerel per gram
Bq/mol	becquerel per mole
c.a.	carrier-added
calcd	calculated
$\text{CDCl}_3$	deuterated chloroform ( $\text{d}_7$ )
CE	conversion electron
CEST	chemical exchange-dependent saturation transfer
CHX	cyclohexane/cyclohexyl
CHX-DTPA	( <i>N</i> -(2-aminoethyl)- <i>trans</i> -1,2-diaminocyclohexane- <i>N,N',N''</i> -pentaacetic acid
CN	coordination number
COSY	correlation spectroscopy
CT	computed tomography
$\text{D}_2\text{O}$	deuterium oxide
Da	dalton
DCC	<i>N,N'</i> -dicyclohexylcarbodiimide
DCM	dichloromethane
DEPA	7-[2-(bis-carboxymethyl-amino)-ethyl]-4,10-bis-carboxymethyl-1,4,7,10-tetraazacyclododec-1-yl-acetic acid
DFO	deferoxamine
DFT	density functional theory

DMSA	dimercaptosuccinic acid
DOTA	1,4,7,10-tetraazacyclododecane-1,4,7,10-tetraacetic acid
dpa	dipicolinate
DTPA	1,1,4,7,7-diethylenetriaminepentaacetic acid
DTPAm	diethylenetriamine- <i>N,N',N',N'',N''</i> -pentaacetamide
DTT	dithiothreitol
EA	elemental analysis
EC	electron capture
ECP	effective core potential
EDC	1-ethyl-3-(3-dimethylaminopropyl)carbodiimide
EDDA	ethylenediamine- <i>N,N'</i> -diacetic acid
EDTA	ethylenediaminetetraacetic acid
EDTMP	ethylenediamine tetra(methylene phosphonic acid)
en	ethylenediamine
EOB	end of bombardment
eq	equivalent(s)
EtOAc	ethyl acetate
EtOH	ethanol
eV	electron volt
FDA	U.S. Food and Drug Administration
[ <sup>18</sup> F]FDG	<sup>18</sup> F-fluorodeoxyglucose
GIAO	gauge-including atomic orbital
GRP	gastrin releasing peptide
H <sub>2</sub> dedpa	<i>N,N'</i> -dipicolinate ethylene diamine
H <sub>4</sub> octapa	<i>N,N'</i> -bis(6-carboxy-2-pyridylmethyl)ethylenediamine- <i>N,N'</i> -diacetic acid
HA	hydroxyapatite
HER2	human epidermal growth factor 2
HOBt	hydroxybenzotriazole
HOMO	highest occupied molecular orbital
HPLC	high-performance liquid chromatography

HR-ESI-MS	high resolution electrospray ionization mass spectrometry
HSAB theory	hard-soft acid-base theory
IEFPCM	integral equation formalism of the polarizable continuum model
ICP-AES	inductively coupled plasma atomic emission spectroscopy
ICP-MS	inductively coupled plasma mass spectrometry
IT	isomeric transition
L	ligand or litre
LET	linear energy transfer
LINAC	linear accelerator
log <i>K</i>	log stability constant
LR-ESI-MS	low resolution electrospray ionization mass spectrometry
LUMO	lowest unoccupied molecular orbital
<i>m/z</i>	mass-to-charge ratio
mAb	monoclonal antibody
MeOH	methanol
MIBI	methoxyisobutylisonitrile
MRI	magnetic resonance imaging
n.c.a.	no-carrier-added
NHS	<i>N</i> -hydroxysuccinimide
NMR	nuclear magnetic resonance
NOC	NaI <sup>3</sup> -octreotide
NOTA	1,4,7-triazacyclononane-1,4,7-triacetic acid
NOTP	1,4,7-triazacyclononane-1,4,7-tri(methylene phosphonic acid)
ORTEP	Oak Ridge Thermal-Ellipsoid Plot
pa	picolinic acid
PBS	phosphate-buffered saline
PCTA	3,6,9,15-tetraazabicyclo[9.3.1]pentadeca-1(15),11,13-triene-3,6,9-triacetic acid
PEG	polyethylene glycol
PET	positron emission tomography

pH	$-\log[\text{H}_3\text{O}^+]$
PSMA	prostate-specific membrane antigen
RCY	radiochemical yield
RGD	arginylglycylaspartic acid, Arg-Gly-Asp
ROS	reactive oxygen species
RP	reverse phase
RSC	relativistic small core
SCF	self-consistent field
SPECT	single-photon emission computed tomography
SST	somatostatin
TAT	targeted alpha therapy
TATE	Tyr <sup>3</sup> -octreotate
TCEP	tris(2-carboxyethyl)phosphine
TCMC	1,4,7,10-tetraaza-1,4,7,10-tetra-(2-carbamoylmethyl)-cyclododecane
TETA	1,4,8,11-tetraazacyclotetradecane-1,4,8,11-tetraacetic acid
TFA	trifluoroacetic acid
TLC	thin-layer chromatography
TOC	Phe <sup>1</sup> -Tyr <sup>3</sup> -octreotide
TOF	time-of-flight
TRAP	1,4,7-triazacyclononane-1,4,7-tris[methyl(2-carboxyethyl)phosphinic acid]
TRT	targeted radionuclide therapy
TTHA	triethylenetetramine- <i>N,N,N',N'',N''',N''''</i> -hexaacetic acid
XRD	X-ray diffraction

## List of Schemes

<b>Scheme 3.1</b> H <sub>6</sub> phospa and H <sub>6</sub> dipedpa synthesis .....	53
<b>Scheme 3.2</b> H <sub>6</sub> eppy synthesis .....	54
<b>Scheme 4.1</b> Design principle of H <sub>6</sub> dappa .....	83
<b>Scheme 4.2</b> Synthetic scheme for H <sub>6</sub> dappa.....	86
<b>Scheme 5.1</b> Synthesis of DTPAm.....	114
<b>Scheme 6.1</b> Reported synthesis of TETA-(PO) <sub>2</sub> that resulted in the production of DEDA-(PO) .....	135
<b>Scheme 6.2</b> Synthesis of H <sub>4</sub> dppa .....	137
<b>Scheme 6.3</b> Synthesis of K <sub>2</sub> [La(XT)] .....	137

## List of Equations

**Equation 3.1** Cumulative formation constant  $\beta(M_p H_q L_r)$  .....60

**Equation 4.1** Percent stability using PD-10 column for serum stability assay .....109

## Acknowledgements

To my parents, brother, and sister, thank you for your endless love and support. My visits home, and your trips to Vancouver, have been highlights of the last five years. I feel very lucky to have such a strong family unit that never hesitates to share positivity and encouragement. I could never have done this without you.

To my research group, our collective time spent together has been the most enriching part of my Ph.D. experience. You've become a family away from my own, and I will sincerely miss you all.

During my early time in the group, I was lucky to become close to Sarah, who embodied the Boss's motto, "work hard, play hard." Thank you for your persistent encouragement, all the laughs and gossip, and for always reminding me that if you want something, you have to go and get it! Thanks to Dave for being the inspiration for much of the research within this thesis, and for showing me that a bit of finesse goes a long way. And to Hunter, for exemplifying the fruits of academic curiosity, and always being a source of stimulating conversation.

Although it was difficult watching the old group move on, the time I've spent with the new group has been its own adventure. Neha, your energy and positivity are never in short supply. Thank you for showing me that we should all try to channel our 'inner kid' every once in a while, and for teaching me that good friends are worth fighting for. Aidan, you have always been a source of thoughtful conversation when I needed it most. Thank you for showing me the depth of friendship that can follow when you show true concern for others. Luke, your work ethic blows me away. No matter how focused you are, you never cease to lend a hand. Thanks for always being such a kind and helpful individual. Lily Southcott, you have most definitely nailed the "work hard, play hard" mentality. Thanks for all the thought-provoking conversations in lab, and all the great times on the slopes. Jeff, thank you for always eagerly embracing the handy-man role and keeping the lab up and running. The only thing we miss more than the upkeep is your quirky, likeable presence in the group.

To the visiting students and undergrads, working with all of you so closely has taught me that no two individuals operate the same. Every project and student have their own quirks, but that's what makes each experience so wonderfully unique. A special thanks to Una Jermilova for the hard work and liveliness you brought to the lab for eight months. Thanks to Felix Lindheimer, Hannah Wagner, Victoria Brown, and Jenasee Mynerich for all your help through the various stages of projects either at UBC or TRIUMF. And thanks to Alex Dimmling, Tom Clough and David Bauer for all the fun times during your stints in Vancouver; you all left too soon. A big thanks to my long-time roommate Jess, whose east-coast attitude always brings me home. And a special thanks to Holly, whose love and support have never waivered and often kept me afloat.

To Dr. Lupita, you are genuinely the kindest person I know. Your unwavering desire to give to others is an inspiration. Thank you for all the love and support over the years, I feel very fortunate to call you a friend.

To the Boss, thank you for accepting me into your group and giving me this unforgettable experience. You've fostered a work environment with rich values, and given each of your students space to grow within it. I can't express how thankful I feel to have been part of such a terrific group of people, and to have been given so much academic and personal freedom to explore the person I want to become. Thank you for always building me up, and for your infectious optimism. I will forever cherish the time I spent in your group.

## **Chapter 1. Introduction**

### **1.1 Nuclear Medicine and Radiopharmaceuticals**

Nuclear medicine is a rapidly growing, interdisciplinary field based on the use of radioactive nuclides for diagnostic and therapeutic purposes. The development of radiopharmaceuticals is a key aspect of expanding the clinical capabilities of nuclear medicine physicians and is achieved by continually improving the existing framework of current drug design. Radiopharmaceuticals are divided into two broad classes; organically-derived and metal-based. These classes primarily differ in their strategy of radionuclide incorporation. Organically-derived radiopharmaceuticals incorporate non-metal radionuclides (e.g.,  $^{18}\text{F}$ ,  $^{11}\text{C}$ ,  $^{13}\text{N}$ ,  $^{15}\text{O}$ ,  $^{123}\text{I}$ ) by covalent bond formation, often replacing one hydrogen atom, whereas metal-based tracers rely on coordination chemistry. The short half-lives and limited decay characteristics of most “organic” radionuclides severely limit their applications. Radiometals offer a variety of decay characteristics (Figure 1.1), and as such, will be the focus of this work.

### **1.2 Metal-Based Radiopharmaceutical Drug Design**

Within the realm of metal-based radiopharmaceuticals, two prominent categories exist; metal essential and metal non-essential. The distinction between these classes is the role of the radiometal. In metal-essential drugs, the radiometal is fundamental for biological targeting. For example,  $^{99\text{m}}\text{Tc}$ -sestamibi (Cardiolite<sup>®</sup>) is a cardiac imaging agent comprised of a  $^{99\text{m}}\text{Tc}^+$  centre coordinated by six methoxyisobutylisonitrile (MIBI) ligands. The arrangement of these lipophilic ligands around the metal facilitates heart uptake of  $^{99\text{m}}\text{Tc}$ -sestamibi; however, if  $^{99\text{m}}\text{Tc}^+$  were replaced by a different metal ion or was absent altogether, the resulting biodistribution would be profoundly different.<sup>1</sup> Although metal-essential drugs are simple to

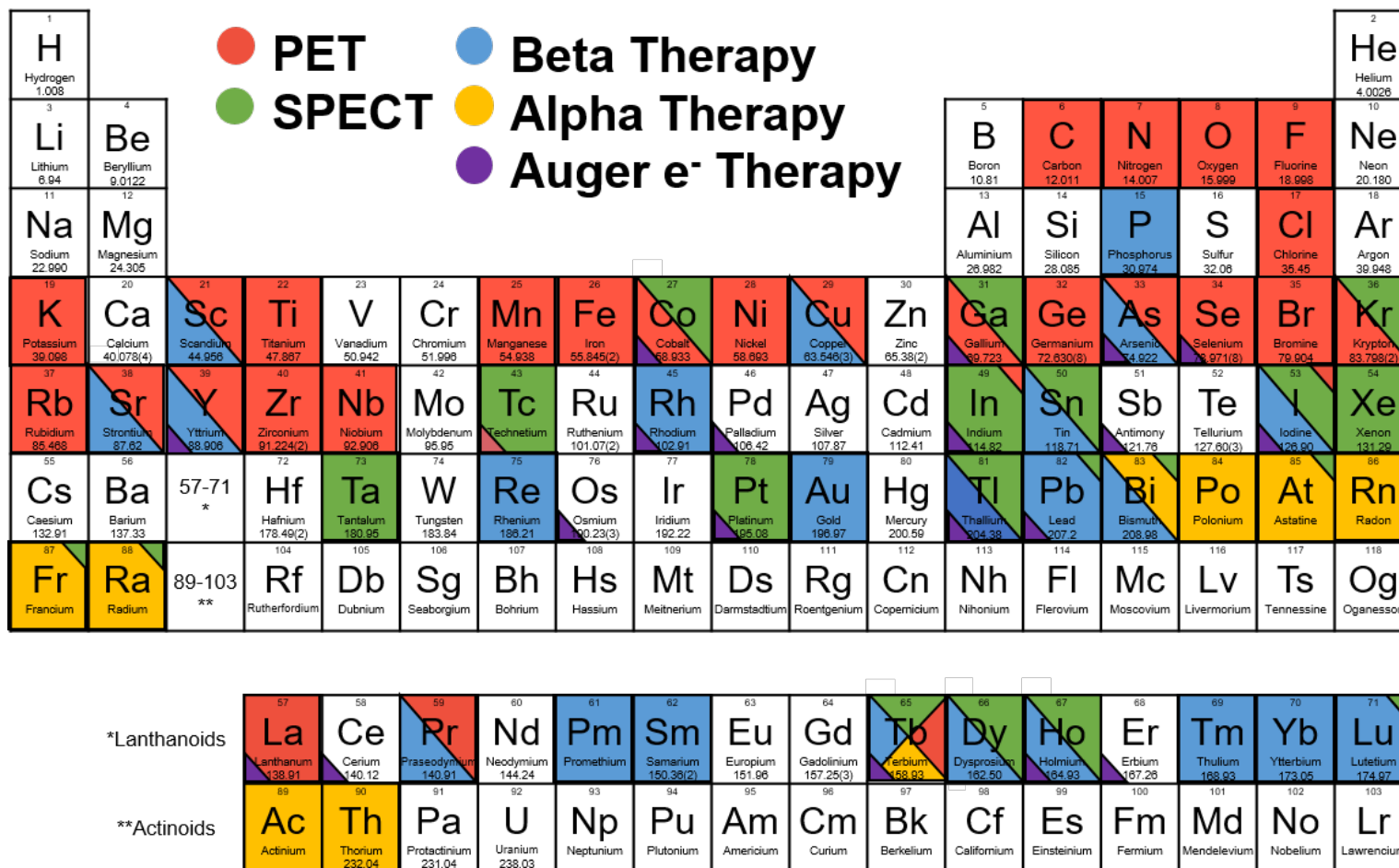


**Figure 1.1** Colour coded Periodic Table with current or potential applications of each element in diagnostic and/or therapeutic radiopharmaceuticals.<sup>2-15</sup> Periodic Table reproduced by permission of International Union of Pure and Applied Chemistry. Copyright © 2018 International Union of Pure and Applied Chemistry. Reproduced from reference 2.

synthesize, they are challenging to derivatize. In contrast, metal non-essential tracers are modular by design and in theory exhibit metal-independent *in vivo* behaviour. Readers are cautioned that in practice, metal choice can influence drug biodistribution (see Section 1.3.3); however, compared to metal essential radiopharmaceuticals, this influence is relatively small. Most metal non-essential design strategies divide the drug into four parts: radiometal, ligand/chelator, linker and bioconjugate/targeting vector (Figure 1.2). In this case, the decay properties of the radiometal are the root of diagnostic/therapeutic function, while the bioconjugate ensures drug accumulation at target cells. The chelator and linker integrate the two otherwise incompatible components. This design is very popular, as it permits alteration of individual components to tune drug function, providing enormous potential for ‘plug-and-play’ drug discovery. Unless otherwise stated, all discussed radiotracers throughout this thesis emulate this design.

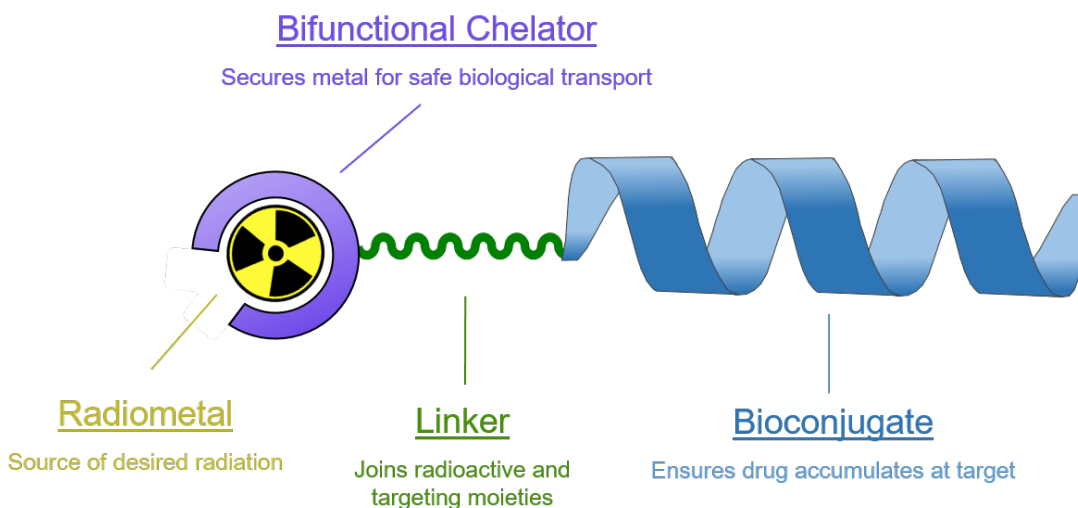


**Figure 1.2** Standard, four-component radiopharmaceutical design. Reproduced from reference 2.

### 1.3 Importance of Radiometal Decay for Drug Function

Radiometal decay properties determine radiopharmaceutical function. Diagnostic radiometals emit radiation that minimally interacts with biological tissue, allowing it to easily escape the body and reach external detectors. Therapeutic radiometals emit radiation intended to maximally interact with surrounding tissue in order to exert a toxic effect locally. These differences in radiation behaviour are heavily reliant on radiometal decay characteristics. Table 1.1 presents decay properties, applications and production routes of popular radiometals, and may be helpful for reference in the following discussion. Figure 1.3 illustrates decay-specific applications.

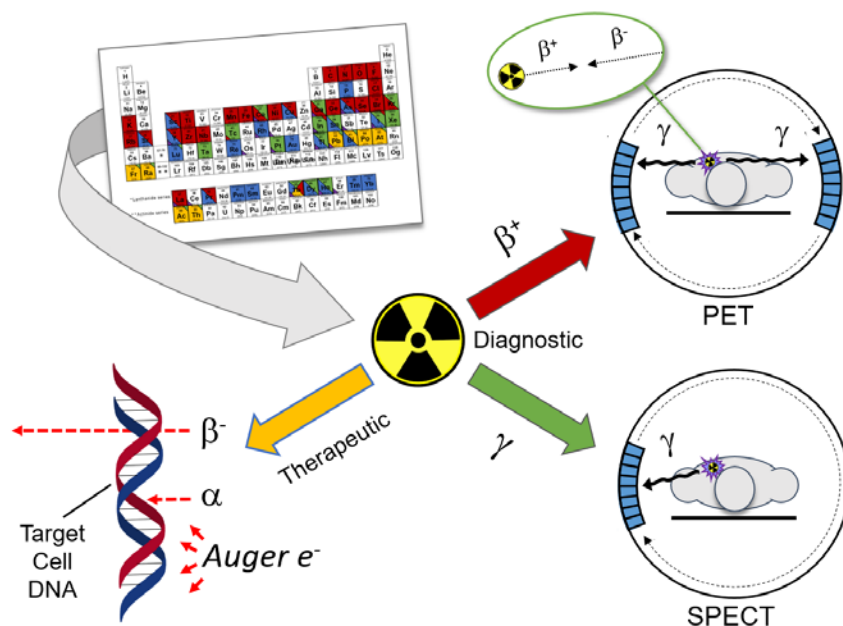


**Figure 1.3** Radiometal decay types, and their corresponding applications in nuclear medicine.

Reproduced from reference 2.

**Table 1.1** Popular subject radiometals with relevant production routes, decay parameters and applications<sup>16-21</sup>

Reproduced from reference 2.

<i>Radionuclide</i>	<i>Production</i>	<i>Half Life (h)</i>	<i>Decay mode and branching</i>	<i>Average energy of decay particle (keV)<sup>a</sup></i>	<i>Max Gamma energy (keV)(Intensity %)</i>	<i>Application</i>
<sup>44</sup> Sc	<sup>44</sup> Ca(p,n) <sup>44</sup> Sc <sup>44</sup> Ti/ <sup>44</sup> Sc generator	4.04	$\beta^+$ (94%) EC (6%)	632	1157 (100%)	PET
<sup>47</sup> Sc	<sup>47</sup> Ti(n,p) <sup>47</sup> Sc <sup>46</sup> Ca(n, $\gamma$ ) <sup>47</sup> Ca $\rightarrow$ <sup>47</sup> Sc	80.4	$\beta$ (100%)	162	159 (68%)	$\beta$ Therapy SPECT
<sup>66</sup> Ga	<sup>66</sup> Zn(p,n) <sup>66</sup> Ga	9.49	$\beta^+$ (57%) EC (43%)	1747	1039 (37%) 2752 (23%)	PET
<sup>67</sup> Ga	<sup>67</sup> Zn(p,n) <sup>67</sup> Ga	78.2	EC (100%) 4.7 e <sup>-</sup> /decay <sup>b</sup>	Auger: 6.3 <sup>b</sup>	93 (39%) 185 (21%) 300 (17%)	SPECT
<sup>68</sup> Ga	<sup>68</sup> Ge/ <sup>68</sup> Ga generator	1.13	$\beta^+$ (89%) EC (11%)	830	-	PET
<sup>86</sup> Y	<sup>86</sup> Sr(p,n) <sup>86</sup> Y	14.7	$\beta^+$ (32%) EC (68%)	664	777 (22%) 1077 (83%) 1153 (31%)	PET
<sup>90</sup> Y	<sup>90</sup> Sr/ <sup>90</sup> Y generator	64.0	$\beta$ (100%)	934	-	$\beta$ Therapy
<sup>110m</sup> In	<sup>110</sup> Cd(p,n) <sup>110m</sup> In	1.15	$\beta^+$ (61%) EC (39%)	1011	658 (98%)	PET
<sup>111</sup> In	<sup>nat</sup> Cd(p,xn) <sup>111</sup> In	67.2	EC (100%) 14.7 e <sup>-</sup> /decay <sup>b</sup>	Auger: 6.8 <sup>b</sup>	245 (94%) 171 (91%)	SPECT
<sup>114m</sup> In	<sup>114</sup> Cd(p,n) <sup>114m</sup> In	1188	IT (97%)	-	190 (16%)	Auger electron therapy
<sup>177</sup> Lu	<sup>176</sup> Lu(n, $\gamma$ ) <sup>177</sup> Lu <sup>176</sup> Yb(n, $\gamma$ ) <sup>177</sup> Yb $\rightarrow$ <sup>177</sup> Lu	159	$\beta$ (100%)	134	113 (6%) 208 (10%)	$\beta$ therapy SPECT
<sup>212</sup> Bi	<sup>228</sup> Th/ <sup>212</sup> Pb/ <sup>212</sup> Bi generator	1.01	$\alpha$ (36%) $\beta$ (64%)	$\alpha$ : 6210 $\alpha$ : 8780 (daughter) $\beta$ : 771	-	$\alpha$ & $\beta$ therapy
<sup>213</sup> Bi	<sup>225</sup> Ac/ <sup>213</sup> Bi generator	0.76	$\alpha$ (2%) $\beta$ (98%)	$\alpha$ : 8.35 MeV <sup>d</sup> (daughter) $\beta$ : 435	440 (26%)	$\alpha$ & $\beta$ therapy
<sup>225</sup> Ac	<sup>229</sup> Th/ <sup>225</sup> Ac generator <sup>226</sup> Ra(p,2n) <sup>225</sup> Ac <sup>232</sup> Th(p,2p6n) <sup>225</sup> Ac	238	$\alpha$ (100%)	$\alpha$ : 5.8-8.4 MeV <sup>d</sup> (chain average)	-	$\alpha$ therapy

<sup>a</sup>Ref. 16 weighted average of average values; <sup>b</sup>Ref 18, 19; <sup>c</sup>Ref 20; <sup>d</sup>Ref 21.

### 1.3.1 Principles of Diagnostic Radiometals

Diagnostic radiotracers emit or indirectly produce photons, which are detected by high density material to produce spatial representations of drug distribution *in vivo*. Positron emission tomography (PET) and single-photon emission computed tomography (SPECT) are the most prevalent imaging modalities for this purpose.

PET imaging requires the use of positron ( $\beta^+$ ) emitters, which are normally neutron deficient radionuclides that balance their nuclear composition through the conversion of a proton to a neutron by  $\beta^+$  emission. When these positrons meet nearby electrons ( $\beta^-$ ), a process known as “annihilation” results in the simultaneous emission of near coincident ( $\sim 180^\circ$ )  $\gamma$ -rays, with a characteristic energy of 511 keV. When PET scanners detect these simultaneous  $\gamma$ -rays, computational methods precisely calculate the radiotracer location by determining the point of annihilation.<sup>22</sup> The distance a  $\beta^+$  travels before annihilation is proportional to its energy, thus emission of low energy positrons is preferred due to their close proximity to the radiotracer at the point of annihilation.<sup>23</sup> By far the most commonly used PET radiotracer is the glucose analogue, [ $^{18}\text{F}$ ]FDG ( $^{18}\text{F}$ -fluorodeoxyglucose), which has a natural propensity to be selectively taken up by aggressively growing tumours because of its similarity to glucose. The high radiotracer concentration in tumours and low background activity facilitates acquisition of high resolution images.<sup>24</sup>

Similar to traditional two-dimensional scintigraphy, SPECT is based on the detection of low-energy  $\gamma$ -rays emitted from radiotracers, often as a result of electron capture (EC) or isomeric transition (IT). Unlike scintigraphy, however, SPECT renders three-dimensional images to produce more spatially oriented representations of tracer behaviour. Due to its reliance on single emission events (as opposed to simultaneous events), SPECT detectors

require narrow  $\gamma$ -ray filtering, or “collimation”, for decay localization and sharp image construction. Low energy  $\gamma$ -rays (100-250 keV) are ideal for SPECT as they are more easily filtered by collimators and efficiently attenuated by SPECT detectors.<sup>25,26</sup> The vast majority of SPECT scans are based on  $^{99m}\text{Tc}$  radionuclides, with one of the most frequently used radiotracers being  $^{99m}\text{Tc}$ -sestamibi for heart perfusion imaging.<sup>1</sup>

Of the two techniques, PET has superior sensitivity and resolution, but is far more expensive than SPECT as a result of higher instrumentation costs and lower radionuclide availability.<sup>26–28</sup> PET and SPECT provide high quality morphological information, but lack anatomical perspective. Accordingly, they are often combined with computed tomography (CT) to produce a more complete biological representation.<sup>27</sup>

### **1.3.2 Principles of Therapeutic Radiometals**

Therapeutic radiometals primarily induce their cytotoxic effects through irreversible DNA damage, resulting in deletions, chromosome aberrations and cell death.<sup>29</sup> DNA damage can be achieved with the emission of beta ( $\beta$ ) particles, alpha ( $\alpha$ ) particles or low-energy electrons (henceforth Auger electrons). The ability of an emitted particle to damage DNA is heavily dependent on its linear energy transfer (LET), which is a measure of atom ionization/excitation per unit length, and is commonly reported in keV/ $\mu\text{m}$  for biological systems. High LET is typical of highly ionizing radiation and signifies dense energy deposition. Particles with high LET deposit their energy over shorter distances than those with low LET and are more effective at causing biological and/or chemical damage.<sup>29,30</sup> Tissue range is dependent on both a particle’s LET and kinetic energy. For example, if two particles have identical energy but different LET, the particle with higher LET will deposit its energy more

rapidly, resulting in shorter tissue range. Alternatively, if two particles have identical LET but different energy, the higher energy particle will take longer to deposit its energy, resulting in greater tissue range. Long tissue range can be useful for treatment of large tumours, but is increasingly regarded as undesirable as it is directly linked to off-target toxicity.<sup>31–33</sup> Particle LET and tissue range vary amongst therapeutic radionuclides, and are heavily influenced by the decay type and energy.

$\beta$  particles have variable energy (0.1–2.2 MeV) and relatively low LET, which typically falls in the realm of 0.2 keV/ $\mu$ m. Although  $\beta$  emitters are the most developed class of radiotherapeutics, it is known that their low LET results in a high decay range (0.5–10 mm; 50–1000 cell diameters) that often extends beyond the diameter of targeted tumours.<sup>15</sup> This can lead to the death of healthy cells (“cross-fire”) and is a major deterrent of  $\beta$  therapy. Currently, low energy  $\beta$  emitters (e.g., <sup>177</sup>Lu) are being heavily investigated due to their lower decay range relative to high energy  $\beta$  emitters (e.g., <sup>90</sup>Y).<sup>34</sup> Alpha particles have high energies (5–8 MeV), and extremely high LET (~80 keV/ $\mu$ m), resulting in low decay range (40–100  $\mu$ m; < 10 cell diameters).<sup>15</sup> Their highly ionizing nature and short tissue range is the cause of current enthusiastic efforts to explore targeted alpha therapy (TAT), notably with <sup>225</sup>Ac. Auger electrons are low-energy particles ejected as a result of energy released during the filling of inner electron-shell vacancies. These particles have high LET (4–26 keV/ $\mu$ m) and very low energy (1–10 keV), resulting in tissue range (1–20  $\mu$ m) that is often less than the diameter of a single cell (~10  $\mu$ m).<sup>15</sup> This makes cross-fire effects essentially non-existent and presents the potential to treat single cell tumour metastasis. Auger electrons are the least explored therapeutic and are currently limited by their need for cell or nucleus internalization to exert any degree of toxic effects.<sup>35</sup>

### 1.3.3 Theranostic Isotopes

Combined therapeutic and diagnostic (“theranostic”) isotopes are an emerging concept and are desirable because of their ability to diagnose, treat and evaluate treatment, simultaneously or following a therapeutic regimen. Some radiometals are inherently theranostic, generally by virtue of a therapeutic nuclide having an imageable  $\gamma$ -line (e.g.,  $^{47}\text{Sc}$ ,  $^{177}\text{Lu}$ ), however the most ideal theranostic agents are comprised of chemically identical radioisotope pairs with similar half-lives and complementary emission. In this way, the diagnostic and therapeutic decay modes are optimal (i.e., high branching, appropriate energy) and the radioisotopes exhibit identical (bio)chemical behaviour, notably with respect to the chelator. This ensures the therapeutic radiotracer behaves identically to the diagnostic radiotracer *in vivo*, which is crucial for accurate dosimetry. This is in contrast to non-chemically identical matched pairs (e.g.,  $^{111}\text{In}/^{90}\text{Y}$ ), where diagnostic information is less representative of therapeutic dose distribution due to differences in radiotracer behaviour.<sup>36</sup>

## 1.4 Production and Purity of Radionuclides

The next two sections will briefly summarize core concepts of radiometal production and purity that are relevant throughout this thesis. It should be noted that this description is by no means all encompassing, but rather an introduction for those interested but unfamiliar with the topic.

### 1.4.1 Radionuclide Production

Cyclotrons and nuclear reactors are commonly used for radionuclide production. Cyclotrons use magnetic fields to accelerate charged particles (e.g., protons, deuterons,  $\alpha$ -

particles) and produce proton-rich nuclides, which typically decay by EC or  $\beta^+$  emission in order to balance their unstable nuclear composition. Cyclotron-based production is contingent on the accelerated particle having sufficient energy to overcome the threshold energy of a given nuclear reaction, which is a result of the mass difference between nuclear reactants (i.e., target nuclide, irradiating particle) and products (i.e., product nucleus, emitted particles), as well as the electrostatic repulsion between the accelerated particle and target nuclide. These parameters are referred to as the  $Q$  value and Coulomb barrier, respectively.<sup>30</sup> Biomedical cyclotrons are most common and have beam energies below 20 MeV. These small cyclotrons are typically found in hospitals or universities, thus production routes that are compatible with low energy cyclotrons are desirable due to their greater potential for clinical use. Intermediate (20-35 MeV) and high (> 35 MeV) energy cyclotrons are also useful for medical radionuclide production, but are far less common.<sup>37</sup> Reactor production is based around the spontaneous fission of fissile materials (within fuel rods), which release neutrons capable of inducing fission or neutron activation of target material. In the latter case, the resulting nuclides are neutron rich and, if radioactive, normally decay via  $\beta$  emission. Unlike nuclide production via charged particle bombardment, no Coulomb barrier exists for neutron reactions since they are not repulsed by the positively charged nucleus or negatively charged electrons of target atoms. As such, low energy neutrons are more desirable for production via neutron capture due to their greater probability of interactions with surrounding nuclei, compared to high energy neutrons. For example, thermal neutrons have relatively low kinetic energy ( $E = 0.025$  eV) and are commonly used to produce a variety of radionuclides. For production via fission however, neutron energies must be on the order of MeV.<sup>30</sup> Cyclotrons and reactors are both vital means of radionuclide production and are often said to have complimentary roles in the field of nuclear medicine due

to the contrasting nature of produced radionuclides.<sup>38</sup> Linear accelerators (LINACS) can also be used for medical radionuclide production,<sup>39</sup> but are far less common.

In a simplified sense, activity production is proportional to the number of target atoms, beam intensity (or flux) and formation cross section, which is a measure of likelihood that a nuclear reaction will occur.<sup>30</sup> For those unfamiliar, cross-sections can be conceptualized through the analogy of trying to hit a target with a projectile. In the same way that a target with a large surface area will be easier to hit, so too does a large cross-section communicate a high probability that a nuclear reaction will occur. Cross-sections ( $\sigma$ ) are measured in barns ( $1\text{b} = 10^{-24}\text{ cm}^2$ ), and are a function of beam energy.<sup>30,40</sup> The relationship between cross-sections and beam energy is often of great interest in order to achieve maximum production yields and radionuclidic purity. Investigations of this nature are often complicated by the co-production of isotopic contaminants, which are especially problematic if long-lived and chemically identical (e.g.,  $^{177}\text{Lu}/^{177\text{m}}\text{Lu}$ ,  $^{225}\text{Ac}/^{227}\text{Ac}$ ).<sup>41,42</sup> Contaminant production can be mitigated through the use of isotopically enriched target material; however, the enrichment process can be prohibitively expensive.<sup>43</sup> Natural targets are far less expensive, but tend to yield lower radionuclidic purity and require careful optimization of irradiation parameters. The most desirable elements for target material are naturally monoisotopic (e.g.,  $^{45}\text{Sc}$ ,  $^{89}\text{Y}$ ), but unfortunately few exist.

Generators are an extremely desirable means of production and rely on long-lived parent radionuclides that can be chemically separated from desired daughters. The parent radionuclides are loaded onto a resin and eluted or “milked” once they near equilibrium (transient or secular) with their daughters, ideally resulting in isolation of activity with high radionuclidic purity. The main benefit of generator use is cyclotron/reactor-independent

radionuclide accesses, which drastically increases radionuclide availability and makes clinical use more feasible.

#### 1.4.2 Nomenclature of Radioactive Purity

Radionuclidic purity is defined as the absence of other radionuclides and is often expressed as a percentage of desired radioactivity from total radioactivity. Not to be confused with radiochemical purity, which refers to the purity of chemical species of a given radionuclide (e.g.,  $^{99m}\text{Tc}$ -sestamibi versus  $^{99m}\text{TcO}_4^-$ ), the term radionuclidic purity describes the purity of a given radionuclide with respect to other radionuclides (e.g.,  $^{72}\text{As}$  versus  $^{73}\text{As}$ ,  $^{72}\text{Ga}$ ,  $^{71}\text{Ge}$ ).<sup>44</sup> While these terms are frequently used to describe purity of radioactive species, they are limited in their ability to describe non-radioactive contaminants, notably those of the same chemical identity as the radionuclide of interest. The non-quantitative terms ‘no-carrier-added’ (n.c.a.) and ‘carrier-added’ (c.a.) are convenient in this respect, as they indicate a level of specific/molar activity (*vide infra*), often as a consequence of stable impurities.<sup>44</sup> The term c.a. indicates a relatively high concentration of other isotopes of the corresponding element, while n.c.a. suggests the activity is essentially free from such contamination. The two caveats of this classification are: 1) the word “essentially” is a vital component of the n.c.a. definition, as the complete absence of undesired isotopes is both rare and challenging to prove, and 2) these classifications only consider isotopes of the element of interest, thus contaminants of different elements may be present. Although these terms are less precise than ‘radionuclidic purity’, they are more practical as colloquial descriptors and are commonly used to distinguish radionuclides that have been chemically separated from their target material (n.c.a.) from those that have not (c.a.).

The foundation of isolating n.c.a. activity is chemical distinctness of the produced radionuclide from the target material, which permits physical separation of the two components through a variety of chemical differences (e.g., solubility, resin affinity, redox potential). For example, production of n.c.a.  $^{67}\text{Ga}$  is achieved via  $^{67}\text{Zn}(p,n)^{67}\text{Ga}$ , resulting in a zinc target that can be chemically separated from the nano-to-picomolar concentrations of produced gallium.<sup>45</sup> This is in contrast to c.a. activity, where the sample may be elementally pure, but the isotope composition is impure. This is often the case with production via neutron activation (e.g.,  $^{152}\text{Sm}(n,\gamma)^{153}\text{Sm}$ ) and is due to the shared chemical identity of the product and target, which results in an inextricable mixture of isotopes. Use of c.a. activity results in undesired competing isotopes occupying coordination sites, which is rarely permissible during subsequent use. The quantity of desirable decays per unit material is commonly described as molar activity (Bq/mol). Thus, it can be said that n.c.a. material is more desirable than c.a., as it results in higher molar activity. It should be noted that specific activity (Bq/g) is also commonly used to describe activity concentration. Readers are cautioned to pay particular attention to these units, as molar activity is frequently described as specific activity in the current literature.

## 1.5 The Chemistry of Radiopharmaceuticals

Chemistry is often referred to as the central science due to its tendency to bridge the gap between physical and life sciences. Similarly, the use of fundamental chemical concepts is vital for the consolidation of radioactive and biological components in modern radiopharmaceuticals. Covalent bond formation (e.g.,  $^{18}\text{F}$ FDG) is one way to achieve “radiolabeling”, however a wider variety of radionuclides are accessible through the use of

radiometals and coordination chemistry. To this end, development of molecules capable of forming strong coordinative bonds with metals is imperative.

Biological and radioactive drug components are often coupled through the use of bifunctional chelators (BFC), which serve the dual purpose of radiometal complexation and bioconjugation (Section 1.5.3). The primary goal of radiometal complexation is the formation of robust coordination complexes to prevent the release of free metals *in vivo*. Stable complexes are formed through identification of compatible chelate-metal matches.<sup>4</sup>

### 1.5.1 Fundamentals of Chelators and Metal Complexation

DOTA (1,4,7,10-tetraazacyclododecane-1,4,7,10-tetraacetic acid; Figure 1.4A) is the most frequently used chelator in nuclear medicine. While the use of DOTA is appropriate in many cases, wide and indiscriminate use has resulted in many instances of poor radiotracer performance due to non-ideal chelator-metal interactions.<sup>46-50</sup> Lacking in these cases is consideration of fundamental metal ion characteristics (i.e., atomic number, charge and radius), which vary from metal ion to metal ion and result in distinct preferences for geometry, coordination number and ionic/covalent bond contribution. For optimal stability, the coordinating functional groups of the chelator should adopt the favoured geometry of the metal ion while simultaneously satisfying metal coordination requirements to prevent competition from extraneous ligands, especially in biological systems (see Section 1.5.2). Developed by Pearson in 1968,<sup>51</sup> hard-soft acid-base (HSAB) theory is a convenient way to discuss ionic/covalent bond character.

In the context of HSAB theory, hard metal ions have high charge density, non-polarizable electron shells and tend to form predominantly ionic bonds, where electrostatic

attraction is the primary driving force of bond formation (e.g.,  $\text{Fe}^{3+}$ ). As a rule, hard metal ions prefer hard donating groups, which possess dense anionic character (e.g., carboxylic acids). Conversely, soft metals have low charge density (e.g.,  $\text{Tl}^+$ ) and polarizable electron shells. They prefer more covalent bonding than do hard metal ions, which is achieved through coordination from softer, more electron disperse donor groups (e.g., thiols). A useful metric for hard-soft character is the Drago-Weyland parameter,  $I_A$ , which conveys the electrostatic ( $E_A$ ) and covalent ( $C_A$ ) contributions to the formation constants of Lewis acid-base complexes (includes metal complexes) in aqueous solution ( $I_A = E_A/C_A$ ).<sup>52</sup> From an energetic perspective, these differences in bonding arise due to energy differences between the highest occupied molecular orbital (HOMO) of the coordinating group and lowest unoccupied molecular orbital (LUMO) of the metal ion. Hard metal ions generally have high energy LUMOs that have poor orbital overlap with low energy HOMOs of hard coordinating groups, resulting in minimal sharing of electrons and electrostatic-dominant bonding. Soft metal ions have lower energy LUMOs, which overlap with high energy HOMOs of soft coordinating groups, resulting in significant sharing of electrons and relatively high covalent bond character.<sup>53</sup> Table 1.2 presents relevant chemical parameters of further discussed metal ions.

When coordinated to a metal ion, a chelator that satisfies the aforementioned criteria will form a highly stable, low energy complex with large energetic costs of dissociation. Multidentate chelators are especially effective at forming robust complexes due to “the chelate effect”, which (in a simplified sense) describes the higher entropic cost of coordination from multiple, monodentate ligands relative to a single, multidentate ligand.<sup>54,55</sup> For this reason, high denticity chelators are preferable. Along the same lines, pre-organized binding pockets are known to have an extraordinary effect on metal complex inertness due to the lower entropic

cost of complexation. This effect is especially pronounced for macrocyclic ligands, and has thus been deemed the “macrocyclic effect”.<sup>56</sup> Two classes of chelators (macrocyclic, Figure 1.4, and acyclic, Figure 1.5) have emerged due to the practical repercussions of this principle.

**Table 1.2** Relevant chemical parameters of discussed metal cations.

Reproduced from reference 2.

<i>Metal Ion</i>	<i>Ionic Radius<sup>a</sup></i>	<i>Hardness<sup>b</sup></i> ( <i>I<sub>A</sub></i> )	<i>pK<sub>a</sub><sup>c</sup></i>
Sc <sup>3+</sup>	0.87 (CN = 8)	Hard (10.49)	4.3
Ga <sup>3+</sup>	0.62 (CN = 6)	Hard (7.07)	2.6
Y <sup>3+</sup>	1.02 (CN = 8)	Hard (10.64)	7.7
In <sup>3+</sup>	0.92 (CN = 8)	Borderline-Hard (6.3)	4.0
Tb <sup>3+</sup>	1.04 (CN = 8)	Hard (10.07-10.30 <sup>d</sup> )	7.9
Lu <sup>3+</sup>	0.98 (CN = 8)	Hard (10.07)	7.6
Bi <sup>3+</sup>	1.17 (CN = 8)	Borderline-Hard (6.39)	1.1
La <sup>3+</sup>	1.03 (CN = 6)	Hard (10.30)	8.5
Ac <sup>3+</sup>	1.12 (CN = 6)	Borderline-Hard?	<10.4

<sup>a</sup>Ref 98, (*I<sub>a</sub>* = *E<sub>A</sub>/C<sub>A</sub>*); <sup>b</sup>Ref. 52 p. 37; <sup>c</sup>As hydrated metal cation ( $M^{3+}_{(aq)} \rightarrow MOH^{2+}_{(aq)}$ ). Ref. 99, pp. 128, 137,319, 327, 383; <sup>d</sup>Lanthanide series range.

In general, macrocyclic chelators are more kinetically inert than their acyclic counterparts due to their rigid, pre-organized binding sites. The disadvantage of using these scaffolds is their slow binding kinetics, which necessitate high temperatures and (long) waiting periods for optimal radiolabeling. These conditions are incompatible with heat-sensitive bioconjugates, such as antibodies, which rely on relatively weak domain interactions to

maintain structural integrity.<sup>57,58</sup> Conversely, acyclic ligands exhibit rapid radiolabeling at ambient temperature as a result of unrestricted bond rotation in their free form. The consequence of such freedom is the high entropic cost of complexation, which results in a greater likelihood of decomplexation *in vivo*, compared to macrocycles.

Historically, the benefits and drawbacks of macrocyclic versus acyclic chelators were unambiguous and unavoidable; however, continued research in the field of chelator development has worked to undermine the disadvantages of each class and has proven quite successful. For example, it is well known that DOTA suffers from sluggish labeling kinetics and requires heating up to 95 °C for radiolabeling of most metal ions. Development of pyridine containing (PCTA, 3,6,9,15-tetraazabicyclo[9.3.1]pentadeca-1(15),11,13-triene-3,6,9-triacetic acid; Figure 1.4G) and iminodiacetic acid functionalized (DEPA, 7-[2-(bis-carboxymethyl-amino)-ethyl]-4,10-biscarboxymethyl-1,4,7,10-tetraazacyclododec-1-yl-acetic acid; Figure 1.4C) DOTA derivatives has addressed this issue and permits more facile radiolabeling while maintaining high kinetic inertness.<sup>59,60</sup> Conversely, DTPA (1,1,4,7,7-diethylenetriaminepentaacetic acid; Figure 1.5A) complexes are known to frequently dissociate *in vivo*. The development of the more preorganized CHX-DTPA (cyclohexane-1,2-diamine-*N,N,N,N*-tetraacetate; Figure 1.5B) has alleviated this issue while maintaining rapid labeling kinetics, and is now widely used with radioimmunoconjugates.<sup>61-63</sup> Although, the choice between macrocyclic and acyclic chelators remains a matter of cost-benefit, the stereotypical shortcomings of each chelator class has been largely diminished.

### 1.5.2 Chelator Evaluation

Assessment and comparison of chelators is crucial for the continued improvement of radiotracers. As chemists, we seek to probe the thermodynamic stability, kinetic inertness, and *in vivo* performance of chelators to build a clear picture of how chelator-metal interactions affect biological behaviour.

Evaluation of a chelator's metal affinity requires knowledge of its acid-base properties (protonation constants) and the thermodynamic stability of its metal complexes. Potentiometric, spectrophotometric, calorimetric and nuclear magnetic resonance (NMR) titrations are commonly employed to study these parameters.<sup>64,65</sup> Thermodynamic stability is evaluated through the calculation of stability constants ( $\log K$ ), which are based around the complex equilibrium of metal ions, protons and ligands (chelators), conventionally written as:  $pM + qH + rL \leftrightarrow M_pH_qL_r$ . Metal ion affinity of different chelators is commonly compared in terms of their stability constants ( $\log K_{M_pH_qL_r}$ ); however, a more useful thermodynamic parameter is the pM value ( $pM = -\log[M]$ ). Introduced by Raymond,<sup>66</sup> pM values are linearly correlated with stability constants and express the extent to which a metal ion complex is formed in solution under physiologically relevant conditions. pM is normally reported under standard conditions ( $[L] = 10 \mu\text{M}$ ,  $[M] = 1 \mu\text{M}$ , pH 7.4) and permits the most suitable comparison of the ability of different ligands with diverse basicities, protonation states and metal complex stoichiometries to sequester specific metal ions.<sup>67,68</sup> High pM values are desirable, as they express low free metal concentrations at physiological pH. Although useful for comparison, thermodynamic parameters are less meaningful than kinetic studies for predicting *in vivo* behaviour.

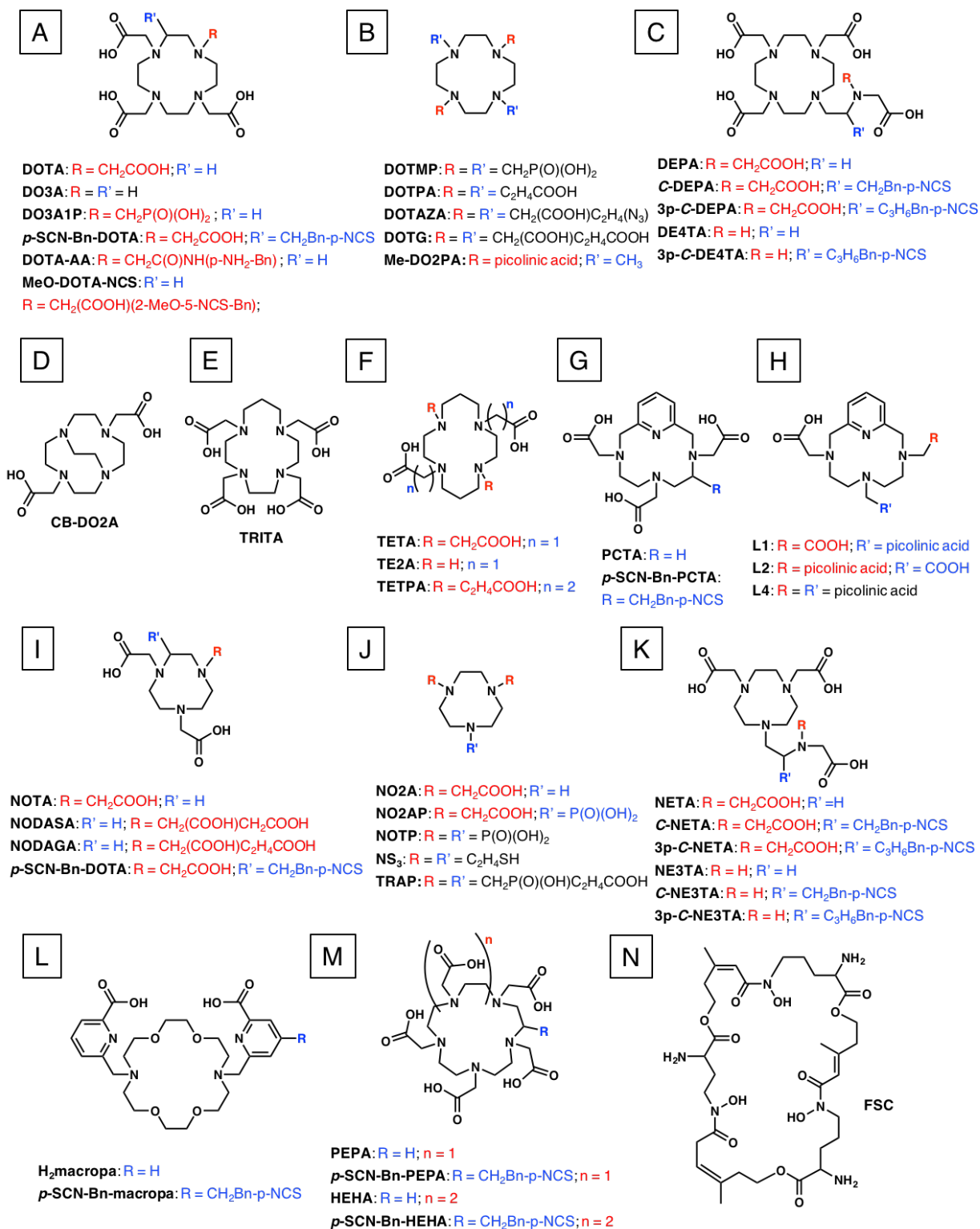


**Figure 1.4** Selected macrocyclic chelators and their respective BFC. Reproduced from reference 2.

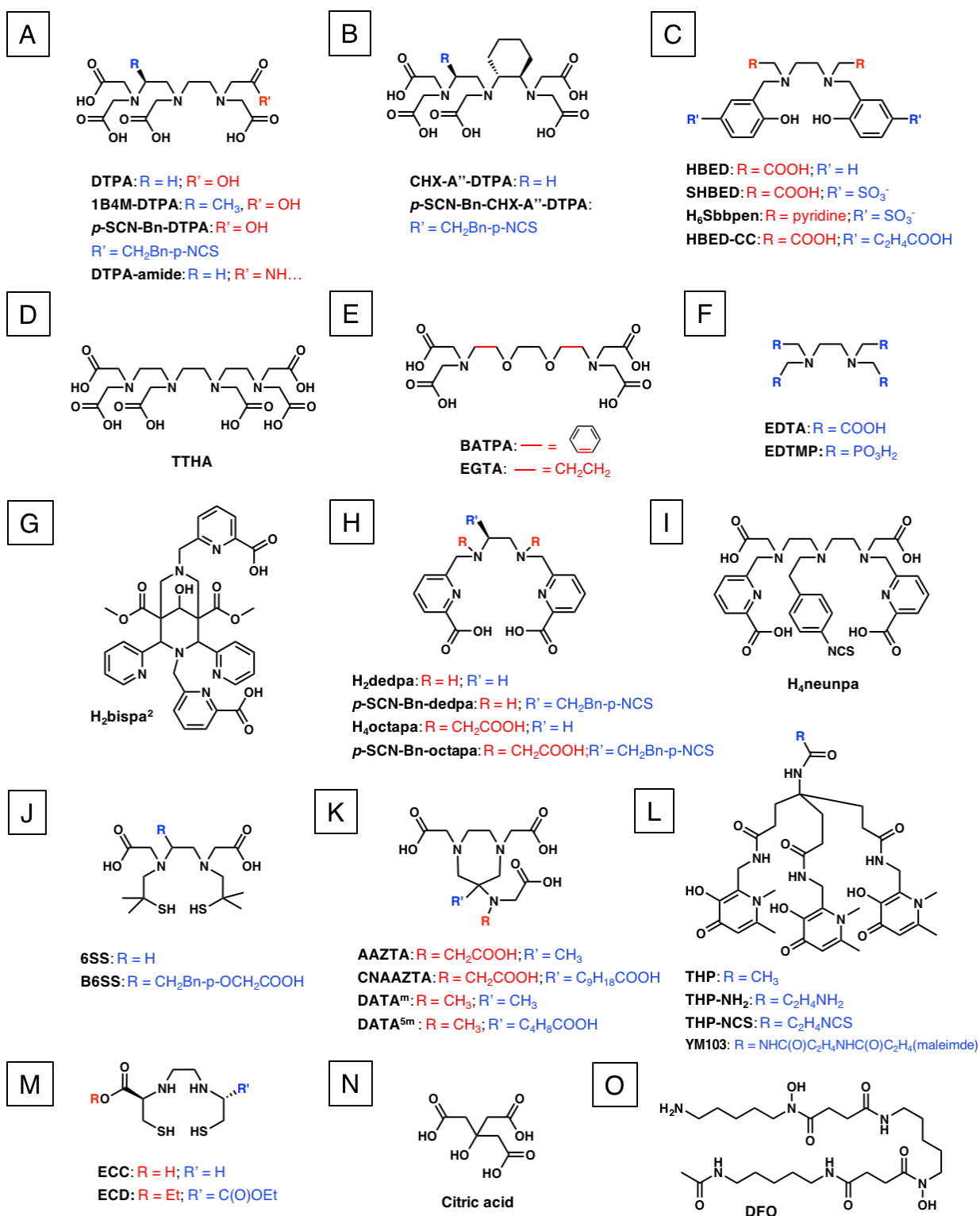


Figure 1.5 Selected acyclic chelators and their respective BFC. Reproduced from reference 2.

Kinetic inertness is normally evaluated through competition studies to determine the degree and/or rate at which extraneous factors induce complex dissociation. As discussed above, metal ion complexation is dependent on proton, metal and chelator concentration. Competition studies expose potential avenues of decomplexation by overloading a given equilibrium element and studying the repercussions from a kinetic standpoint. Subjecting metal complexes to acidic conditions ( $\text{pH} \leq 2$ ) often induces acid-catalyzed dissociation<sup>69,70</sup> and is a measure of how effectively protons can compete with metals for coordinating atoms. Acid dissociation studies are relatively uncommon due to their lack of direct applicability to physiological conditions. Conversely, *in vitro* transmetallation studies emulate *in vivo* conditions relevant to dissociation and are extremely common. Incubation of radiometal-complexes with a large excess of biologically relevant metal ions (e.g.,  $\text{Fe}^{3+}$ ,  $\text{Zn}^{2+}$ ,  $\text{Ca}^{2+}$ ,  $\text{Cu}^{2+}$ ) probes the likelihood of free radiometal ion release *in vivo* as a result of displacement by endogenous ions.<sup>71</sup> Incubation with serum proteins or enzymes explores the potential of radiometal transmetallation by endogenous ligands.<sup>72</sup> Methods to distinguish free radiometal ions from complexes are well-established and commonly involve thin-layer chromatography (TLC) or high-performance liquid chromatography (HPLC).

The most decisive evaluation of chelator utility is observation of *in vivo* performance with PET or SPECT. Mice are common models for this purpose, although non-human primates and pigs are occasionally reported.<sup>73-75</sup> Common signs of free metal ion release are bone,<sup>76,77</sup> kidney<sup>78</sup> or liver<sup>14</sup> accumulation; however, the latter two are somewhat ambiguous as they are common sites of bioconjugate accumulation and/or excretion. Studies can also be done with non-functionalized, “naked” chelators; however, with no targeting moiety, most metal ion-chelate complexes are rapidly excreted due to their small/hydrophilic nature.<sup>79-81</sup> These studies

are not particularly useful for probing long-term decomplexation, but rather are a gauge of short-term instability or the fate of a chelator if it were cleaved from its bioconjugate. Proper BFC design should, however, minimize this possibility.

### 1.5.3 Bifunctional Chelators and Linkers

Bifunctional chelators serve two purposes 1) secure the radiometal ion (see Section 1.5.1) and 2) provide a covalent link between the complex and targeting vector. BFCs are normally adapted from non-bifunctional analogues through the addition of pendant arms bearing a functional group available for facile bioconjugate coupling. For synthetic ease, coordinating groups are sometimes replaced by coupling groups (e.g., DO3A; Figure 1.4A); however, this strategy can negatively impact complex stability.<sup>82–84</sup> The alternative is functionalization at a less critical position, such as an ethylene diamine bridge (e.g., *p*-SCN-Bn-DOTA; Figure 1.4A), which avoids direct interference with metal-binding, but is generally more synthetically challenging.

Coupling of the targeting vector to the BFC often relies on nucleophilic attack from the bioconjugate. Free amines from the N-terminus, amino acid side-chains (e.g., lysine) or linker are common for this purpose. Amine coupling to carboxylic acids is achieved through the use of coupling agents (e.g., 1-ethyl-3-[3-dimethylamoniopropyl]carbodiimide [EDC], *N,N'*-dicyclohexylurea [DCC], hydroxybenzotriazole [HOBt]), or by first activating the electrophile (e.g., *N*-hydroxysuccinimide [NHS]).<sup>85</sup> A very common amine coupling strategy employs isothiocyanate groups, which are installed through the reduction and subsequent conversion (via thiophosgene) of *p*-NO<sub>2</sub>-Bn groups.<sup>86–88</sup> The benefit of such an approach is facile coupling to the highly electrophilic carbon, which results in a stable thiourea linkage. The drawback of

this approach is the use of highly toxic thiophosgene, as well as the tendency of the product to degrade due to the reactive isothiocyanate group. Thiol coupling via maleimide groups is possible given the presence of free cysteine residues. The use of copper-mediated “click-chemistry” and Diels-Alder coupling have also been demonstrated.<sup>85</sup>

Linkers are often employed to separate the chelator and bioconjugate to in order to avoid detrimental interactions (i.e., bioconjugate interference with coordination or chelate disruption of receptor targeting). Aliphatic, amino acid or polyethylene glycol (PEG) chains are frequently used. Although often overlooked, linker properties are rather important, as the addition of side-groups can be used as a powerful tool to optimize radiotracer pharmacokinetics and biodistribution.<sup>89</sup>

## **1.6 Bioconjugates**

Bioconjugates (also known as targeting vectors) dictate the biodistribution and pharmacokinetics of the radiopharmaceutical. Accurate targeting is crucial to obtain meaningful diagnostic information and/or selectively kill diseased cells. Promising bioconjugates exhibit high affinity for (or are internalized by) receptors that are highly expressed on target cells, but are absent or minimally expressed on healthy cells. Other desirable bioconjugate characteristics include: minimal renal/hepatic accumulation, high thermal and *in vivo* stability, as well as a compatible (biological) half-life with the radiometal (physical half-life).

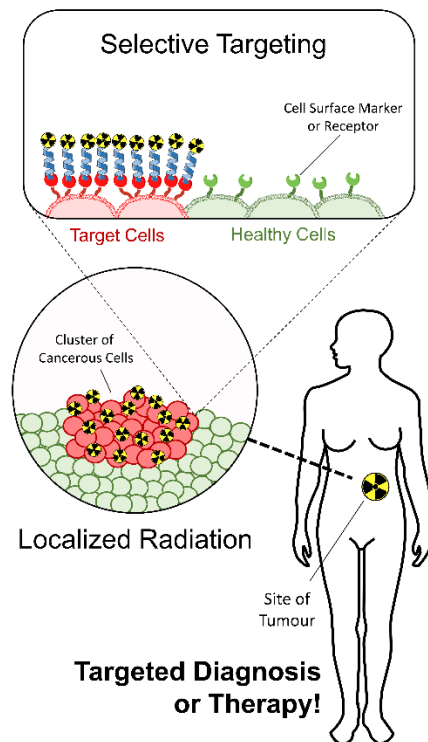


**Figure 1.6** Simplified illustration of radiopharmaceutical targeting. Reproduced from reference 2.

Peptides (or more specifically, oligopeptides) are of growing interest for use in radiopharmaceuticals largely due to their size, which has ramifications on stability, biological circulation and synthesis. As short chains (2-20 amino acids), peptides do not rely on high-level structures (i.e., secondary, tertiary, quaternary) and exhibit considerable thermal stability. Although endogenous peptides are readily degraded by numerous biological processes *in vivo*, structural modifications can drastically slow degradation without altering receptor affinity, making the application of endogenous peptides to radiotracers viable.<sup>90</sup> In a simplified sense, biological circulation time is inversely proportional to size. Accordingly, peptides experience fast circulation and can rapidly accumulate at target receptors. Unbound peptide-radiotracers quickly clear from circulation, resulting in high tumour-to-background ratios.<sup>91-93</sup> A caveat to this point is that excessively high rates of circulation and clearance can prevent adequate

tumour accumulation. Lastly, unlike larger biomolecules (e.g., proteins, antibodies), the simple structure of peptides makes them amenable to straightforward *ex vivo* synthesis, which can be achieved through increasingly powerful solid-phase peptide synthesis.<sup>94</sup> Common peptide bioconjugates are Arg-Gly-Asp (RGD) analogues for integrin targeting; PSMA-specific peptides for prostate-specific membrane antigen (PSMA) targeting; bombesin (BBN) fragments for gastrin-releasing peptide (GRP) receptor targeting and DOTA-conjugated octreotide analogues (i.e., DOTA-TATE, -TOC, -NOC) for somatostatin (SST) receptor targeting.

Antibodies are large, Y-shaped glycoproteins central to the human immune system. The appeal of using antibodies as targeting vectors is their highly specialized targeting capabilities, which can facilitate very selective tumour localization.<sup>95</sup> Due to their large size, antibodies experience slow circulation, have long biological half-lives and are suitable for use only with long-lived radiometals. While this extended period of circulation is beneficial for tumour targeting, slow clearance rates generally require long waiting periods to achieve high tumour-to-background ratios.<sup>96</sup> Antibodies also heavily rely on weakly bound domains to exert their biological function and as such are frequently sensitive to thermal degradation.<sup>57,58</sup> The use of antibody fragments is increasingly popular, as aforementioned disadvantages are alleviated while maintaining high receptor affinity and specificity.<sup>97</sup> Common antibody bioconjugates are Trastuzumab for human epidermal growth factor receptor 2 (HER2) targeting; J591 for PSMA targeting; HuM195 for CD33 targeting; Rituximab for CD20 targeting and Cetuximab for EGFR targeting.

## 1.7 Thesis Overview

The research presented in this thesis focuses on several aspects of (radio)pharmaceutical development. As discussed in Section 1.4 the production and purification of radiometals is a key stage of drug production. While many therapeutic radionuclides are routinely produced and purified for clinical use, the desire to use next-generation radiometals with superior decay characteristics compared to modern radiopharmaceuticals prompted the investigation of  $^{119}\text{Sb}$  as a radionuclide for Auger electron therapy in Chapter 2. Proton irradiation of natural tin targets have led us to produce a number of radioantimony species, which were then radiochemically separated from bulk tin. Subsequent radiolabeling was also explored using a trithiol ligand.

Chapter 3 is based around three phosphonate-containing picolinic acid-based chelators named  $\text{H}_6\text{phospa}$ ,  $\text{H}_6\text{dipedpa}$  and  $\text{H}_6\text{eppy}$ . These ligands were designed to be similar to one another with the intention of drawing conclusions between structure and complex stability with a range of trivalent metal ions (i.e.  $\text{Sc}^{3+}$ ,  $\text{Y}^{3+}$ ,  $\text{In}^{3+}$ ,  $\text{La}^{3+}$ ,  $\text{Lu}^{3+}$ ). Synthesis, metal complexation, solution studies and density functional theory (DFT) studies are presented in this section. Chapter 4 builds upon the former chapter, and is focused on another phosphonate/picolinic acid-based chelator named  $\text{H}_6\text{dappa}$ . This ligand is a bifunctional derivative of the most promising ligand from Chapter 3 ( $\text{H}_6\text{phospa}$ ), and explores synthesis, metal complexation, solution studies, simple DFT studies, radiolabeling optimization and serum stability studies.

Chapter 5 strays away from the picolinic acid motif that has become so popular within our research group, and looks at a new ligand design geared towards the theranostic isotope pair  $^{203/212}\text{Pb}$ . The availability of these isotopes at TRIUMF led to the straightforward synthesis

of DTPAm and is preceded by metal complexation studies, potentiometric titrations, crystal structure analysis and radiolabeling studies.

Chapter 6 is a culmination of three projects all united by their inclusion of phosphonate-based chelators for bone targeting. The ligands (XT, H<sub>4</sub>dppa and DEDA-(PO)) had each been studied previously in our group; however, special analyses were required to complete each project. Final studies with the La<sup>3+</sup> complex of XT (denoted La(XT)) required ICP-MS analysis, as well as exploration of the raw data. H<sub>4</sub>dppa and DEDA-(PO) both individually required NMR titrations to confirm what was observed during potentiometric titrations. In all three cases, a brief overview of previous work has been given, as well as detailed reports of the final experiments completed.

Chapter 7 will discuss ongoing work and future directions.

## Chapter 2. Production and Radiochemistry of Antimony-120m: Efforts

### Toward Auger Electron Therapy

#### 2.1 Introduction

##### 2.1.1 Therapeutic Radionuclides and Auger Electron Therapy

For many years, diagnostic radionuclides were the most intensively studied facet of nuclear medicine; however, technology surrounding therapeutic radionuclides has recently seen drastic improvement and led to increased clinical efficacy. This proven merit of targeted radionuclide therapy (TRT) has garnered much attention in the realm of basic research, and has accelerated the search for radionuclides with optimal therapeutic decay properties. Ideal therapeutic radionuclides deposit their radiation locally once the drug has accumulated at the target site. Moreover, they can efficiently cause double-strand breaks in DNA leading to cell death; a trait that is commonly held by  $\beta^-$ ,  $\alpha$ - and Auger electron-emitters.<sup>2</sup> While  $\beta^-$  and  $\alpha$ -emitters have gained much clinical popularity in recent years, notably [<sup>177</sup>Lu]Lu<sup>3+</sup> and [<sup>225</sup>Ac]Ac<sup>3+</sup>, respectively, Auger electron-emitters have been overlooked as therapeutic candidates despite their many potentially advantageous properties.

Auger electron emission is a process by which the filling of an inner electron shell vacancy causes the emission of an electron in the same atom. This process occurs due to energy released during the filling of the shell vacancy. Since the vacancy is filled from an electron in a higher energy shell, the electron must lose energy in order to fill the vacancy. In general, this energy is released as a photon; however, when the energy closely matches the ionization energy of an electron within the same atom, it may cause electron emission, otherwise known as Auger electron emission.<sup>100</sup> The kinetic energy of the ejected electron corresponds to the difference in energy between the energy released during electron shell vacancy filling and the ionization

energy of the electron. As the source of energy for electron emission is the (relatively small) difference in electron shell energies, the resultant kinetic energy of the ejected electron will be similarly low, often on the order of just tens of keV. Compared to  $\beta^-$  (0.1–2.2 MeV) and  $\alpha$ -emission (5–8 MeV), this is a miniscule amount of energy. The consequence of using energy on this order of magnitude for therapy has both benefits and drawbacks. While the small energy can make it more challenging for Auger electrons to reach target cell DNA, the advantage of applying these low-energy particles for therapy is their range of decay.<sup>101</sup> “Crossfire effects” are radiative collateral damage that affect cells near tissue being targeted during radionuclide therapy.  $\beta^-$  therapy is plagued with high levels of crossfire due to high particle energy and low LET, resulting in a large decay-range (0.5-10 mm).<sup>15</sup>  $\alpha$ -therapy is much improved over  $\beta^-$  therapy, as the high particle energy is accompanied with very high LET, resulting in short decay range (40-100  $\mu\text{m}$ ). Unfortunately, large-scale production of  $\alpha$ -emitters is often arduous, as these heavy radionuclides cannot reliably be obtained from the few available generators, and otherwise typically require reactors or high-energy cyclotrons for production, which are uncommon and in high demand.<sup>10,102,103</sup> The advantage of Auger electron therapy over  $\beta^-$  and  $\alpha$ -therapy is not only their capacity for routine production, but also their decay range. The energy of Auger electrons is so small, that the decay range is typically cited as less than the length of one cell (<10  $\mu\text{m}$ ).<sup>15</sup> This exciting phenomenon presents the potential to theoretically treat single cell metastases, with the notable caveat that highly specific biological targeting remains a nontrivial prerequisite.

### 2.1.2 Radionuclides for Auger Electron Therapy

Only a limited volume of research exists in the literature surrounding Auger electron therapy; few of those studies employ carefully selected radionuclides, instead most use incidental Auger electron emitters for convenience. Radionuclides such as  $^{111}\text{In}$ ,  $^{67}\text{Ga}$ ,  $^{125}\text{I}$  and  $^{99\text{m}}\text{Tc}$  are clinically used radiotracers (for SPECT) and as such are readily accessible in many hospitals and research centers across the globe. While these  $\gamma$ -emitters do undergo Auger emission to a certain degree, in no way were their properties tailored to serve as therapeutics. Rather, their study in Auger electron therapy is a matter of availability. Despite the non-optimal radionuclides investigated, the modest number of studies yield encouraging therapeutic results, demonstrating antitumor efficacy and the ability to induce double strand DNA breaks.<sup>104–108</sup> While the use of radionuclides for convenience over performance is valid for proof of principle, the study of more sophisticated radionuclides is necessary to realize the full potential of Auger electron emitters.

A 2001 paper analyzed the theoretical therapeutic potential of several low-energy electron emitters, and among the top five was  $^{119}\text{Sb}$  ( $t_{1/2} = 38.1 \text{ h}$ ).<sup>7</sup> Several criteria were considered in this selection, with the most obvious being the energy of ejected electrons. Antimony-119 releases a high volume of low energy (<40 keV) electrons upon decay to  $^{119}\text{Sn}$ . Furthermore, the decay of  $^{119}\text{Sb}$  is characterized as having a low photon-to-electron ratio, meaning upon filling of the inner electron shell vacancy (*vide supra*), the radionuclide releases a photon instead of ejecting an electron relatively infrequently ( $p/e = 0.09$ ), which increases its potential therapeutic capacity. From a logistical standpoint, the half-life of  $^{119}\text{Sb}$  is long enough to be convenient for radiopharmaceutical preparation and administration, but not so long that the patient will be exposed to radiation long-term. Moreover, routine production of  $^{119}\text{Sb}$  is

possible with low-energy protons via  $^{119}\text{Sn}(p,n)^{119}\text{Sb}$ , making production at hospital cyclotrons an attractive prospect. Despite these appealing features, few reports have focused on producing  $^{119}\text{Sb}$ , let alone purifying and radiolabeling for eventual study as an Auger electron therapeutic.

Herein, we report irradiation of  $^{\text{nat}}\text{Sn}$  to produce a broad array of antimony radioisotopes. Anticipating biological use, two methods (i.e., liquid-liquid extraction and cation-exchange chromatography) were developed to purify radioantimony from bulk tin target material; following purification, preliminary radiolabeling studies with a trithiol ligand were conducted.

## 2.2 Results and Discussion

### 2.2.1 Target Irradiation

The goals of this work are to produce and purify adequate quantities of  $^{119}\text{Sb}$  via (p,n) reaction to explore therapeutic efficacy; however, to solely focus on this radionuclide during the early stages of radiochemical investigation would present a number of avoidable challenges. In terms of radionuclide quantification, while the scant decay of  $\gamma$ -rays is an advantageous aspect of  $^{119}\text{Sb}$  ( $E\gamma = 23.9$  keV;  $I\gamma = 16.5\%$ ) medicinal use, this deficiency precludes the use of standard HPGe detector  $\gamma$ -spectroscopy to accurately measure radionuclide activity. Typically, a low-energy Ge detector or Si(Li) detector are required to quantify such low-energy  $\gamma$ -rays; unfortunately, facilities at TRIUMF are not equipped with either of these detectors. To make matters more challenging,  $^{119}\text{Sb}$  and a (p,n) byproduct  $^{119\text{m}}\text{Sn}$  ( $t_{1/2} = 293.1$  d) have near-identical  $\gamma$ -ray energies ( $^{119\text{m}}\text{Sn}$   $E\gamma = 23.9$  keV;  $I\gamma = 16.5\%$ ), thus exact  $^{119}\text{Sb}$  activity can only be determined after its full decay and following multiple measurements. From a financial perspective, to produce pure  $^{119}\text{Sb}$  with low energy protons would require enriched  $^{119}\text{Sn}$ , which

is expensive given the low natural abundance of the isotope (~8.6%). Moreover, the recovery of this material would be an absolute necessity, complicating such early stage research aimed towards radionuclide production and purification. It is for these reasons that the experiments throughout this chapter were focused on the radionuclides produced following proton irradiation of a natural tin target (Figure 2.1).

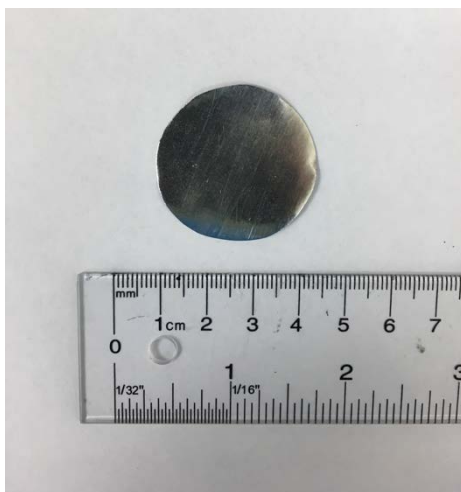


**Figure 2.1** Natural tin target (99.9%, 3.0 cm diameter, 0.127 mm thick) used for production of radioantimony.

Proton irradiations were conducted on the TR13 at TRIUMF, using a 12.8 MeV proton beam. The water-cooled target was irradiated at 5  $\mu$ A for 1 hr. This very low current was used to avoid damage to the target, which was a concern due to the low melting point of tin ( $T_m = 232^\circ\text{C}$ ). In the future if production of more activity were desired, a higher current could be used, the upper limit of which would require appropriate calculation. As seen in Table 2.1, due to the diverse makeup of natural tin and their moderate (p,x) cross-sections for low energy protons,<sup>109</sup> several radionuclides are produced under these irradiation conditions. Fortunately, following a suitable cooling period (>28 h) ample  $^{120\text{m}}\text{Sb}$  remains to serve as the primary

antimony tracer, and  $^{117}\text{Sb}$  ( $t_{1/2} = 2.8$  h) completely decays, producing a detectable amount of  $^{117\text{m}}\text{Sn}$  ( $t_{1/2} = 14.0$  d) in the process. At end of bombardment (EOB), 1.42 MBq of  $^{120\text{m}}\text{Sb}$  and 28.5 kBq  $^{117\text{m}}\text{Sn}$  were produced (Table A.1). The presence of these two radiotracers in solution makes it possible to monitor subsequent radiochemical separation using  $\gamma$ -spectroscopy, rather than requiring more arduous inductively coupled plasma atomic emission spectroscopy (ICP-AES) or inductively coupled plasma mass spectroscopy (ICP-MS) to acquire information regarding species separation.

**Table 2.1** Abundance of natural tin isotopes and their produced (p,n) radionuclides.

Isotope	Natural Abundance (%) <sup>a</sup>	Radionuclide Produced via (p,n) <sup>b</sup>
$^{117}\text{Sn}$	7.68	$^{117}\text{Sb}$ ( $t_{1/2} = 2.8$ h) $\rightarrow$ $^{117\text{m}}\text{Sn}$ ( $t_{1/2} = 14.0$ d)
$^{118}\text{Sn}$	24.22	$^{118}\text{Sb}$ ( $t_{1/2} = 3.6$ min)
$^{119}\text{Sn}$	8.59	$^{119}\text{Sb}$ ( $t_{1/2} = 38.2$ h)
$^{120}\text{Sn}$	32.58	$^{120\text{m}}\text{Sb}$ ( $t_{1/2} = 5.7$ d)
$^{122}\text{Sn}$	4.63	$^{122}\text{Sb}$ ( $t_{1/2} = 2.7$ d)

<sup>a</sup>Ref 16. <sup>b</sup>Radionuclides decay to stable daughters.

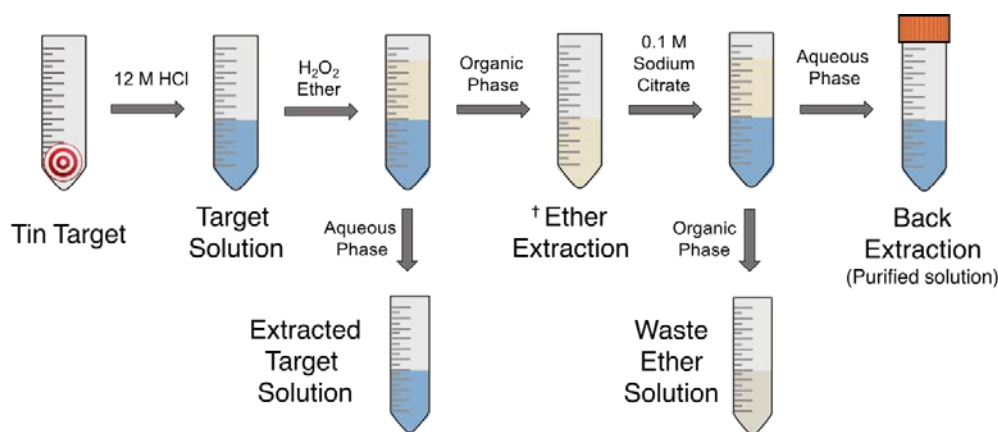
## 2.2.2 Purification of $^{120\text{m}}\text{Sb}$ by Liquid-Liquid Extraction

Separation of a desired radionuclide from bulk target material often involves exploitation of chemical differences between the two species, and can be achieved through a wide variety of techniques, including solid-phase chromatography, liquid-liquid extraction, precipitation, complexation and thermal diffusion, among others.<sup>110–114</sup> While each approach has its own advantages and downfalls, reproducibility should undoubtedly be a necessity for a robust separation technique. Recent attempts at radioantimony/tin separation in the literature highlight that consistency is a challenge. Sadeghi *et al.* report a technique<sup>109</sup> based on silica-

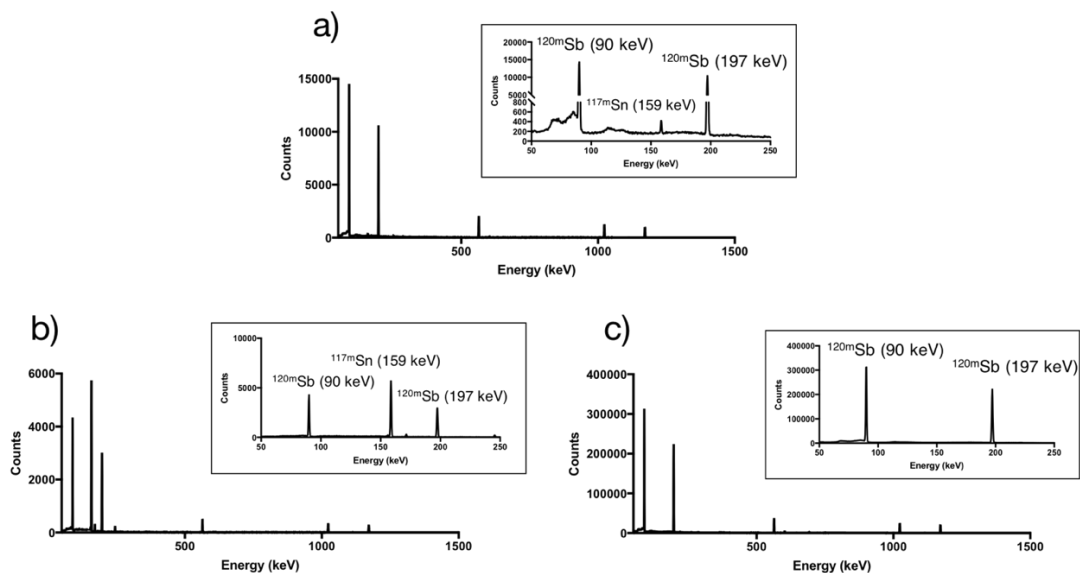
gel column chromatography and HCl as a eluent; however, not only does this presumably lead to a relatively high concentration of silica in the final solution,<sup>115</sup> but reproducibility of this technique is apparently problematic.<sup>116</sup> Another study has reported a more concrete method based on previously established anion-exchange chromatography;<sup>117</sup> however, despite the successful separation, the newly reported chromatograms are drastically different from those of the original paper, perhaps as a result of different anion-exchange solid phases.<sup>116,118</sup> It was also noted that the timing between target dissolution and breakthrough have a “critical impact on the success of the separation”, with increased time increasing tin breakthrough, likely as a result of hydrolysis.<sup>116,118</sup> These consistency issues were the motivation to develop a reliable method of separation. Given historic success with liquid-liquid extraction,<sup>119,120</sup> this method was selected for further study.

Figure 2.2 illustrates the technique used to separate the bulk tin target material from the desired antimony radionuclides. Following an overnight cool down period, the non-irradiated edges of the tin target are trimmed to reduce bulk tin to approximately 400 mg, which is then dissolved in 12 M HCl at room temperature for 24 h. It is crucial that H<sub>2</sub>O<sub>2</sub> is added to the target solution shortly before performing the separation (as opposed to during target dissolution), otherwise the yield will be drastically reduced. We hypothesize this is necessary to ensure all antimony is oxidized to the pentavalent oxidation state. Once this has occurred, [<sup>120m</sup>Sb]Sb<sup>5+</sup> can be selectively extracted from the aqueous solution with dibutyl ether - only 10 minutes of vortexing is required for (near) quantitative extraction. In strong HCl, the species present in solution are [SnCl<sub>6</sub>]<sup>2-</sup> and [SbCl<sub>6</sub>]<sup>-</sup>; thus the selective uptake of the latter into ether is likely a result of more diffuse charge distribution, resulting in a more hydrophobic species that prefers organic solvation. Following separation of the phases, two washing steps with 10 M

HCl (not shown in diagram) help remove minute amounts of  $\text{Sn}^{4+}$  that likely have partitioned into the organic phase. Lastly, since radiolabeling is most desirably performed from aqueous solution, the  $\text{Sb}^{5+}$  is then back-extracted into a 0.1 M sodium citrate solution, whose pH (5.5) is essential. The citrate is not only required for successful back-extraction, but is also a preventative measure to mitigate  $\text{Sb}^{5+}$  hydrolysis, as is done for  $\text{Sb}^{3+}$ .<sup>121</sup> The success of this procedure is quantified in Table A.2 and can be seen in Figure 2.3, where  $\gamma$ -ray spectra of the target solution, extracted target solution and back extracted solution are shown. The target solution most notably shows diagnostic signals from  $^{120\text{m}}\text{Sb}$  ( $E_{\gamma} = 90 \text{ keV}, 197 \text{ keV}$ ) and  $^{117\text{m}}\text{Sn}$  ( $E_{\gamma} = 159 \text{ keV}$ ), with activities 1.42 MBq and 28.5 kBq, respectively (Table A.1). The extracted target solution has retained only a small amount of  $^{120\text{m}}\text{Sb}$  (4%) and the vast majority of  $^{117\text{m}}\text{Sn}$  (>95%), as can be qualitatively noted by the relative intensities of peaks. Finally, the back extracted solution contains no observable  $^{117\text{m}}\text{Sn}$ . The net yield of  $^{120\text{m}}\text{Sb}$  in the final solution (relative to target solution) was 76%. When correcting for sacrificed volume, the yield is >90% (Table A.3)



**Figure 2.2** Visual representation of radioantimony purification. <sup>†</sup> Wash ether with equal volume 10 M HCl (x2) prior to back extraction.



**Figure 2.3**  $\gamma$ -ray spectra of a) target solution b) extracted target solution c) back extracted solution.

### 2.2.3 Purification of $^{120m}\text{Sb}$ by Solid-Phase Chromatography

The success of liquid-liquid extraction to isolate  $^{120m}\text{Sb}$  provided a reliable means of obtaining purified activity. Unfortunately, compared to solid-phase chromatography, the previous method generates substantially more radioactive waste (both solid and liquid) and leads to higher hand dose due to the handling of solution required to perform the extraction. In search of an improved purification technique, chromatography was explored.

Several solid-phase media were investigated for separation of  $\text{Sn}^{4+}$  and  $\text{Sb}^{5+}$ , but ultimately cation-exchange chromatography yielded the most promising results. Taking inspiration from a protocol originally reported by Kraus *et al.* in 1959,<sup>122</sup> the target was dissolved in HCl (12 M), oxidized with  $\text{H}_2\text{O}_2$ , and an aliquot (1 mL) of target solution loaded onto a preconditioned cation-exchange resin. As seen in Figure 2.4 and Figure 2.5, loading of the column followed by additional washing with HCl (12 M) resulted in selective elution of  $^{117m}\text{Sn}$ , likely as  $[\text{}^{117m}\text{Sn}][\text{SnCl}_6]^{2-}$ , supported by the lack of affinity for the anionic solid-phase.

Changing the eluent to NaOH (1 M) resulted in elution of  $^{120\text{m}}\text{Sb}$ , likely as antimonate, as noted in the original report.<sup>122</sup>

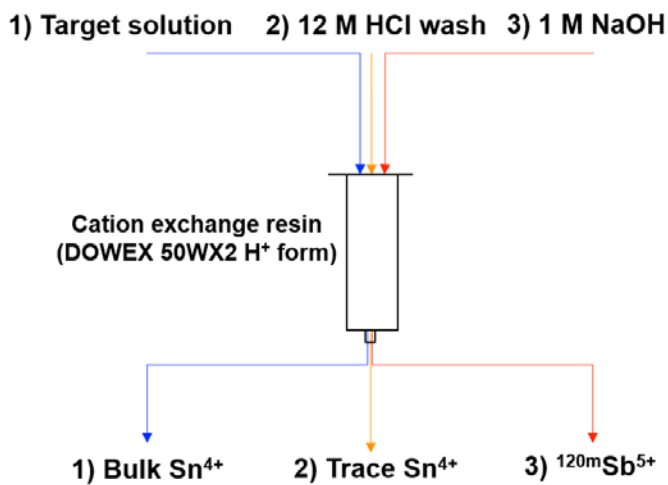


**Figure 2.4** Cation-exchange chromatography system for  $\text{Sn}^{4+}/\text{Sb}^{5+}$  separation.

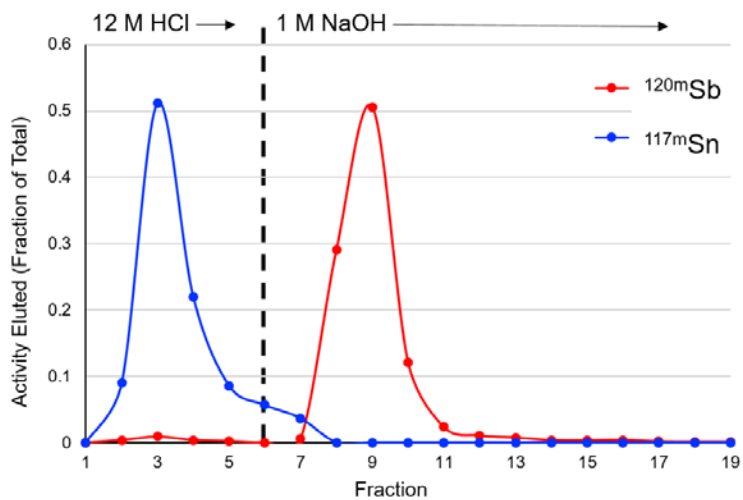


**Figure 2.5** Elution profile of  $[\text{}^{117\text{m}}\text{Sn}]\text{Sn}^{4+}$  and  $[\text{}^{120\text{m}}\text{Sb}]\text{Sb}^{5+}$  during cation-exchange chromatography.

The pursuit of solid-phase chromatography as an improvement over liquid-liquid extraction was successful in terms of reducing waste and minimizing direct handling of radioactive solutions; however, some disadvantages were realized in the process of developing this technique. Unsurprisingly, the first issue was consistency of separation. While consistency of elution profiles between successful trials was promising, some led to extreme streaking of  $^{120\text{m}}\text{Sb}$ . Unfortunately, it was impossible to determine the cause of streaking, as common variables known to change elution profiles (e.g., pH, temperature, time, flow-rate) were held constant between trials. Another difficulty of this method is the chemical form of  $^{120\text{m}}\text{Sb}$  as eluted. While conversion to antimonate nicely induces selective elution, radiolabeling often requires non-oxidized metal ions, which is non-trivial to achieve with hydrolyzed  $\text{Sb}^{5+}$ . While attempts were made to radiolabel following elution with NaOH, none were successful. Improvements to this method may be made by eluting with chelating agents such as citrate, ethylenediaminetetraacetic acid (EDTA) or mercaptoacetate; however, few trials have been attempted thus far.

#### **2.2.4 Preliminary Radiolabeling Studies**

Production and purification of  $^{120\text{m}}\text{Sb}$  were undertaken as a prerequisite for eventual radiolabeling and biological studies. To our knowledge, no radiolabeling with any antimony radionuclide has ever been reported. Furthermore, the chemical properties of  $\text{Sb}^{5+}$  are dissimilar to those of commonly studied radiometals (e.g.,  $^{68}\text{Ga}^{3+}$ ,  $^{177}\text{Lu}^{3+}$ ) due to its very high oxidation state, as well as its tendency to undergo hydrolysis at low pH in aqueous solution. Initially, these tendencies were presumed to be analogous to other high charge radionuclides, such as  $^{89}\text{Zr}^{4+}$ ; however, all attempts to radiolabel  $^{120\text{m}}\text{Sb}^{5+}$  proved ineffective, even

with very hard ligands, such as deferoxamine (DFO). It was only when inspiration was drawn from a fellow pnictogen that progress was made.

The radiochemistry of arsenic has recently become a topic of interest due to the  $^{72/77}\text{As}$  theranostic pair. Similar to antimony, arsenic commonly exists as  $\text{As}^{3+}$  or  $\text{As}^{5+}$ . Recent studies by Jurisson and co-workers demonstrated that arsenic can most readily be radiolabeled in the trivalent oxidation state. Evidently,  $\text{As}^{3+}$  is thiophilic in nature and forms strong bonds with thiol donors.<sup>123</sup> To determine if antimony follows this trend, attempts were made to first reduce  $^{120\text{m}}\text{Sb}^{5+}$  to  $^{120\text{m}}\text{Sb}^{3+}$  with a variety of thiol donors, including dimercaptosuccinic acid (DMSA), dithiothreitol (DTT) and mercaptoacetate. While not definitive, following incubation with reducing agents, radio-TLC chromatograms demonstrated broadening of activity across the center of the plate, as opposed to activity rising with the solvent front ( $R_f \sim 1$ ), which occurs with  $^{120\text{m}}\text{Sb}^{5+}$  in citrate solution (Figure 2.6). Following the proposed reduction, the trithiol ligand (kindly provided by S. Jurisson) originally designed for  $\text{As}^{3+}$  was used to attempt radiolabeling. Following addition of the ligand ( $10^{-3}$  M) and incubation for 1 h, radio-TLC data shows activity remaining at the bottom of the TLC plate instead of streaking to the middle as was shown for the reduced species. This change in behaviour was attributed to the formation of a neutral  $^{120\text{m}}\text{Sb}[\text{Sb}(\text{S}_3\text{C}_6\text{H}_{11})]$  complex. A radiochemical yield (RCY) of approximately 70% was achieved. This transchelation method, wherein three mercaptoacetates are displaced by one trithiol ligand (due to the chelate effect) is analogous to the labeling method used for  $^{77}\text{As}\text{As}^{3+}$ .<sup>123</sup> It was confirmed that reduction by mercaptoacetate is necessary for labeling, as attempts to directly radiolabel  $^{120\text{m}}\text{Sb}^{5+}$  with the trithiol ligand were unsuccessful. Given the novelty of these results, the long reaction times and harsh conditions are satisfactory; however,

a number of improvements could be made to this method to make it more convenient moving forward. These are discussed in the following section and Chapter 7.

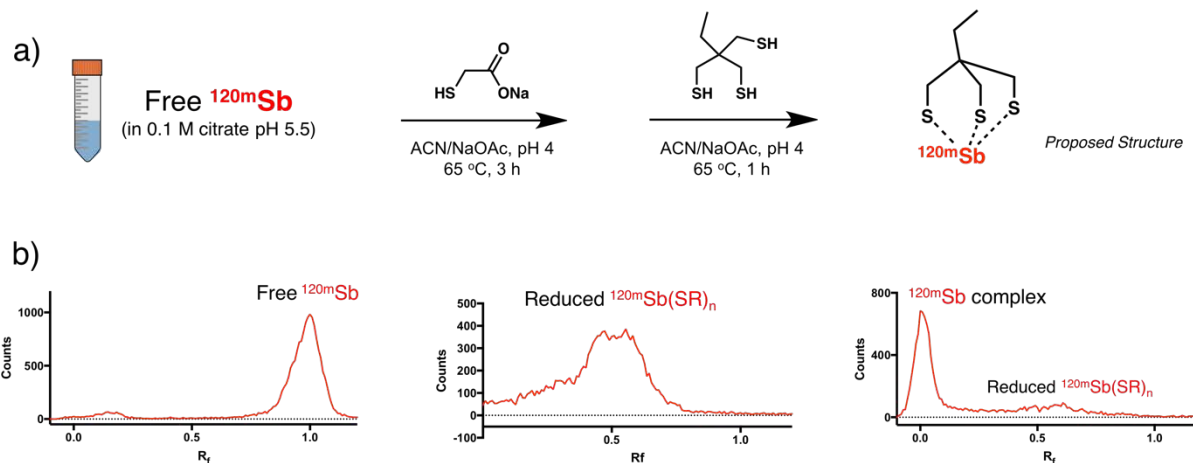


**Figure 2.6** a) Schematic of radiolabeling method for  $^{120\text{m}}\text{Sb}$ ; b) radio-TLC data for radiolabeling of  $^{120\text{m}}\text{Sb}$ .

## 2.3 Conclusions

A natural tin target was irradiated with 12.8 MeV protons to produce a variety of antimony radionuclides. Following a two-day waiting period, the primary radionuclides of interest were  $^{120\text{m}}\text{Sb}$  and  $^{117\text{m}}\text{Sn}$ . At EOB, 1.42 MBq and 28.5 kBq were produced. Two methods were developed to separate bulk tin from  $^{120\text{m}}\text{Sb}$ . The first method used liquid-liquid extraction, where, following target dissolution in 12 M HCl and oxidation by  $\text{H}_2\text{O}_2$ ,  $[\text{Sb}^{5+}]$  was selectively extracted using dibutyl ether.  $\gamma$ -spectroscopy was used to follow both radiotracers, and it was determined that 76% of  $^{120\text{m}}\text{Sb}$  was extracted into the final solution with no observable  $^{117\text{m}}\text{Sn}$ . The second method used cation-exchange chromatography, and involved loading an aliquot of the target solution onto the resin, washing with 12 M HCl to elute  $\text{Sn}^{4+}$ , and subsequently eluting  $^{120\text{m}}\text{Sb}$  with 1 M NaOH. Due to hydrolysis of antimony during elution,

activity isolated from the first method was used for radiolabeling. Preliminary radiolabeling studies demonstrated reduction of  $[^{120\text{m}}\text{Sb}]\text{Sb}^{5+}$  to  $[^{120\text{m}}\text{Sb}]\text{Sb}^{3+}$  using mercaptoacetate, then successively transchelating the monothiols with a trithiol ligand was a successful method for radiolabeling. Long reaction times and harsh conditions were necessary, but could likely be mitigated by increasing pH of solution during reduction and labeling. Furthermore, if mercaptoacetate could be used to back-extract  $[^{120\text{m}}\text{Sb}]^{5+}$  during liquid-liquid extraction, labeling times could be drastically reduced and lead to increased RCY.

## 2.4 Experimental

### 2.4.1 Materials and Methods

All solvents, reagents and resins were purchased from commercial suppliers (Sigma-Aldrich, Fisher Scientific, TCI America, Alfa Aesar, AK Scientific, Fluka) and were used as received. Radiolabeling reactions were monitored by TLC (Silicagel 60 RP-18 F254S, aluminum sheet) and scanned using a radioisotope thin layer analyzer (BIOSCAN system 200 imaging scanner) with Winscan radio-TLC software (Bioscan Inc., Washington, DC) Water used was ultrapure ( $18.2 \text{ M}\Omega \text{ cm}^{-1}$  at 298 K, Milli-Q, Millipore, Billerica, MA). Irradiations were performed by operators (Dave Prevost, Linda Graham) at the TR13 cyclotron at TRIUMF (Vancouver, Canada). The gamma spectroscopy detector was a N-type co-axial HPGe gamma spectrometer from Canberra fitted with a 0.5 mm beryllium window. Detector energy, width and efficiency calibrations were performed using a  $^{152}\text{Eu}$  and  $^{133}\text{Ba}$  source. Instrument specifics are described by A.K.H Robertson *et al.*<sup>124</sup>

### **2.4.2 Irradiation and Handling of Tin Target**

The TR13 cyclotron at TRIUMF was used to irradiate natural tin targets (3.0 cm diameter, 0.127 mm thick). Targets were irradiated with a negative hydrogen ion beam (entrance energy 12.8 MeV) for 1 h with a current of 5  $\mu$ A. According to SRIM calculations, the beam deposits 1.7 MeV into the foil. The 5  $\mu$ A beam increases the temperature of the target to no more than 160°C, far away from the tin melting point of 232°C. The foil was cooled by a double helium-cooling window configuration. Irradiated targets were left in the cyclotron target area for 2 hours following irradiation. The target was then removed from the cyclotron and was carried to a nearby shielded fumehood where the target apparatus was disassembled and the target foil retrieved and placed into a lead container for transport. The container was then transported to a radiochemistry lab where further processing was performed in a shielded fumehood. Twenty-four hours after EOB, the outside of foils (non-irradiated portions) were trimmed with scissors to reduce tin weight. Typical target mass before trimming was approximately 1.0 g; and after trimming was approximately 0.4 g. For dissolution, target foils were added to 12 mL of HCl (12 M), and allowed to stand in a covered (not sealed) 16 mL borosilicate KIMAX tube at room temperature overnight.

### **2.4.3 Liquid-Liquid Extraction**

To begin purification, 4 mL of target solution was set aside, while 8 mL is transferred into a 50 mL Falcon centrifuge tube. A small amount of HCl (12 M, 800  $\mu$ L) was used to rinse KIMAX tube, and was transferred to 8 mL of target solution. H<sub>2</sub>O<sub>2</sub> (30% w/w, 800  $\mu$ L) was added to the target solution, upon which point the solution starting gently bubbling, became warm and turn light yellow in colour. The cap was loosely placed on the falcon tube and the solution allowed

to sit for 30 minutes, or until bubbling ceased. Dibutyl ether (10 mL) was added to the target solution (9.6 mL) and the biphasic solution vortexed for 15 min. After the solution settled, the phases were separated by pipetting the organic phase from the Falcon centrifuge tube into a new 50 mL Falcon tube. Of the 10 mL dibutyl ether initially added, only 9 mL were obtained to ensure no aqueous contamination. Two washing steps were next carried out, where 9 mL of HCl (10 M) were added to the dibutyl ether, the solution vortexed for 10 min, then separated in a similar fashion to the previous step. It should be noted that for the first wash, no dibutyl ether was sacrificed; however, after the second wash, 1 mL of dibutyl ether was sacrificed, leaving 8 mL of dibutyl ether solution. The final back-extraction was completed by adding 8 mL of sodium citrate solution (0.1 M, pH 5.5) to the organic phase. The solution was vortexed for 30 min, and the phases separated as described above. A total of 7 mL of citrate solution was obtained following phase separation.

Gamma spectroscopy on six samples were carried out after separation (target solution, extracted target solution, HCl wash #1, HCl wash #2, extracted ether solution and final back-extracted solution). 1 mL of each solution was added to separate 2 mL HPLC vials (to ensure geometry compatible with calibration). Solutions were run at a height of 15 cm until activity error reached below 10%. Gamma-ray libraries built using data from the National Nuclear Data Center database were used to confirm diagnostic emission from solutions, as described by Robertson *et al.*<sup>124,125</sup> Data can be found in Tables A1-A3.

#### **2.4.4 Cation-Exchange Chromatography**

Prior to purification, cation-exchange resin was packed into a column and pretreated with HCl. Approximately 1.5 g of DOWEX 50 WX2-200 H resin was weighed and transferred to a 15

mL Falcon centrifuge tube. The resin was wet with approximately 2 mL of H<sub>2</sub>O and transferred to a 4 mL column (pre-packed with frit) to the 3 mL mark. Excess water was allowed to drip out, and an additional frit was placed on top of the resin and gently pushed down to secure in place. The column was pre-conditioned with 5 x 1 mL of 12 M HCl. Flow was induced by gravity.

Separation was achieved by loading 1 mL of target solution onto the column eluting with 6 x 1 mL of HCl (12 M). Each 1 mL fraction was collected in an HPLC vial and again the column was gravity run. Next, the eluent was switched to 1 M NaOH, which was used to elute 10 x 1 mL fraction. Activity quantification was accomplished as described in Section 2.4.3.

#### **2.4.5 Radiolabeling**

As described in Section 2.2.4, the method devised for radiolabeling of radioantimony requires reduction of [<sup>120m</sup>Sb]Sb<sup>5+</sup> to [<sup>120m</sup>Sb]Sb<sup>3+</sup> with mercaptoacetate. To achieve this, 57 mg (500 μmol) of sodium mercaptoacetate was dissolved in 1 mL of H<sub>2</sub>O to achieve a solution concentration of 500 mM. To 200 μL of final back-extracted solution (containing <sup>120m</sup>Sb) was added 67 μL of mercaptoacetate solution. An additional 233 μL of ACN/H<sub>2</sub>O (1:1) solution was added to the mixture, then it was heated to 65°C for 3 h. The trithiol ligand described in Section 2.2.4 is commonly stored as the SCN protected ligand, requiring deprotection prior to radiolabeling. Deprotection was achieved by dissolving 1 mg (3.89 mmol) of ligand in 0.5 mL of ACN. In a separate container, 10 mg (40 mmol) of tris(2-carboxyethyl)phosphine hydrochloride (TCEP•HCl) was dissolved in 0.5 mL H<sub>2</sub>O. The ligand and TCEP solutions were then combined together and heated at 55°C for 2 h. Note, final ligand concentration is 3.89 mM. Radiolabeling was achieved by adding 173 μL of deprotected trithiol solution to the

solution containing [ $^{120\text{m}}\text{Sb}$ ] $\text{Sb}^{3+}$ , which was heated to 65°C for 1 h. Silica on aluminum backing TLC plates were used to monitor reactions, with 0.1 M NaOAc (pH 4) solution used as a mobile phase. In each case, 10  $\mu\text{L}$  of solution were spotted on TLC plates before being placed in mobile phase, dried and counted.

## Chapter 3. Phosphonate Chelators for Medicinal Metal Ions

### 3.1 Introduction

#### 3.1.1 Medicinal Applications of Chelators

Chelators have a wide range of medicinal uses. As described in Section 1.5, bifunctional chelators are often key components of contemporary radiopharmaceuticals, as they prevent the release of free inorganic radionuclides *in vivo* by maintaining high thermodynamic stability and kinetic inertness to ensure secure delivery of radioactive cargo.<sup>2,126</sup> Magnetic resonance imaging (MRI) contrast agents similarly require the metal complex to remain intact for optimal performance. Unlike radiopharmaceuticals however, MRI detects the T1 relaxation of water within magnetic fields, and so these contrast agents aim to deliver metal ions capable of increasing the water relaxation rate at specific sites (e.g., brain), often as a result of water coordination to a non-coordinatively saturated highly paramagnetic metal ion (e.g.,  $\text{Gd}^{3+}$ ,  $\text{Mn}^{2+/3+}$ ,  $\text{Cu}^{2+}$ ).<sup>127</sup> While these applications necessitate delivery of metal ions without their release, delivery and release of metal ions can be achieved through rational tuning of chelators, and can be particularly useful when metal ion incorporation into tissue is required to elicit the desired biological response. Imaging of bone metastases and treatment of bone resorption disorders with  $\text{La}^{3+}$  are applications that illustrate this point. In these cases, chelators chauffeur (radio)metal ions to regions with abnormally high bone growth rate or rapid bone turnover. Upon release, the (radio)metal ions may become adsorbed onto bone, or even incorporated into hydroxyapatite (HA; the mineral matrix that makes up cortical bone), where they can evoke a localized response.<sup>128</sup> Moreover, chelators may be used to decrease unusually high levels of free metal ions *in vivo*, as is commonly achieved during chelation therapy. In this case, toxic concentrations of endogenous (e.g.,  $\text{Fe}^{3+}$ ,  $\text{Cu}^{2+}$ ) or exogenous (e.g.,  $\text{Pb}^{2+}$ ,  $\text{Hg}^{2+}$ ) metal ions can

be diminished through administration of chelators to sequester free metal ions and more rapidly excrete them, mitigating deleterious effects such as excessive formation of reactive oxygen species (ROS).<sup>129,130</sup> Chelators also serve in many useful roles outside the medical realm (e.g., water treatment, heavy metal extraction), however for the sake of brevity, these topics will not be discussed further. Clearly, chelators offer much utility to the medical world and beyond (Chart 3.1).

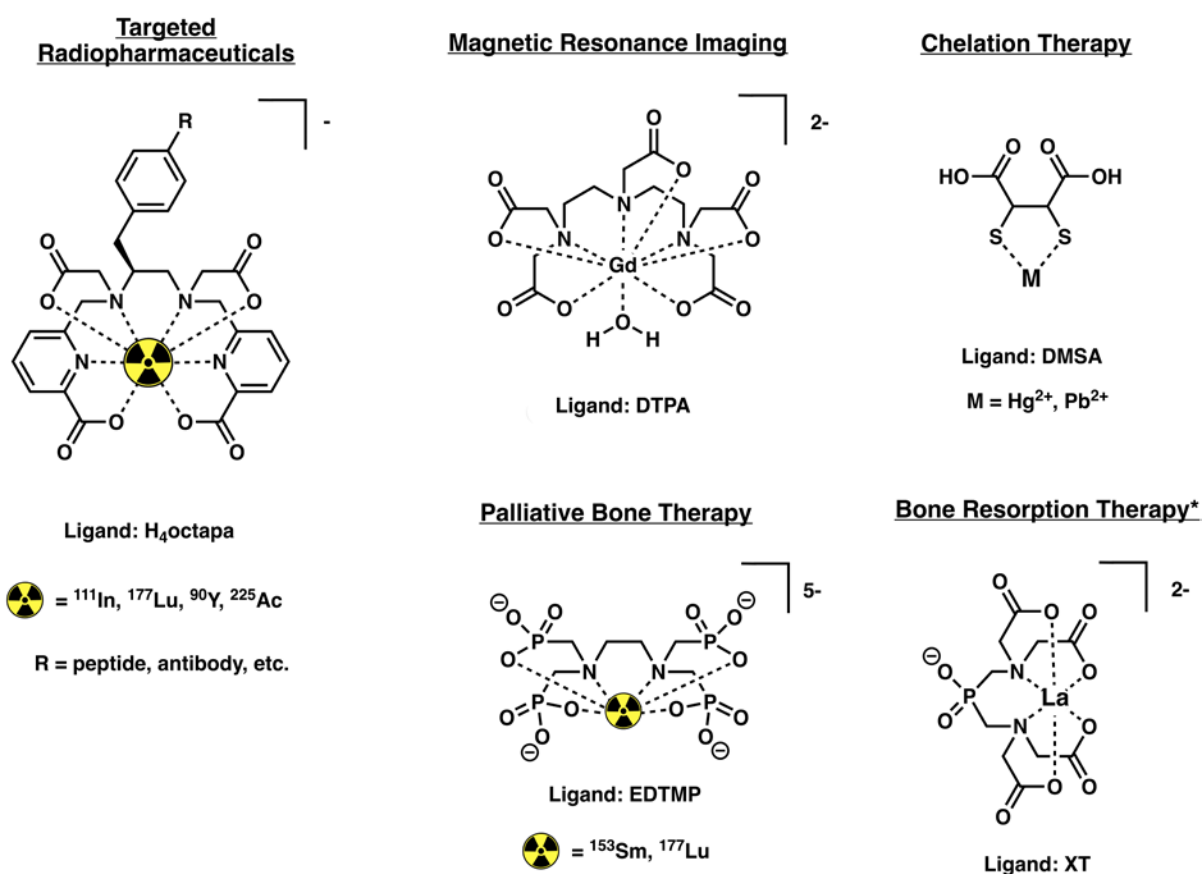


**Chart 3.1** Medicinal applications and corresponding examples of chelating ligands. \*Under investigation; not clinically tested.

### 3.1.2 Development of Chelators

The development of new chelators is a worthy goal that may ultimately uncover new roles for these versatile agents, or lead to improved performance within their many established roles. In order to achieve this goal and appropriately explore this scientific landscape, not only must new chelators be synthesized, but their interactions with a variety of suitable metal ions must be explored. While X-ray diffraction (XRD) data are ideal for fully elucidating complex structure, obtaining suitable crystals is a non-trivial process. Understanding of the physical chelator-metal interactions can most reliably be achieved using NMR spectroscopy (assuming metal ions are diamagnetic), as NMR spectra are far less elusive and often provide adequate information for rough structural determination and pH dependence of complex formation.

Investigating the thermodynamics of metal complexation provides complementary information to that of structural determination. Discerning complex structure is fundamental for characterization, but provides little insight into how geometrically or electronically favourable a coordination complex is. Conversely, thermodynamic studies yield no structural information, but provide essential information to quantify the energetic drive of complex formation. Thermodynamics of complexation can be studied through a variety of titration methods, most commonly potentiometry, spectrophotometry, or NMR titrations.<sup>64,65</sup> Determination of chelator protonation constants ( $pK_a$ ) is required prior to studying metal complexes, because protons play a competitive role in the complex formation equilibria with metal ions.<sup>131</sup> Following determination of chelator  $pK_a$  values, thermodynamic stability constants such as  $pM_{\text{Metal}}$  ( $pM = -\log[\text{metal}]$ ) values and formation constants ( $K_{\text{ML}}$ ) can be calculated. The power in calculating these values is the ability to compare thermodynamic stability of metal complexes between ligands, and in the case of  $pM$ , across different

protonation states, denticities, and metal ions. Indeed, the thermodynamic comparison of metal complexes is crucial for understanding complex behavior and ligand performance in solution, and for their eventual rational improvement. Focusing on a molecular niche can be helpful particularly in the latter case, as fewer variables help draw conclusions from limited data more readily.

### 3.1.3 Phosphonate- and Picolate-Bearing Chelators

Phosphonate-bearing chelators have seen continued interest over recent years due to their well-known “hard” (predominantly ionic) coordination electronics, as well as their rapid kinetics of complexation. In comparison to much more commonly employed carboxylic acids, phosphonates are particularly well suited towards coordination of “hard” metal ions, such as high valence main group (e.g.,  $\text{Ga}^{3+}$ ,  $\text{In}^{3+}$ ) and transition metals (e.g.,  $\text{Fe}^{3+}$ ,  $\text{Sc}^{3+}$ ), as well as the entire lanthanide series.<sup>52</sup> Another interesting feature of (bis)phosphonates is their natural tendency to interact with bone tissue. Phosphonates are a fundamental component of HA (along with  $\text{Ca}^{2+}$  and  $\text{OH}^-$ ) and so naturally their interactions have been studied to investigate any medicinal properties that can be harnessed to treat bone disorders.<sup>128</sup> While the long-term efficacy remains unclear,<sup>132</sup> bisphosphonates such as alendronate (trade name: Fosamax) have long been established as agents capable of increasing bone density in patients suffering from osteoporosis. Taken together, the “hard” and labile coordination properties of phosphonates, along with their affinity towards HA has led to their elegant application as metal-based bone-targeting agents.  $[\text{}^{153}\text{Sm}][\text{Sm}(\text{EDTMP})]^{5-}$  and (more recently)  $[\text{}^{177}\text{Lu}][\text{Lu}(\text{EDTMP})]^{5-}$  are prime examples of multifunctional phosphonate species.<sup>133,134</sup> Not only does  $(\text{P-O})_4 \rightarrow \text{M}^{3+}$  ( $\text{M} = \text{Sm}, \text{Lu}$ ) coordination form the majority of energetic drive for this species to exist, but the delivery of the radionuclides to their target (i.e., bone metastases) is also firmly rooted in phosphonate-

dominated interactions. Clearly, phosphonates are multifaceted functional groups whose application in chelating ligands warrants further investigation.

Picolinic acids are another motif commonly found in modern chelators. Their broad success, notably in radiopharmaceuticals,<sup>72,81,86,87,135–137</sup> has led to a tremendous number of chelator variants; however, few bearing both picolinic and phosphonic acids have been reported. H<sub>6</sub>phospa is a well-known derivative due to its simplicity of design, and was originally studied as a Gd<sup>3+</sup>-based contrast agent.<sup>138</sup> As a BFC for radiopharmaceuticals, incompatibility with [<sup>89</sup>Zr]Zr<sup>4+</sup> and complex lability with [<sup>111</sup>In]In<sup>3+</sup> and [<sup>177</sup>Lu]Lu<sup>3+</sup> when conjugated to trastuzumab (HER2/*neu*-targeting monoclonal antibody; mAb) have been reported.<sup>139</sup> No investigation of H<sub>6</sub>phospa thermodynamic parameters have been explored to date. Another more recent report is of the phosphinate-bearing picolinic acid derivative H<sub>6</sub>dappa.<sup>140</sup> While similar lability with [<sup>111</sup>In]In<sup>3+</sup> was reported, in-depth thermodynamic studies and DFT calculations provide insight into the reason behind the complex's low kinetic inertness and how to mitigate lability if desired. Lastly, H<sub>4</sub>dppa is a condensed, hexadentate scaffold intended for use with [<sup>68</sup>Ga]Ga<sup>3+</sup>, as well as for the potential delivery of La<sup>3+</sup> to HA for treatment of bone resorption disorders.

Herein, we report the synthesis and characterization of three ligands: H<sub>6</sub>phospa, H<sub>6</sub>dipedpa and H<sub>6</sub>eppy. Crystal structures of the first two ligands were obtained. Metal complexation of these three ligands were investigated by NMR spectroscopy with five trivalent metals with varying size and electronics (i.e., In<sup>3+</sup>, Lu<sup>3+</sup>, Y<sup>3+</sup>, Sc<sup>3+</sup> and La<sup>3+</sup>). Thermodynamic parameters (log *K*<sub>ML</sub> and pM) were calculated for all fifteen complexes and were used to compare and rationalize stability across varying ligand and metal series. Lastly, DFT structures

of several  $\text{La}^{3+}$  and  $\text{Sc}^{3+}$  complexes were calculated and some validated through comparison of experimental and theoretical NMR spectra.

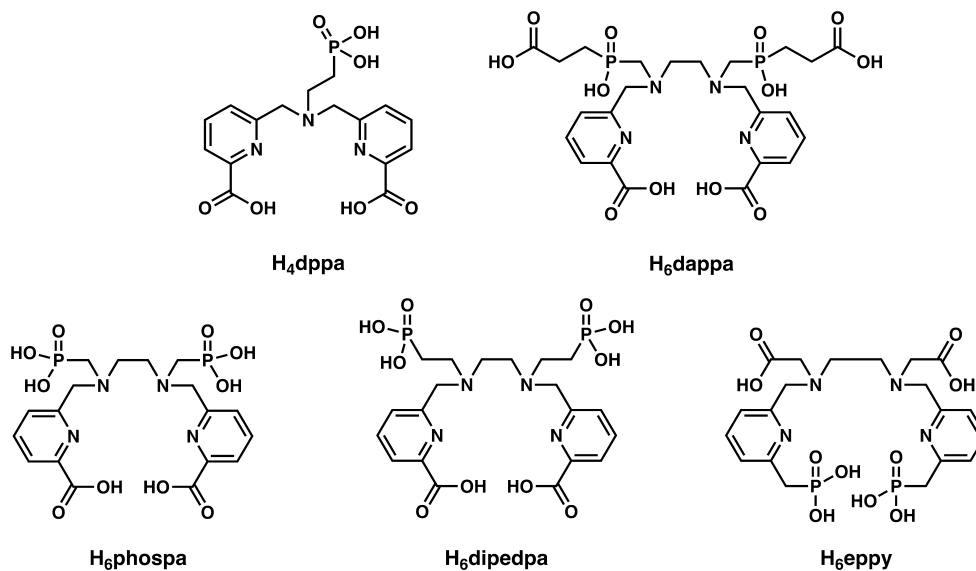


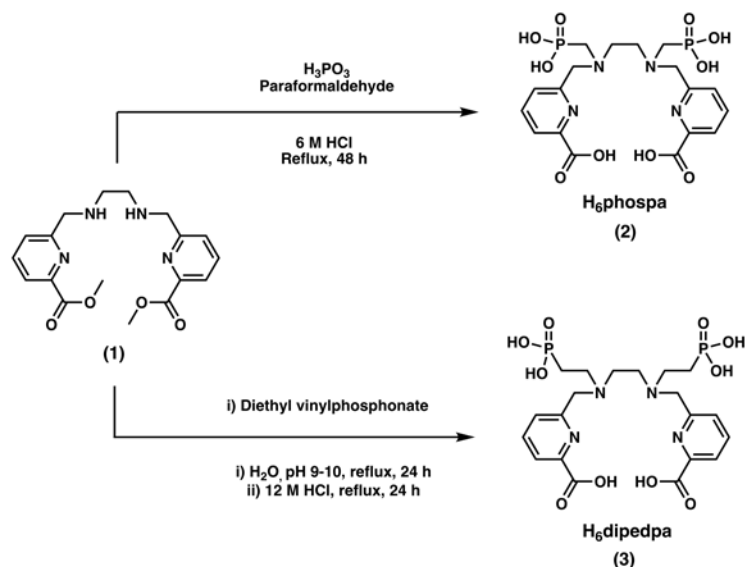
**Chart 3.2** Phosphonate-bearing picolinic acid-based chelators. Top: previously reported (not described); Bottom: under investigation in this work.

## 3.2 Results and Discussion

### 3.2.1 Ligand Synthesis and Characterization

The strategy for the synthesis of  $\text{H}_6\text{phospa}$  and  $\text{H}_6\text{dipedpa}$  (Scheme 3.1) was to first build the dipicolinate ethylene diamine scaffold through synthesis of **1** (as reported elsewhere<sup>139,140</sup>) then to functionalize the resultant secondary amines to yield two distinct ligands, differing only in the length of the amine-phosphonate bridging unit.  $\text{H}_6\text{phospa}$  was synthesized via Kabachnik-Fields reaction, which forms a methylene bridge between the amine and phosphonate group following dissolution and heating of **1** and phosphorous acid in HCl (6 M) and slow addition of paraformaldehyde. The harsh conditions required for this reaction also

conveniently deprotect the methyl esters of **1**, obviating the need for an additional deprotection step. H<sub>6</sub>dipedpa was synthesized through an aza-Michael addition between **1** and diethyl vinylphosphonate in refluxing aqueous solution at pH 9–10 to ensure adequate nucleophilicity of secondary amines. Upon addition of two phosphonate arms, the excess diethyl vinylphosphonate can be extracted with dichloromethane. Although the intermediate is somewhat hydrophobic due to the pyridine rings and ethyl-protected phosphonate groups, the picolinic acid groups become deprotected under reaction conditions due to the combination of basic pH and high heat, as supported by mass spectroscopy (low resolution electrospray ionization mass spectrometry; LR-ESI-MS). This results in the desired intermediate remaining in the aqueous phase. Deprotection of the phosphonate groups is achieved through rotary evaporation of solution followed by addition and refluxing of *conc.* hydrochloric acid (HCl). Unlike most other “pa” (picolinic acid) family ligands, H<sub>6</sub>phospa and H<sub>6</sub>dipedpa do not require HPLC for purification. The presence of phosphonate groups on both ligands instead enables the use of two-solvent precipitation to yield pure products. Following the HCl reflux and complete evaporation of solvent, dissolving the crude product in minimal water, then precipitating out the product with acetone yields a crude brown oil once the precipitate is allowed to settle. Decanting of the solution and washing of the oil with acetone yields the pure ligand as a hydrated HCl salt (i.e., H<sub>6</sub>phospa·0.3HCl·1.8H<sub>2</sub>O and H<sub>6</sub>dipedpa·4HCl·2H<sub>2</sub>O). The simplicity of these syntheses and the luxury of eluding time-consuming HPLC purification are very attractive features indeed!



**Scheme 3.1**  $\text{H}_6\text{phospa}$  and  $\text{H}_6\text{dipedpa}$  synthesis.

$\text{H}_6\text{eppy}$  is a unique derivative from pa family ligands, as the picolinic acid groups have been replaced with methylene-phosphonates. While (by definition) it is not part of the pa family,  $\text{H}_6\text{eppy}$  does provide an interesting opportunity for a comparative study with the aforementioned ligands and was therefore the aim of this synthetic endeavor. Similar to the synthesis of  $\text{H}_6\text{phospa}$  and  $\text{H}_6\text{dipedpa}$ , the strategy to make  $\text{H}_6\text{eppy}$  (Scheme 3.2) was to base the design around an ethylene diamine backbone, and add the desired arms sequentially. Taking inspiration from the optimized synthesis of  $\text{H}_4\text{octapa}$ ,<sup>141</sup> instead of adding acetate arms to a protected ethylene diamine starting material, a simple Fischer esterification of ethylenediamine-*N,N'*-diacetic acid (EDDA) resulted in the desired backbone (8), with secondary amines available for subsequent arm attachment via  $\text{S}_{\text{N}}2$ . The synthesis of the pyridine-phosphonate arm (7) builds upon the methyl-6-bromomethylpicolinate arm (4) used in the above syntheses. Using triethylphosphite and zinc(II) bromide as a catalyst, the Michaelis-Arbuzov reaction results in replacement of the bromine group with a protected phosphonate. Reduction of the methyl ester with  $\text{NaBH}_4$  primes the alcohol for bromination



### 3.2.2 X-ray Crystal Structures

X-ray quality single crystals of both H<sub>6</sub>phospa and H<sub>6</sub>dipedpa were obtained through the two-vial vapour diffusion technique, where acetone slowly diffused into an aqueous solution containing the compound of interest, with an approximate concentration of 8 mM and no further adjustment of pH. The ORTEP (Oak Ridge Thermal-Ellipsoid Plot) diagrams of the ligands are shown in Figure 3.1. Crystallographic information and selected bond lengths/angles can be found in Tables A.4 and A.6-9, respectively. From Figure 3.1, it can be seen that H<sub>6</sub>phospa and H<sub>6</sub>dipedpa are neutral, zwitterionic species (deprotonated phosphonates; protonated amines) consistent with calculated pK<sub>a</sub> values (*vide infra*), given the pH of the solution from which the crystals were grown (pH ≈ 2). The configuration of H<sub>6</sub>phospa reveals a symmetric, closed-structure conformation with intramolecular hydrogen-bonding between the protonated picolinic acid, deprotonated phosphonate and protonated amine groups. Conversely, the configuration of H<sub>6</sub>dipedpa is a symmetric, open-chain structure, with evident phosphonate-water hydrogen-bonding (shown in Figure A1) in lieu of intramolecular interactions.

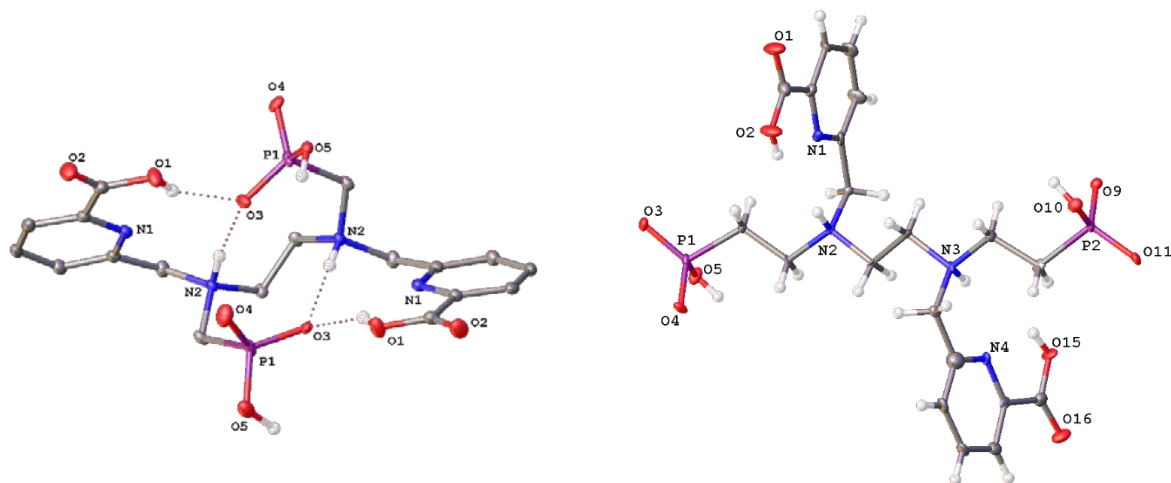


**Figure 3.1** ORTEP diagrams of H<sub>6</sub>phospa (left) and H<sub>6</sub>dipedpa (right).

### 3.2.3 Metal Complexation Studies

Complexation studies were conducted primarily through the use of  $^1\text{H}$  NMR spectroscopy and  $^1\text{H}$ - $^1\text{H}$  correlation spectroscopy (COSY), as well as  $^{31}\text{P}\{^1\text{H}\}$  NMR spectroscopy and high-resolution electrospray ionization mass spectrometry (HR-ESI-MS). These studies were carried out not only to confirm metal chelation, but also to gain insight into complex symmetry, fluxionality and approximate ligand configurations in solution. The trivalent metal ions  $\text{In}^{3+}$ ,  $\text{Sc}^{3+}$ ,  $\text{Lu}^{3+}$  and  $\text{Y}^{3+}$  were selected because of the availability of radioisotope counterparts (i.e.,  $[^{111}\text{In}]\text{In}^{3+}$ ,  $[^{44}\text{Sc}]\text{Sc}^{3+}$ ,  $[^{177}\text{Lu}]\text{Lu}^{3+}$ ,  $[^{90}\text{Y}]\text{Y}^{3+}$ ), which have varying degrees of clinical utility, ranging from primarily preclinical research (e.g.,  $[^{44}\text{Sc}]\text{Sc}^{3+}$ ) to routine clinical use (e.g.,  $[^{177}\text{Lu}]\text{Lu}^{3+}$ ). Moreover,  $\text{La}^{3+}$  was studied as (in the absence of a more suitable candidate) it is considered a “cold” surrogate for the now famous  $\alpha$ -emitter,  $[^{225}\text{Ac}]\text{Ac}^{3+}$ . Additionally, excluding  $\text{In}^{3+}$ , this series of (pseudo)lanthanides presents an opportunity to study how ionic radius impacts chelation chemistry, as size increases across the series, yet chemical hardness remains virtually identical (as measured by the Drago–Wayland metric  $I_{\text{A}}$ ).<sup>52</sup>

Typical evidence of ligand chelation is qualitative observation of diastereotopic splitting in  $^1\text{H}$  NMR spectra, which can be confirmed by  $^1\text{H}$ - $^1\text{H}$  COSY. These splitting patterns are a result of previously equivalent protons from freely rotating, symmetric ligands (often  $C_{2v}$  point groups for pa ligands) becoming inequivalent due metal ion chelation, which results in structural rigidity. For example, the observation of a singlet peak in the  $^1\text{H}$  NMR spectra of a free ligand being replaced by two doublet peaks (each with half integration of the singlet) following addition of a metal ion is a common sign of chelation. For symmetric complexes, the simplicity of resulting splitting patterns often makes spectra straightforward to interpret.

However, when metal complexes are asymmetric, interpretation can be more challenging due to the two-fold increase in signals, which can overlap and become difficult to differentiate.

Figure 3.2 illustrates characteristic spectral changes as a result of chelation, both from symmetric and asymmetric complexes. Lanthanum(III) complexes derived from pa family chelators are often rigid and symmetric as a result of lanthanum's large radius (1.16 Å, CN = 8),<sup>98</sup> which fills the dedpa-like (*N,N'*-dipicolinate ethylenediamine<sup>81</sup>) coordination sphere and permits facile coordination of pendant arms to coordinatively saturate the metal ion. Indeed, both H<sub>6</sub>phospa and H<sub>6</sub>dipedpa conform to this tendency, as supported by simple diastereotopic splitting patterns in <sup>1</sup>H NMR spectra. Medium-sized metal ions (e.g., Y<sup>3+</sup>, In<sup>3+</sup>, Lu<sup>3+</sup>) have less predictable behaviour with pa family chelators, as small differences in functional groups have historically led to a range of behaviours with respect to isomers, fluxionality and symmetry,<sup>143–146</sup> as is the case with the pa ligands studied in this work (Figures A2-A26). Scandium(III) complexes of pa family ligands have only recently<sup>147</sup> seen interest due to the increasing availability of [<sup>44/47</sup>Sc]Sc<sup>3+</sup>. Interestingly, with both H<sub>6</sub>phospa and H<sub>6</sub>dipedpa, resulting complexes are rigid and asymmetric. Figure 3.2a and 3.2b illustrate the differences in spectral complexity between these symmetric La<sup>3+</sup> and asymmetric Sc<sup>3+</sup> complexes.

While the coordinating functional groups of H<sub>6</sub>ep<sub>py</sub> are identical to H<sub>6</sub>phospa and H<sub>6</sub>dipedpa [N<sub>4</sub>O<sub>2</sub>(PO)<sub>2</sub>], the rearrangement of phosphonate and carboxylate groups exclude H<sub>6</sub>ep<sub>py</sub> from the pa family, and have led to a number of interesting differences in metal ion chelation. The most striking difference comes from comparison of the Sc<sup>3+</sup> complexes. Scandium(III) complexes of H<sub>6</sub>phospa and H<sub>6</sub>dipedpa are asymmetric, likely as a result of the pyridine rings conforming to a perpendicular coordination environment (~90° N<sub>py</sub>–Sc–N<sub>py</sub> bond angle) to accommodate the small metal ion (Sc<sup>3+</sup> ionic radius = 0.87 Å, CN = 8),<sup>98</sup> which does

not adequately fill the usual dedpa-like coordination sphere. Conversely, replacement of the aromatic carboxylic acids with methylene-bridged phosphonate groups results in less contortion of the pyridine rings and ethylene backbone as a result of the additional points of free rotation [i.e., py-**CH**<sub>2</sub>-P(O)(OH)<sub>2</sub>]. As supported by the simple diastereotopic splitting of Figure 3.2c a rigid, symmetric Sc<sup>3+</sup> complex is the result of this alteration. The relative broadness of the [La(H<sub>2</sub>eppy)]<sup>-</sup> complex can also be rationalized when considering ligand flexibility. The rigid nature of picolinic acid groups and close match of La<sup>3+</sup> to the binding pocket of pa family ligands generally lead to symmetric and highly rigid La<sup>3+</sup> complexes, as seen in Figure 3.2a and 3.2b. While H<sub>6</sub>eppy appears to maintain symmetry when chelating La<sup>3+</sup>, peak broadness in the <sup>1</sup>H NMR spectrum suggests fluxional behaviour of the complex, which is logically a result of decreased ligand rigidity.

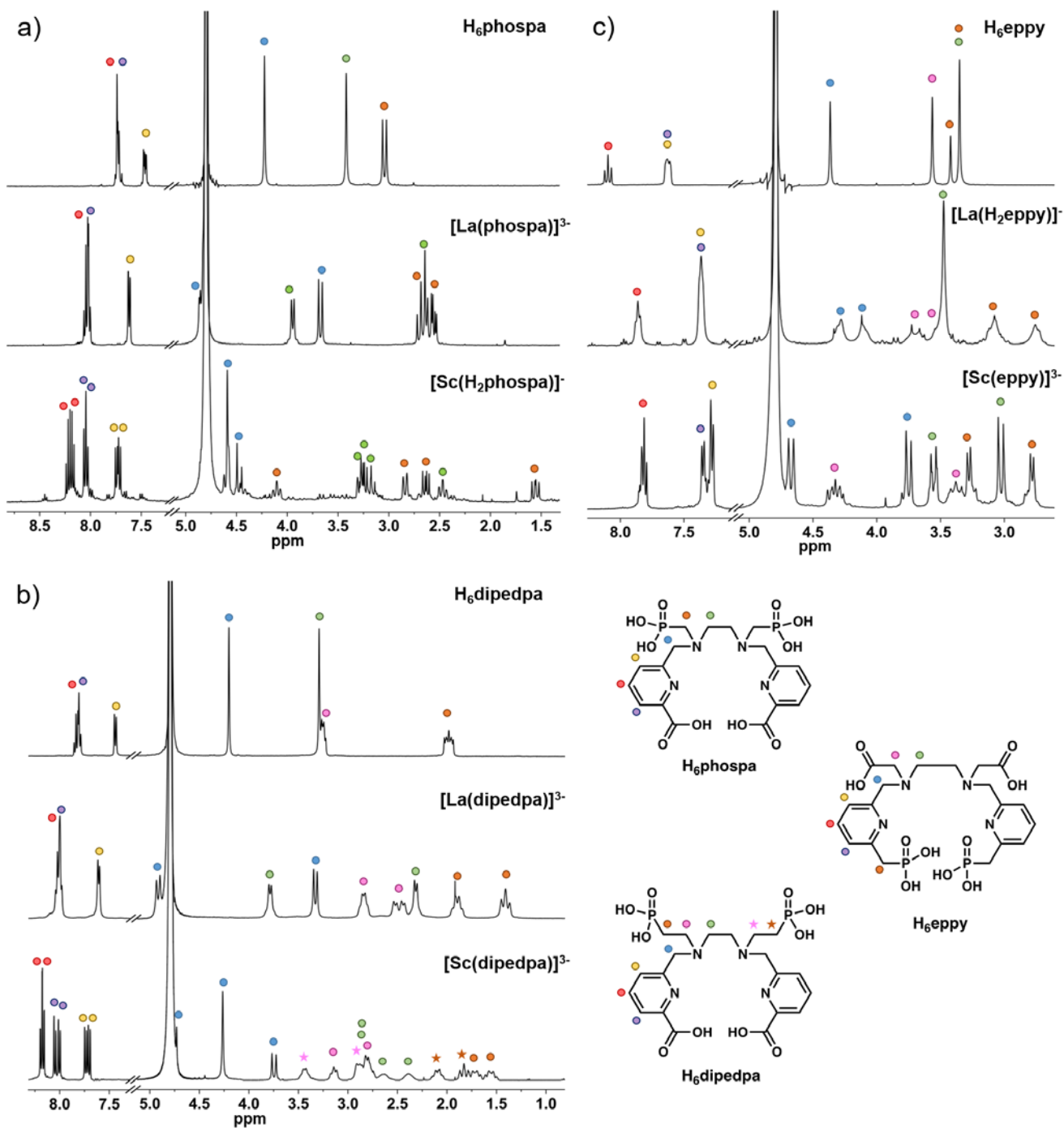
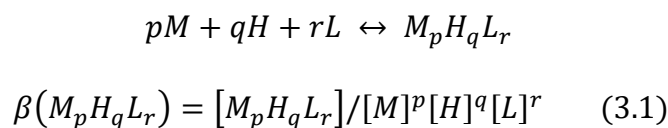


**Figure 3.2**  $^1\text{H}$  NMR spectra of a)  $\text{H}_6\text{phospa}$ , b)  $\text{H}_6\text{dipedpa}$  and c)  $\text{H}_6\text{eppy}$  and their corresponding  $\text{La}^{3+}$  and  $\text{Sc}^{3+}$  complexes. Stars in  $[\text{Sc}(\text{dipedpa})]^{3-}$  spectrum represent neighboring ethylene protons of the asymmetric complex.

### 3.2.4 Solution Thermodynamics of H<sub>6</sub>phospa, H<sub>6</sub>dipedpa and H<sub>6</sub>eppy

In general, aqueous metal-ligand systems and their cumulative stability constants, defined by the associations  $\beta(M_pH_qL_r)$  (e.g., ligand species H<sub>q</sub>L, metal complexes species M<sub>p</sub>H<sub>q</sub>L<sub>r</sub>, and metal hydrolysis species M<sub>p</sub>H<sub>q</sub>), can be defined by Equation 3.1, where M is the metal ion, and L is the fully deprotonated chelating ligand and p, q and r are the stoichiometric numbers of the components.



Since basicity of different donor atoms of the ligand affects metal complexation, protonation constants of H<sub>6</sub>phospa, H<sub>6</sub>dipedpa and H<sub>6</sub>eppy were determined. For each of the ligands, ten protonation sites are possible; however, even in very acidic solutions, protonation constants of the two most acidic donor atoms were not found. Thus, at that acidic pH, those donor atoms are deprotonated and can readily coordinate metal ions. For each ligand, two different methods were used for pK<sub>a</sub> determination: acidic UV-in-batch spectrophotometric titrations and combined UV-potentiometric titrations. The spectral evolution of each ligand, with respect to pH, and the corresponding speciation plots are shown in Figures A28-A30. For H<sub>6</sub>phospa, additional <sup>31</sup>P and <sup>1</sup>H NMR titrations were performed to more accurately assign and determine the most acidic and most basic pK<sub>a</sub> values (Figure 3.3 and A27). Protonation constants were calculated with HypSpec2014<sup>148</sup>, HypNMR2008<sup>149</sup> and HyperQuad2013<sup>150</sup> software and are presented in Table 3.1.

**Table 3.1** Protonation constants (log  $K_a$ ) of discussed ligands.

Equilibrium Reaction	H <sub>6</sub> phospa	H <sub>6</sub> dipedpa	H <sub>6</sub> eply
$L^{6-} + H^+ \rightleftharpoons HL^{5-}$	11.43 (1) <sup>a</sup> ; 11.50 (1) <sup>b</sup> (N <sub>en</sub> )	11.02 (1) <sup>b</sup> (N <sub>en</sub> )	9.22 (1) <sup>b</sup> (N <sub>en</sub> )
$HL^{5-} + H^+ \rightleftharpoons H_2L^{4-}$	10.05 (1) <sup>b</sup> (N <sub>en</sub> )	9.20 (1) <sup>b</sup> (N <sub>en</sub> )	7.86 (1) <sup>b</sup> (P-OH)
$H_2L^{4-} + H^+ \rightleftharpoons H_3L^{3-}$	8.00 (2) <sup>b</sup> (P-OH)	7.42 (1) <sup>b</sup> (P-OH)	7.13 (1) <sup>b</sup> (P-OH)
$H_3L^{3-} + H^+ \rightleftharpoons H_4L^{2-}$	5.83 (2) <sup>b</sup> (P-OH)	6.40 (1) <sup>b</sup> (P-OH)	5.74 (1) <sup>b</sup> (N <sub>en</sub> )
$H_4L^{2-} + H^+ \rightleftharpoons H_5L^-$	4.73 (1) <sup>b</sup> (py-COOH)	4.97 (1) <sup>b</sup> (py-COOH)	3.71 (1) <sup>b</sup> (COOH)
$H_5L^- + H^+ \rightleftharpoons H_6L$	3.18 (2) <sup>b</sup> (py-COOH)	3.19 (1) <sup>b</sup> (py-COOH)	2.29 (2) <sup>b</sup> (COOH)
$H_6L + H^+ \rightleftharpoons H_7L^+$	1.85 (9) <sup>b</sup> (P-OH)	2.30 (2) <sup>b</sup> (P-OH)	0.88 (3) <sup>c</sup> (P-OH)
$H_7L^+ + H^+ \rightleftharpoons H_8L^{2+}$	0.11 (1) <sup>a</sup> (P-OH)	0.8 (1) <sup>c</sup> (P-OH)	-0.16 (2) <sup>c</sup> (P-OH)
$\Sigma \log K \{[H_iL] / [H_{i-1}L][H^+]\}$	<b>45.3 (1); 45.44 (1)</b>	<b>45.3 (1)</b>	<b>36.67 (2)</b>

<sup>a</sup>Using <sup>1</sup>H and <sup>31</sup>P NMR titrations; <sup>b</sup> using UV-potentiometric titrations; <sup>c</sup> using UV batch titration, T = 298K, I = 0.16 M NaCl

(when possible).

Thanks to the structural similarity of the studied ligands, several comparisons can be made to investigate how the position and nature of substituents can affect the ligand protonation constants and the metal coordination. H<sub>6</sub>phospa and H<sub>6</sub>dipedpa differ on the amine-phosphonate bridging group. H<sub>6</sub>phospa has a methylene bridge while H<sub>6</sub>dipedpa has an ethylene bridge (Chart 3.2). The most basic groups in these ligands are the tertiary N atoms (N<sub>en</sub>) in the ethylenediamine backbone. The basicity of those amines in H<sub>6</sub>phospa (log  $K_1$  = 11.43(1); 11.50(1); log  $K_2$  = 10.05(1)) are greater than those in H<sub>6</sub>dipedpa (log  $K_1$  = 11.02(1); log  $K_2$  = 9.20(1)). This is due to the greater stabilization due to strong intramolecular hydrogen bond interactions of the phosphonates in H<sub>6</sub>phospa with the protonated tertiary amines and it is supported by the X-ray structure of the ligand (Figure 3.1). <sup>31</sup>P{<sup>1</sup>H} NMR and <sup>1</sup>H NMR

titrations of H<sub>6</sub>phospa support the existence of H-bond interactions in these protonation steps, as a large change in chemical shift with occurs when 10 < pH < 12 (Figures 3.3 and A27). Protonation constants of the phosphonate functionalities for the two ligands are close to the ones found for similar ligands<sup>151,152</sup> (Table 3.1). The differences in phosphonate protonation constants between H<sub>6</sub>phospa (log *K*<sub>3</sub> - log *K*<sub>4</sub> = 2.17) and H<sub>6</sub>dipedpa (log *K*<sub>3</sub> - log *K*<sub>4</sub> = 1.02) are also worth noting, and explained by the higher intramolecular hydrogen bond interaction in H<sub>6</sub>phospa together with the higher charge repulsion with the closer phosphonate moieties. Following those protonations are the pyridylcarboxylic acid substituents (py-COOH), which compared to the ones in H<sub>4</sub>octapa are slightly higher. Finally, the protonation constants for the most acidic phosphonates in both ligands are comparable, with the H<sub>6</sub>phospa values being slightly more acidic. The protonation scheme of H<sub>6</sub>phospa, assignments and values are confirmed through the dependence of experimental chemical shifts on pH in <sup>31</sup>P NMR and <sup>1</sup>H NMR titrations.

Another effect on p*K*<sub>a</sub> caused by the replacement of substituents can be observed through the comparison of H<sub>6</sub>phospa with H<sub>6</sub>eppy. The exchange of the carboxylic acid in the pyridine ring for a phosphonic acid drastically lowers the overall ligand basicity (Table 3.1). The higher protonation constants found for the N<sub>en</sub> atoms in H<sub>6</sub>phospa now are reduced ~ 2.28 units for the most basic proton (log *K*<sub>1</sub> = 9.22) and 4.31 units for the second most basic proton (log *K*<sub>4</sub> = 5.74). This is reasonable and supported by the H bond interaction between the N<sub>en</sub> and the phosphonate groups in H<sub>6</sub>phospa, which are presumably absent in H<sub>6</sub>eppy. These lower p*K*<sub>a</sub> values are very close to those of H<sub>4</sub>octapa<sup>141</sup> due to their identical ethylenediamine diacetic acid backbone. Protonation constants of the phosphonate substituents (log *K*<sub>2</sub> = 7.86; log *K*<sub>3</sub> = 7.13) are now closer to one another, followed by the protonation of the carboxylic acid

substituents ( $\log K_5 = 3.71$ ;  $\log K_6 = 2.29$ ). The most acidic protons are most likely bound to the remaining phosphonate groups ( $\log K_7 = 0.88$ ;  $\log K_8 = -0.16$ ).

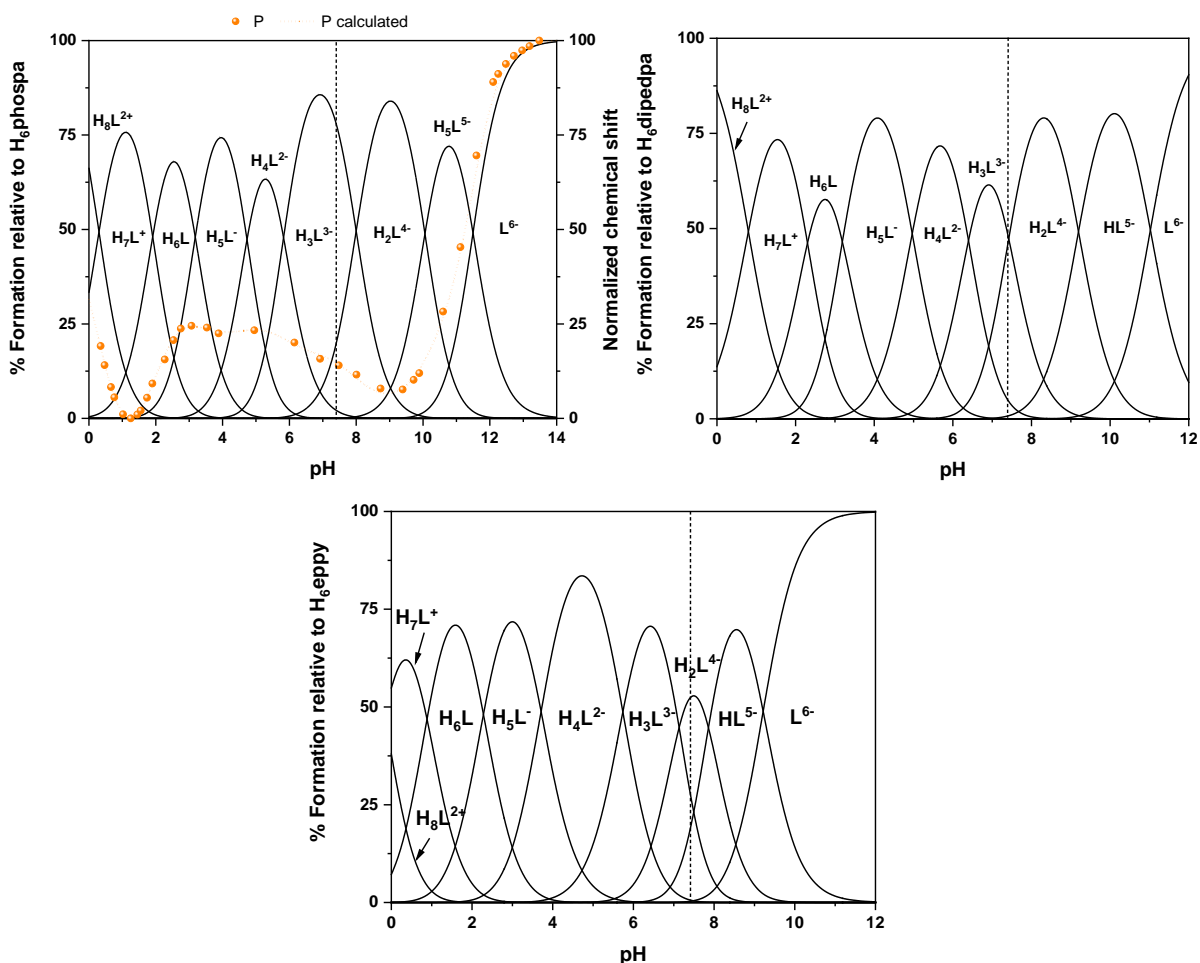


**Figure 3.3** Speciation plot of  $H_6$ phospa,  $H_6$ dipeda and  $H_6$ eppy.  $^{31}\text{P}$  chemical shift dependence on pH of  $H_6$ phospa and HypNMR2008<sup>149</sup> fitting overlaps the speciation plot.

We recently reported a decadentate phosphinate containing ligand  $H_6$ dappa<sup>140</sup> (Chart 3.2), which can also be compared to  $H_6$ phospa. The substitution of a carboxyethyl phosphinic acid for a phosphonic acid greatly increases the basicity of the  $N_{en}$  atoms (from  $\log K_1 = 7.96(1)$  and  $\log K_2 = 5.48(2)$  to  $\log K_1 = 11.43(1)$  and  $\log K_2 = 10.05(1)$ ) and the overall basicity over

those two steps  $\log \beta_2$  (from 13.44(1) to 21.48(1)) due to the electronic differences between phosphonates and phosphinates, as well as the hydrogen bonding present in H<sub>6</sub>phospa.

A final comparison between H<sub>6</sub>dipedpa and its smaller analogue H<sub>4</sub>dppa<sup>151</sup> can be made. The presence of the ethylenediamino-*N,N'*-diethyl phosphonic acid backbone as opposed of the aminoethyl phosphonic acid not only increases the overall basicity but also the coordination number and the metal complex stability with lanthanum metal ions. Nonetheless, H<sub>6</sub>dipedpa and H<sub>4</sub>dppa share the same protonation scheme, with the most acidic p*K*<sub>a</sub> belonging to the phosphonate group(s), followed by both picolinic acid protonation constants, then the more basic phosphonate value(s). Lastly, in each case the amine backbone has/have the most basic p*K*<sub>a</sub> value(s) of each ligand. Due to the very acidic phosphonate protons, for both ligands protonation constants were obtained using both potentiometric and <sup>31</sup>P and <sup>1</sup>H NMR titrations<sup>151</sup>.

### **3.2.5 Complex Formation Equilibria of H<sub>6</sub>phospa, H<sub>6</sub>dipedpa and H<sub>6</sub>eppy with In<sup>3+</sup>, Lu<sup>3+</sup>, Y<sup>3+</sup>, Sc<sup>3+</sup>, La<sup>3+</sup>**

Complex formation equilibria of H<sub>6</sub>phospa, H<sub>6</sub>dipedpa and H<sub>6</sub>eppy with Sc(III), In(III), Lu(III), Y(III) and La(III) metal ions was studied through combined UV-potentiometric titrations and, for metal complexes where metal complexation occurred below the electrode threshold, acidic UV-in-batch spectrophotometric titrations were carried out to determine the first protonated metal complex species. Stability constants were calculated with HypSpec2014<sup>148</sup> and Hyperquad2013<sup>150</sup> (Table 3.2) and the speciation plots generated with Hyss.<sup>153</sup> For all three ligands, metal complexes species M(H<sub>3</sub>L), [M(H<sub>2</sub>L)]<sup>-</sup>, [M(HL)]<sup>2-</sup>, [ML]<sup>3-</sup> and [M(OH)L]<sup>4-</sup> were identified, as well as [M(OH)<sub>2</sub>L]<sup>5-</sup> for H<sub>6</sub>dipedpa and H<sub>6</sub>eppy.

Metal complex stability for the three ligands follow the order H<sub>6</sub>phospa > H<sub>6</sub>dipedpa > H<sub>6</sub>eppy. It is worth noting that despite the equal overall basicity of H<sub>6</sub>phospa and H<sub>6</sub>dipedpa, complex formation equilibria are energetically more favoured for H<sub>6</sub>phospa. Complex formation of H<sub>6</sub>phospa for each of the metal ions starts at lower pH than the corresponding ones for H<sub>6</sub>dipedpa or H<sub>6</sub>eppy. Additionally, in Table 3.2 it can be noted that when comparing H<sub>6</sub>phospa and H<sub>6</sub>dipedpa metal complexes, protonation constants of [M(HL)]<sup>2-</sup> and [M(H<sub>2</sub>L)]<sup>-</sup> species are comparable for both ligands. The major difference lies in the protonation of the [ML]<sup>3-</sup> species for each of the metal ions (excluding La<sup>3+</sup>), which is higher for H<sub>6</sub>dipedpa, ultimately leading to higher stability of the [ML]<sup>3-</sup> species for H<sub>6</sub>phospa complexes.

When comparing metal complex stability with different chelating ligands, a superior metric than log K<sub>ML</sub> is given by the pM value. Not only is pM linearly correlated to the stability of metal complexes, but it also accounts for ligand basicity, denticity and stoichiometries of metal complexes. pM is defined as -log [M]<sub>free</sub> at standard conditions ([L] = 10 μM, [M] = 1 μM and pH = 7.4). It is generally considered as the metal scavenging ability of a ligand (the lower the [M]<sub>free</sub> the higher the pM), and allows the comparison of both the affinity of different ligands for a specific metal ion as well as the metal selectivity of a ligand for different metal ions. Figure 3.4 is a plot of pM values (M = Sc<sup>3+</sup>, In<sup>3+</sup>, Lu<sup>3+</sup>, Y<sup>3+</sup>, La<sup>3+</sup>) of the ligands studied in this work, as well as similar ligands developed for use as radiopharmaceutical agents. For H<sub>6</sub>phospa, H<sub>6</sub>dipedpa and H<sub>6</sub>eppy, pM follow the trend pIn > pSc > pLu > pY > pLa, with the exception of H<sub>6</sub>dipedpa, for which pLa is higher than pY and pLu. More interestingly; however, is Figure 3.4, where the free metal (pSc) has been plotted vs. pH for comparable chelators. In addition to comparison of the metal scavenging ability of different chelators at pH 7.4, essential in medicinal applications to avoid transmetallation reactions *in vivo*, pM values

**Table 3.2** Stability constants ( $\log K_{ML}$ ) and the corresponding stepwise protonation constants  $\log K_{1n1}(\text{MH}_n\text{L})^a$  of  $\text{H}_6\text{phospa}$ ,  $\text{H}_6\text{dipedpa}$  and  $\text{H}_6\text{eppy}$  with metals of interest ( $T = 25^\circ\text{C}$ ,  $I = 0.16 \text{ M NaCl}$ ).

	$\text{Sc}^{3+}$	$\text{In}^{3+}$	$\text{Lu}^{3+}$	$\text{Y}^{3+}$	$\text{La}^{3+}$
<b><math>\text{H}_6\text{phospa}</math></b>					
$\log K_{101}(\text{ML})$	<b>34.92 (3)</b>	<b>38.64 (3)</b>	<b>29.90 (6)</b>	<b>28.01 (4)</b>	<b>27.99 (4)</b>
$\log K_{111}(\text{MHL})$	5.94 (4)	5.45 (6)	6.47 (7)	6.19 (1)	5.41 (1)
$\log K_{121}(\text{MH}_2\text{L})$	4.28 (4)	4.06 (3)	4.07 (6)	4.68 (2)	4.57 (3)
$\log K_{131}(\text{MH}_3\text{L})$	2.96 (2)	2.98 (3)	3.55 (1)	2.38 (2)	2.97 (2)
$\log K_{1-11}(\text{M}(\text{OH})\text{L})$	9.65 (4)	10.43 (3)	9.48 (7)	11.44 (4)	10.54 (4)
<b><math>\text{H}_6\text{dipedpa}</math></b>					
$\log K_{101}(\text{ML})$	<b>25.17 (3)</b>	<b>31.12 (2)</b>	<b>23.96 (3)</b>	<b>23.90 (2)</b>	<b>25.82 (3)</b>
$\log K_{111}(\text{MHL})$	6.59 (3)	6.93 (2)	7.13 (3)	7.11 (2)	4.71 (2)
$\log K_{121}(\text{MH}_2\text{L})$	4.52 (2)	4.11 (2)	5.00 (1)	4.74 (2)	3.40 (3)
$\log K_{131}(\text{MH}_3\text{L})$	3.05 (2)	3.19 (1)	2.76 (1)	2.89 (3)	3.40 (3)
$\log K_{1-11}(\text{M}(\text{OH})\text{L})$	8.08 (2)	8.74 (3)	9.17 (3)	9.47 (3)	7.02 (3)
$\log K_{1-21}$ $(\text{M}(\text{OH})_2\text{L})$	9.76 (2)	-	-	-	10.22 (3)
<b><math>\text{H}_6\text{eppy}</math></b>					
$\log K_{101}(\text{ML})$	<b>22.03 (2)</b>	<b>26.56 (2)</b>	<b>18.44 (3)</b>	<b>17.85 (1)</b>	<b>15.60 (2)</b>
$\log K_{111}(\text{MHL})$	4.74 (4)	6.40 (2)	8.29 (3)	8.45 (1)	7.32 (2)
$\log K_{121}(\text{MH}_2\text{L})$	4.35 (3)	4.35 (3)	4.42 (4)	4.01 (1)	5.26 (2)
$\log K_{131}(\text{MH}_3\text{L})$	3.06 (4)	2.88 (3)	-	-	-
$\log K_{1-11}(\text{M}(\text{OH})\text{L})$	7.73 (2)	8.62 (3)	10.65 (5)	10.65 (2)	10.73 (2)
$\log K_{1-21}$ $(\text{M}(\text{OH})_2\text{L})$	9.93 (3)	-	-	-	-

<sup>a</sup> $K_{1n1} = [\text{MH}_n\text{L}]/[\text{MH}_{n-1}\text{L}][\text{H}]^n$ ; (n-1) = -1 denotes OH.

allow for the quantification of the free metal ions from pH 0–12. This can be useful when high selectivity is required at a specific pH (e.g., radionuclide purification, water purification). It is interesting to note the different profiles of the curves. For ligands like  $\text{H}_6\text{dappa}$  and  $\text{H}_4\text{pypa}$  with similar and lower overall basicities, pSc grows from lower pH exponentially reaching a plateau before pH 7.4, while for more basic ligands like  $\text{H}_6\text{phospa}$ ,  $\text{H}_6\text{dipedpa}$  and  $\text{H}_6\text{eppy}$ , pSc follows exponential growth. This reflects how ligands with lower overall basicities have less proton competition for the metal ion and have a broader pH range with static complex stability (due to the stability plateau). On an encouraging note, as shown by the graph,  $\text{H}_6\text{phospa}$  has the highest pSc value reported at physiological pH and above, which provides auspicious evidence for further study with the theranostic radionuclide pair  $^{44/47}\text{Sc}[\text{Sc}]^{3+}$ .

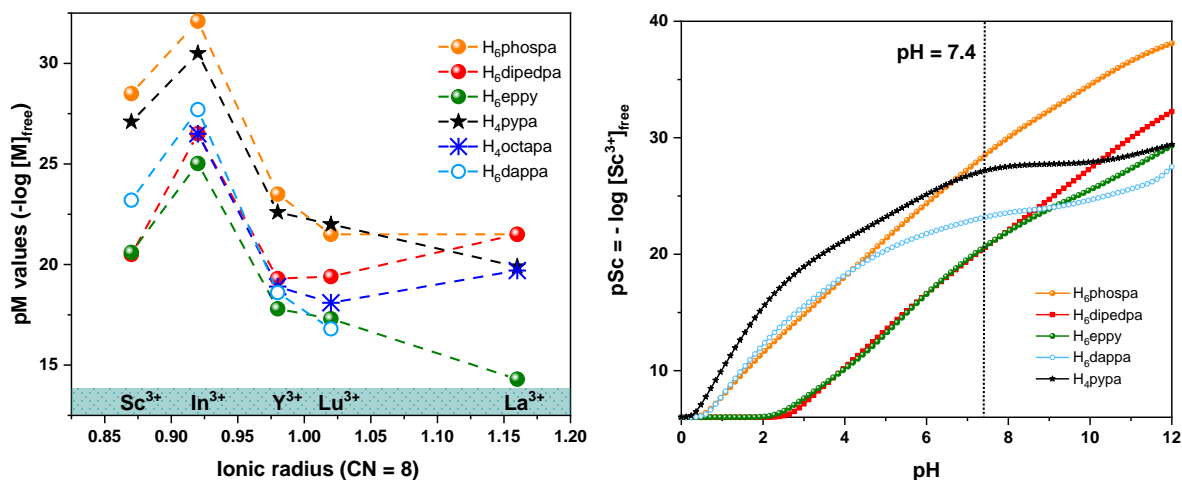


**Figure 3.4** pM values ( $M^{3+} = Sc^{3+}, In^{3+}, Y^{3+}, Lu^{3+}, La^{3+}$ ) versus ionic radii (CN=8) for discussed chelating ligands (left) and  $Sc^{3+}$  scavenging ability of discussed ligands with pH (right).

### 3.2.6 Density Functional Theory Calculations

The structures and coordination geometry of  $[La(H_2phospa)]^-$  and  $[Sc(H_2phospa)]^-$  were studied using DFT calculations. These complexes were chosen because of the interesting features noted in  $^1H$  NMR spectra. Moreover, as rare earths,  $La^{3+}$  and  $Sc^{3+}$  have similar ionic bonding character despite their drastic differences in ionic radii.<sup>52,98</sup> Thus, comparison of  $La^{3+}$  and  $Sc^{3+}$  metal complexes affords the opportunity to directly observe the effect of metal ion size on corresponding coordination complexes. Structures are presented in Figure 3.5, and bond distances in Table 3.3.

As discussed in Section 3.2.3, the most evident difference between  $La^{3+}$  and  $Sc^{3+}$  complexes of  $H_6phospa$  is symmetry. As seen in Figure 3.5, the larger  $La^{3+}$  ion completely fills the binding pocket of  $H_6phospa$ , resulting in a rigid, symmetric complex that becomes coordinatively saturated upon with the inclusion of an explicit water molecule. Conversely, the smaller  $Sc^{3+}$  ion is too small to accommodate the typical twisted picolinic acid binding motif

of many pa family ligands, and as such conforms to an asymmetric configuration, where pyridine rings coordinate perpendicular to one-another, and phosphonate arms lie uncharacteristically adjacent. No water coordination is possible in  $[\text{Sc}(\text{H}_2\text{phospa})]^-$  due to the small metal ion size, and coordination requirements of  $\text{Sc}^{3+}$ . Despite its structural differences with  $[\text{La}(\text{H}_2\text{phospa})(\text{H}_2\text{O})]^-$ ,  $[\text{Sc}(\text{H}_2\text{phospa})]^-$  is also rigid in solution, as evidenced by the peaks in the  $^1\text{H}$  NMR spectrum. Analysis of bond lengths in Table 3.3 reveals predictably longer bond lengths for the  $\text{La}^{3+}$  complex as a consequence of a larger ionic radii. Surprisingly, despite the asymmetric conformation of the  $\text{Sc}^{3+}$  complex, bond distances of identical functional groups (i.e.,  $\text{N}_{\text{tertiary}1}$  vs.  $\text{N}_{\text{tertiary}2}$ ) are very uniform. For both complexes, coordinative phosphonate bonds are the shortest, followed sequentially by pyridine amines, picolinate and backbone tertiary amines.

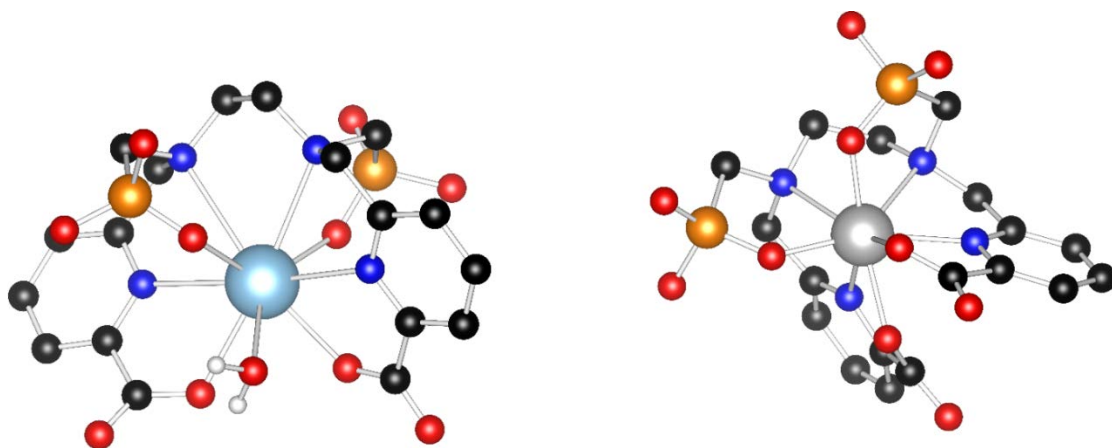


**Figure 3.5** DFT calculated structures of  $[\text{La}(\text{H}_2\text{phospa})(\text{H}_2\text{O})]^-$  (left) and  $[\text{Sc}(\text{H}_2\text{phospa})]^-$  (right). Ligand hydrogens omitted for clarity.

**Table 3.3** Comparison of DFT calculated metal coordination bond lengths of La<sup>3+</sup> and Sc<sup>3+</sup> phospha complexes.<sup>a</sup>

<b>LaH<sub>2</sub>phospa</b>			<b>ScH<sub>2</sub>phospa</b>		
Atom 1	Atom 2 <sup>b</sup>	Distance (Å)	Atom 1	Atom 2 <sup>b</sup>	Distance (Å)
La	<b>N</b> <sub>tertiary1</sub>	2.95	Sc	<b>N</b> <sub>tertiary1</sub>	2.63
La	<b>N</b> <sub>tertiary2</sub>	3.04	Sc	<b>N</b> <sub>tertiary2</sub>	2.58
La	<b>PO</b> 1	2.44	Sc	<b>PO</b> 1	2.04
La	<b>PO</b> 2	2.39	Sc	<b>PO</b> 2	2.10
La	<b>N</b> <sub>py1</sub>	2.42	Sc	<b>N</b> <sub>py1</sub>	2.24
La	<b>N</b> <sub>py2</sub>	2.59	Sc	<b>N</b> <sub>py2</sub>	2.20
La	<b>COO</b> 1	2.67	Sc	<b>COO</b> 1	2.35
La	<b>COO</b> 2	2.80	Sc	<b>COO</b> 2	2.33
La	<b>H<sub>2</sub>O</b>	2.70	Sc	<b>H<sub>2</sub>O</b>	-

<sup>a</sup>Structures calculated in H<sub>2</sub>O with additional 12 explicit water molecules. <sup>b</sup>Coordinating atom is bolded.

In an effort to validate the calculated structures, theoretical <sup>1</sup>H NMR spectra were generated and compared with experimental spectra. It should be noted that no coupling constants have been included in the rendering of theoretical spectra. Figure 3.6 illustrates this comparison, and also the effect of additional explicit waters on the accuracy of the model. Evidently, theoretical NMR spectra are not only very sensitive to structural differences, but also differences introduced by explicit solvent molecules. In general, the calculations agree with the experimental spectra, but it appears that increasing the number of explicit solvent molecule has a beneficial effect on the accuracy of generated spectra, and therefore structures. The methylene protons (coloured orange) bridging amine and phosphonate groups are in particularly good agreement. While challenges still exist for more complex structures (i.e., [Sc(H<sub>2</sub>phospa)]<sup>-</sup>), and further validation through binding energy calculations could be investigated, given the close spectral agreement in Figure 3.6, the calculated structures shown in Figure 3.5 can be considered accurate.

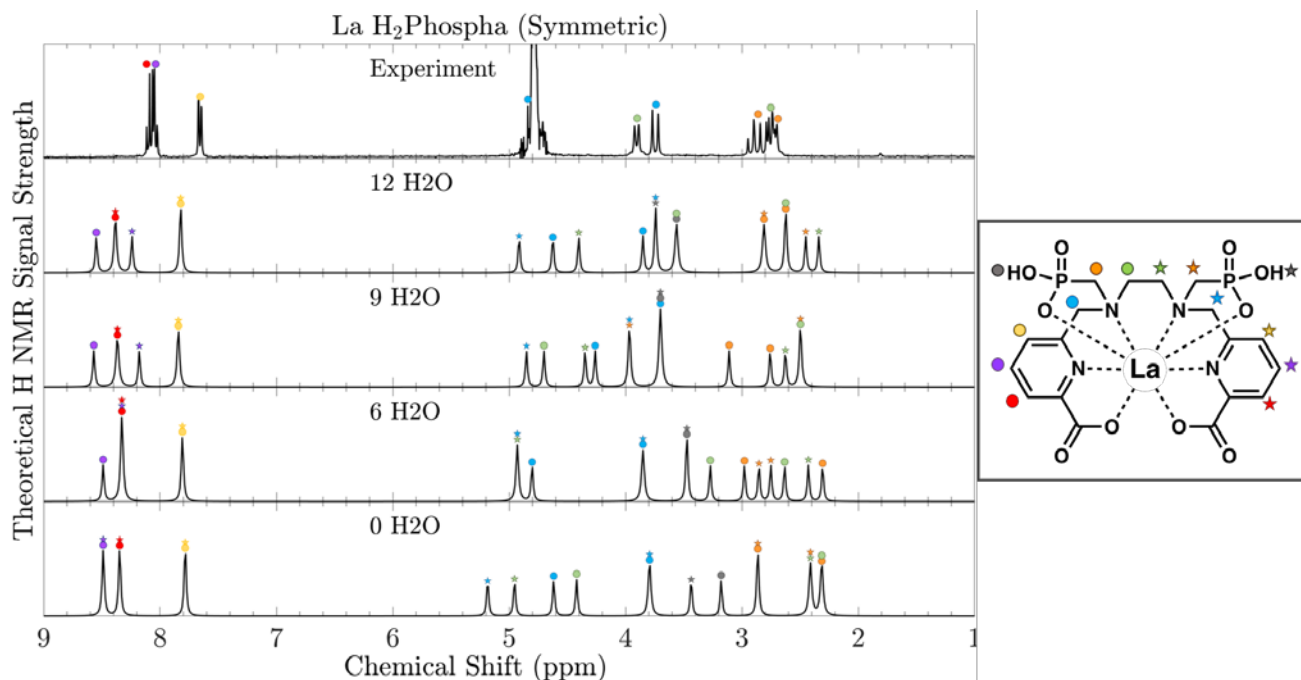


**Figure 3.6** Experimental and DFT calculated  $^1\text{H}$  NMR spectra of  $[\text{La}(\text{H}_2\text{phospa})]$ . Molecule structure and corresponding peak assignments shown.

### 3.3 Conclusions

$\text{H}_6\text{phospa}$ ,  $\text{H}_6\text{dipedpa}$  and  $\text{H}_6\text{eppy}$  were successfully synthesized and fully characterized. X-ray quality crystals of  $\text{H}_6\text{phospa}$  and  $\text{H}_6\text{dipedpa}$  further confirmed characterization, and in the prior case, revealed intramolecular hydrogen bonding. Metal ion chelation was studied by NMR ( $^1\text{H}$ ,  $^{31}\text{P}\{^1\text{H}\}$ ) spectroscopy and  $^1\text{H}$ - $^1\text{H}$  COSY. Picolinic acid bearing ligands were determined to form rigid, symmetric complexes with  $\text{La}^{3+}$  and rigid, asymmetric complexes with  $\text{Sc}^{3+}$ . This tendency was not observed with  $\text{H}_6\text{eppy}$ , where a rigid, symmetric complex was observed with  $\text{Sc}^{3+}$ , and broad peaks were noted in the  $^1\text{H}$  NMR spectrum with  $\text{La}^{3+}$ . Solution studies (potentiometric, spectrophotometric) were conducted to determine the protonation constants of each ligand. The most basic  $\text{pK}_a$  of  $\text{H}_6\text{phospa}$  was validated by  $^{31}\text{P}\{^1\text{H}\}$  and  $^1\text{H}$  NMR titrations. Thermodynamic stability of each ligand with  $\text{In}^{3+}$ ,

$Y^{3+}$ ,  $Sc^{3+}$ ,  $Lu^{3+}$  and  $La^{3+}$  were determined; in each case speciation diagrams and pM values were calculated. In general,  $H_6phospa$  produced the most stable complexes and  $H_6epy$  the least stable complexes. Moreover,  $In^{3+}$  complexes were the most stable and the  $La^{3+}$  complexes least stable. Structures of  $La^{3+}$  and  $Sc^{3+}$  complexes of  $H_6phospa$  and  $H_6dipedpa$  were calculated. The symmetry of calculated complexes is consistent with observations from NMR spectra. To further validate data, NMR spectra of  $[La(H_2phospa)]^+$  were generated from calculated structures and compared to experimental spectra. The number of explicit water molecules was varied in an attempt to discern their importance for modeling these coordination complexes. The model with the most explicit waters (12) was observed to qualitatively fit experimental data best.

## 3.4 Experimental

### 3.4.1 Materials and Methods

All solvents and reagents were purchased from commercial suppliers (Sigma-Aldrich, Fisher Scientific, TCI America, Alfa Aesar, AK Scientific, Fluka) and were used as received. Synthetic reactions were monitored by TLC (MERCK Silicagel 60 F254, aluminum sheet). Flash chromatography was performed using Redisep Rf HP silica columns and a Teledyne Isco (Lincoln, NE) Combiflash Rf automated system. Water used was ultrapure ( $18.2\text{ M}\Omega\text{ cm}^{-1}$  at 298 K, Milli-Q, Millipore, Billerica, MA).  $^1H$ ,  $^{13}C\{^1H\}$  and  $^{31}P\{^1H\}$  NMR spectra were recorded at ambient temperature on Bruker AV300 and AV400 instruments; unless otherwise specified the NMR spectra are expressed on the  $\delta$  scale and referenced to residual solvent peaks. LR-ESI-MS was performed using a Waters ZG spectrometer with an ESCI electrospray/chemical-ionization source, and HR-ESI-MS was performed on a Micromass LCT

time-of-flight instrument at the Department of Chemistry, University of British Columbia. Microanalyses for C, H and N were performed on a Carlo Erba elemental analyzer EA 1108.

### 3.4.2 Synthesis and Characterization.

*Dimethyl-6,6'-([ethane-1,2-diylbis{azanediy}]bis[methylene])dipicolinate (1)*. Compound **1** was prepared according to the literature with appropriate characteristic spectra.<sup>140</sup>

*H<sub>6</sub>phospa (2)*. Compound **2** was prepared according to the literature with appropriate characteristic spectra.<sup>139</sup> HR-ESI-MS calcd for [C<sub>18</sub>H<sub>24</sub>N<sub>4</sub>O<sub>12</sub>P<sub>2</sub> + K]<sup>+</sup>: 557.0605 ; found [M + K]<sup>+</sup> = 557.0601. Elemental analysis: calcd % for H<sub>6</sub>phospa·0.3HCl·1.8H<sub>2</sub>O: C 38.55, H 5.00, N 9.99; found: C 39.03, H 4.95, N 9.78.

*H<sub>6</sub>dipedpa (3)*. Compound **1** (400 mg, 1.12 mmol) was added to a stirring solution of deionized water (diH<sub>2</sub>O, 4 mL) in a 10 mL round-bottom flask and the solution pH adjusted to 9-10 (measured by pH paper) with 1 M NaOH. Compound **1** was observed to dissolve only above ~pH 7. Diethyl vinylphosphonate (720 μL, 769 mg, 4.68 mmol) was added to the stirring aqueous solution, after which point the solution was heated to reflux and left to stir overnight. Following confirmation of the desired intermediate (double Michael-addition product) by mass spectrometry, the solution was cooled, and extracted with DCM (5 mL x 3) in a separatory funnel to remove excess diethyl vinylphosphonate. The aqueous phase was evaporated, and upon drying, *conc.* HCl (6 mL) added to the resultant oil. The solution was refluxed and stirred overnight. The solution was allowed to cool to ambient temperature (precipitate was noted following cooling) and the HCl evaporated *in vacuo*. Residual HCl was removed by repeatedly

adding H<sub>2</sub>O (10 mL x 3) and evaporating to near-dryness. To the residual water, acetone (15 mL) was added, at which point a fine whitish-brown precipitate formed. After sitting untouched for 30 minutes, the fine precipitate formed small droplets of oil-like liquid along the sides and bottom of the flask. The acetone solution was decanted, and the oil washed with acetone and filtered to yield a fine white powder. The acetone solution was evaporated, and the process repeated twice or thrice until the purity of product declined. <sup>1</sup>H NMR (400 MHz, D<sub>2</sub>O, 298 K): δ 7.84 (t, *J* = 7.7 Hz, 1H), 7.80 (d, *J* = 7.6 Hz, 1H), 7.44 (d, *J* = 7.3 Hz, 1H), 4.20 (s, 2H), 3.29 (s, 2H), 3.25 (m, 2H), 1.98 (m, 2H). <sup>13</sup>C{<sup>1</sup>H} NMR (75 MHz, D<sub>2</sub>O, 298 K): δ 172.2, 152.7, 138.7, 125.5, 123.3, 51.6, 48.8, 25.0, 23.7. <sup>31</sup>P{<sup>1</sup>H} NMR (162 MHz, D<sub>2</sub>O, 298 K): 19.07. HR-ESI-MS calcd for [C<sub>20</sub>H<sub>28</sub>N<sub>4</sub>O<sub>12</sub>P<sub>2</sub> + H]<sup>+</sup>: 547.1359 ; found [M + K]<sup>+</sup> = 547.1362. Elemental analysis: calcd % for H<sub>6</sub>dipedpa·4HCl·2H<sub>2</sub>O: C 32.94, H 4.99, N 7.68; found: C 32.92, H 5.09, N 7.56.

*Methyl-6-bromomethylpicolinate* (**4**). Compound **4** was prepared according to literature with appropriate characteristic spectra.<sup>154</sup>

*Methyl 6-((diethoxyphosphoryl)methyl)picolinate* (**5**). To a solution of (**4**) (1.5 g, 6.52 mmol) in ACN (100 mL) in a 250 mL round bottom flask was added P(OEt)<sub>3</sub> (2.85 mL, 16.6 mmol) and ZnBr<sub>2</sub> (0.44 g, 1.96 mmol). The reaction mixture was heated to 60 °C and stirred for 48 h and monitored by TLC (DCM, 10% MeOH) until completion. The reaction mixture was quenched with distilled water, extracted with DCM (4 x 100 mL), the organic layers combined and dried over anhydrous MgSO<sub>4</sub>. After filtration, the crude product was adsorbed to silica and purified by silica chromatography (CombiFlash Rf automated column system 40 g HP silica;

solid (pause) preparation; A: DCM, B: MeOH, 100% A to 20% B, to yield semi-pure product.  $^1\text{H}$  NMR (300 MHz,  $\text{CDCl}_3$ , 298 K):  $\delta$  8.04 (d, 1H), 7.84 (t, 1H), 7.66 (d, 1H), 4.17 – 4.05 (m, 4H), 4.00 (s, 3H), 3.60 (d, 2H), 1.27 (t, 6H). LR-ESI-MS calcd for  $[\text{C}_{12}\text{H}_{18}\text{NO}_5\text{P} + \text{Na}]^+$ : 310.0; found  $[\text{M} + \text{H}]^+ = 310.1$ .

*Diethyl ((6-(hydroxymethyl)pyridin-2-yl)methyl)phosphonate (6)*. To a solution of **(5)** (1.69 g, 5.9 mmol) in a mixture of 7:3 DCM:MeOH (100 mL) in a 250 mL round bottom flask at 0 °C was added  $\text{NaBH}_4$  (0.27 g, 7.1 mmol) over 1 h. The reaction mixture was stirred, allowed to warm to room temperature and left to react overnight (~16 h). The reaction mixture was quenched with distilled water, phases separated, and the aqueous evaporated to remove MeOH. The aqueous phase was then washed with DCM (3 x 100mL) and the organic phases were then combined and dried over anhydrous  $\text{MgSO}_4$ . After filtration, the crude product was adsorbed to silica and purified by silica chromatography (CombiFlash Rf automated column system 40 g HP silica; solid (pause) preparation; A: DCM, B: MeOH, 100% A to 25% B, to yield the pure product (58% over two steps, 0.98 g).  $^1\text{H}$  NMR (400 MHz,  $\text{CDCl}_3$ , 298 K):  $\delta$  7.62 (t,  $J = 7.7$  Hz, 1H), 7.28 – 7.22 (m, 1H), 7.15 (d,  $J = 7.3$  Hz, 1H), 4.70 (s, 2H), 4.05 (dq,  $J = 8.2, 7.1$  Hz, 4H), 3.40 (d,  $J = 22.0$  Hz, 2H), 1.24 (t,  $J = 7.1$  Hz, 6H).  $^{13}\text{C}\{^1\text{H}\}$  NMR (101 MHz,  $\text{CDCl}_3$ , 298 K): 159.2 (d,  $J = 2.4$  Hz), 151.7 (d,  $J = 8.4$  Hz), 137.4 (d,  $J = 2.7$  Hz), 122.9 (d,  $J = 5.3$  Hz), 118.8 (d,  $J = 3.3$  Hz), 64.0, 62.4 (d,  $J = 6.6$  Hz), 36.4 (d,  $J = 135.7$  Hz), 16.5 (d,  $J = 6.1$  Hz).  $^{31}\text{P}\{^1\text{H}\}$  NMR (162 MHz,  $\text{CDCl}_3$ , 298 K, externally referenced to 85% phosphoric acid): 23.08. LR-ESI-MS calcd for  $[\text{C}_{11}\text{H}_{18}\text{NO}_4\text{P} + \text{Na}]^+$ : 282.1; found  $[\text{M} + \text{Na}]^+ = 282.2$ .

*Diethyl ((6-(bromomethyl)pyridin-2-yl)methyl)phosphonate (7)*. To a solution of **(6)** (0.35 g, 1.35 mmol) in ACN (20 mL) in a 50 mL round bottom flask at 0 °C was added PBr<sub>3</sub> (0.13 mL, 1.35 mol) dropwise. The reaction mixture was stirred, allowed to warm to room temperature and monitored by TLC (DCM, 10% MeOH). After 3 hours, the reaction mixture was quenched with dilute NaHCO<sub>3</sub> and extracted with DCM (4 x 20 mL). The organic phases were combined and dried over anhydrous MgSO<sub>4</sub>. Filtration and evaporation yielded the pure product (85%, 0.37 g). *Note: product prone to decomposition— use immediately, or refrigerate and use within 48 h.* <sup>1</sup>H NMR (400 MHz, CDCl<sub>3</sub>, 298K): δ 7.64 (t, *J* = 7.7 Hz, 1H), 7.36 – 7.27 (m, 2H), 4.51 (s, 2H), 4.08 (dq, *J* = 7.2 Hz, 4H), 3.40 (d, *J* = 22.0 Hz, 2H), 1.26 (t, *J* = 7.0 Hz, 6H). <sup>13</sup>C{<sup>1</sup>H} NMR (101 MHz, CDCl<sub>3</sub>, 298 K) 156.5 (d, *J* = 2.5 Hz), 152.8 (d, *J* = 8.2 Hz), 137.6 (d, *J* = 2.7 Hz), 123.6 (d, *J* = 4.8 Hz), 121.7 (d, *J* = 3.1 Hz), 62.3 (d, *J* = 6.5 Hz), 36.5 (d, *J* = 134.7), 33.8, 16.4 (d, *J* = 6.2 Hz). <sup>31</sup>P{<sup>1</sup>H} NMR (162 MHz, CDCl<sub>3</sub>, 298 K, externally referenced to 85% phosphoric acid): 24.53. LR-ESI-MS calcd for [C<sub>11</sub>H<sub>18</sub>BrNO<sub>3</sub>P + H]<sup>+</sup>: 322.0; found [M + H]<sup>+</sup> = 322.1

*Ethylenediaminediacetic acid dimethyl ester dihydrochloride (8)*. Thionyl chloride (6.2 mL, 56.8 mmol) was slowly added to MeOH (150 mL) at 0 °C in a 500 mL round bottom flask and was allowed to stir for 30 minutes. Ethylenediaminediacetic acid (5.00 g, 28.4 mmol) was then added, and the reaction mixture heated to reflux for 24 h. Solvent was then evaporated, and the crude product washed twice with hexanes to remove residual HCl. The resulting solid was recrystallized in MeOH to yield the pure product as the 2HCl salt (80%, 6.27 g, 22.6 mmol). <sup>1</sup>H NMR (400 MHz, D<sub>2</sub>O, 298 K): δ 4.04 (s, 2H), 3.77 (s, 3H), 3.50 (s, 2H). <sup>13</sup>C{<sup>1</sup>H} NMR (100 MHz, 298 K, D<sub>2</sub>O + NaOD): 167.5, 53.7, 47.7, 42.9. LR-ESI-MS calcd for [C<sub>8</sub>H<sub>16</sub>N<sub>2</sub>O<sub>4</sub>

+ H]<sup>+</sup>: 205.1; found [M + H]<sup>+</sup> = 205.3 Elemental analysis: calcd % for C<sub>16</sub>H<sub>20</sub>N<sub>2</sub>·2 HCl: C 8.94, H 7.08, N 8.94; found: C 61.67, H 6.95, N 8.94.

*Dimethyl 2,2'-(ethane-1,2-diylbis(((6-((diethoxyphosphoryl)methyl)pyridin-2-yl)methyl)-azanediyl))diacetate (9)*. To a solution of **(8)** (0.2 g, 0.62 mmol) in ACN (5 mL) in a 20 mL conical vial was added Na<sub>2</sub>CO<sub>3</sub> (0.1 g, 1.2 mmol). The solution was stirred and heated to 40 °C before the slow addition of **(9)** (65 mg, 0.27 mmol). The reaction mixture was allowed to stir for 3 d and monitored by ESI-MS. Upon completion, the reaction mixture was washed with water to remove salt and extracted with DCM (3 x 20 mL). The organic phases were combined and dried over anhydrous MgSO<sub>4</sub>. After filtration, the product was absorbed to silica and purified by silica chromatography (CombiFlash Rf automated column system 12 g HP silica; solid (pause) preparation; A: DCM, B: MeOH, 100% A to 20% B, to yield the pure product (42%, 78 mg). <sup>1</sup>H NMR (400 MHz, CDCl<sub>3</sub>, 298 K): δ 7.56 (br s, 1H), 7.32-7.28 (br m, 1H), 7.21 (d, 1H) 4.02 (m, 4H), 3.89 (s, 2H), 3.63 (s, 3H), 3.42-3.35 (m, 4H), 2.84 (s, 2H) 1.21 (t, 6H). <sup>13</sup>C{<sup>1</sup>H} NMR (101 MHz, CDCl<sub>3</sub>, 298 K): 171.7, 158.8, 152.0, 137.0, 122.6, 121.1, 62.2 (d, *J*<sub>1<sup>PC</sup></sub> = 6.5 Hz), 60.0, 54.9, 52.2, 51.4, 37.0, 36.3 (d, *J*<sub>1<sup>PC</sup></sub> = 136.0 Hz), 16.3 (d, *J*<sub>2<sup>PC</sup></sub> = 6.2 Hz). <sup>31</sup>P{<sup>1</sup>H} NMR (162 MHz, CDCl<sub>3</sub>, 298 K): 25.8. LR-ESI-MS calcd for [C<sub>30</sub>H<sub>48</sub>N<sub>4</sub>O<sub>10</sub>P<sub>2</sub> + Na]<sup>+</sup>: 709.3; found [M + Na]<sup>+</sup> = 709.3

*H6eppy (10)*. To *conc.* HCl (5 mL) in a 20 mL conical vial was added **(9)** (78 mg, 0.11 mmol), which was stirred and heated at reflux for 48 h. The solvent was then evaporated, and the product dissolved in minimal water. Next, acetone was added to the solution, forming a slurry of white solid, as well as a sticky oil. The mixture was allowed to sit for 30 minutes, then

decanted and dried under reduced pressure to yield the pure product (75%, 47 mg).  $^1\text{H}$  NMR (300 MHz,  $\text{D}_2\text{O}$ , 298 K): 8.30 (t, 1H), 7.80 (m, 2H), 4.50 (s, 2H) 3.83 (s, 2H), 3.53 (d, 2H), 3.42 (s, 2H).  $^{13}\text{C}\{^1\text{H}\}$  NMR (75 MHz,  $\text{D}_2\text{O}$ , 298 K): 171.8, 152.3, 148.7, 145.5, 127.6, 127.6, 125.4, 55.6, 54.4, 51.4, 35.5, 34.3.  $^{31}\text{P}\{^1\text{H}\}$  NMR (120 MHz,  $\text{CDCl}_3$ , 298 K): 14.7 (s). HR-ESI-MS: calcd for  $[\text{C}_{20}\text{H}_{28}\text{N}_4\text{O}_{10}\text{P}_2 + \text{H}]^+$ : 547.1359; found: 547.1360. Elemental analysis: calcd % for  $\text{H}_6\text{eppy}\cdot 4.5\text{HCl}\cdot 3\text{H}_2\text{O}$ : C 31.38, H 5.10, N 7.32; found: C 31.46, H 5.19, N 7.22.

### 3.4.3 Metal Complexation

NMR spectra of  $\text{H}_6\text{phospa}$ ,  $\text{H}_6\text{dipedpa}$  and  $\text{H}_6\text{eppy}$  complexes with  $\text{In}^{3+}$ ,  $\text{Lu}^{3+}$ ,  $\text{Y}^{3+}$ ,  $\text{Sc}^{3+}$  and  $\text{La}^{3+}$  were obtained by making separate ligand and metal solutions in  $\text{D}_2\text{O}$  (16 mM) and then mixing the given ligand solution with a given metal solution in a molar ratio of 1:1.1/L:M ( $V_t = 525 \mu\text{L}$ ). If necessary, solution pD was altered with freshly prepared  $\sim 0.1$  M and/or 1 M NaOD (diluted from 40 wt % NaOD) and measured with a Ross combined electrode and corrected  $\text{pD} = \text{pH}_{\text{measured}} + 0.4$ . Solutions were allowed to stand for at least 15 min at room temperature before collecting NMR spectra.

### 3.4.4 X-ray Crystallography

Single white needle-shaped crystals of  $\text{H}_6\text{phospa}$  (compound **2**) and  $\text{H}_6\text{dipedpa}$  (compound **3**) were obtained by recrystallisation from slow evaporation of acetone into ligand solution. Suitable crystals  $0.03 \times 0.01 \times 0.001 \text{ mm}^3$  and  $0.01 \times 0.01 \times 0.001 \text{ mm}^3$  (respectively) were selected and mounted on a suitable support on a Bruker APEX II area detector diffractometer. The crystal was kept at a steady  $T = 90$  K during data collection. The structure was solved with the ShelXT<sup>155</sup> structure solution program using the Intrinsic Phasing solution method and by using

Olex2<sup>156</sup> as the graphical interface. The model was refined with version 2018/1 of ShelXL<sup>155</sup> using least squares minimization.

### 3.4.5 Solution Thermodynamics

All combined UV-potentiometric titrations were carried out in a 20 mL 298 K thermostated glass cell with an inlet—outlet tube for nitrogen gas (purified through a 10% NaOH solution to exclude CO<sub>2</sub> prior to and during the course of the titration). The titration apparatus consisted in a Metrohm Titrand 809, a Metrohm Dosino 800 equipped with a Ross combined electrode and an optic dip probe (0.2 cm) connected to a Varian Cary 60 UV/Vis spectrophotometer (200–400 nm). The electrode was calibrated daily in hydrogen ion concentration by direct titration of HCl with freshly prepared NaOH solution and the results were analyzed with Gran procedure<sup>157</sup> in order to obtain the standard potential ( $E^{\circ}$ ) and the ionic product of water  $pK_w$ ,  $T = 298$  K and 0.16 M NaCl as a supporting electrolyte. Solutions were titrated with carbonate-free NaOH (~0.16 M) that was standardized against freshly recrystallized potassium hydrogen phthalate. Protonation equilibria of the ligands ( $H_6L = H_6\text{phospa}$ ,  $H_6\text{dipedpa}$  and  $H_6\text{eppy}$ ), were studied by combined UV-potentiometric titrations of solutions containing the ligands ( $[H_6\text{phospa}] = 4.84 \times 10^{-4}$  M,  $[H_6\text{dipedpa}] = 6.76 \times 10^{-4}$  M and  $[H_6\text{eppy}] = 7.15 \times 10^{-4}$  M) at  $T = 298$  K,  $l = 0.2$  cm and 0.16 M NaCl ionic strength in the pH range 1.8–11.5. The most acidic protonation constants corresponding to a phosphonate functionality, were determined by acidic UV-batch experiments ( $l = 1$  cm). The  $H^+$  concentration in this UV in batch titration procedure at low pH solutions ( $2 > \text{pH} \geq 0$ ) was calculated from solution stoichiometry, not measured with a glass electrode and the correct acidity scale  $H^0$  was used.<sup>158</sup> In batch solutions were

prepared by adding to the ligand solutions, standardized HCl and NaCl to set the ionic strength constant at 0.16 M when possible.

All the spectrophotometric and potentiometric data were analyzed with HypSpec2014<sup>148</sup> and HyperQuad2013<sup>150</sup> to obtain the protonation constants in Table 3.1. Additional <sup>31</sup>P and <sup>1</sup>H NMR titrations were employed to better determine the most acidic protonation constant (P-OH) and more basic pKa (N<sub>en</sub>) in H<sub>6</sub>phospa. NMR data were processed using the HypNMR<sup>149</sup> software.

Complex formation equilibria of H<sub>6</sub>phospa, H<sub>6</sub>dipedpa and H<sub>6</sub>eppy with In(III), Sc(III), Y(III), Lu(III) and La(III) metal ions was carried out by two different methods. The first method used UV-Vis batch spectrophotometric measurements (l = 1 cm) on a set of solutions containing 1:1 metal to ligand molar ratio ([H<sub>6</sub>phospa] = 7.44 × 10<sup>-5</sup> M and M<sup>3+</sup> = In<sup>3+</sup>, Sc<sup>3+</sup>, Y<sup>3+</sup>, Lu<sup>3+</sup>, La<sup>3+</sup>; [H<sub>6</sub>dipedpa] = 7.10 × 10<sup>-5</sup> M and M<sup>3+</sup> = In<sup>3+</sup>; [H<sub>6</sub>eppy] = 7.32 × 10<sup>-5</sup> M and M<sup>3+</sup> = In<sup>3+</sup>) and different amounts of standardized HCl and NaCl to set the ionic strength constant at 0.16 M when possible. The molar absorptivities of all the protonated species of each of the ligands calculated with HypSpec2014<sup>148</sup> from the protonation constant experiments described above were included in the calculations of the metal complexes. The second method as in the case of protonation constants was combined UV-potentiometric titrations (298K, I = 0.16 M NaCl and l = 0.2 cm). Ligands and metal concentrations were in the range of 4.05-5.9 × 10<sup>-4</sup> M. M<sup>3+</sup> metal ion solutions were prepared by adding the atomic absorption (AA) standard solution to each of the different ligands of known concentration in the 1:1 metal to ligand molar ratio. The exact amount of acid present in the AA standard solution was determined by Gran's method<sup>157</sup> titrating equimolar solutions of M(III) and Na<sub>2</sub>H<sub>2</sub>-EDTA. Each titration consisted of 100-150 equilibrium points in the pH range 1.6-11.5, equilibration time for titrations was up to 5 min

for metal complex titrations. Three replicates of each titration were performed. Relying on the stability constants for the species  $M(H_3L)$  obtained by the acidic batch method, the fitting of the direct potentiometric titrations was possible yielding the stability constants in Table 3.2. All the potentiometric measurements were processed using the Hyperquad2013 software<sup>150</sup> while the obtained spectrophotometric data were processed with the HypSpec2014<sup>148</sup> program. Proton dissociation constants corresponding to hydrolysis of  $M(III)$  aqueous ions included in the calculations were taken from Baes and Mesmer.<sup>99</sup> The overall equilibrium (formation) constants  $\log \beta$  referred to the overall equilibria:  $pM + qH + rL \rightleftharpoons M_pH_qL_r$  (the charges are omitted), where  $p$  might also be 0 in the case of protonation equilibria and  $q$  can be negative for hydroxide species. Stepwise equilibrium constants  $\log K$  correspond to the difference in log units between the overall constants of sequentially protonated (or hydroxide) species. The parameter used to calculate the metal scavenging ability of a ligand towards a metal ion,  $pM$ , is defined as  $-\log [M^{n+}]_{\text{free}}$  at  $[\text{ligand}] = 10 \text{ mM}$  and  $[M^{n+}] = 1 \text{ }\mu\text{M}$  at  $\text{pH} = 7.4$ .<sup>66</sup>

### 3.4.6 DFT Calculations

All DFT calculations were performed using Gaussian 16 revision c01.<sup>159</sup> Self-consistent field (SCF) convergence criteria were set to their default values (SCF=Tight in Gaussian). Structure optimizations were performed without symmetry constraints using the Berny algorithm<sup>160</sup> with default settings, starting from initial structures built manually. Each structure was optimized, and free energies calculated, using DFT with the PBE0 hybrid exchange-correlation functional,<sup>161</sup> added D3(BJ)<sup>162–164</sup> dispersion corrections, and the def2-TZVP basis set<sup>165</sup> for all non-metal atoms. Effective core potentials (ECPs) were used to account for scalar relativistic effects in metal core electrons. Specifically, the Stuttgart relativistic small core (RSC) 1997

ECP basis set<sup>166,167</sup> was used for scandium atoms, while the Stuttgart RSC segmented valence basis set and ECP<sup>168,169</sup> was used for lanthanum. These metal basis sets were also used in NMR shielding calculations. Metal basis sets were downloaded from the Basis Set Exchange website.<sup>170–172</sup> The PBE0 functional was chosen due to its previous success in structure prediction and thermochemistry of transition metal complexes,<sup>173–177</sup> while the def2-TZVP basis was chosen as a reasonable trade-off between speed and accuracy for the large system sizes under study.<sup>178,179</sup> A local minimum of energy was confirmed after each optimization via harmonic frequency analysis using analytical second derivatives, which also yields calculated Gibbs free energies under standard state conditions (298 K, 1 atm). The integral equation formalism of the polarizable continuum model (IEFPCM) was used as an implicit water model in all calculations to simulate the average dielectric effects of the solvent. Default IEFPCM parameters were used, as implemented in Gaussian ( $\epsilon = 78.36$ , Van der Waals surface without “added spheres”). Each calculation was repeated with 0, 6, 9, and 12 explicit water molecules which were placed randomly by the PACKMOL code<sup>180</sup> in a sphere up to 4.5 Å from each system’s center of mass. Adjustments were then made before optimization to move the randomly placed water molecules closer to hydrogen bond centers, such as phosphonate and carboxyl groups.

<sup>1</sup>H NMR isotropic shielding constant calculations were performed on the fully optimized structures using DFT with the gauge-including atomic orbital (GIAO) method<sup>181,182</sup> and PBE0 functional, as it has also been shown to perform well for the calculation of <sup>1</sup>H NMR shielding constants.<sup>183–185</sup> Choice of basis set is extremely important for the calculation of accurate NMR shielding constants, especially on the atoms of interest and those directly bound. Hence, we adopted the “locally dense” approach<sup>186</sup> for the calculation of <sup>1</sup>H NMR shielding constants by

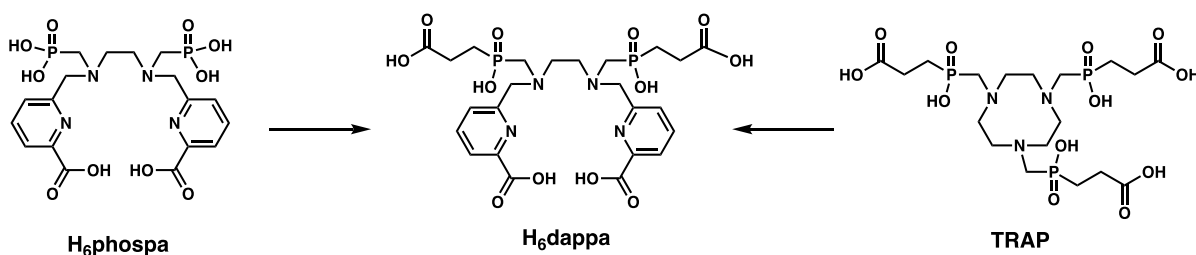
utilizing the pcSseg-3 basis set<sup>187</sup> (quadruple-zeta valence quality) on H atoms within the ligand and on any atom directly bound to ligand H atoms. Any atom two bonds away from a ligand H atom was given the smaller pcseg-2 basis set,<sup>188</sup> and all remaining atoms (including solvent atoms but not metal atoms) were given the pcseg-1 basis set. Calculation results were visualized using GaussView version 6.0<sup>189</sup> and Avogadro version 1.2.0.<sup>190</sup>

## Chapter 4. Investigation of a Bifunctional Phosphonate-Bearing Chelator for Trivalent Radiometals

### 4.1 Introduction

#### 4.1.1 Rational Design of H<sub>6</sub>dappa

Chapter 3 was focused on the fundamental aspects of chelator development in order to rationally select a promising candidate to be developed as a BFC. Much care was taken to explore the underlying reasons for differences in stability between the three chelators and ultimately H<sub>6</sub>phospa was deemed the chelator with the most potential due to its superior stability with all studied trivalent metals over H<sub>6</sub>dipedpa and H<sub>6</sub>eppy. One previous attempt to bifunctionalize H<sub>6</sub>phospa (*p*-SCN-Bn-H<sub>6</sub>phospa) was made by our group in 2014.<sup>139</sup> While high molar activity with [<sup>111</sup>In]In<sup>3+</sup> and [<sup>177</sup>Lu]Lu<sup>3+</sup> was achieved, bone accumulation *in vivo* was a clear sign of poor complex kinetic inertness. In search of an alternative to NCS functionalization, inspiration was drawn from the highly successful triphosphinate ligand known as TRAP (1,4,7-triazacyclononane-1,4,7-tris[methyl(2-carboxyethyl)phosphinic acid]). It was our hypothesis that the conversion of the phosphonates to phosphinates would mitigate bone accumulation, as well as present an interesting alternative to *p*-SCN-Bn bifunctionalization of our family of pa chelators (Scheme 4.1).



**Scheme 4.1** Design principle of H<sub>6</sub>dappa. Reproduced from reference 140.

#### 4.1.2 Selection of Metal Ions for Study with H<sub>6</sub>dappa

As in Chapter 3, In<sup>3+</sup>, Lu<sup>3+</sup>, Y<sup>3+</sup> and Sc<sup>3+</sup> were selected to be studied with the novel H<sub>6</sub>dappa. These metal ions were selected based on interest in eventual study of radioisotope counterparts. [<sup>111</sup>In]In<sup>3+</sup> ( $t_{1/2} = 67.2$  h) is a clinically used single-photon emission computed tomography (SPECT) imaging radionuclide due to its low energy  $\gamma$ -emission ( $E_{\gamma} = 171$  and  $245$  keV;  $I_{\gamma} = 91$  and  $94\%$ , respectively) following electron capture, which has led to its inclusion in a number of clinically approved radiotracer agents.<sup>2,191</sup> [<sup>177</sup>Lu]Lu<sup>3+</sup> ( $t_{1/2} = 159$  h) is a therapeutic radionuclide due to its low-energy  $\beta$  emission ( $E_{\beta_{\text{avg}}} = 134$  keV,  $100\%$ ), which has been proven to exert a significant therapeutic effect and recently received FDA (U.S. Food and Drug Administration) approval for the treatment of somatostatin receptor-positive gastroenteropancreatic neuroendocrine tumors under the brand name Lutathera® ([<sup>177</sup>Lu][Lu-DOTA-TATE]).<sup>192,193</sup> [<sup>90</sup>Y]Y<sup>3+</sup> ( $t_{1/2} = 64.0$  h) is a well-established, pure  $\beta$  emitting radionuclide with high energy emission ( $E_{\beta_{\text{avg}}} = 934$  keV,  $100\%$ ) and relatively long soft-tissue range ( $11$  mm).<sup>194,195</sup> [<sup>86</sup>Y]Y<sup>3+</sup> ( $t_{1/2} = 14.7$  h) is a low branching ( $32\%$ )  $\beta^+$  emitter, whose tandem use with <sup>90</sup>Y has made the radioisotopes an attractive theranostic option. Finally, [<sup>44</sup>Sc]Sc<sup>3+</sup> has garnered attention as a PET radionuclides due to its high  $\beta^+$  branching ratio ( $E_{\beta^+_{\text{avg}}} = 632$  keV,  $94\%$ ) and long physical half-life ( $t_{1/2} = 4.04$  h).<sup>196</sup> Also possessing a therapeutic counterpart, [<sup>47</sup>Sc]Sc<sup>3+</sup> ( $t_{1/2} = 80.4$  h) is a high branching, low energy  $\beta$  emitter ( $E_{\beta_{\text{avg}}} = 162$  keV,  $100\%$ ) suitable for treatment of small tumours and cancer metastasis.<sup>197</sup>

Reported herein is the study of the bifunctional chelator, H<sub>6</sub>dappa, as a phosphinate-containing octadentate chelator for the high coordination number radiometal ions [<sup>90</sup>Y]Y<sup>3+</sup>, [<sup>111</sup>In]In<sup>3+</sup> and [<sup>177</sup>Lu]Lu<sup>3+</sup>; we describe the synthesis, cold metal complexation, solution studies, radiolabeling and structural analysis via DFT calculation of H<sub>6</sub>dappa.

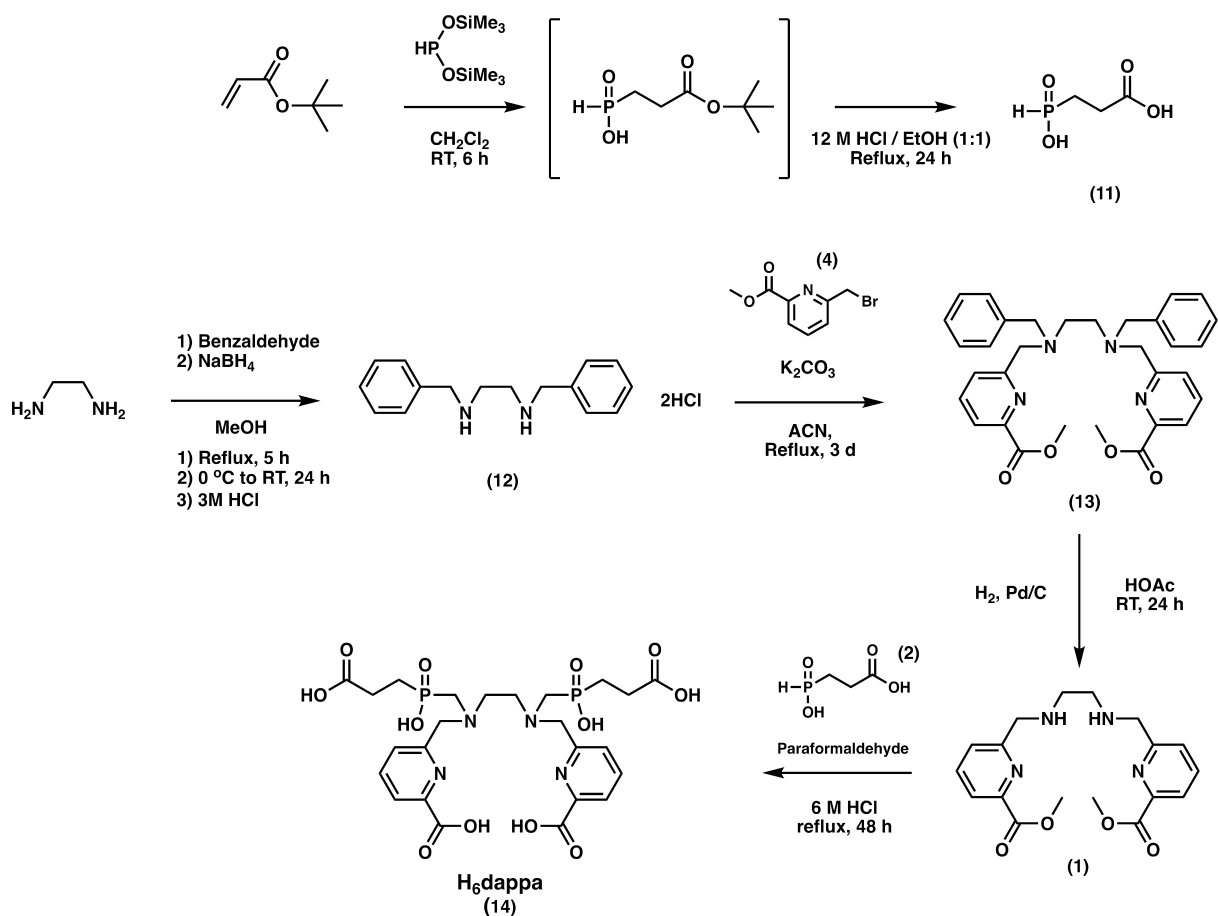
## 4.2 Results and Discussion

### 4.2.1 Ligand Synthesis and Characterization

To synthesize H<sub>6</sub>dappa, each pair of coordinating arm groups (compounds **4** and **2**) were separately synthesized then added stepwise to ethylene diamine following appropriate benzyl protection and deprotection (Scheme 4.2). Compound **4** (methyl-6-bromomethylpicolinate) has been describe in Chapter 3. Compound **11** is somewhat challenging to synthesize due to the pyrophoric nature of bis(trimethylsilyl) phosphonite and the time-dependent nature of the Michael-type addition. Fortunately, these steps do not require purification (when appropriately monitored) and are high yielding. These reactions are also easily scalable (~10-40 g). Reductive alkylation of ethylene diamine with benzaldehyde and sodium borohydride was high yielding and conveniently purified, as 3 M HCl was used to salt-out the desired product as a dihydrochloride salt. Again, this reaction is very reliable and easy, ultimately yielding three components (compounds **4**, **11** and **12**) that can be produced in large quantities in preparation for the following three reactions (Scheme 4.2).

Compound **13** is produced through an S<sub>N</sub>2 reaction with **4**. A large excess (~7 eq) of K<sub>2</sub>CO<sub>3</sub> is used to neutralize the two equivalents of HCl from **12** and maintain a very basic environment to facilitate amine deprotonation. Liquid-liquid (DCM/H<sub>2</sub>O) extraction and purification via silica column chromatography with hexane and ethyl acetate led to a moderate yield (57%) on a sufficiently large scale (~1.5-2.0 g). Palladium on carbon deprotection then yields **1**. This straightforward procedure is achieved at ambient temperature and does not require further purification following filtration (to remove Pd/C) and evaporation of solvent. The final ligand (H<sub>6</sub>dappa; **14**) is prepared via tandem acid-mediated methyl ester hydrolysis and Kabachnik-Fields reaction, where **1** and an excess of **11** (4 eq) are dissolved in refluxing 6

M HCl and a large excess of paraformaldehyde (15 eq) added over 48 h. Removal of the excess **11** and presumed side-product (3-[hydroxyl{hydroxymethyl}phosphoryl]propanoic acid) is challenging due to their similar retention on our HPLC column (Phenomenex Synergi 4  $\mu\text{m}$  hydro-RP 80  $\text{\AA}$ ), which led to inefficient and time consuming separation. Instead, crude purification by cation-exchange chromatography (DOWEX 50WX2,  $\text{H}^+$  form) easily separated the amine-containing  $\text{H}_6\text{dappa}$  from neutral and anionic impurities. Following concentration of the semi-pure eluate, HPLC purification and lyophilization yielded pure  $\text{H}_6\text{dappa}$  as a fluffy white solid.



**Scheme 4.2** Synthetic scheme for  $\text{H}_6\text{dappa}$ . Reproduced from reference 140.

#### 4.2.2 NMR Studies on Metal Complexation

The non-radioactive metal ions  $\text{In}^{3+}$ ,  $\text{Y}^{3+}$ ,  $\text{Lu}^{3+}$  and  $\text{Sc}^{3+}$  were studied with  $\text{H}_6\text{dappa}$  due to our interest in eventual study of their radioisotope counterparts (i.e.,  $^{111}\text{In}]\text{In}^{3+}$ ,  $^{86/90}\text{Y}]\text{Y}^{3+}$ ,  $^{177}\text{Lu}]\text{Lu}^{3+}$  and  $^{44/47}\text{Sc}]\text{Sc}^{3+}$ ). Additional experiments were conducted with  $\text{Bi}^{3+}$  and  $\text{La}^{3+}$  to gain further understanding of  $\text{H}_6\text{dappa}$  coordination chemistry. Characterization was confirmed by  $^1\text{H}/^{31}\text{P}\{^1\text{H}\}$  NMR spectroscopy and HR-ESI-MS, as well as  $^1\text{H}-^1\text{H}$  COSY when appropriate.

Diastereotopic splitting of protons is a characteristic sign of metal complex formation. In the case of pa family ligands, the methylene/ethylene protons stemming from N–C–H bonds are particularly telling. This phenomenon is observed with each of the studied metal ions, with varying degrees of spectral complexity and fluxionality. For example, the  $[\text{In}(\text{H}_2\text{dappa})]^-$   $^1\text{H}$  NMR spectrum reveals relatively sharp peaks, with protons on the ethylene backbone, amine-methylene-phosphinate bridge and protons adjacent the terminal aliphatic carboxylic acids exhibiting diastereotopic splitting (confirmed by  $^1\text{H}-^1\text{H}$  COSY). The downfield shift in the  $^{31}\text{P}\{^1\text{H}\}$  NMR spectra also confirms the coordination of the phosphinate group. The simplicity of all  $[\text{In}(\text{H}_2\text{dappa})]^-$  NMR spectra suggests a rigid symmetric complex ( $\text{In}^{3+}$  ionic radius = 0.92 Å, CN = 8).<sup>98</sup> Spectra of the yttrium(III), lutetium(III) and scandium(III) complexes are increasingly complicated. Complexation of  $\text{Y}^{3+}$ , the largest of the three rare-earth metals (ionic radius = 1.02 Å, CN = 8)<sup>98</sup> results in a moderately convoluted  $^1\text{H}$  NMR spectrum; however, identification of major and minor isomers was possible by analyzing the aromatic protons with  $^1\text{H}-^1\text{H}$  COSY. Lutetium(III) (ionic radius = 0.98 Å, CN = 8)<sup>98</sup> and scandium(III) (ionic radius = 0.87 Å, CN = 8)<sup>98</sup> were more complicated. The  $^{31}\text{P}\{^1\text{H}\}$  NMR spectra of both complexes reveal the presence of multiple isomers, which can also be noted in the aromatic region of the

$^1\text{H}$  NMR spectra. The complicated nature of these spectra made it difficult to draw conclusions beyond confirming complexation.<sup>140</sup>

Two additional metal ions were studied to further investigate the relationship between metal ion size and spectra complexity:  $\text{La}^{3+}$  (ionic radius = 1.16 Å, CN = 8)<sup>98</sup> and  $\text{Bi}^{3+}$  (ionic radius = 1.17 Å, CN = 8).<sup>98</sup> As seen in Figure 4.1a, the  $\text{La}^{3+}$  complex behaved as expected, with the  $^1\text{H}$  NMR spectrum displaying sharp peaks with characteristic diastereotopic splitting, indicative of a highly rigid and symmetrical structure.  $^1\text{H}$ - $^1\text{H}$  COSY (Figure 4.1c) confirmed peak assignments. The  $^1\text{H}$  NMR spectrum of the  $\text{Bi}^{3+}$  complex was also easily interpreted and clearly representative of a symmetrical coordination complex, albeit with a minor isomer present.

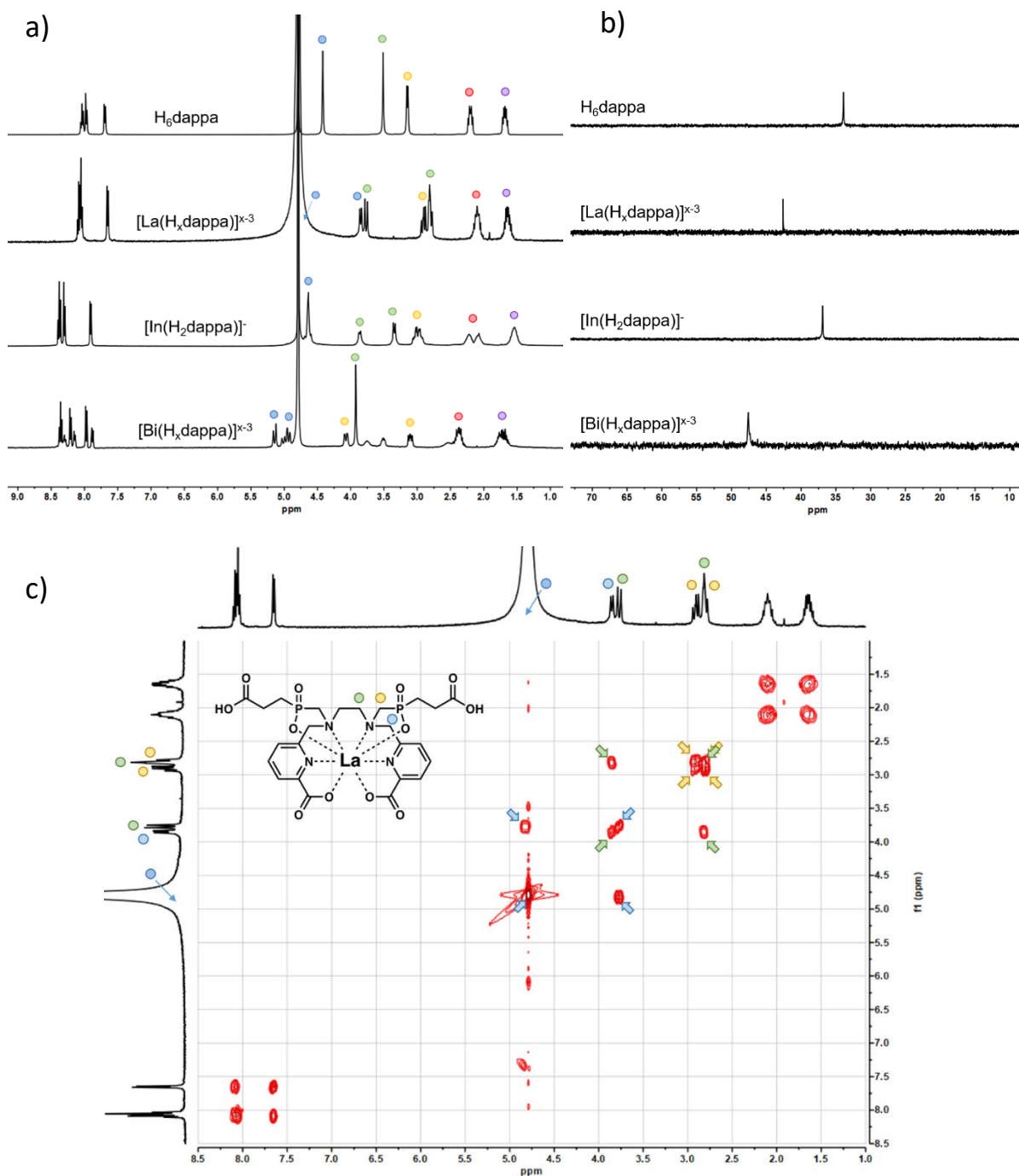


**Figure 4.1** (a)  $^1\text{H}$  NMR spectra of  $\text{H}_6\text{dappa}$ ,  $[\text{La}(\text{H}_x\text{dappa})]^{x-3}$ ,  $[\text{In}(\text{H}_2\text{dappa})]^-$  and  $[\text{Bi}(\text{H}_x\text{dappa})]^{x-3}$  (top-bottom) ( $\text{D}_2\text{O}$ , 400 MHz, 298 K). (b)  $^{31}\text{P}\{^1\text{H}\}$  NMR spectra of  $\text{H}_6\text{dappa}$ ,  $[\text{La}(\text{H}_x\text{dappa})]^{x-3}$ ,  $[\text{In}(\text{H}_2\text{dappa})]^-$  and  $[\text{Bi}(\text{H}_x\text{dappa})]^{x-3}$  (top-bottom) ( $\text{D}_2\text{O}$ , 162 MHz, 298 K). (c)  $^1\text{H}$ - $^1\text{H}$  COSY-45 NMR spectrum of  $[\text{La}(\text{H}_x\text{dappa})]^{x-3}$  ( $x = \text{not determined}$ ). Ligand/ $\text{La}^{3+}$  spectra pD 7,  $\text{In}^{3+}/\text{Bi}^{3+}$  spectra pD 1. Reproduced from reference 140.

### 4.2.3 Ligand Solution Thermodynamics

Combined potentiometric-spectrophotometric titrations were performed to determine protonation constants of H<sub>6</sub>dappa between pH 2-11.5. Acidic in-batch UV titrations were conducted to determine the most acidic pK<sub>a</sub> values, as electrode limitations below pH 2 rendered potentiometric titrations unfeasible. In theory, ten H<sub>6</sub>dappa pK<sub>a</sub> values should be observed; however, determination of the most acidic proton dissociation was not possible due to the highly acidic nature (pK<sub>a</sub> < 0). HypSpec2014<sup>148</sup> and Hyperquad2013<sup>150</sup> programs were used to fit spectrophotometric and potentiometric titration data ; these values are presented in Table 4.1.

From acidic to basic, the first deprotonation observed was at pH -0.11(1) and is attributed to a pyridine proton. This assignment is based on precedent from similar compounds<sup>136,141,143</sup> and the decrease in UV absorbance upon deprotonation of the picolinate chromophore. The next two deprotonation events occur at pH 1.00(1) and 1.67(2) and are attributed to the phosphinate groups, both because of the theoretical acidity of phosphinates *versus* other ionizable protons on H<sub>6</sub>dappa, as well as the agreement of the less acidic phosphinate's pK<sub>a</sub> with that reported for TRAP.<sup>198</sup> The remaining four acid groups deprotonate in their typical pH ranges– the picolinic acids at 2.42(2) and 2.71(3), followed by the aliphatic carboxylic acids at 4.13(2) and 4.63(2). These values also closely match similar pa based ligands<sup>136,143</sup> and TRAP,<sup>198</sup> respectively. The remaining deprotonation events must then be a result of amine deprotonation at pH 5.48(2) and 7.96(1).

**Table 4.1** Protonation constants of H<sub>6</sub>dappa. Reproduced from reference 140.

Equilibrium Reaction	log $\beta$	log $K$	Assignment
$L^{6-} + H^+ \rightleftharpoons HL^{5-}$	7.96(1)	7.96(1) <sup>a</sup>	Backbone N-H
$HL^{5-} + H^+ \rightleftharpoons H_2L^{4-}$	13.44(2)	5.48(2) <sup>a</sup>	Backbone N-H
$H_2L^{4-} + H^+ \rightleftharpoons H_3L^{3-}$	18.07(2)	4.63(2) <sup>a</sup>	Aliphatic Acid
$H_3L^{3-} + H^+ \rightleftharpoons H_4L^{2-}$	22.20(2)	4.13(2) <sup>a</sup>	Aliphatic Acid
$H_4L^{2-} + H^+ \rightleftharpoons H_5L^-$	24.91(3)	2.71(3) <sup>a</sup>	Picolinic Acid
$H_5L^- + H^+ \rightleftharpoons H_6L$	27.33(2)	2.42(2) <sup>a</sup>	Picolinic Acid
$H_6L + H^+ \rightleftharpoons H_7L^+$	29.00(2)	1.67(2) <sup>b</sup>	Phosphinate
$H_7L^+ + H^+ \rightleftharpoons H_8L^{2+}$	30.00(1)	1.00(1) <sup>b</sup>	Phosphinate
$H_8L^{2+} + H^+ \rightleftharpoons H_9L^{3+}$	29.89(1)	-0.11(1) <sup>b,c</sup>	Pyridine Ring

<sup>a</sup>From potentiometric and spectrophotometric titrations,  $I = 0.16$  M (NaCl) and 298 K. <sup>b</sup>From in-batch UV spectrophotometric titrations,  $I = 0.16$  M (NaCl) and 298 K. <sup>c</sup>At 298 K, not evaluated at constant ionic strength.

#### 4.2.4 In<sup>3+</sup>, Lu<sup>3+</sup>, Sc<sup>3+</sup> and Y<sup>3+</sup> Complex Formation Equilibria

Complex formation equilibria studies with H<sub>6</sub>dappa were carried out with natural isotopes of In<sup>3+</sup>, Lu<sup>3+</sup>, Sc<sup>3+</sup>, and Y<sup>3+</sup> with several methods to ensure data completeness and result validation. Direct potentiometric-spectrophotometric titrations were used to detect MH<sub>x</sub>L (x = 3, 2, 1, 0, -1) deprotonation events and ligand-ligand competition titrations (with EDTA or TTHA; triethylenetetramine-*N,N,N',N'',N''',N''''*-hexaacetic acid) were used to confirm the validity of these values. Metal complexes formed below pH 2 for each metal selected. This is likely a result of deprotonated phosphinate groups maintaining high affinity for free metal ions as low as pH 0.5. Thus, acidic in-batch UV spectrophotometric titrations were necessary to monitor complex formation, and were achieved by taking advantage of differences between ligand and metal-ligand complex UV absorbance profiles. Stability constants are presented in Table 4.2 and speciation plots (calculated using Hyss software<sup>153</sup>) in Figure 4.2.

**Table 4.2** Stepwise stability constants (log *K*) of H<sub>6</sub>dappa with In<sup>3+</sup>, Lu<sup>3+</sup>, Sc<sup>3+</sup> and Y<sup>3+</sup>. Reproduced from reference 140.

Equilibrium reaction	In <sup>3+</sup>	Lu <sup>3+</sup>	Sc <sup>3+</sup>	Y <sup>3+</sup>
M + L ⇌ ML	27.39(2) <sup>a</sup> ; 27.55(5) <sup>b</sup>	18.35(3) <sup>a</sup> , 18.71(5) <sup>b</sup>	22.86(4) <sup>a</sup> ; 22.75(3) <sup>d</sup>	16.50(3) <sup>a</sup> ; 16.79(6) <sup>d</sup>
ML + H <sup>+</sup> ⇌ MHL	4.81(2) <sup>a</sup> ; 4.82(5) <sup>b</sup>	4.73(5) <sup>a</sup> , 5.19(5) <sup>b</sup>	4.75(4) <sup>a</sup> ; 4.69(3) <sup>d</sup>	4.83(4) <sup>a</sup> ; 4.56(6) <sup>d</sup>
MHL + H <sup>+</sup> ⇌ MH <sub>2</sub> L	4.43(4) <sup>c</sup> ; 3.99(6) <sup>b</sup>	3.72(2) <sup>c</sup> , 3.79(5) <sup>b</sup>	3.20(5) <sup>a</sup> ; 3.69(5) <sup>d</sup>	3.96(3) <sup>c</sup> ; 4.12(8) <sup>d</sup>
MH <sub>2</sub> L + H <sup>+</sup> ⇌ MH <sub>3</sub> L	-	-	1.26(6) <sup>c</sup>	-
ML(OH) + H <sup>+</sup> ⇌ ML	9.67(3) <sup>a</sup> ; 9.78(5) <sup>b</sup>	9.89(4) <sup>a</sup>	9.23(6) <sup>a</sup> ; 9.42(5) <sup>d</sup>	9.55(4) <sup>a</sup> ; 9.46(8) <sup>d</sup>
<b>pM<sup>c</sup></b>	<b>27.7</b>	<b>18.6</b>	<b>23.2</b>	<b>16.8</b>

<sup>a</sup>Potentiometric and spectrophotometric titrations, *I* = 0.16 M (NaCl) and 298 K. <sup>b</sup>Ligand-ligand potentiometric competition with H<sub>6</sub>ttha, *I* = 0.16 M (NaCl), 298 K. <sup>c</sup>In-batch acidic spectrophotometric titration, T = 298 K. <sup>d</sup>Ligand-ligand potentiometric competition with H<sub>6</sub>edta at *I* = 0.16 M (NaCl), 298 K. <sup>e</sup>pM is defined as  $-\log [M]_{\text{free}}$  at  $[L] = 10 \mu\text{M}$ ,  $[M] = 1 \mu\text{M}$  and pH 7.4. Charges omitted for clarity.

As is evident by the high stability constants and pM values (Figure 4.3), H<sub>6</sub>dappa forms highly stable complexes with In<sup>3+</sup>, Lu<sup>3+</sup>, Sc<sup>3+</sup> and Y<sup>3+</sup>. Of particular interest is the impressive pIn value (27.7), which is greater than that for either widely used and commercially available chelators DOTA (18.8) or DTPA (25.7), as well as other strongly performing chelators such as H<sub>4</sub>octapa<sup>143</sup> (26.5), H<sub>4</sub>neunpa<sup>86</sup> (23.6), and H<sub>4</sub>octox<sup>199</sup> (25.0). The pLu value (18.6) is also notable; it exceeds that of DOTA<sup>87</sup> (17.1) and H<sub>4</sub>octox<sup>199</sup> (18.2), and is comparable to those of DTPA<sup>87</sup> (19.1) or H<sub>4</sub>octapa<sup>87</sup> (19.8). The speciation diagrams illustrate that one species is present at physiological pH for each metal complex— a desirable characteristic as multiple species can present challenges throughout additional studies, most notably *in vivo*. Ultimately, these encouraging results led to further experiments probing the ability of H<sub>6</sub>dappa to serve as a bifunctional chelator for radiopharmaceutically relevant metal ions.

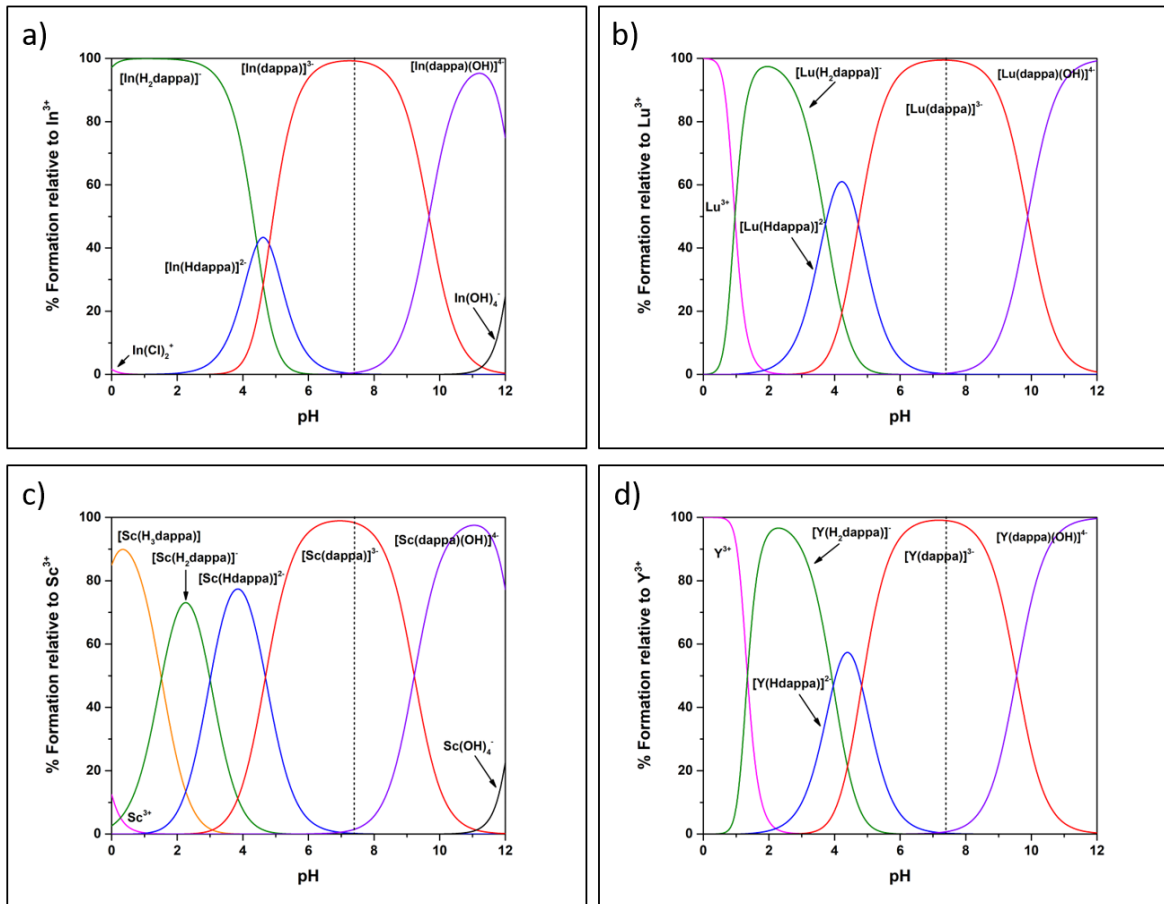


**Figure 4.2** Speciation diagrams for  $H_6dappa$  complexes calculated from values in Table 4.2 (298 K,  $I = 0.16$  M NaCl); dashed lines indicate physiological pH (7.4) (conditions simulated with HySS:  $[H_6dappa] = 1$  mM,  $[M^{3+}] = 1$  mM). Reproduced from reference 140.

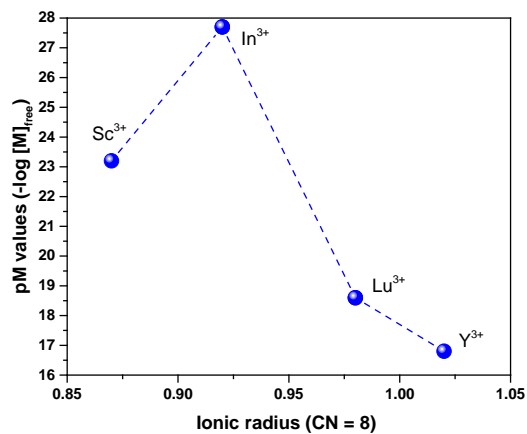


**Figure 4.3** pM values versus ionic radii for  $[M(dappa)]^{3-}$  complexes (CN = 8). Reproduced from reference 140.

#### 4.2.5 Radiolabeling and Serum Stability Experiments

The ability to achieve high molar activity (i.e., high RCY at low ligand concentration) and for the complex to remain kinetically inert when challenged with extraneous ligands or metal ions is a desirable chelator trait for radiopharmaceutical applications. Our preliminary radiolabeling experiments sought to explore the highest possible molar activity achievable with H<sub>6</sub>dappa using a variety of clinically relevant radionuclides. This was achieved through concentration-, temperature-, time- and pH-dependent radiolabeling experiments, which were monitored by radio-TLC. The mobile phase used was a mixture of NH<sub>4</sub>OH/MeOH/H<sub>2</sub>O (1/10/20), which has been used to study RCY with a number of other phosphonate-bearing chelators.<sup>200–203</sup>

Given the promising thermodynamic results with Y<sup>3+</sup>, In<sup>3+</sup> and Lu<sup>3+</sup> optimizing the RCYs with [<sup>90</sup>Y]Y<sup>3+</sup>, [<sup>111</sup>In]In<sup>3+</sup> and [<sup>177</sup>Lu]Lu<sup>3+</sup> was the focus. Radiochemical studies were conducted at pH 2, 4, 5.5 and 7. Labeling reaction mixtures were spotted on TLC plates at 1, 5, 10, 15 and 30 minutes to study radiolabeling kinetics. Ligand concentrations were also varied stepwise, decreasing by a factor of 10 from 10<sup>-4</sup> M until 10<sup>-7</sup> M. Reactions were also done at ambient temperature and at 50°C to study the effect of heating on RCY and labeling kinetics. Several trends can be noted from the preliminary results presented in Figure 4.4. Radiolabeling H<sub>6</sub>dappa with [<sup>177</sup>Lu]Lu<sup>3+</sup> at higher pH resulted in higher RCY, most notably at 10<sup>-6</sup> M and 10<sup>-7</sup> M ligand concentration– a molar activity of 28.2 GBq/μmol was achieved. Figure 4.4d illustrates a unique feature of H<sub>6</sub>dappa– not only is there no difference between RCY at ambient temperature versus 50°C labeling experiments, but under both conditions maximum radiolabeling occurs after just one minute. Indeed, this characteristic could translate well into

a clinical setting - the current gold-standard (DOTA) requires high temperature (95°C) and a long waiting period (~30 minutes) to radiolabel.

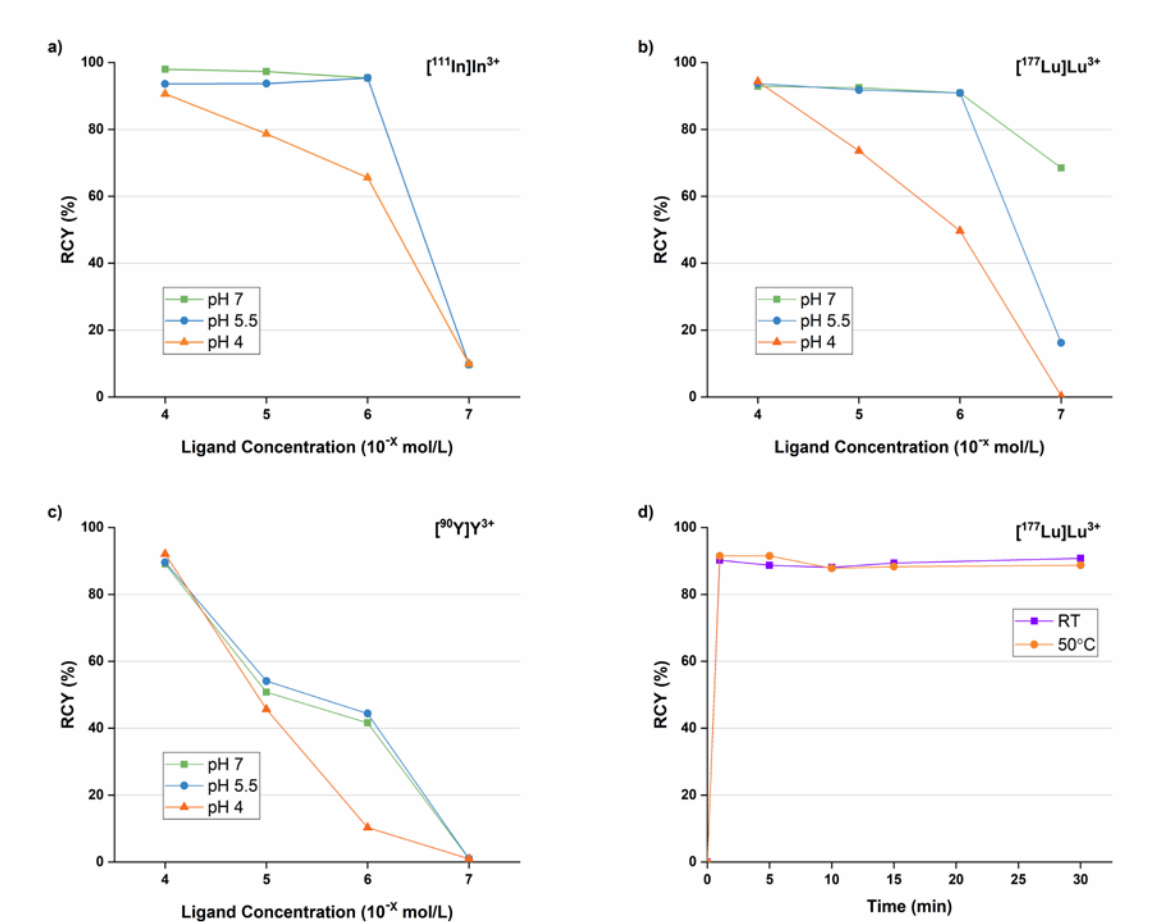


**Figure 4.4** Concentration- and pH-dependent radiolabeling of H<sub>6</sub>dappa (10 min, RT) in NH<sub>4</sub>OAc solution (0.1 M) with (A) [<sup>111</sup>In]In<sup>3+</sup>, (B) [<sup>177</sup>Lu]Lu<sup>3+</sup> and (C) [<sup>90</sup>Y]Y<sup>3+</sup>. (D) Time- and temperature-dependent radiolabeling of H<sub>6</sub>dappa (10<sup>-5</sup> M) in NH<sub>4</sub>OAc solution (0.1 M, pH 5.5) with [<sup>177</sup>Lu]Lu<sup>3+</sup>. Reproduced from reference 140.

H<sub>6</sub>dappa radiolabeling with [<sup>111</sup>In]In<sup>3+</sup> is slightly superior than with [<sup>177</sup>Lu]Lu<sup>3+</sup>. Similar time-, temperature-, pH- and concentration-dependent labeling was observed, with the 95% RCY at pH 7 to obtain molar activity of 29.8 GBq/μmol being the most notable trial. It was

hypothesized that studies with  $^{90}\text{Y}^{3+}$  would be the least successful due to discouraging thermodynamic parameters with  $^{nat}\text{Y}^{3+}$  in the solution studies. While at high ligand concentration, RCYs in the realm of 90% were observed, a sharp decrease in RCY was noted even at  $[\text{L}] = 10^{-5}$  M. As the main difference between  $\text{Y}^{3+}$  and  $\text{Lu}^{3+}$  is the ionic radius, which is quite stark due to the well-known lanthanide contraction,<sup>204</sup> it is speculated that the size of yttrium(III) is poorly suited to the binding cavity of  $\text{H}_6\text{dappa}$ .

The combination of encouraging results from thermodynamic studies and RCY optimization with  $^{nat/111}\text{In}^{3+}$  (respectively) led us to conduct human serum challenge experiments with  $^{111}\text{In}[\text{In}(\text{dappa})]^{3-}$ . The complex was formed at pH 7.5, diluted with PBS (phosphate-buffered saline) buffer, and then incubated in equal volume human serum. PD-10 size-exclusion desalting columns were used to separate  $^{111}\text{In}[\text{In}(\text{dappa})]^{3-}$  from serum-bound  $^{111}\text{In}^{3+}$ . Aliquots were taken at 1, 48, 72, 96 and 120 h to yield a time-dependent plot describing the percentage of intact complex remaining in solution. Table 4.3 illustrates the rapid decomplexation of  $^{111}\text{In}[\text{In}(\text{dappa})]^{3-}$ , where after just 1 h nearly half of the initial  $^{111}\text{In}^{3+}$  becomes dissociated from the chelator. Decomplexation continues at a slower rate for the next five days. The low kinetic inertness of the  $\text{H}_6\text{dappa}$  complex is easily rationalized when considering the rate of radiolabeling. The kinetic barrier towards complex formation must be low for such rapid labeling to occur; while this is beneficial during formation, it inherently leads to an easily transmetallated complex due to kinetic lability.

**Table 4.3** Serum stability of [<sup>111</sup>In][In(dappa)]<sup>3-</sup>. Reproduced from reference 140.

Time (h)	Stability (%) <sup>a</sup>
1	53 ± 1
48	44 ± 2
72	41 ± 1
96	35 ± 1
120	31 ± 2

<sup>a</sup>Experiments done in triplicate. 37 MBq (1 mCi) quantitatively labeled with 10<sup>-5</sup> M Hdappa<sup>5-</sup> (pH 7.5) then mixed with an equal volume of human serum and incubated at 37°C. PD10 size exclusion columns used to separate intact complexes versus transchelated radiometal ions. Reported error is standard deviation of triplicates.

#### 4.2.6 Density Functional Theory Calculations of H<sub>6</sub>dappa Complexes

The structures and coordination geometry of In<sup>3+</sup> and La<sup>3+</sup> complexes in solution were studied using DFT calculations. Results are presented in Figure 4.5. The calculated In<sup>3+</sup> complex reveals coordination of all 8 donor atoms (N<sub>4</sub>O<sub>4</sub>) with distorted square antiprism geometry, resulting in a symmetric structure. We also compared our calculated structure with the similar but more inert [In(octapa)]<sup>-</sup> to gain additional insight into the kinetic inertness of [<sup>111</sup>In][In(dappa)]<sup>3-</sup>.<sup>143</sup> These results are summarized in Table 4.4. The metal coordination geometries of the two structures are almost identical, with the main differences arising from the geometric and electronic influence of the phosphinate groups - the bite angle of phosphinate is known to be larger than that of carboxylate. Not only does this induce strain within the five membered N-In-OP coordination ring, but the steric constraint on the backbone also prevents the picolinic acids from conforming to the highly favorable twisted confirmation (illustrated in Figure 2 of Boros *et al.*<sup>81</sup>). The asymmetry of coordinative bond lengths (Table 4.4) is also likely a result of this steric strain. In terms of electronics, the hardness of the phosphinate groups

draws the  $\text{In}^{3+}$  away from the backbone and pyridine amines and closer to the picolinic acid groups (relative to  $[\text{In}(\text{octapa})]^-$ ) resulting in shallower encapsulation of the metal ion within the binding pocket. Calculated coordinative bond lengths support this assertion, and can be found in Table 4.4.

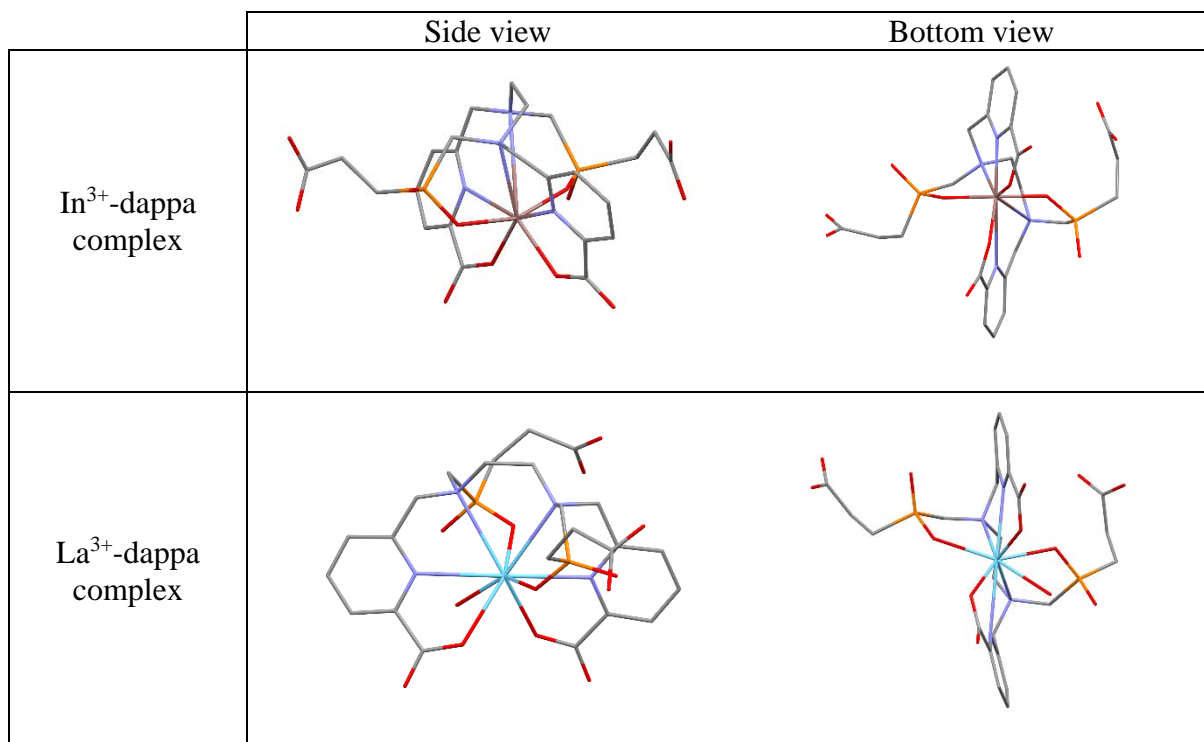


**Figure 4.5** Structures of selected DFT calculated metal complexes. Reproduced from reference 140.

NMR spectra of In-dappa at physiological pH point to the presence of fluxional isomers, as indicated by broad peaks in the  $^1\text{H}$  NMR spectrum and a single broadened peak in the  $^{31}\text{P}$  NMR spectrum. In addition to the structure shown in Figure 4.5 (minimum energy isomer), additional structures and their energies have been calculated (Figure 4.6) to explore the isomers responsible for this fluxionality. Coordination of both picolinic acid groups is supported by the single set of aromatic peaks in the  $^1\text{H}$  NMR spectrum, thus the ultimate goal of these

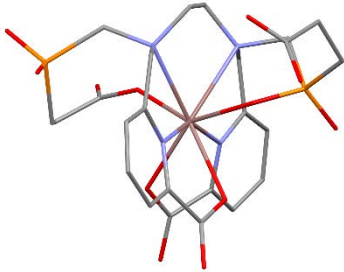
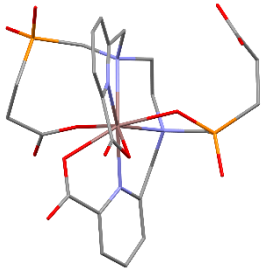
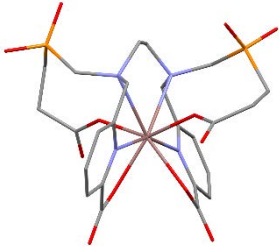
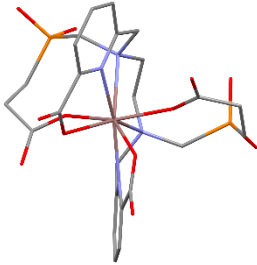
calculations was to determine which two of the six remaining coordinating groups can reasonably be non-coordinating (since  $CN_{In} = 8$ ).<sup>98</sup> All calculations with non-coordinating backbone amines either failed or were too energetically unfavorable, confirming a dedpa-like (*N,N'*-dipicolinate ethylenediamine) metal binding pocket.<sup>81</sup> Calculations with one or both carboxylic acids replacing adjacent phosphinates in the  $In^{3+}$  coordination sphere yielded reasonable geometries and energies, allowing us to conclude that NMR spectral broadness results from fluxional coordination between phosphinate and aliphatic carboxylic groups.

In summary, the strained geometry, poor metal ion embedment within the binding cavity and complex fluxionality at physiological pH likely all contribute to the rapid dissociation of  $[^{111}In][In(dappa)]^{3-}$  observed during serum stability experiments

**Table 4.4** Comparison of DFT calculated In-O and In-N bond lengths in In-octapa and In-dappa complexes.

Reproduced from reference 140.

<b>In<sup>3+</sup>-octapa</b>			<b>In<sup>3+</sup>-dappa</b>		
Atom 1	Atom 2	Length (Å)	Atom 1	Atom 2	Length (Å)
In	N1	2.9416	In	N1	2.6227
In	N2	2.9309	In	N2	3.7031
In	N3	2.3387	In	N3	3.0942
In	N4	2.3423	In	N4	2.2961
In	O1	2.1098	In	O1	2.1749
In	O2	2.1128	In	O2	2.0946
In	O3	2.1607	In	O3	2.0218
In	O4	2.1578	In	O4	2.0600

	Side view	Bottom view
In <sup>3+</sup> -dappa complex (P-O, COO)		 $\Delta G = 41.4 \text{ kJ/mol}^*$
In <sup>3+</sup> -dappa complex (COO, COO)		 $\Delta G = 40.8 \text{ kJ/mol}^*$

**Figure 4.6** DFT simulated structures of In<sup>3+</sup>-dappa complexes. \*Energies referenced to In-dappa structure in Figure 4.5 (set to zero). Reproduced from reference 140.

The La<sup>3+</sup>-dappa complex (Figure 4.5) is also of interest due to its distinct differences from previously reported pa ligands, [La(octapa)]<sup>-</sup> and [La(octox)]<sup>-</sup>.<sup>141,199</sup> These octadentate ligands (N<sub>4</sub>O<sub>4</sub>) encapsulate La<sup>3+</sup> while two water molecules coordinatively saturate the resulting decadentate metal ion. Conversely, due to crowding around the oxygen coordinating plane of La<sup>3+</sup>, the dappa complex only permits coordination of one water molecule, resulting in a nonadentate metal ion. Furthermore, in agreement with <sup>1</sup>H and <sup>31</sup>P NMR spectra (Figures 4.1a and 4.1b, respectively), the optimized DFT structure is symmetrical.

### 4.3 Conclusions

H<sub>6</sub>dappa was successfully synthesized and fully characterized; its metal ion chelation was studied with a number of “cold” metal ions (In<sup>3+</sup>, Lu<sup>3+</sup>, Y<sup>3+</sup>, Sc<sup>3+</sup>, La<sup>3+</sup>, Bi<sup>3+</sup>), which were chosen based on the existence of “hot” radioisotopes that are of clinical interest for nuclear medicine. Metal chelation was first studied with NMR to confirm the formation of metal complexes, as well as gain insight into the degree of symmetry and/or disorder of the molecule. As evidenced by the clear diastereotopic splitting in the <sup>1</sup>H NMR spectra, it was determined that the La<sup>3+</sup> and In<sup>3+</sup> complexes were highly symmetrical. Conversely, Bi<sup>3+</sup>, Y<sup>3+</sup>, Lu<sup>3+</sup>, and Sc<sup>3+</sup> complexes exhibited increasingly convoluted <sup>1</sup>H NMR spectra, likely as a result of the formation of multiple isomers and contortion of the chelator resulting in complex asymmetry. Solution studies (potentiometric and spectrophotometric titrations) were undertaken to probe the protonation constants of H<sub>6</sub>dappa and thermodynamic stability of its complexes with In<sup>3+</sup>, Lu<sup>3+</sup>, Y<sup>3+</sup> and Sc<sup>3+</sup>. Speciation diagrams, formation constants and pM values were calculated. In each case, only one species predominated at physiological pH (7.4). The In<sup>3+</sup> complex demonstrated the highest formation constant (log  $K_{ML} = 27.5$ ) and pM value (27.7), making it the most stable complex of the four studied. Radiolabeling experiments were conducted to investigate the highest molar activity achievable with three clinically relevant radionuclides ([<sup>111</sup>In]In<sup>3+</sup>, [<sup>177</sup>Lu]Lu<sup>3+</sup>, [<sup>90</sup>Y]Y<sup>3+</sup>). As expected, these results mimicked those found during solution studies. High molar activity was observed when radiolabeling [<sup>111</sup>In]In<sup>3+</sup> with H<sub>6</sub>dappa, with the maximum of 29.8 GBq/μmol occurring at [H<sub>6</sub>dappa] = 10<sup>-6</sup> M with a RCY > 95%. Studies with [<sup>177</sup>Lu]Lu<sup>3+</sup> also yielded high molar activity (28.2 GBq/μmol at [H<sub>6</sub>dappa] = 10<sup>-6</sup> M with a RCY > 90%). The formation constant and pM value of Y<sup>3+</sup>-dappa was the lowest of the studied metal ions, and similarly the radiolabeling of [<sup>90</sup>Y]Y<sup>3+</sup> resulted in

the lowest RCYs and molar activities. Very mild and rapid radiolabeling was observed for all radionuclides studied, as only one minute at room temperature was required to reach the maximum RCY. The kinetic inertness of the  $[^{111}\text{In}^{3+}][\text{In}(\text{dappa})]^{3-}$  complex was explored via serum stability studies. It was observed that rapid decomplexation occurred upon introduction of human serum proteins to a solution containing  $[^{111}\text{In}][\text{In}(\text{dappa})]^{3-}$ , with near 50% degradation in 1 h. This outcome highlights the point that thermodynamic stability is not a valid predictor of kinetic inertness or *in vivo* stability. DFT calculations revealed the rapid dissociation is likely a result of poor encapsulation of  $[^{111}\text{In}]\text{In}^{3+}$  in the binding pocket of  $\text{H}_6\text{dappa}$ . This is unlike what has previously been observed with  $\text{H}_4\text{octapa}$ ,<sup>143</sup> leading to the conclusion that the replacement of carboxylic acids with phosphinates has an undesirable kinetic effect for pa family targeted radionuclide delivery, likely as a result of the steric and electronic effects of these newly introduced functional groups.

## 4.4 Experimental

### 4.4.1 Materials and Methods

For details regarding synthetic materials or instrumentation, see Section 3.4.1. Human serum was purchased frozen from Sigma-Aldrich. Radiolabeling reactions were monitored by TLC (Silicagel 60 RP-18 F254S, aluminum sheet) and HPLC (Knauer Smartline System consisting of Smartline 1000 pump, K2501 diode array detector, Raytest Ramona Star activity detector, Chromgate 2.8 software and a Smartline 5000 manager with a Zobax SB-C18 column; Agilent 4.6x250 mm, 5  $\mu\text{m}$ ). Radio-TLC chromatograms were scanned using a radioisotope thin layer analyzer (BIOSCAN system 200 imaging scanner, Rita Star or Fuji BAS-1800II, raytest); evaluation program AIDA. The HPLC system used for analysis and purification of

nonradioactive compounds consisted of a Waters 600 controller, Waters 2487 dual wavelength absorbance detector and a Waters delta 600 pump with a Phenomenex Synergi 4  $\mu\text{m}$  hydro-RP 80  $\text{\AA}$  column (250 mm x 21.2 mm semipreparative) or a Zorbax (Agilent) 300SB-C18, 300  $\text{\AA}$ , 5  $\mu\text{m}$ , 9.4 mm x 250 mm column were used for purification of H<sub>6</sub>dappa (**6**). <sup>111</sup>InCl<sub>3</sub> was cyclotron-produced [<sup>112</sup>Cd(p,2n)<sup>111</sup>In; no carrier added; Fe, Cd, Cu, Pb, Zn, Ni each  $\leq$  100 ng/mCi] and purchased from BWX Technologies as 0.05 M HCl solution or from Curium Pharma as 0.02 M HCl solution. <sup>177</sup>LuCl<sub>3</sub> was produced by reactor-based indirect strategy<sup>41,205</sup> [<sup>176</sup>Yb(n, $\gamma$ )<sup>177</sup>Yb $\rightarrow$ <sup>177</sup>Lu, no carrier added; specific activity 3800-3000 GBq/mg] and was purchased from ITG (Isotope Technologies Garching) GmbH as 0.04 M HCl solution. <sup>90</sup>YCl<sub>3</sub> [<sup>90</sup>Sr/<sup>90</sup>Y generator; carrier free] was purchased from Eckert & Ziegler Strahlen- und Medizintechnik AG as 0.04 M HCl solution. Radionuclide solutions were used within one half-life (upon arrival) to minimize reduction in specific activity.

#### 4.4.2 Synthesis and Characterization

(2-Carboxyethyl)phosphinic acid (**11**). Compound **11** was prepared according to the literature preparation with appropriate characteristic spectra.<sup>198</sup>

*N,N'*-dibenzylethane-1,2-diamine • 2HCl (**12**). Ethylene diamine (3.00 g, 3.34 mL, 49.9 mmol) and benzaldehyde (11.7 g, 11.2 mL, 110 mmol) were dissolved in MeOH (150 mL) in a round-bottom flask. The solution was stirred and heated to reflux for five hours, during which time the yellow solution darkened into a yellow-orange color. The solution was then allowed to cool to ambient temperature, then cooled to 0°C in an ice bath. NaBH<sub>4</sub> (6.61 g, 175 mmol) was added in several portions, and the solution was allowed to warm to ambient temperature and

stirred for 24 h. After LR-ESI-MS revealed complete reduction of the imine intermediate, the solution was evaporated via rotary evaporator to yield a yellow oil. Aqueous HCl (3 M, 50 mL) was slowly added to the oil to yield a white solid that was filtered out and washed with acetone to yield **3** as a dihydrochloric acid salt (13.1 g, 95%).  $^1\text{H}$  NMR (300 MHz, 298 K,  $\text{D}_2\text{O}$  + NaOD):  $\delta$  7.51-7.46 (m, 10H), 4.23 (s, 4 H), 3.37 (s, 4H).  $^{13}\text{C}\{^1\text{H}\}$  NMR (100 MHz, 298 K,  $\text{D}_2\text{O}$  + NaOD): 131.3, 129.6, 129.6, 129.3, 51.6, 43.0. LR-ESI-MS: calcd for  $[\text{C}_{16}\text{H}_{20}\text{N}_2 + \text{H}]^+$ : 241.2; found  $[\text{M} + \text{H}]^+$ : 241.3. Elemental analysis: calcd % for  $\text{C}_{16}\text{H}_{20}\text{N}_2 \bullet 2\text{HCl}$ : C 61.35, H 7.08, N 8.94; found: C 61.67, H 6.93, N 8.94.

*Dimethyl-6,6'([ethane-1,2-diylbis{benzylazanediy}]bis[methylene])dipicolinate* (**13**).

Compounds **4** (3.40 g, 14.7 mmol) and **12** (1.87 g, 5.97 mmol) were dissolved in ACN (120 mL) in a round-bottom flask.  $\text{K}_2\text{CO}_3$  (5.61 g, 40.6 mmol) was then added and the solution was stirred and heated to reflux for 3 d. The reaction mixture was quenched with  $\text{H}_2\text{O}$  (100 mL), then DCM (140 mL) added for the first extraction. The phases were separated and the aqueous phase was further washed with DCM ( $3 \times 100$  mL); the combined organic phases were dried over  $\text{MgSO}_4$ , filtered, and loaded onto Celite and dried. The product was purified via column chromatography using a silica column (CombiFlash  $R_f$  automated column system, 120 g gold silica column, 100% hexane to 100% EtOAc). The product fractions were rotary evaporated to yield an oil, which solidified to a yellow solid upon standing at ambient temperature (1.82 g, 57%).  $^1\text{H}$  NMR (400 MHz, 298 K,  $\text{CDCl}_3$ ):  $\delta$  7.95 (t,  $J = 4.4$  Hz, 1H), 7.69 (d,  $J = 4.5$  Hz, 2H), 7.30-7.15 (m, ~5H; overlap with  $\text{CDCl}_3$ ), 3.97 (s, 3H), 3.82 (s, 2H), 3.57 (s, 2H), 2.68 (s, 2H).  $^{13}\text{C}\{^1\text{H}\}$  NMR (100 MHz, 298 K,  $\text{CDCl}_3$ ): 165.8, 161.1, 147.1, 139.0, 137.3, 128.7, 128.3,

127.0, 125.9, 123.5, 60.5, 59.1, 52.9, 52.0. LR-ESI-MS: calcd for  $[C_{32}H_{34}N_4O_4 + H]^+$ : 539.3; found  $[M + H]^+$ : 539.3.

*Dimethyl-6,6'-([ethane-1,2-diylbis{azanediy}]bis[methylene])dipicolinate (1)*. Compound **13** (1.18 g, 2.19 mmol) was dissolved in 50 mL of glacial acetic acid in a two-neck round-bottom flask. The flask was purged with  $N_2$  and 10% w/w Pd/C (375 mg, 0.35 mmol) added under a stream of  $N_2$ . The flask was thrice purged with  $N_2$  and then filled with  $H_2$  from a balloon. The mixture was stirred at room temperature overnight under  $H_2$ , then Pd/C was removed by filter paper, which was washed alternately with ACN ( $3 \times 30$  mL) and 3 M aqueous HCl ( $2 \times 10$  mL). The solution was evaporated and the dark orange oil dissolved in minimal ACN, and then run through a small Celite plug to remove residual Pd/C. The solvent was removed by rotary evaporator with EtOH added and evaporated twice to remove residual acetic acid. Following *in vacuo* solvent removal, the dark orange oil solidified (712 mg, 90%) and was used without further purification.  $^1H$  NMR (400 MHz, 298 K,  $D_2O$ ):  $\delta$  8.20 (d,  $J = 7.4$  Hz, 1H), 8.12 (t,  $J = 7.8$  Hz, 1H), 7.75 (d,  $J = 7.7$  Hz, 1H), 4.70 (s, 2H), 3.91 (s, 3H), 3.73 (s, 2H).  $^{13}C\{^1H\}$  NMR (100 MHz, 298 K,  $D_2O$ ): 166.7, 151.1, 146.5, 140.0, 127.4, 125.7, 53.5, 50.6, 43.9. LR-ESI-MS: calcd for  $[C_{18}H_{22}N_4O_4 + H]^+$ : 359.2; found  $[M + H]^+$ : 359.1.

*H6dappa (14)*. Compounds **1** (500 mg, 1.40 mmol) and **11** (773 mg, 5.60 mmol) were added to 6 M HCl (1.5 mL) in a two-dram (7.4 mL) vial. Upon heating to  $80^\circ C$  the components dissolved to yield a brownish-orange solution. Over the course of 24 h, paraformaldehyde (628 mg, 20.9 mmol) was added in small portions. After full addition of the paraformaldehyde, the solution was refluxed for an additional 24 h. The solvent was removed by rotary evaporator and most

of the remaining HCl removed by repeatedly adding small portions of water and then evaporating to dryness. The dark brown oil was dissolved in water (5 mL) and neutralized with 1 M NaOH. The crude product was first purified by chromatography on ion exchange resin (DOWEX 50W2, H<sup>+</sup>-form, 100-200 mesh; column size 32 cm × 2 cm; eluent: water). Impurities were removed with the first 200 mL of eluate. The next 250 mL of eluate, containing semi-pure product, was collected and the solvent removed by rotary evaporator. The pale yellow oil was dissolved in water (2 mL) and purified by HPLC (Phenomenex Synergi 4 μm hydro-RP 80 Å column, 250 mm × 21.2 mm semipreparative; A: H<sub>2</sub>O 0.1% TFA, B: ACN, 100% A to 85% A-15% B over 20 min, maintain 85% A-15% B for 5 min. *t<sub>R</sub>* = 22.6 min). Pure fractions were combined, evaporated to ~3-5 mL and lyophilized to yield pure product as a fluffy white powder (241 mg, 18%). <sup>1</sup>H NMR (400 MHz, 298 K, D<sub>2</sub>O): 8.04 (t, *J* = 7.8 Hz, 1H), 7.97 (d, *J* = 7.7 Hz, 1H), 7.69 (d, *J* = 7.7 Hz, 1H), 4.42 (s, 2H), 3.51 (s, 2H), 3.15 (d, *J* = 7.4 Hz, 2H), 2.20 (dt, *J*<sub>3<sup>PH</sup></sub> = 12.6 Hz, *J*<sub>3<sup>HH</sup></sub> = 7.8 Hz, 2H), 1.68 (dt, *J*<sub>2<sup>PH</sup></sub> = 14.9 Hz, *J*<sub>3<sup>HH</sup></sub> = 7.8 Hz, 2H). <sup>13</sup>C{<sup>1</sup>H} NMR (100 MHz, 298 K, D<sub>2</sub>O): 176.2 (d, *J* = 14.3 Hz), 164.9, 151.3, 144.8, 143.2, 129.1, 126.1, 58.0, 52.4, 52.3 (d, *J* = 92.8 Hz), 26.3 (d, *J* = 3.2 Hz), 24.2 (d, *J* = 96.5 Hz). <sup>31</sup>P{<sup>1</sup>H} NMR (162 MHz, 298 K, D<sub>2</sub>O, externally referenced to 85% phosphoric acid): 33.91. HR-ESI-MS: calcd for [C<sub>24</sub>H<sub>32</sub>N<sub>4</sub>O<sub>12</sub>P<sub>2</sub> + H]<sup>+</sup>: 631.1570; found [M + H]<sup>+</sup>: 631.1572. Elemental analysis: calcd % for H<sub>6</sub>dappa•2.6TFA•1.8H<sub>2</sub>O: C 36.56, H 4.01, N 5.84; found: C 36.61, H 4.08, N 5.79. Calculated EA comes from best fit of H<sub>6</sub>dappa with TFA and H<sub>2</sub>O contaminants. Resultant molecular weight is validated during thermodynamic solution studies; as precise knowledge of solution concentrations is required.

#### 4.4.3 Metal Complexation

NMR spectra of  $[M(H_x\text{dappa})]^{3-x}$  ( $M = \text{In}^{3+}, \text{Lu}^{3+}, \text{Y}^{3+}, \text{Sc}^{3+}, \text{La}^{3+}$ ;  $x = 2, 1, 0, -1$ ) were obtained by making separate ligand and metal solutions in  $\text{D}_2\text{O}$  (5-20 mM), and then mixing the solutions in a molar ratio of 1:1.1/L:M ( $V_t > 300 \mu\text{L}$ ). If necessary, solution pD was altered with freshly prepared  $\sim 0.1 \text{ M NaOD}$  (diluted from 40 wt. % NaOD) and measured with a Ross combined electrode and corrected  $\text{pD} = \text{pH}_{\text{measured}} + 0.4$ . Solutions were allowed to stand for at least 5 minutes at room temperature before collecting NMR spectra. Due to the poor solubility of  $\text{Bi}(\text{NO}_3)_3 \cdot 5\text{H}_2\text{O}$  in neutral  $\text{D}_2\text{O}$ , for  $[\text{Bi}(\text{H}_x\text{dappa})]^{x-3}$ , the desired amount of  $\text{Bi}(\text{NO}_3)_3 \cdot 5\text{H}_2\text{O}$  was weighted on an analytical balance, then a 1:1.1 (L:M) molar ratio of  $\text{dappa}^{6-}$  solution was added to the metal salt. Following dissolution of the solid,  $\text{D}_2\text{O}$  was used to dilute the solution by a factor of two.

#### 4.4.4 Solution Thermodynamics

See Section 3.4.5 for general details regarding solution thermodynamics. Protonation equilibria of  $\text{H}_6\text{dappa}$  was studied by combined UV-potentiometric titrations of solutions containing  $[\text{H}_6\text{dappa}] = 0.968 \text{ mM}$  at  $T = 298\text{K}$ ,  $l = 0.2 \text{ cm}$  and  $0.16 \text{ M NaCl}$  ionic strength in the pH range 2.0-11.5. The most acidic protonation constants corresponding to phosphinate functionalities were determined by acidic UV-batch experiments ( $l = 1 \text{ cm}$ ) with  $[\text{H}_6\text{dappa}] = 0.233 \text{ mM}$  at  $298 \text{ K}$ ,  $l = 1 \text{ cm}$  and  $0.16 \text{ M NaCl}$  concentration when possible.

Complex formation equilibria of  $\text{H}_6\text{dappa}$  with  $\text{In}^{3+}$ ,  $\text{Sc}^{3+}$ ,  $\text{Y}^{3+}$  and  $\text{Lu}^{3+}$  was carried out by UV-Vis batch spectrophotometric measurements ( $[\text{H}_6\text{dappa}] = 0.183 \text{ mM}$ ) and combined UV-potentiometric titrations ( $[\text{H}_6\text{dappa}] = 0.739$ ,  $T = 298\text{K}$ ,  $I = 0.16 \text{ M NaCl}$  and  $l = 0.2 \text{ cm}$ ), as described in Section 3.4.5. Competition pH-potentiometric titrations with  $\text{ttha}^{6-}$  and  $\text{edta}^{4-}$  as

ligand competitors were also conducted. The third method solely used potentiometry, but made use of ligand-ligand competition with  $ttha^{6-}$  ( $[In^{3+}] = 0.704$  mM,  $[H_6dappa] = 0.235$  mM,  $[ttha^{6-}] = 0.471$  mM,  $T = 25^\circ C$ ,  $I = 0.16$  M NaCl) or  $edta^{4-}$  ( $[Lu^{3+}] = 0.467$  mM,  $[H_6dappa] = 0.237$  mM,  $[Na_2H_2edta] = 0.235$  mM;  $[Sc^{3+}] = 0.633$  mM,  $[H_6dappa] = 0.317$  mM,  $[Na_2H_2edta^{2-}] = 0.628$  mM;  $[Y^{3+}] = 0.752$  mM,  $[H_6dappa] = 0.237$  mM,  $[Na_2H_2edta] = 0.812$  mM,  $T = 25^\circ C$ ,  $I = 0.16$  M NaCl). Metal solutions were prepared by adding atomic absorption (AA) standard metal ion solution to a  $H_6dappa$  solution of known concentration in a 1:1 metal to ligand molar ratio. The exact amount of acid present in the indium, lutetium, scandium and yttrium standards was determined by Gran's method<sup>157</sup> titrating equimolar solutions of the chosen metal ions and  $Na_2H_2-EDTA$ .

#### 4.4.5 Radiolabeling and Human Serum Challenge Experiments

For concentration-dependent radiolabeling, an aliquot of a ligand solution (25  $\mu L$ ) of desired concentration was mixed with  $[^{90}Y]Y^{3+}$  or  $[^{111}In]In^{3+}$  or  $[^{177}Lu]Lu^{3+}$  (7.5 MBq, 0.2 mCi) and diluted to a final volume (250  $\mu L$ ) with ammonium acetate solution (0.1 M, pH = 2, 4, 5.5, 7 or 7.5). The final mixture was incubated at room temperature or  $50^\circ C$  for the specific amount of time (i.e., 1, 5, 10, 15 or 30 min) before determination of radiochemical yield. Initial attempts to quantify RCY with HPLC (Zorbax SB-C18 column; Agilent  $4.6 \times 250$  mm, 5  $\mu m$ ; solvent A =  $H_2O$  0.1% TFA, solvent B = ACN 0.1% TFA) were unsuccessful due to the expected high hydrophilicity of the many  $dappa^{6-}$  metal complexes, resulting in identical retention times for the free ligand and metal complexes (which eluted at the solvent front). Accordingly, RP-18 silicagel TLC plates were used to quantify RCY - typically 2-5  $\mu L$  was spotted per plate.  $NH_4OH/MeOH/H_2O$  (1/10/20) was used as a mobile phase for TLC. In the absence of  $dappa^{6-}$

(denoted “control”) the free radiometal remained at the baseline of the TLC plate. When dappa<sup>6-</sup> was present, the activity moved up the TLC plate, with the degree of streaking being dependent on the radiometal ion under investigation. For the human serum challenge, GE Healthcare Life Sciences PD-10 desalting columns (size exclusion for MW <5000 Da) and a Capintec CRC 55t dose calibrator were used, as was previously described.<sup>72</sup> Briefly, 37 MBq (1 mCi) of [<sup>111</sup>In]In<sup>3+</sup> was near-quantitatively labeled with 10<sup>-5</sup> M H<sub>6</sub>dappa (pH 7.5), diluted to 1 mL with PBS buffer, then mixed with an equal volume of human serum and incubated at 37°C. Aliquots were taken at 1 h, 2 d, 3 d, 4 d and 5 d. Aliquots were diluted to 2.5 mL with PBS, loaded onto a conditioned PD-10 column and eluted with an additional 3.5 mL of PBS. Activity of the vial containing the diluted aliquot was measured prior to loading of the column (initial activity), as well as following loading (residual activity). Stability was calculated through equation (4.1).

$$stability = 1 - (eluted\ activity / (initial\ activity - residual\ activity)) \quad (4.1)$$

#### 4.4.6 Density Functional Theory Calculations

All DFT calculations were performed as implemented in the Gaussian 09 revision D.01 suite of ab initio quantum chemistry programs (Gaussian Inc., Wallingford, CT)<sup>159</sup> and visualized using Mercury 4.1. The structure geometry was optimized using the TPSSh functional,<sup>206</sup> TZVP basis set<sup>207</sup> for first- and second-row elements. The Stuttgart/Dresden and associated effective core potentials’ basis set was used for In and La,<sup>167,208</sup> in the presence of water solvent (IEF PCM as implemented in G09) without the use of symmetry constraints.

## Chapter 5. Amide-Dominant Chelator for Lead(II) Radiopharmaceuticals

### 5.1 Introduction

#### 5.1.1 Radioactive Lead as a Therapeutic

From a medicinal standpoint, lead is rarely a topic of discussion. From its inclusion in paint to airborne particulates at industrial sites, lead is a famously toxic element that requires only micrograms per decilitre ( $\mu\text{g/dL}$ ) to exert a toxic effect.<sup>209</sup> While its chemical properties result in a number of adverse health effects, channeling the physical decay of certain lead radioisotopes is a field with proven success that is continuing to grow with radionuclide availability.

The two notable theranostic radioisotopes of lead are  $^{203}\text{Pb}$  ( $t_{1/2} = 51.9$  h) and  $^{212}\text{Pb}$  ( $t_{1/2} = 10.6$  h). The prior is a neutron deficient radionuclide and consequently decays via electron capture, resulting in the release of 81 keV  $\gamma$ -rays (among few others) that can be used for SPECT imaging. The latter is a proton deficient radionuclide best known for its appearance in the decay chain of  $^{224}\text{Ra}$  (Figure 5.1). Like its parent nuclide,  $^{212}\text{Pb}$  has a decay chain resulting in release of multiple therapeutic particles; however, the decay to  $^{208}\text{Pb}$  is limited to one  $\alpha$  and two  $\beta$  decays.<sup>210</sup>

Indeed, these radionuclides have been exploited to diagnose and treat prostate cancer,<sup>211,212</sup> neuroendocrine tumours<sup>213</sup> and melanoma,<sup>214</sup> among other illnesses, and are increasingly being researched due to the convenience of a theranostic pair containing an  $\alpha$ -emitter with a mid-range half-life. A glance at other highly regarded therapeutic  $\alpha$ -emitters reveals both a lack of chemically identical diagnostic isotopes and often inconveniently long or short half-lives. For example,  $^{225}\text{Ac}$  ( $t_{1/2} = 10.0$  d) is a most promising therapeutic radionuclide currently under investigation; however, its half-life is sub-optimal providing

persistent patient dosage. Furthermore, there is no diagnostic or nonradioactive actinium radioisotope, as heavy radionuclides such as actinium tend to emit alpha particles and/or be at extrema of stability (i.e., millisecond or multiyear half-life).<sup>16</sup> Other illustrative examples are the two therapeutic bismuth isotopes  $^{212}\text{Bi}/^{213}\text{Bi}$  ( $t_{1/2} = 1.01$  h and 0.76 h half-lives, respectively).<sup>2</sup> In this case, not only are chemically identical theranostic pairs absent, but the half-lives of both isotopes can lead to logistical challenges during preparation/administration, as well as present high dose-risks to radiopharmacists and nuclear medicine technicians (who prepare the drugs). Thus, development of  $^{203/212}\text{Pb}$ -based radiopharmaceuticals represents a rare opportunity to explore the efficacy of a true theranostic pair.

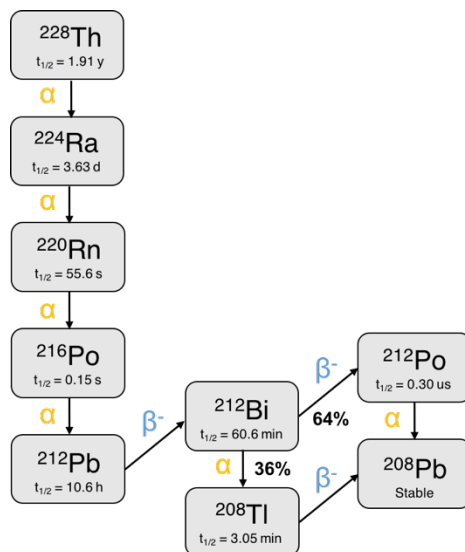


**Figure 5.1** Thorium-228 decay chain. Reproduced from reference 2.

While the availabilities of both radionuclides are far from that of routine clinical production, interest in the pair has recently intensified at TRIUMF due to the co-production of  $^{228}\text{Th}$  ( $t_{1/2} = 1.91$  y) during spallation of a  $^{232}\text{Th}$  target, intended to produce  $^{225}\text{Ac}$ .<sup>124</sup> Thorium-228 is a parent nuclide of  $^{212}\text{Pb}$  and can be used as a long-lived generator due to its lengthy

half-life (see Section 1.4.1). Milking of the generator yields  $^{212}\text{Pb}$ , which depending on the system may require purification from  $^{224}\text{Ra}$  and  $^{212}\text{Bi}$ .<sup>215</sup> Production of the diagnostic surrogate is achieved via low-energy proton bombardment of  $^{203}\text{Tl}$  to induce a (p,n) reaction and yield pure  $^{203}\text{Pb}$  following removal and recovery of the enriched target material by resin chromatography.<sup>216,217</sup> Thanks to being closely affiliated with the Life Sciences Division at TRIUMF, the opportunistic production of these radioisotopes has afforded me a rare and exciting chance to work with cutting edge nuclides.

### 5.1.2 Lead Chelation and Project Rationale

Unlike most clinical metalloradionuclides, the standard chelator used for  $^{203/212}\text{Pb}$  is not DOTA. The soft, bulky nature of  $\text{Pb}^{2+}$  does not optimally pair with the hard coordination properties of DOTA's four carboxylic acids. Instead, it has been determined that the best chelator for lead-based radiopharmaceuticals is 1,4,7,10-tetraaza-1,4,7,10-tetra-(2-carbamoylmethyl)-cyclododecane (TCMC; Figure 5.2).<sup>4</sup> Replacement of the carboxylic acids with coordinating amide groups drastically improves the kinetic inertness of  $\text{Pb}^{2+}$  complexes, as well as the molar activity of drugs *in vitro*.<sup>218,219</sup>

Classically, the most studied high-denticity chelators in coordination chemistry are DOTA and DTPA (Figure 5.2). These two represent the most widely studied macrocyclic and non-macrocyclic ligands in the field, and have been studied with the vast majority of metal ions on the periodic table. If TCMC is an amide derivative of DOTA that has shown great improvement based on a simple design alteration, then it would logically follow that a similar modification of DTPA would result in improved performance of the pentaamide product over its carboxylic acid-bearing predecessor (Figure 5.2). While the literature reveals this design is

not original, only one report of this ligand, denoted DTPAm (diethylenetriamine-*N,N',N'',N''',N''''*-pentaacetamide), has been published. In 2008, Burdinski *et al.* reported a number of amide-bearing derivatives of common acyclic ligands (e.g., DTPA, EDTA, TTHA) and studied their potential use as MRI contrast agents when complexed with  $\text{Yb}^{3+}$ .<sup>220</sup> The work was of high quality; however, no follow-up appears to have been published, nor was DTPAm considered a top candidate for the purposes of their work.

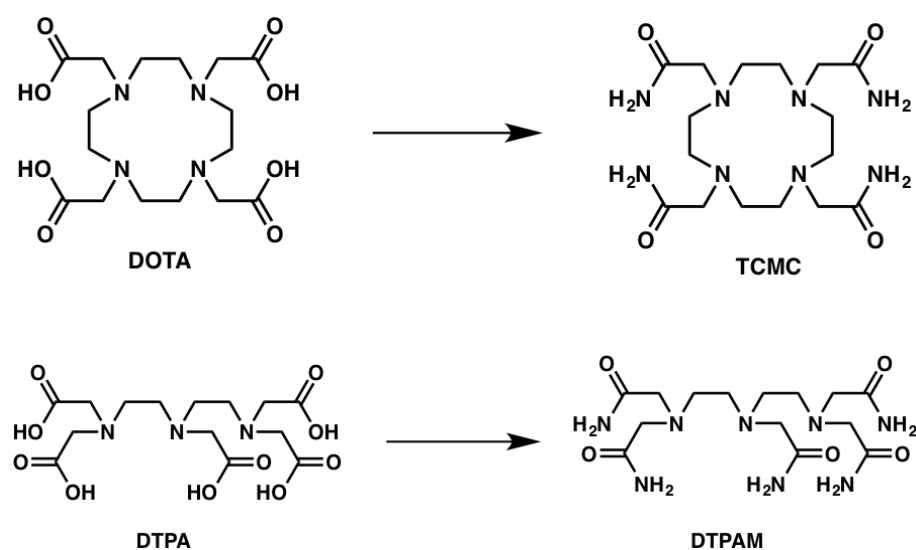


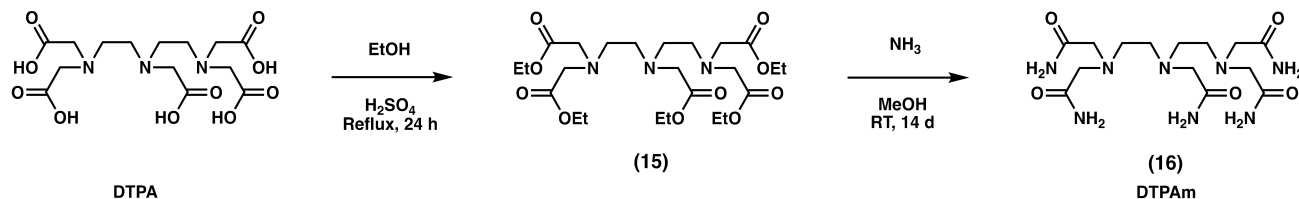
**Figure 5.2** Design principle behind DTPAm.

Overall, the availability of  $^{203/212}\text{Pb}$  at a nearby facility and the lack of exploration in the literature of a simple amide-based ligand with clear potential for lead chelation has poised this project to yield intriguing results. Reported herein are the synthesis, cold metal complexation, crystal structure analysis, solution studies and radiolabeling of DTPAm with a focus on  $[\text{nat}/^{203}\text{Pb}]\text{Pb}^{2+}$  towards lead-based theranostic radiopharmaceuticals.

## 5.2 Results and Discussion

### 5.2.1 Ligand Synthesis and Characterization

The straightforward synthesis of DTPAm is a very appealing aspect of its study (Scheme 5.1). This two-step synthesis is not only high yielding, scalable and achieved with widely available, inexpensive materials, but neither the ester intermediate (compound **15**) nor the final product require column purification. The first reaction is a Fischer esterification, using  $\text{H}_2\text{SO}_4$  as the acid catalyst and ethanol as the solvent and nucleophile. As this name reaction is well known for simplicity and efficiency, it is not surprising that tandem acid-neutralization and extraction of DTPA with a basic aqueous phase (1.5 M NaOH) results in a pure ester product. The following reaction requires a ten-to-fourteen day reaction time, presumably due to the low nucleophilicity of ammonia in methanol. Fortunately, the product is insoluble in methanol, so filtration of the reaction mixture followed by washing with cold methanol yields pure product. Interestingly, the choice of solvent for characterization via NMR spectroscopy has a drastic effect on spectral complexity. Using  $\text{D}_2\text{O}$  yields a simple spectrum comprised of three singlet peaks in the aliphatic region (backbone peaks overlap), which is expected for such a symmetric, non-aromatic molecule. Conversely, the use of  $\text{DMSO-d}_6$  (as was originally done by Burdinski *et al.*) reveals inequivalent amide protons, suggesting intramolecular  $\text{C(O)-H-N}$  hydrogen bonding.<sup>220</sup>



**Scheme 5.1** Synthesis of DTPAm.

### 5.2.2 NMR Complexation Studies with $[\text{natPb}]\text{Pb}^{2+}$

Complexation of  $[\text{natPb}]\text{Pb}^{2+}$  by DTPAm was studied by  $^1\text{H}$  NMR spectroscopy and  $^1\text{H}$ - $^1\text{H}$  COSY. Radiolabeling studies for lead(II) radionuclides are almost always done at near physiological pH; thus, solutions of both the free ligand and metal complex were adjusted to  $\text{pD} = 7$  before collecting each spectrum.

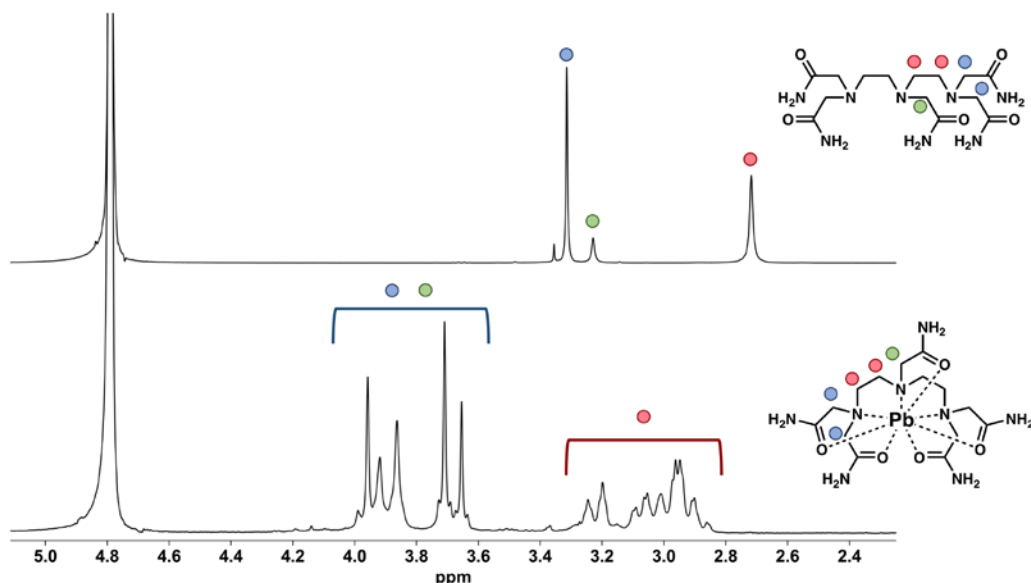
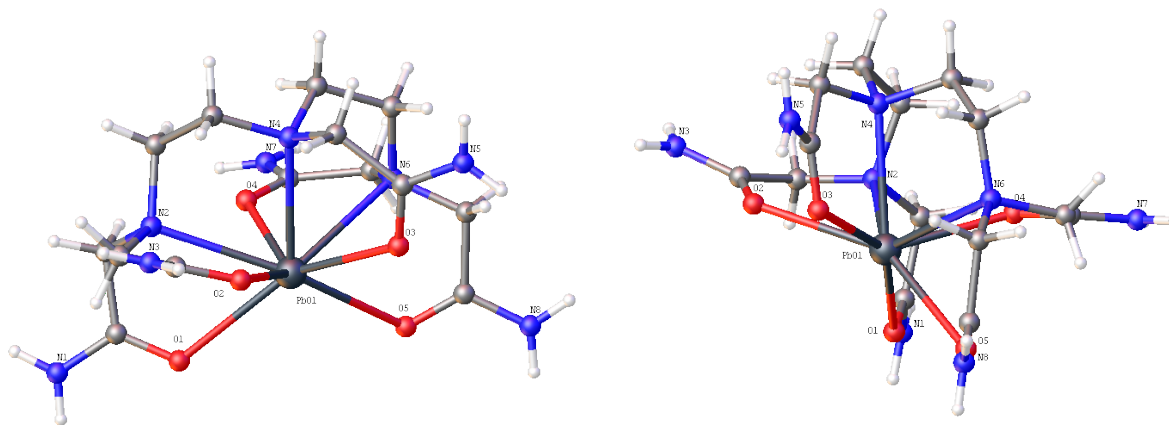


**Figure 5.3.**  $^1\text{H}$  NMR spectra of DTPAm (top) and  $[\text{Pb}(\text{DTPAm})]^{2+}$  (bottom) ( $\text{D}_2\text{O}$ ,  $\text{pD} = 7$ , RT, 300 MHz).

As seen in Figure 5.3, three signals are present in the  $^1\text{H}$  NMR spectrum of the ligand. The backbone protons are all found within the same environment, and are assigned to the most upfield shifted peaks. The peaks corresponding to the amido groups that stem from terminal amines are the most downfield shifted and have four times the integration of the small peak directly adjacent. This small peak corresponds to the amide arm stemming from the central backbone amine. When lead is introduced to the system, a number of spectral changes occur

that confirm complex formation, the most obvious of which is the increased complexity. This results from previously equivalent proton environments becoming inequivalent [e.g., N-(CH<sub>2</sub>)-(CH<sub>2</sub>)-N], which also subsequently induces <sup>2</sup>J<sub>H-H</sub> diastereotopic splitting, further increasing the number of observed <sup>1</sup>H peaks. The other key difference between the spectra in Figure 5.3 are the differences in chemical shifts. The downfield shift of proton signals commonly occurs during metal complexation, and is a result of electron density being donated to the metal ion from the ligand, and effectively providing less shielding to the observed proton environments. Peak assignments of the metal complex were done on this basis of integration, as well as with support from the <sup>1</sup>H-<sup>1</sup>H COSY, which showed dense peak correlation between the four backbone environments, and expectedly less correlation amongst amido peaks.

### 5.2.3 X-ray Crystal Structure of [Pb(DTPAm)]<sup>2+</sup>



diagrams of the ligands are shown in Figure 5.4 (counter ions omitted) and its crystallographic information can be found in the Table A.10. From Figure 5.4, it can be seen that in the solid structure, DTPAm coordinates as expected, with the three backbone amines and five amido-oxygens coordinating to coordinatively saturate the  $\text{Pb}^{2+}$  ion. The geometry of the metal ion is distorted square antiprism. Qualitative analysis of the structure presents evidence that ligand distortion is a result of repulsion from the metal ion's lone-pair. This is unlike the solid-state structure of  $[\text{Pb}(\text{TCMC})]^{2+}$ , where coordination bond distances remain relatively constant as a result of the lone-pair pointing along the  $C_{4v}$  axis.<sup>221</sup> As shown in Table 5.1, the  $[\text{Pb}(\text{DTPAM})]^{2+}$  coordinative bond lengths of oxygen atoms 1–4 and nitrogen atoms 2/4 are relatively uniform, with a standard deviation of 0.073 Å and 0.023 Å (respectively). The coordinating atoms nearest to the lone-pair (N6 and O5) however, are skewed due to electron repulsion, resulting in longer bond lengths than for other coordinating heteroatoms. The crystal structure of  $[\text{Bi}(\text{DTPA})]^{2-}$  reported by Bulimestru *et al.* is a reasonable comparison due to ligand and metal similarities, and exemplifies how in the absence of a lone-pair, the metal ion geometry is much closer to non-distorted square antiprism.<sup>222</sup>

**Table 5.1** List of selected  $[\text{Pb}(\text{DTPAm})]^{2+}$  bond lengths.

Atom	Atom	Length (Å)
Pb	O1	2.727(2)
Pb	O2	2.613(2)
Pb	O3	2.578(2)
Pb	O4	2.568(2)
Pb	O5	2.921(2)
Pb	N2	2.696(2)
Pb	N4	2.664(2)
Pb	N6	2.836(2)

#### 5.2.4 Solution Thermodynamics of DTPAm and Complex Formation Equilibria with Pb<sup>2+</sup>

While the original report of DTPAm contained preliminary solution studies on the ligand, the pH range investigated was somewhat limited ( $1 < \text{pH} < 8$ ) and no investigation of formation constants was conducted, as chemical exchange-dependent saturation transfer (CEST) was the primary application of interest. As the goal of this work was to probe this ligand's utility as a chelator for lead-based radiopharmaceuticals, solution thermodynamics of the ligand were studied over a broad pH range (2–10) and complex formation equilibria studied with Pb<sup>2+</sup> to gain insight into the energetic drive towards complex formation of [Pb(DTPAM)]<sup>2+</sup>.

While three protonation constants from DTPAm could theoretically be measured, only two were observed during potentiometric titrations. The more basic proton [ $\text{p}K_{\text{a}} = 5.99(1)$ ] closely matches the previously reported literature value of 6.02(3).<sup>220</sup> The more acidic proton [ $\text{p}K_{\text{a}} = 2.33(1)$ ] was not reported in the original work, but was successfully calculated and refined (with HyperQuad)<sup>150</sup> with low standard deviation in this work (Table 5.2).

**Table 5.2** Protonation constants of selected ligands.

Equilibrium <sup>a</sup>	DTPAm	DTPA <sup>b</sup>	DTPA-BMA <sup>b</sup>
[HL] $\rightleftharpoons$ [L]	5.99(1) <sup>c</sup> , 6.02(3) <sup>d</sup>	10.49	9.37
[H <sub>2</sub> L] $\rightleftharpoons$ [HL]	2.33(1) <sup>c</sup>	8.60	4.38
[H <sub>3</sub> L] $\rightleftharpoons$ [H <sub>2</sub> L]	-	4.28	3.31

<sup>a</sup>Charges omitted for clarity. <sup>b</sup>Ref 223, most acidic protons omitted. <sup>c</sup>This work. <sup>d</sup>Ref 220.

An odd feature of these results is the relative acidity of the calculated values, considering the molecule contains three tertiary amines and no acid functional groups. Furthermore, only two  $\text{p}K_{\text{a}}$  values were observed despite the fact that three can reasonably be

discerned. This is analogous to results from solution studies of TCMC, where only two  $pK_a$  values could be calculated despite the theoretical observation of four ionisable protons.<sup>221</sup> The addition of a third more basic  $pK_a$  value to the DTPAm model would seemingly correct both abnormalities, and match protonation constants of other closely related (Table 5.2); however, the data suggest only two protonation events over our measured pH range. Figure 5.5a is an overlay of measured titration data (blue curve) with a model that only considers total base titrated (no  $pK_a$  values included; red curve). From this data, we can determine that four equivalents of base were required to complete the titration, further supported by the addition of four equivalents of acid prior to the titration. Thus, with the initial quantity of ligand and acid fixed, the remaining parameters that can be adjusted to fit the data are the  $pK_a$  values. Figure 5.5b is an overlay of measured titration data (blue curve) with a model that considers total base titrated and  $pK_a$  values (red curve). The blue curve comprises data that were used to calculate the two protonation constants reported above. In this curve, the first two equivalents of acid are not ligand bound, while the final two equivalents of acid are ligand deprotonation events. The red curve in Figure 5.5b is a model with three protonation constants ( $pK_a = 9.37, 5.99, 2.33$ ) as might be expected from the previous comparison with similar ligands. Clearly, the addition of this third protonation constant is in stark disagreement with the data, not only at the given  $pK_a$  point, but with the shape of the entire curve. Also of note in this incorrect model is that the second equivalent of acid is a ligand deprotonation event, which is unequivocally not the case based on the experimental data. It is because of these data that we can confidently state that within our measured pH, only two protonation constants can be measured from DTPAm. The resultant speciation diagram calculated from DTPAm protonation constants is shown in Figure 5.6.

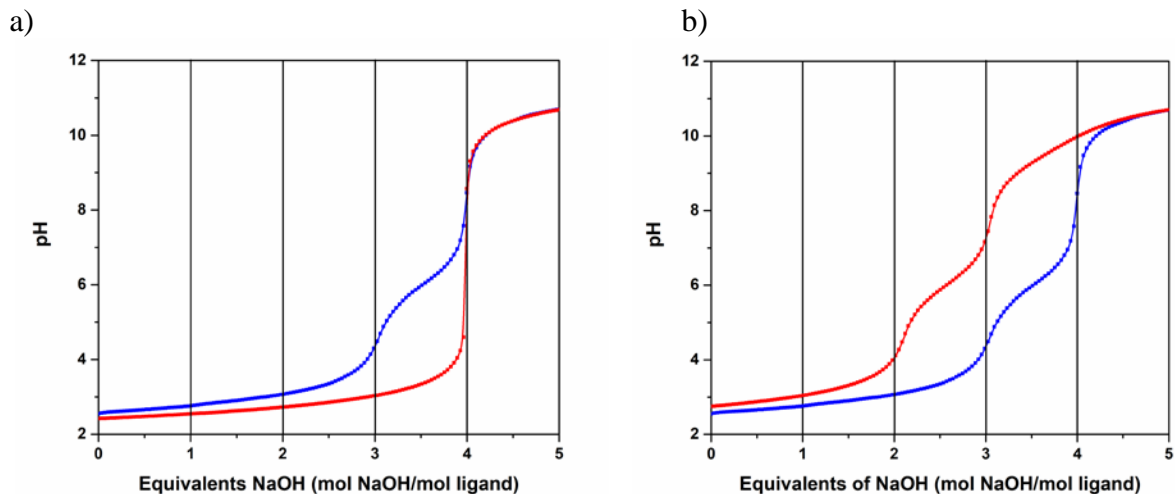


**Figure 5.5** Experimental (blue) and calculated (red) titration curves for DTPAm; a) calculated curve does not include  $pK_a$  values; b) calculated curve includes three  $pK_a$  values (9.37, 5.99, 2.33).

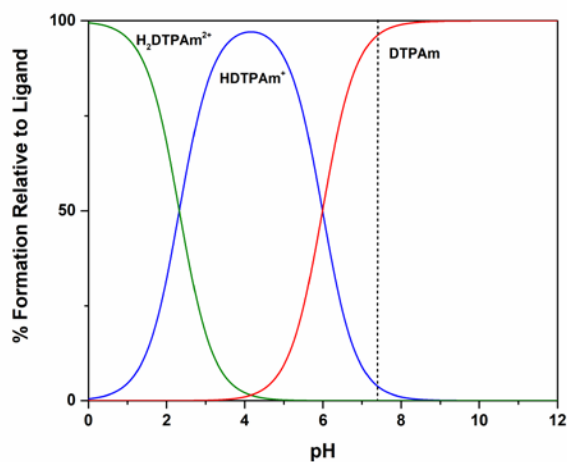


**Figure 5.6** Speciation diagram of DTPAm calculated from values shown in Table 5.2 using HySS software.<sup>153</sup>

Following determination of ligand protonation constants, titrations with  $Pb^{2+}$  were conducted to probe the thermodynamic drive towards complexation. Log  $\beta$  values were calculated for the  $[Pb(H_xDTPAm)]^{3-x}$  complex ( $x = 1, 0, -1$ ), and similar to the free ligand, three

protonation states and two  $pK_a$  values were calculated. As can be seen in the corresponding speciation diagram (Figure 5.7) the protonated complex begins to form at very acidic pH ( $< 0$ ) and reaches the deprotonated state just above pH 4. The dicationic complex is the dominant species in solution across a broad pH range (4-10); above pH 10 the complex becomes a hydroxo species while simultaneously decomplexing to a significant degree. Complete hydrolysis of  $Pb^{2+}$  occurs above pH 12, at which point none of the DTPAm complex remains intact.

**Table 5.3** Stepwise stability constants ( $\log K$ ) of DTPAm with  $Pb^{2+}$ .

Species <sup>a</sup>	$\log \beta$	$pK_a$
$M + L \rightleftharpoons ML$	8.79(2)	
$ML + H \rightleftharpoons MHL$	11.01(4)	2.22
$ML(OH) + H \rightleftharpoons ML$	-1.95(3)	10.74

<sup>a</sup>Charges omitted for clarity

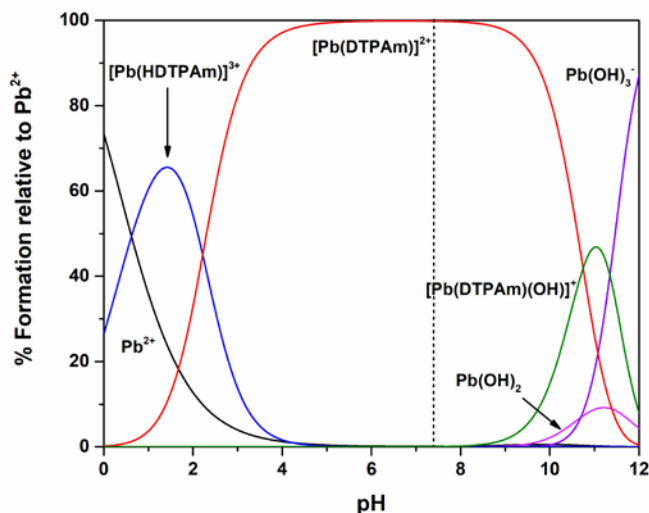


**Figure 5.7** Speciation diagram of the  $Pb^{2+}$ -DTPAm complex.

As previously discussed in Chapters 1 and 3 (Sections 1.5.2 and 3.1.2), formation constants and  $pM$  values are useful metrics to compare thermodynamic stability of metal complexes. Problems can arise; however, when comparing a ligand's suitability between metals, as the higher acidity of certain metals (e.g.,  $Fe^{3+}$ ,  $Zr^{4+}$ ) will lead to generally higher formation constants and  $pM$  values than those of less acidic metals (e.g.,  $Hg^{2+}$ ,  $Ba^{2+}$ ). While higher values technically translate to greater stability, values need to be understood as relative. For example, a ligand capable of achieving a  $pBa = 15$  and  $pFe = 25$  is a very impressive barium chelator, and a substandard iron chelator, despite what initial values might suggest. In the same way that metal ion acidity needs to be taken into account when considering solution thermodynamics, so too do ligand basicities.

Table 5.4 is a comparison of formation constants,  $pPb$  values and ligand basicities of six relevant ligands. The table is divided into three sets of two ligands; within each set is a carboxylate-containing ligand (e.g.,  $H_4DOTA$ ) and the corresponding amide derivative (e.g., TCMC). In each case, the carboxylate derivatives are much more basic and achieve higher  $\log K_{ML}$  values than the amide derivatives. Despite this differential, stability of the lead complexes of amide-bearing ligands compare well to the carboxylate derivatives. In particular, the drastic decrease in basicity of DTPAm compared to DTPA is met with only a modest decrease in  $pPb$ , suggesting favourable coordinative geometry about the metal ion. Of the amide ligands; however, TCMC is more thermodynamically stable than DTPAm. This is likely a result of the four tertiary amines of TCMC, compared to the three of DTPAm, resulting in significantly greater basicity.

**Table 5.4** Formation constants, pPb values and basicity of selected ligands.

	H <sub>4</sub> DOTA	TCMC	H <sub>4</sub> ETDA	EDTAm	H <sub>5</sub> DTPA	DTPAm
Ligand Basicity	30.6 <sup>a</sup>	14.9 <sup>b</sup>	22.5 <sup>a</sup>	4.4 <sup>c</sup>	27.7 <sup>a</sup>	8.3 <sup>d</sup>
Log $K_{ML}$	24.3 <sup>e</sup>	≥19 <sup>b</sup>	18.0 <sup>e</sup>	5.9 <sup>c</sup>	18.7 <sup>e</sup>	8.8 <sup>d</sup>
pPb <sup>f</sup>	18.4 <sup>e</sup>	≥18.4 <sup>g</sup>	15.9 <sup>e</sup>	6.9 <sup>h</sup>	15.0 <sup>e</sup>	9.7 <sup>d</sup>

<sup>a</sup>Ref 224 <sup>b</sup>Ref 221. <sup>c</sup>Ref 225. <sup>d</sup>This work. <sup>e</sup>Ref 226. <sup>f</sup>Calculated from  $-\log [Pb^{2+}]_{free}$  ( $[Pb^{2+}] = 10^{-6}$  M;  $[L] = 10^{-5}$  M;

pH 7.4) <sup>g</sup>Calculated in this work, using values from 221. <sup>h</sup>Calculated in this work, using values from Ref 225.

### 5.2.5 Radiolabeling and Serum Stability Assay with [<sup>203</sup>Pb]Pb<sup>2+</sup>

Concentration-dependent radiolabeling studies of [<sup>203</sup>Pb]Pb<sup>2+</sup> were conducted with DTPAm to determine the lowest concentration of ligand possible to quantitatively radiolabel a given amount of activity. Since the gold-standard chelator in the field for radio-lead chelation is TCMC, labeling results with DTPAm were also compared to analogous studies with TCMC. Results are summarized in Table 5.5. It should be noted that TLC was used to determine RCY for TCMC, with EDTA (pH 5, 50 mM) used as a mobile phase to separate the free and chelated radionuclide (unpublished data kindly provided by A. K. H. Robertson and W. Fu). However, due to the chemical similarities between [<sup>203</sup>Pb]Pb<sup>2+</sup> and [<sup>203</sup>Pb][Pb(DTPAm)]<sup>2+</sup>, no tested TLC system could separate the free radiometal from complex product. Thus, RCY determination for DTPAm was achieved using reverse-phase HPLC. Interestingly, even with an isocratic, aqueous (H<sub>2</sub>O 0.1% TFA) solvent gradient, the difference in retention time between [<sup>203</sup>Pb]Pb<sup>2+</sup> and [<sup>203</sup>Pb][Pb(DTPAm)]<sup>2+</sup> was 1 min (Figure 5.8).

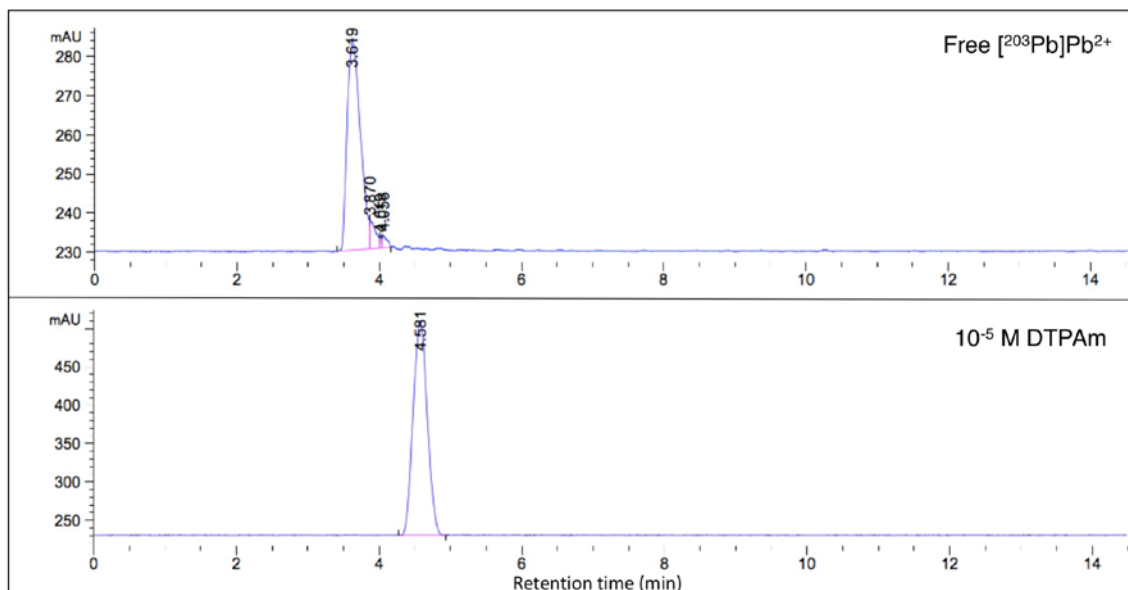


**Figure 5.8** HPLC radiochromatograms of free  $[^{203}\text{Pb}]\text{Pb}^{2+}$  (top) and  $[^{203}\text{Pb}][\text{Pb}(\text{DTPAm})]^{2+}$  (bottom).

Several trends can be noted when comparing the  $[^{203}\text{Pb}]\text{Pb}^{2+}$  radiolabeling results of DTPAm and TCMC. While all experiments at  $[\text{ligand}] = 10^{-4}$  M have high RCY and all experiments at  $[\text{ligand}] = 10^{-6}$  M have very low RCY, trials with the intermediate ligand concentration yield the most fruitful data. Under these conditions, DTPAm is a superior chelator to TCMC, notably at room temperature where TCMC only achieves 81.1% RCY while DTPAm quantitatively radiolabels. This result highlights the main advantage of using DTPAm, which is not requiring heat to achieve optimal radiolabeling— an important advantage if radioimmunotherapy is the desired application. Under elevated temperature, TCMC comes closer to quantitative radiolabeling, but is still inferior to DTPAm.

**Table 5.5** Concentration-dependent labeling of [<sup>203</sup>Pb]Pb<sup>2+</sup> with DTPAm and TCMC.<sup>a</sup>

Ligand Concentration	Radiochemical Yield		
	DTPAm (RT) <sup>b</sup>	TCMC (RT) <sup>c</sup>	TCMC (85°C) <sup>c</sup>
10 <sup>-4</sup> M	>99%	96.6%	91.8%
10 <sup>-5</sup> M	>99%	81.1%	93.4%
10 <sup>-6</sup> M	<1%	7.1%	18.4%

<sup>a</sup>Labeling conditions: pH 7 NH<sub>4</sub>OAc (1 M) buffer, 30–40 kBq [<sup>203</sup>Pb]Pb<sup>2+</sup> per reaction. Time and temperature varied.

<sup>b</sup>Determined using reverse-phase HPLC. Mobile phases a) H<sub>2</sub>O 0.1% TFA b) ACN 0.1% TFA. Gradient: 0–5 min 100% A, 5–15 min 100%A → 100% B. 15 min reaction time. <sup>c</sup>Determined using SA-TLC plates, mobile phase 50 mM EDTA (pH 5). 30 min reaction time. Data kindly provided by A. K. H. Robertson and W. Fu

Following promising radiolabeling results, investigating the kinetic inertness of the [<sup>203</sup>Pb][Pb(DTPAm)]<sup>2+</sup> complex was the next goal. Similar to what was done in Section 4.2.4, the complex was incubated with human serum at 37°C and aliquots taken over time to determine percent stability. Furthermore, size exclusion (PD10) columns were used to separate serum proteins with intact complexes to quantify stability. For this experiment to be successful, the vast majority of activity should be eluted with the serum proteins during the negative control trial (no chelator added). Unfortunately, during these experiments, no [<sup>203</sup>Pb]Pb<sup>2+</sup> was eluted with the serum proteins, suggesting Pb<sup>2+</sup> does not significantly associate with human serum proteins. While this is logical considering the low stability constant of Pb<sup>2+</sup> with human serum albumin (log *K*<sub>ML</sub> = 4.9),<sup>227</sup> it precludes comparison of [<sup>203</sup>Pb][Pb(DTPAm)]<sup>2+</sup> serum stability studies with a negative control, making the PD10 method invalid. Fortunately, another comparison could be made that provided meaningful data. Following elution of serum proteins from the PD10 columns, the remaining volume contains [<sup>203</sup>Pb]Pb<sup>2+</sup>, be it as a free metal ion in the case of the negative control, or potentially a complex in the case of the DTPAm trials. To determine the coordinative state of the radionuclide, HPLC was applied exactly as it was

during concentration-dependent radiolabeling studies. At the one hour time point, following elution from a PD10 column, the control solution was injected into an HPLC, and as expected, activity eluted at the solvent front ( $t_R \sim 3.6$ ), suggesting free  $[^{203}\text{Pb}]\text{Pb}^{2+}$ . The same procedure was followed for the DTPAm triplicates, and in each case, the activity also eluted at the solvent front ( $t_R \sim 3.6$ ). This indicates that over the course of the serum stability studies, that  $[^{203}\text{Pb}][\text{Pb}(\text{DTPAm})]^{2+}$  complexes fully dissociate over one hour.

**Table 5.6** Serum stability of  $[^{203}\text{Pb}][\text{Pb}(\text{DTPAm})]^{2+}$ .

Timepoint	Serum Stability
0 h	100%
1 h	0%

Whether this rapid dissociation is due to protein–metal interactions, protein–ligand interactions or perhaps just decomplexation as a result of dilution (which requires a truly low kinetic barrier), it is clear that this complex is not robust enough to withstand non-optimal coordination environments. It is postulated that low ligand basicity is a contributing factor to the low kinetic inertness of the metal complex. Further detail on the shortcomings of DTPAm and possible means of improvement are discussed in Chapter 7.

### 5.3 Conclusions

DTPAm was successfully synthesized and fully characterized in agreement with the previous report from Burdinski *et al.*<sup>220</sup> Cold  $\text{Pb}^{2+}$  chelation was studied to gain insight into species coordination chemistry as a prelude to eventual interest with  $^{203/212}\text{Pb}$ . Beyond

confirming the formation of a coordination complex through observation of diastereotopic splitting and a general downfield shift of peaks in  $^1\text{H}$  NMR, additional structural information was difficult to garner. X-ray quality single crystals of  $[\text{Pb}(\text{DTPAm})](\text{NO}_3)_2$  were obtained and the structure solved to reveal the expected coordination environment of the complex. The lone pair of  $\text{Pb}^{2+}$  can be seen to distort ligand coordination, resulting in distorted square-antiprism geometry about the metal ion. Solution studies were conducted to determine ligand  $\text{p}K_{\text{a}}$  values, and to permit further study into thermodynamics of  $\text{Pb}^{2+}$  complexation. Two ligand  $\text{p}K_{\text{a}}$  values were determined [5.99(1) and 2.33(1)], the more basic being in agreement with the previous report. Care was taken to ensure that only two values are possible to calculate within the pH range ( $0 < \text{pH} < 10$ ) investigated. Titrations of  $\text{Pb}^{2+}$  and DTPAm revealed three protonation states and that the complex fully dissociates above pH 12 due to lead hydrolysis. The formation constant and  $\text{pPb}$  values were compared to similar amide bearing ligands, as well as their more basic counterparts. It was noted that despite the modest stability values calculated for DTPAm, when considering ligand basicity, these values are within the realm of warranting further study with radionuclides. Concentration-dependent radiolabeling studies with  $^{203}\text{Pb}$  proved promising, as DTPAm was able to achieve a higher RCY than TCMC at  $[\text{L}] = 10^{-5}$  M. Unfortunately, serum stability studies exposed the lability of the complex, as quantitative dissociation was noted after just one hour. The high degree of exposure of the metal ion (as noted in the crystal structure), as well as the low ligand basicity are likely responsible for the observed low kinetic inertness. Improvements could be made by increasing ligand basicity (through conversion of 2-3 amides to carboxylic acids) and/or increasing inherent rigidity of the ligand backbone.

## 5.4 Experimental

### 5.4.1 Materials and Methods

For details regarding synthetic materials or instrumentation, see Section 3.4.1. For details regarding materials or instrumentation used for radiochemistry, see Section 4.4.1. Lead-203 was kindly provided by A. K. H. Robertson and W. Fu. Briefly, production via  $^{203}\text{Tl}(p,n)^{203}\text{Pb}$  was achieved by irradiation of an enriched thallium target with 12.8 MeV protons. Following dissolution of the target in nitric acid, a Pb resin (Eichrom) was used to retain the  $^{203}\text{Pb}] \text{Pb}^{2+}$  while eluting bulk target material. The desired activity was subsequently eluted and used in radiolabeling studies. Further information can be found in a forthcoming publication.

### 5.4.2 Synthesis and Characterization

*Pentaethyldiethylenetriamine-N,N,N',N'',N'''-pentaacetate (15)*. Compound **15** was prepared according to the literature with appropriate characteristic spectra.<sup>220</sup> Briefly, diethylenetriamine-*N,N,N',N'',N'''*-pentaacetic acid (10.0 g, 23.2 mmol) was dissolved in concentrated  $\text{H}_2\text{SO}_4$  (4.5 mL) and ethanol (200 mL) and refluxed for 24 h. The solvent was then evaporated, and the resulting oil diluted with dichloromethane (75 mL). The organic phase was extracted with a mixture of 1.5 M NaOH (125 mL) and brine (50 mL). Following drying of the organic phase with  $\text{MgSO}_4$ , the solution was filtered over a neutral alumina plug and dried to yield pure product (12.0 g, 90%).  $^1\text{H}$  NMR (300 MHz, 298 K,  $\text{CDCl}_3$ ):  $\delta$  4.17 (q, 10 H), 3.59 (s, 8 H), 3.49 (s, 2H), 2.83 (q, 8 H), 1.28 (t, 15 H). LR-ESI-MS: calcd for  $[\text{C}_{24}\text{H}_{43}\text{N}_3\text{O}_{10} + \text{H}]^+$ : 534.3; found  $[\text{M} + \text{H}]^+$ : 534.3.

*DTPAm* (**16**). *DTPAm* was prepared according to the literature with appropriate characteristic spectra.<sup>220</sup> Briefly, Compound **16** (2.0 g, 3.75 mmol) was dissolved in 7 N NH<sub>3</sub> in MeOH (27 mL). After stirring at room temperature for fourteen days, the white precipitate was filtered and washed with cold methanol to yield the pure product (1.02 g, 70%). <sup>1</sup>H NMR (300 MHz, 298 K, D<sub>2</sub>O):  $\delta$  3.22 (s, 8H), 3.14 (s, 2H), 2.63 (s, 8H). <sup>13</sup>C{<sup>1</sup>H} NMR (75 MHz, 298 K, D<sub>2</sub>O):  $\delta$  177.4, 177.0, 58.2, 57.5, 53.0, 52.8. HR-ESI-MS: calcd for [C<sub>14</sub>H<sub>28</sub>N<sub>8</sub>O<sub>5</sub>]: 388.2183; [M] found: 388.2184. Elemental analysis: calcd % for *DTPAm*•H<sub>2</sub>O: C 41.46, H 7.43, N 27.63; found: C 42.02, H 7.02, N 27.06.

#### 5.4.3 Metal Complexation

NMR spectra of [Pb(H<sub>x</sub>*DTPAm*)]<sup>2-x</sup> (x = 1, 0, -1) were obtained by making separate ligand and metal solutions in D<sub>2</sub>O (14 mM), and then mixing the solutions in a molar ratio of 1:1.1/L:M (V<sub>t</sub> > 300  $\mu$ L). If necessary, solution pD was altered with freshly prepared ~0.1 M NaOD (diluted from 40 wt. % NaOD) and measured with a Ross combined electrode and corrected pD = pH<sub>measured</sub> + 0.4. Solutions were allowed to stand for at least 15 minutes at room temperature before collecting NMR spectra.

#### 5.4.4 X-ray Crystallography

Single white needle-shaped crystals of [Pb(*DTPAm*)](NO<sub>3</sub>)<sub>2</sub> were obtained by recrystallisation from slow evaporation of acetone into a solution 7 mM solution of the metal complex. Suitable crystals 0.32×0.27×0.07 mm<sup>3</sup> were selected and mounted on a suitable support on a Bruker APEX II area detector diffractometer. See Section 3.4.4 for further information. Crystallographic information can be found in Table A.10.

#### 5.4.5 Solution Studies

Refer to Section 3.4.5 for details regarding data collection, model fitting and plotting of potentiometric titrations. Protonation equilibria of DTPAm were studied by potentiometric titrations of solutions containing  $[DTPAm] = 9.60 \times 10^{-4} \text{ M}$  at  $T = 298 \text{ K}$ ,  $l = 0.2 \text{ cm}$  and  $0.16 \text{ M}$  NaCl ionic strength in the pH range 2-11.5. Complex formation equilibria of DTPAm with  $Pb^{2+}$  was carried out by potentiometric titration ( $[DTPAm] = [Pb^{2+}] = 6.35 \times 10^{-4} \text{ M}$  at  $T = 298 \text{ K}$  and  $0.16 \text{ M}$  NaCl ionic strength) in the pH range 2-11.5.

#### 5.4.6 Radiolabeling and Serum Stability Studies

Concentration-dependent radiolabeling studies were conducted by diluting an aliquot ( $100 \mu\text{L}$ ) of ligand ( $[L] = 10^{-x} \text{ M}$ ;  $x = 3, 4, 5$ ) by a factor of 10 with  $NH_4OAc$  ( $1 \text{ M}$ , pH 7,  $895 \mu\text{L}$ ) and adding 30-35 kBq of  $^{203}Pb$  ( $5 \mu\text{L}$ ). Control trials contained  $995 \mu\text{L}$   $NH_4OAc$  ( $1 \text{ M}$ , pH 7) buffer and  $5 \mu\text{L}$   $^{203}Pb$  solution. The final mixture was incubated at room temperature for 15 min. Initial attempts to use TLC for RCY determination proved unsuccessful due to similar  $R_f$  of free and complexed activity. Accordingly, reverse-phase HPLC was used to separate the two species and calculate RCY. Mobile phases a)  $H_2O$  0.1% TFA b) ACN 0.1% TFA. Gradient: 0–5 min 100% A, 5–15 min 100%A  $\rightarrow$  100% B. For the human serum challenge, GE Healthcare Life Sciences PD-10 desalting columns (size exclusion for MW  $<5000 \text{ Da}$ ) and a Capintec CRC 55t dose calibrator were used, as was previously described.<sup>72</sup> Briefly, 44 kBq of  $[^{203}Pb]Pb^{2+}$  was quantitatively labeled with  $10^{-4} \text{ M}$  DTPAm (pH 7), diluted to 1 mL with PBS buffer, then mixed with an equal volume of human serum and incubated at  $37^\circ\text{C}$ . Aliquots were taken at 1 h. Aliquots were diluted to 2.5 mL with PBS, loaded onto a conditioned PD-10 column and eluted with an additional 3.5 mL of PBS. Activity of the vial containing the diluted aliquot was

measured prior to loading of the column (initial activity), as well as following loading (residual activity). Due to the failure of the negative control (no protein association of [ $^{203}\text{Pb}$ ]Pb $^{2+}$ ), following elution of activity from PD10 columns, the solutions were injected into a reverse-phase HPLC under identical conditions to those described for concentration-dependent radiolabeling.

## Chapter 6. Phosphonate- and Phosphinate-Containing Ligands for Bone

### Resorption Disorders

#### 6.1 Introduction

While prior chapters in this thesis focused primarily on chelator development for radiopharmaceuticals, the principles used to design chelators are similar outside the realm of radiochemistry. Since the majority of medicinal chelator use is with nonradioactive metal ions (e.g., MRI contrast agents, iron overload therapy), this final chapter will focus on my contributions to several projects unified by the use of lanthanum(III) complexes for the treatment of bone resorption disorders. Moreover, all studied ligands either contain a phosphonate or phosphinate group, further narrowing the theme of this chapter. H<sub>4</sub>dppa (**20**) is a dipicolinate scaffold bearing a single phosphonate arm, bearing clear resemblance to H<sub>6</sub>phospa.<sup>151</sup> XT (**21**) is a tetracarboxylate phosphinate-bearing ligand, most extensively studied in our group as the lanthanum complex [La(XT)]<sup>2-</sup>, commonly written as La(XT) (**22**).<sup>228,229</sup> Lastly, DEDA-(PO) (**17**) is a ligand similar to XT, with the difference arising from the amine-bound carboxylates being replaced by an ethylene bridge, as seen in Chart 6.1.<sup>230</sup>

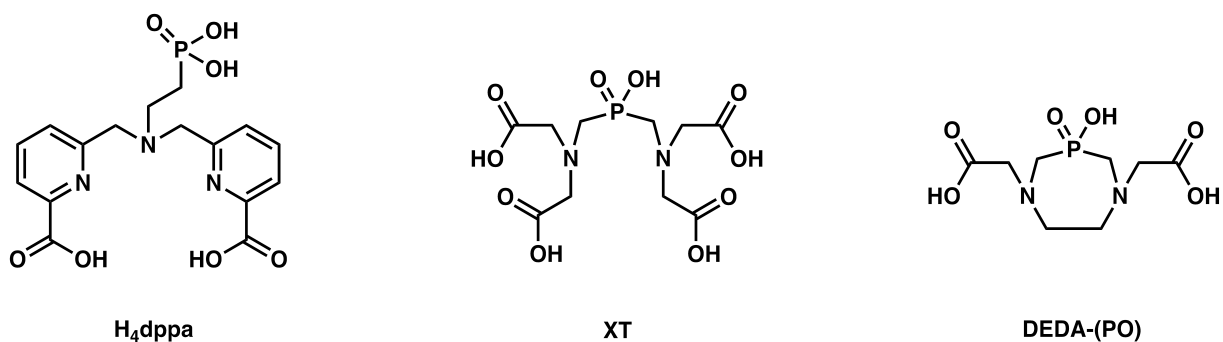


**Chart 6.1** Structures of ligands discussed throughout Chapter 6.

### 6.1.1. Dipicolinate Ligands

As described in Chapters 3 & 4, dipicolinate scaffolds are extremely versatile and are generally well-suited for trivalent metal ions, whether they are small and hard (e.g.,  $\text{Ga}^{3+}$ ) or large and soft (e.g.,  $\text{La}^{3+}$ ).<sup>81,141</sup> In 2015, our group reported a series of penta- or hexadentate chelators, all sharing the common dipicolinate (dpa) motif, with both pyridine rings bound to the same amine via methylene bridge.<sup>151</sup> Complexation studies were carried out with  $\text{Ga}^{3+}$  due to the relatively small binding pocket of the dpa series, and  $\text{La}^{3+}$  as the work was geared towards the treatment of bone resorption disorders. While a variety of intriguing experiments probed the structure and stability of these metal complexes, the primary challenge upon my introduction to this project was determination of the most acidic phosphonate  $\text{p}K_{\text{a}}$  of  $\text{H}_4\text{dppa}$ , which was presumed to be well below pH 2, on the basis of similar phosphonate-bearing species.<sup>151</sup> The work reported here regarding dpa-type ligands focuses on  $^1\text{H}$  and  $^{31}\text{P}\{^1\text{H}\}$  NMR titrations to calculate the most acidic  $\text{H}_4\text{dppa}$   $\text{p}K_{\text{a}}$ , and validate the method through comparison of other calculated  $\text{p}K_{\text{a}}$  values. Moreover, the some of the stability constants of the  $[\text{La}(\text{H}_x\text{dppa})]^{1-x}$  ( $x = 1, 0, -1$ ) complex were calculated using NMR titrations.

### 6.1.2. Previous Work with La(XT)

Bis- $\{[\text{bis}(\text{carboxymethyl})\text{amino}]\text{methyl}\}$ phosphinate (XT) was first synthesized by Maier and Smith in 1980,<sup>231</sup> and was used in our group twenty years ago to produce a number of lanthanide metal ion complexes, most notably a lanthanum(III) complex, deemed  $\text{La}(\text{XT})$ .<sup>232</sup> The primary goal of producing  $\text{La}(\text{XT})$ , and our other lead compound  $\text{La}(\text{dpp})_3$  (not described in detail here), was to study its potential to increase bioavailability of lanthanum following oral administration. This is because lanthanum has been shown to have beneficial effects on patients

suffering from osteoporosis, but lacks the natural ability to be taken up in the gut. Accordingly, a number of studies have previously been performed (primarily by Drs. Y. Mawani, J. Cawthray, C. Barta and D. Weekes) on our lead compounds to investigate solubility, lipophilicity, cellular uptake, cytotoxicity and binding to hydroxyapatite.<sup>233,234</sup> Briefly, it was found that both complexes exhibited a significant increase in uptake and permeability of Caco-2 cells, which are known to mimic human intestinal tissue.<sup>233</sup> MG-63 cells were used to evaluate the potential toxicity of our compounds to osteoblasts and it was established that La(XT) and La(dpp)<sub>3</sub> are non-toxic to these cells.<sup>234</sup> A series of experiments also confirmed that the structure of hydroxyapatite was not significantly altered by lanthanide incorporation, or many types of anionic/cationic substitution for that matter.<sup>235</sup> Finally, it was determined that both lead compounds distributed lanthanum short-term in a similar manner, with major tissue accumulation occurring in the spleen, liver and bone, with effectively no accumulation in the brain or heart. Moreover, La(XT) was noted as inherently more stable because of its hexadentate nature, versus the tris(bidentate) coordination of La(dpp)<sub>3</sub>.<sup>228</sup> Moving forward from these findings, the goal was to determine biodistribution profiles from oral dosing of rats over four weeks and (in a separate study) three months using ICP-MS.

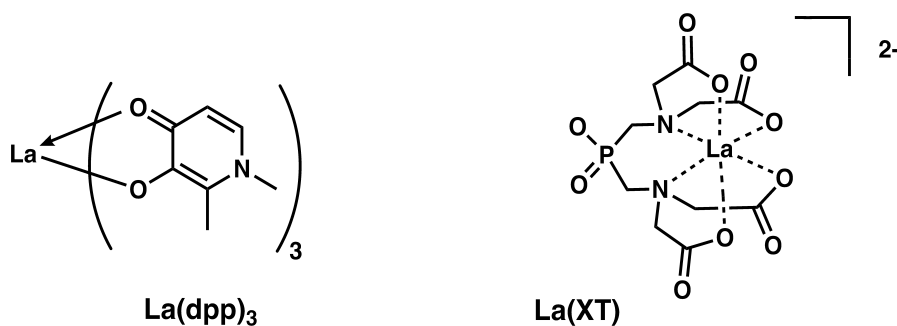
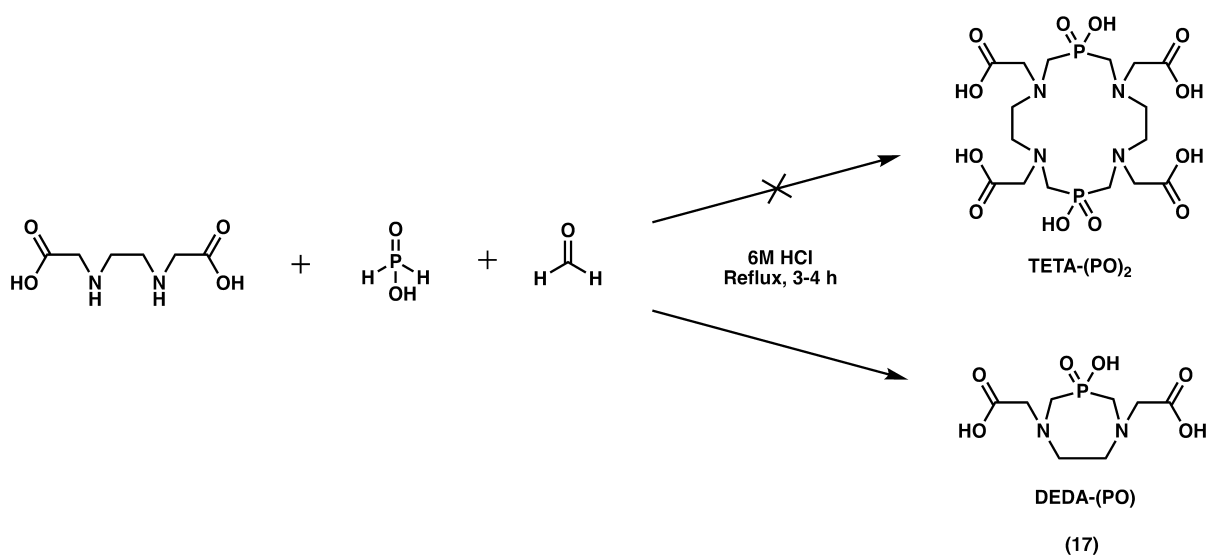


**Chart 6.2** Structures of the two lanthanum-based lead compounds discussed in this section.

### 6.1.3. Previous Work with TETA-(PO)<sub>2</sub>

In 2002, our group reported a multidentate hexaprotic macrocycle, derived from the macrocycle H<sub>4</sub>TETA (1,4,8,11-tetraazacyclotetradecane-1,4,8,11-tetraacetic acid).<sup>236</sup> The new ligand, deemed TETA-(PO)<sub>2</sub> differed in its inclusion of ring-bound phosphinate group, which served to alter the macrocycle ring size and provide additional ionisable protons for potential coordination with bound metal ions. Fifteen years following the publication of this work, in an attempt to resynthesize TETA-(PO)<sub>2</sub>, Dr. Weekes discovered unambiguous evidence (in the form of a crystal structure) that the previously described fourteen-member macrocycle was in reality a much smaller, seven-membered ring. Inspection of the synthetic scheme (Scheme 6.1) illustrates the reason for this outcome; in the absence of metal ion template, the 1:1:2 (EDDA:H<sub>3</sub>PO<sub>2</sub>:CH<sub>2</sub>O) reaction is favoured over the 2:2:4 reaction. Additionally, due to the symmetry of TETA-(PO)<sub>2</sub>, the ratio of distinct proton, phosphorous and carbon nuclei is identical between the two compounds, as well as the mass-to-charge (m/z) ratio.



**Scheme 6.1** Reported synthesis of TETA-(PO)<sub>2</sub> that resulted in the production of DEDA-(PO).<sup>230</sup>

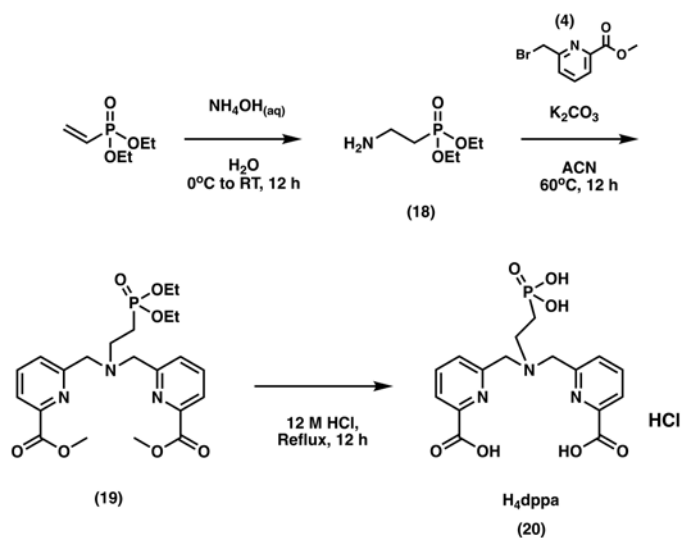
Following the discovery of this error, Dr. Weekes and Dr. Orvig corrected this error in the literature with a retraction<sup>236</sup> and publication<sup>230</sup> of a new article. In the process, Dr. Jaraquemada-Peláez was recruited to conduct solution studies on the new ligand, which required NMR studies to validate certain aspects of the metal complex speciation. Thus, the focus of this Chapter 6 subsection will focus on my efforts by <sup>1</sup>H and <sup>31</sup>P NMR spectroscopy to confirm her observations made during potentiometric titrations.

## 6.2 Results and Discussion

### 6.2.1 Synthesis of H<sub>4</sub>dppa, LaXT and DEDA-(PO)

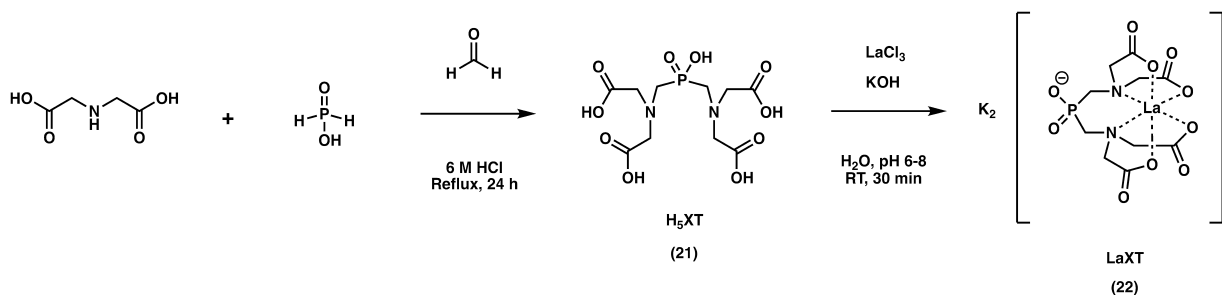
The synthesis of H<sub>4</sub>dppa is a straightforward process first involving an aza-Michael addition, followed by a simple S<sub>N</sub>2 reaction, then completed by acid-mediated ester deprotection (Scheme 6.2). The aza-Michael addition is the most challenging reaction of the three due to the possibility of a doubly- or triply-alkylated amine. The kinetics of addition are dependent on the amine nucleophilicity; thus, upon standard mixing of the reagents, aqueous ammonia is converted to a primary amine (**18**), giving the desired product the natural propensity to over-alkylate faster than it is being formed (since nucleophilicity follows the trend: NR<sub>3</sub> > NHR<sub>2</sub> > NH<sub>2</sub>R > NH<sub>3</sub>). To counter this tendency, the reaction was carried out by adding the Michael-acceptor (diethyl vinylphosphonate) dropwise to a very dilute and cold solution of aqueous NH<sub>4</sub>OH. In this way, the drastic concentration differential between ammonium and the desired product (**18**) ensured the kinetics of over-alkylation be overcome by the higher concentration (and therefore probability of addition) of the starting amine. A maximum of four hours was found to be the optimal balance between product yield and minimal side-product

formation. Due to the difficulty purifying the primary amine product (**18**) and the compatibility of the crude mixture in the following step, no purification step at this stage was necessary.



**Scheme 6.2** Synthesis of H<sub>4</sub>dppa. Reproduced from reference 151.

The S<sub>N</sub>2 reaction was carried out with crude product (**18**) and the bromopicolinate (**4**) described in Chapters 3 & 4. The reaction proceeds under expected conditions (i.e., K<sub>2</sub>CO<sub>3</sub>, ACN, 60°C) and the product is easily purified via silica column chromatography to yield the protected ligand (**19**). Lastly, the methyl esters and ethyl phosphate esters are deprotected by refluxing in *conc.* HCl, inducing acid-mediated hydrolysis. The product is purified following evaporation of aqueous HCl, dissolution in minimal water and precipitation in acetone (much like for ligands in Chapter 3), yielding H<sub>4</sub>dppa as an HCl salt.



**Scheme 6.3** Synthesis of K<sub>2</sub>[La(XT)].<sup>232</sup>

The syntheses of the ligand XT and final lanthanum(III) complex LaXT (Scheme 6.3) are straightforward and well established in the literature.<sup>232</sup> Their brief inclusion in this thesis is primarily to point out the scalability of these reactions. In order to complete three-month animal studies on ~18 Sprague-Dawley (SD) rats receiving 100 mg/kg/day, 200 g of LaXT was needed! H<sub>5</sub>XT was synthesized several times in batches of 54 g (0.4 mol) of iminodiacetic acid starting material, yielding approximately 60 g of product (0.17 mol, 42% yield). While no existing literature value exists from our group, this yield is closely related to the small-scale preparation reported in 2013.<sup>237</sup> The subsequent complexation reactions with La<sup>3+</sup> were completed on scales of 20–35 g of H<sub>5</sub>XT (60.0–95.5 mmol) and 23–41 g of La(NO<sub>3</sub>)<sub>3</sub>·6H<sub>2</sub>O (60.0–95.5 mmol).

Synthesis of DEDA-(PO) (Scheme 6.1) is a simple, one-step, Kabachnik-Fields reaction, which results in bridging of the EDDA and hypophosphite units. Vacuum filtration and washing with cold acetone yields the pure product.

### 6.2.2 <sup>1</sup>H and <sup>31</sup>P{<sup>1</sup>H} NMR Titrations of H<sub>4</sub>dppa and [La(H<sub>x</sub>dppa)]<sup>x-1</sup> (x = 1, 0, -1)

<sup>1</sup>H and <sup>31</sup>P{<sup>1</sup>H} NMR titrations were conducted to calculate the most acidic H<sub>4</sub>dppa pK<sub>a</sub>. The method was validated through comparison of NMR calculated pK<sub>a</sub> values with previously calculated values using potentiometric titrations. Forty-two in-batch solutions were made using a 10 mM dppa ligand solution and DCl/NaOD solutions depending on the desired solution pD. Spectra were taken of each sample, and chemical shifts of each <sup>1</sup>H or <sup>31</sup>P plotted vs. solution pH (pH = pD + 0.4)<sup>238</sup> using HypNMR2008.<sup>149</sup> Log K<sub>a</sub> values for dppa were calculated by simultaneously refining <sup>1</sup>H and <sup>31</sup>P experimental chemical shifts.

**Table 6.1** Comparison of the stepwise protonation constants for dppa obtained by NMR titrations and potentiometry. Reproduced from reference 151.

	Species	$^{31}\text{P}\{^1\text{H}\}$ and $^1\text{H}$ NMR $\log K_a$	Potentiometry $\log K_a$
$\log K_{a1}$	$\text{Hdppa}^{3-}$	8.54(2)	8.51(2)
$\log K_{a2}$	$\text{H}_2\text{dppa}^{2-}$	6.33(5)	6.33(3)
$\log K_{a3}$	$\text{H}_3\text{dppa}^-$	3.55(6)	3.63(4)
$\log K_{a4}$	$\text{H}_4\text{dppa}$	2.78(1)	2.76(2)
$\log K_{a5}$	$\text{H}_5\text{dppa}^+$	0.78(4)	ND

ND = not determined

As can be noted from Table 6.1, the values calculated from NMR titrations are in excellent agreement with values calculated using potentiometric titrations, and therefore are considered valid. Additionally, it was possible to calculate the previously undetermined lowest  $\text{p}K_a$  for dppa using NMR titrations ( $\log K_{a5} = 0.78$ ), which has been attributed to the more acidic phosphonate proton. Not only does this value match other literature precedents,<sup>142,239</sup> but the large shift in the  $^{31}\text{P}\{^1\text{H}\}$  NMR (Figure 6.1) signal is indicative of phosphonate deprotonation. Similar logic was used to attribute the other phosphonate  $\text{p}K_a$  to  $\log K_{a2}$  (6.33). Two consecutive protonation constants occur at the picolinic acid groups between the phosphonate protonation events ( $\log K_{a3} = 3.55$ ;  $\log K_{a4} = 2.78$ ). The highest dppa  $\text{p}K_a$  was assigned to the tertiary amine group ( $\log K_{a1} = 8.54$ ). Interestingly, the large shift in the  $^{31}\text{P}\{^1\text{H}\}$  NMR (Figure 6.1) signal at  $\text{p}K_{a5}$  is likely due to hydrogen bonding between the deprotonated phosphonate and the protonated amine, as has been noted in similar  $\text{R}_3\text{HN}^+(\text{CH}_2)_n\text{-P}(\text{O})\text{-O}^-$  ( $n = 1, 2$ ) species.<sup>240</sup>

Following determination of all dppa  $\text{p}K_a$  values, focus turned to the study of  $\text{La}^{3+}$  complexation. As was the case for protonation constants, the primary means of stability constant determination for the La-dppa system was potentiometric titration. Table 6.2 and Figure 6.2 contain calculated  $[\text{La}(\text{H}_x\text{dppa})]^{x-1}$  ( $x = 1, 0, -1$ ) stability constants and complex speciation respectively.

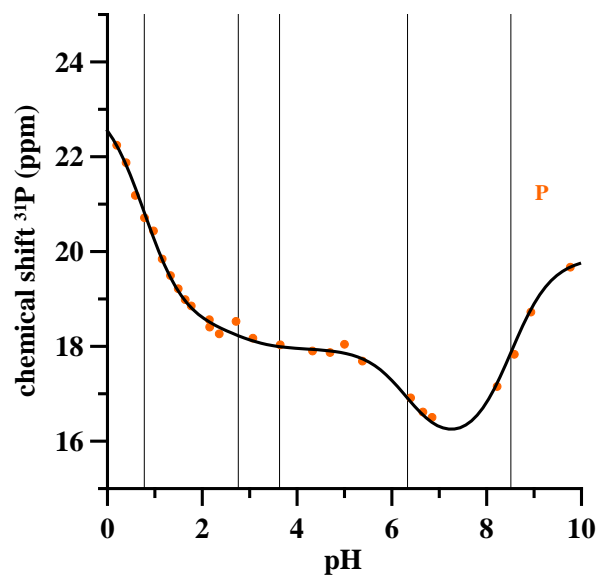


**Figure 6.1** Plot of pH dependent  $^{31}\text{P}$  chemical shift applied to calculate  $\text{p}K_a$  values of  $\text{H}_4\text{dppa}$  using the HypNMR2008 software. Reproduced from reference 151.

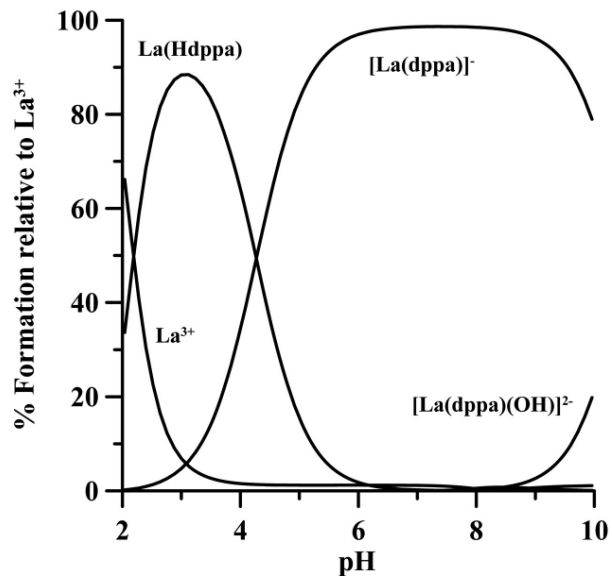


**Figure 6.2** Speciation diagram for the  $\text{La}^{3+}$ -dppa system derived from Table 6.2 (298 K,  $I = 0.16$  M NaCl).  $[\text{La}^{3+}] = 6.64 \times 10^{-4}$  M;  $[\text{dppa}] = 6.55 \times 10^{-4}$  M. Reproduced from reference 151.

**Table 6.2** Lanthanum complex formation constants for dppa.<sup>a</sup> Reproduced from reference 151.

Species	$\log \beta$	$pK_a$
MLH	18.26(6) <sup>b</sup>	
ML	13.99(6) <sup>c</sup>	4.27
MLH <sub>-1</sub>	3.43(7) <sup>c</sup>	10.56
<b>pLa<sup>d</sup></b>	13.8	

<sup>a</sup>Standard deviations are reported in parentheses after the experimentally determined values. <sup>b</sup>Determined via NMR titrations. <sup>c</sup>Determined via potentiometric titrations using HyperQuad2013.<sup>150</sup> <sup>d</sup>Calculated from  $-\log [La^{3+}]_{free}$  ( $[La^{3+}] = 10^{-6}$  M;  $[L] = 10^{-5}$  M; pH 7.4; 298 K;  $I = 0.16$  M NaCl).

While the calculated stability constants and pLa for the La-dppa system seemed reasonable, the beginning of complex formation below pH 2 precluded the use of potentiometry to verify the validity of this aspect of the model. In order to prove complex formation occurs as the model predicted, <sup>1</sup>H and <sup>31</sup>P{<sup>1</sup>H} NMR titrations were conducted.

As seen in the <sup>1</sup>H NMR spectrum of a 1:1.5 La/dppa solution (Figure 6.3), complex formation is evidenced by the emergence of two signals for the diastereotopic methylene protons ( $\delta$  4.1 and 3.8) above pH 1.8. While the methylene signal resulting from uncoordinated dppa likely decreases as the pH increases (as with dpa), the residual solvent peak (H<sub>2</sub>O) precludes analysis of these signals. Complex formation is supported by the disappearance of ethylene proton signals of the arm of the uncoordinated ligand ( $\delta$  3.75 and 2.35) above pH 1.8 and the emergence of new signals ( $\delta$  2.83 and 1.83), which are attributed to the same protons, but in the complex rather than free ligand form. These spectra confirm that the phosphonate moiety is coordinating the lanthanum ion from the onset of complex formation and likely contributes significantly to the overall stability of the complex. The speciation diagram (Figure

6.2) produced from titration data confirms this hypothesis, as initially the LaHdppa species is formed >50% at pH ~ 2.2 and the phosphonate-bound proton is lost with  $pK_a = 4.17$ . The assignment of this deprotonation event occurring at the phosphonate was confirmed by  $^{31}\text{P}\{^1\text{H}\}$  NMR titrations (Figure 6.3).

From the speciation diagram, the  $[\text{La}(\text{H}_x\text{dppa})]^{x-1}$  ( $x = 1, 0, -1$ ) complex exhibits favorable speciation across a broad pH range, as at physiological pH, only the 1:1:0 metal/ligand/proton species is present. Moreover, the  $\log \beta_{\text{ML}}$  value illustrates that the phosphonate moiety leads to a 1:1  $\text{La}^{3+}$  complex approximately 3–4 orders of magnitude higher than the unfunctionalized ligand (dpa).<sup>151</sup> The pM value also confirmed the contribution from the phosphonate group greatly enhancing stability.

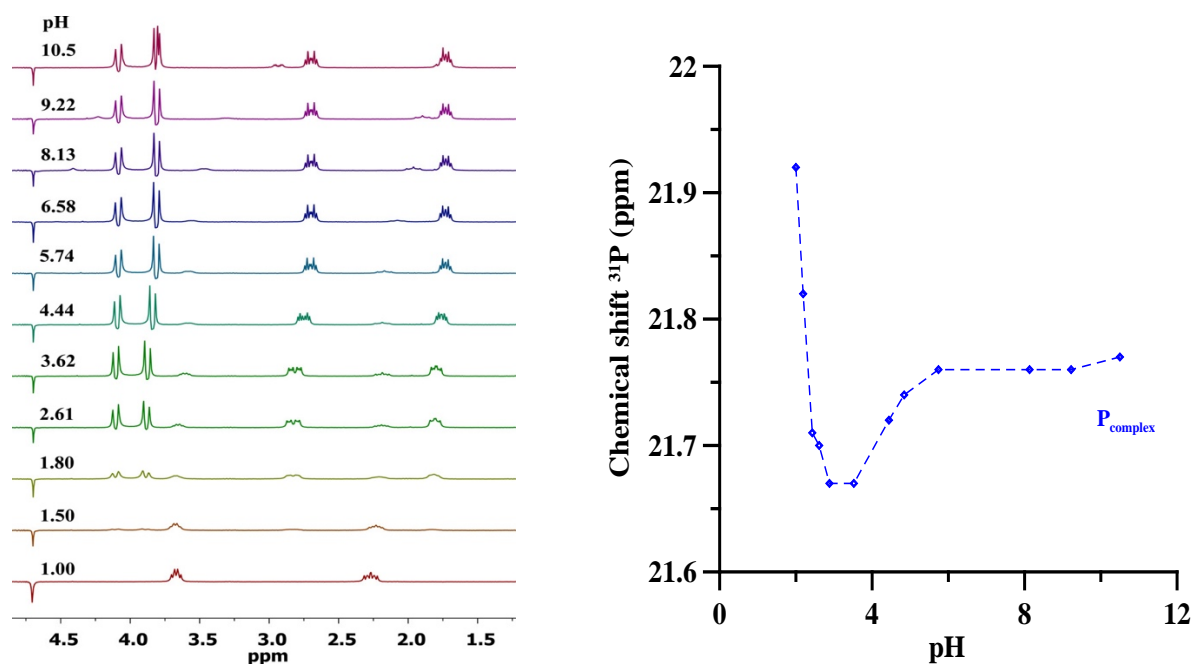


**Figure 6.3** (left) Portion of the  $^1\text{H}$  NMR spectra for the  $\text{La}^{3+}$ -dpa system at various pH levels (400 MHz, 298 K);  $[\text{La}^{3+}] = 0.010 \text{ M}$ ;  $[\text{dpa}] = 0.015 \text{ M}$ . (right)  $^{31}\text{P}\{^1\text{H}\}$  NMR chemical shift dependence on pH of the  $\text{La}^{3+}$ -dpa system ( $[\text{La}^{3+}] = 0.010 \text{ M}$ ;  $[\text{dpa}] = 0.015 \text{ M}$ ) at 298 K. Reproduced from reference 151.

### 6.2.3 ICP-MS of Animal Tissues to Determine La Content Following La(dpp)<sub>3</sub> and La(XT) Dosing

Tissue distribution in healthy SD rats (n = 4) from oral dosing (50 mg kg<sup>-1</sup> day<sup>-1</sup>) of either La(dpp)<sub>3</sub> or La(XT) for 4-weeks was obtained by ICP-MS analysis and is shown in Figure 6.4. La(XT) was administered as a 1% glycerine solution in water (v/v). Two La(dpp)<sub>3</sub> formulations were tested due the low water solubility of the complex.

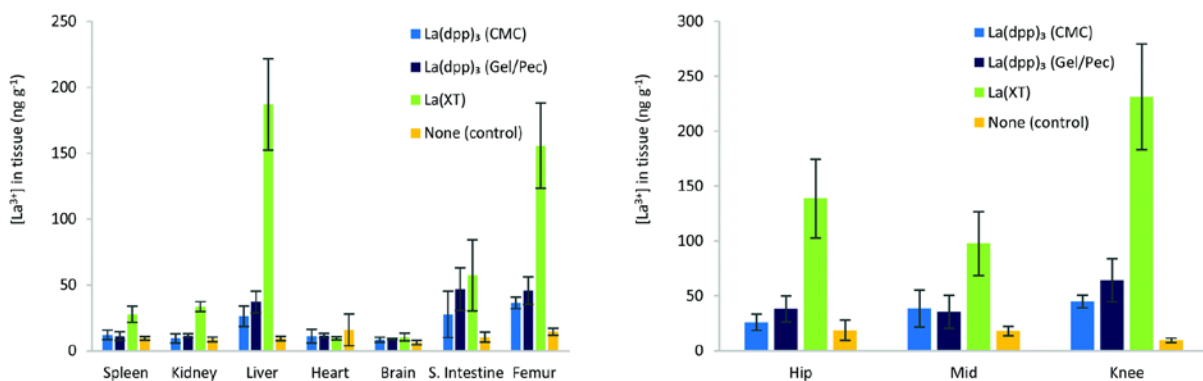


**Figure 6.4** (left) La<sup>3+</sup> tissue distribution from the oral administration of La(dpp)<sub>3</sub> (two formulations) or La(XT) (50 mg/kg/day) in healthy female SD rats (n = 4; mean std. dev.). The control group (no drug given) is also included; (right) La<sup>3+</sup> distribution within the femurs of SD rats (n = 4) in hip, mid, and knee sections from the oral administration of La(dpp)<sub>3</sub> (two formulations) or La(XT) (50 mg/kg/day) for 4-weeks, relative to a control (no drug) group. Reproduced from reference 229.

Lanthanum(III) concentrations in all tissues following oral dosing with either compound are significantly lower than those following IV administration (see Weekes *et al.* 2017).<sup>229</sup> This was an expected result considering the poor bioavailability of La<sup>3+</sup>. For La(dpp)<sub>3</sub>, detected La<sup>3+</sup> concentrations in the kidney, spleen, brain and heart are not statistically different from the control group (no drug administered). Only minor uptake in the liver, small intestine, and femur was noted with both formulations. For La(XT), greater levels of La<sup>3+</sup> in the liver,

spleen, kidney, small intestine, and femur were detected, compared to La(dpp)<sub>3</sub>. Specifically, the liver and femur exhibit 3–5 times higher La<sup>3+</sup> levels for La(XT) dosed groups (187 ± 35 ng/g, 156 ± 32 ng/g, respectively) than for either formulation of La(dpp)<sub>3</sub> (26 ± 8 ng/g, 36 ± 4 ng/g for CMC; 37 ± 8 ng/g, 46 ± 10 ng/g for Gel/Pec, respectively). While La<sup>3+</sup> is known to accumulate at greater levels in the liver relative to other organs, these levels plateau after about 6-weeks with no observable adverse effects after extended (20-weeks) oral dosing of La<sub>2</sub>(CO<sub>3</sub>)<sub>3</sub> (1000 mg/kg/day) in Wistar rats.<sup>241</sup> Our results confirm previous findings that demonstrate La<sup>3+</sup> ion redistribution occurs in the bone.<sup>229</sup> This observation is indeed noteworthy when considering Figure 6.4, which suggests that following La(XT) administration, La<sup>3+</sup> is retained within osseous tissue. These findings suggest that selective bone accumulation of La<sup>3+</sup> can be achieved.

Lanthanum distribution in the hip, mid, and knee sections of femurs following oral dosing with the lanthanum complexes was also assessed. The results (Figure 6.5) indicate superior lanthanum delivery to bone with La(XT) administration versus La(dpp)<sub>3</sub>. The distinct differences are in the knee and hip sections, which undergo a higher degree of bone turnover. This indicates that increased rate bone turnover lead to higher incorporation of the metal ion into bone mineral.

From results presented thus far (both past and present), evidence that La(XT) is the prime drug candidate of the two systems is clear. Administration of La(XT) exhibits greater La<sup>3+</sup> uptake in the bone; greater metal ion redistribution from the liver; and more favourable kinetic/thermodynamic properties than La(dpp)<sub>3</sub>.<sup>229</sup> Furthermore, neither formulation of La(dpp)<sub>3</sub> improved uptake of the drug. Overall, these results have prompted further studies to focus exclusively on La(XT).

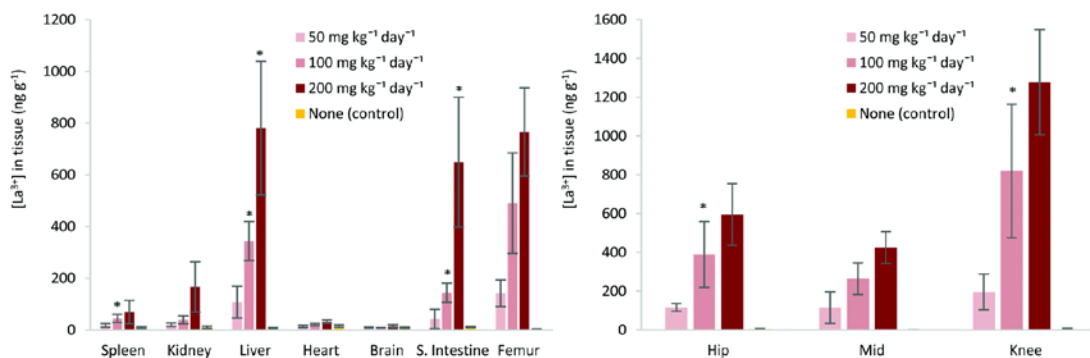


**Figure 6.5** (left) La<sup>3+</sup> distribution in tissue resulting from 3 different dosing levels of La(XT) (50, 100, and 200 mg/kg/day) and compared to a control group (no drug) in female SD rats (n = 4; mean std. dev.). \*p < 0.05 versus previous treatment group. (right) La<sup>3+</sup> distribution in femurs of SD rats (n = 4) following oral administration of La(XT) (50, 100, or 200 mg/kg/day) for 4-weeks relative to a control (no drug). \*p < 0.05 versus previous treatment group. Reproduced from reference 229.

The biodistribution profile of La<sup>3+</sup> from three different dosing levels (50, 100, and 200 mg/kg/day) of oral administration of La(XT) at 4 weeks in healthy female SD rats (n = 4) is shown in Figure 6.5. Heart and brain uptake are very low across all concentrations (<16 ng/g), indicating no tendency for drug distribution to these organs. A clear dose-dependent relationship is evident in all other tissues. As was noted in earlier studies, La<sup>3+</sup> levels are highest in the femur and liver, which are the chief organs of localization and accumulation, respectively.

A roughly proportional (statistically significant with p < 0.05) increase in La<sup>3+</sup> levels in the small intestine, liver, femur (hip and knee sections) and spleen is observed when comparing the low (50 mg/kg/day) and the mid (100 mg/kg/day) dosing levels. However, only a non-statistically significant (p > 0.05) difference in femur La<sup>3+</sup> is observed when comparing the mid and the high (200 mg/kg/day) dosing levels. When taken with a significant (p < 0.05) increase

in liver and small intestine  $\text{La}^{3+}$  increase, the conclusion was that 100 mg/kg/day is the optimal oral dosing rate for future trials.

#### **6.2.4 NMR Studies with DEDA-(PO) and $\text{La}^{3+}$**

Potentiometric titrations with DEDA-(PO) and  $\text{La}^{3+}$  (not discussed in detail here) were conducted to evaluate complex stability and metal scavenging ability of the ligand. The calculated stability constants were then used to create 1:1 and 1:2 (M:L) speciation diagrams, which are presented in Figure 6.6. These speciation diagrams reveal that when the solution contains a 1:1 metal-to-ligand ratio, the initial 1/1/0 (metal/ligand/proton) complex forms to a significant degree around pH 3 and persists until approximately pH 9, at which point the 1/2/0 complex is formed. When considering a solution with a 1:2 metal-to-ligand ratio, the 1/1/0 complex similarly forms around pH 3; however, only persists to pH 5, as the 1/2/0 complex forms at higher pH. While it is logical that a system should have a higher propensity to form a 1:2 metal-to-ligand complex when an excess of ligand is present (as opposed to when no great excess of ligand exists), the atypical stoichiometry of the system prompted further efforts to validate the model.

Accordingly, two NMR titrations were conducted to attempt to observe formation of the 1:2 (M:L) complex at different pH values and metal-to-ligand ratios. The  $^1\text{H}$  NMR spectra in Figure 6.7 illustrate complex formation with increasing pH in solutions with 1:1 and 1:2 metal-to-ligand ratios. As seen in the 1:1  $^1\text{H}$  NMR spectra, complex formation begins between pH 2.1 and 2.6. The 1:1 complex (labeled “A”) is fully formed by pH 3.9 and persists until pH 9.4, at which point formation of another species occurs. At pH 10.4 a distinct complex (labeled “B”) has formed, and according to the calculated model, this is the 1:2 complex. Indeed, the

progression of complexation with increasing pH matches closely for solutions containing a 1:1 metal-to-ligand ratio, so next a solution with 1:2 ratio was observed.

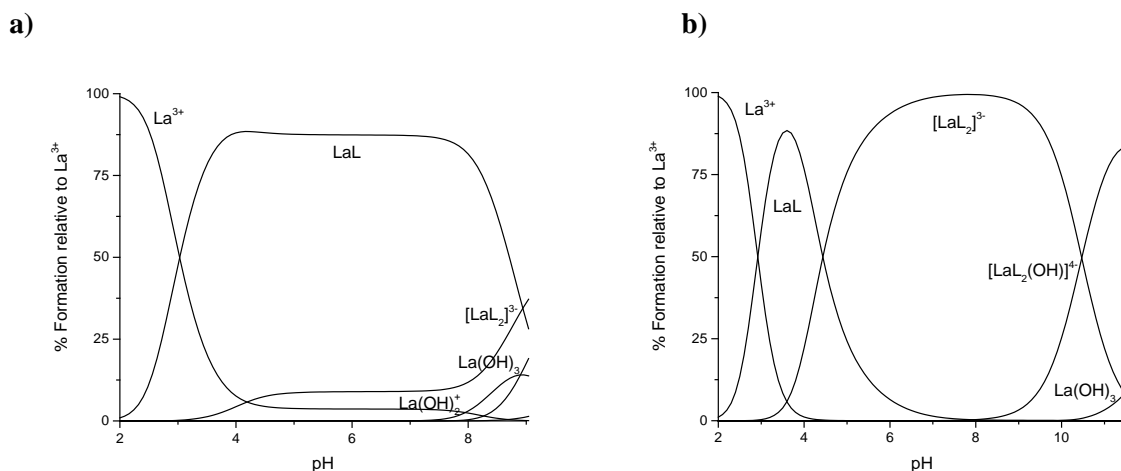


**Figure 6.6** Speciation diagram of the La<sup>3+</sup>-DEDA-(PO) system from potentiometric titrations. (25 °C,  $I = 0.16$  M). a)  $[L] = 8.11 \times 10^{-4}$  M;  $[La^{3+}] = 7.70 \times 10^{-4}$  M. b)  $[L] = 9.52 \times 10^{-4}$  M;  $[La^{3+}] = 4.67 \times 10^{-4}$  M. Reproduced from reference 230.

Similar to the 1:1 system, complex formation occurs between pH 2.2 and 3.4 in the 1:2 system. By pH 4.7; however, the <sup>1</sup>H NMR spectrum begins to closely resemble “B” from the above NMR titration, which was previously attributed to the 1:2 complex. By pH 6.3, the 1:2 complex appears to be fully formed, and remains intact until the highest measured pH (11.3). These observations provide evidence that the model calculated from potentiometric titrations is accurate. Not only does the model predict the pH at which complexes initially form, but it also correctly predicts the existence of the 1:2 complex at high pH in the 1:1 system, yet at much lower pH in the 1:2 system. The <sup>31</sup>P NMR similarly fits the model, and can be seen in Figure 6.8.

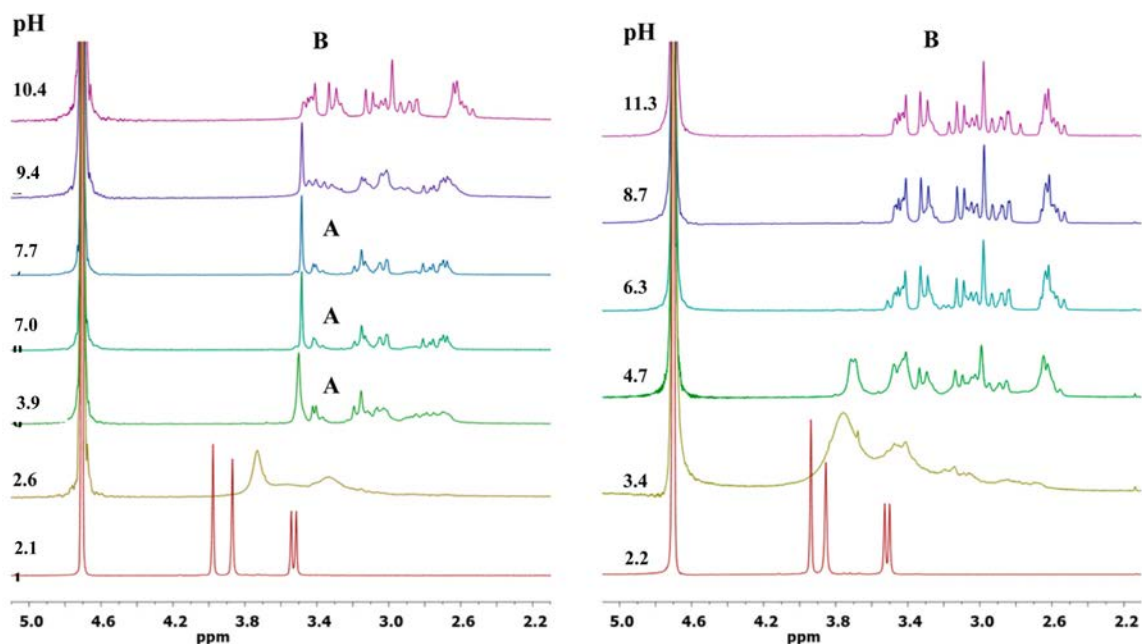


**Figure 6.7** Portions of the  $^1\text{H}$  NMR spectra of the  $\text{La}^{3+}$ -DEDA-(PO) system (400 MHz, 298 K): (left) 1:1 M/L molar ratio and  $[\text{L}] = 0.008 \text{ M}$ ; (right) 1:2 M/L molar ratio and  $[\text{L}] = 0.008 \text{ M}$ . **A**:  $\text{La}(\text{DEDA}-(\text{PO}))$ . **B**:  $\text{La}(\text{DEDA}-(\text{PO}))_2^{3-}$ . Reproduced from reference 230.

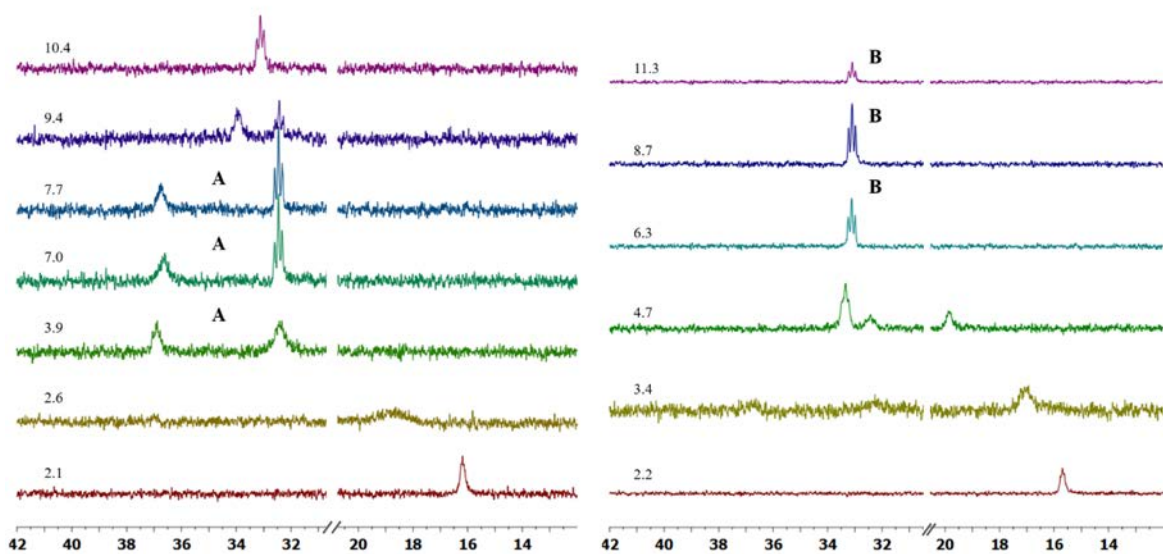


**Figure 6.8** Portions of the  $^{31}\text{P}$  NMR spectra of the  $\text{La}^{3+}$ -DEDA-(PO) system (162 MHz, 298 K): (left) 1:1 M/L molar ratio and  $[\text{L}] = 0.008 \text{ M}$ ; (right) 1:2 M/L molar ratio and  $[\text{L}] = 0.008 \text{ M}$ . **A**:  $\text{La}(\text{DEDA}-(\text{PO}))$ . **B**:  $\text{La}(\text{DEDA}-(\text{PO}))_2^{3-}$ . Reproduced from reference 230.

### 6.3 Conclusions

Three ligands were successfully synthesized and characterized, each possessing the unifying theme of containing a coordinating phosphinate or phosphonate functional group, and each intended for study with  $\text{La}^{3+}$ .

$\text{H}_4\text{dppa}$  bears a single phosphonate group that was shown to enhance thermodynamic stability when coordinating  $\text{La}^{3+}$ . Following potentiometric titrations to determine ligand  $\text{p}K_a$  values,  $^1\text{H}$  and  $^{31}\text{P}$  NMR titrations were conducted to validate values and calculate the most acidic  $\text{p}K_a$ , which was hypothesized to fall below the acceptable pH range ( $\text{pH} > 2$ ) for electrode use. The NMR titrations indeed validated values calculated by potentiometry, and were then used to calculate the most acidic protonation constant ( $\text{p}K_{a5} = 0.78$ ). NMR titrations were also used to confirm complex formation near pH 4, as predicted by the speciation diagram, and calculate the first  $\text{p}K_a$  of the  $[\text{La}(\text{H}_x\text{dppa})]^{x-1}$  ( $x = 1, 0, -1$ ) complex. This deprotonation event was determined to take place at the phosphonate group via  $^{31}\text{P}\{^1\text{H}\}$  NMR.

$\text{La}(\text{XT})$  was synthesized on a large  $> 200$  g scale to accommodate a three-month study in  $\sim 18$  SD rats, demonstrating the scalability of this straightforward synthesis. Tissues were analyzed by ICP-MS to determine lanthanum concentration based on administered drug (i.e.,  $\text{La}(\text{XT})$  or  $\text{La}(\text{dpp})_3$ ) and dose (i.e., 50, 100 or 200 mg/kg/day of  $\text{La}(\text{XT})$ ). Through comparison of lanthanum distribution between drugs, it was determined that  $\text{La}(\text{XT})$  should be the lead compound moving forward. This was due to the greater propensity of  $\text{La}(\text{XT})$  to induce  $\text{La}^{3+}$  bone uptake, which was hypothesized to be a consequence of superior complex stability, resulting in greater metal-ion uptake in the gut following oral drug administration. A subsequent variable-dose trial with  $\text{La}(\text{XT})$  determined that 100 mg/kg/day was an optimal oral dose, as 100 mg/kg/day leads to a dose-dependent increase of  $\text{La}^{3+}$  femur incorporation over

50 mg/kg/day. Moreover, an oral dose of 200 mg/kg/day does not significantly increase  $\text{La}^{3+}$  incorporation into bone, but results in higher concentrations of  $\text{La}^{3+}$  in the small intestine and liver.

The true identity of DEDA-(PO) was discovered through a crystal structure of a previously assumed TETA-(PO)<sub>2</sub> solution. New solution studies were conducted to re-evaluate the ligand stability with divalent (i.e.,  $\text{Ca}^{2+}$ ,  $\text{Zn}^{2+}$ ,  $\text{Cu}^{2+}$ ) and trivalent metal ions (i.e.,  $\text{La}^{3+}$ ,  $\text{Gd}^{3+}$ ,  $\text{Lu}^{3+}$ ). To confirm the calculated model for  $[\text{La}(\text{DEDA}-(\text{PO}))]$  was accurate, NMR titrations with 1:1 and 1:2 metal-to-ligand ratios were conducted. In <sup>1</sup>H NMR spectra, the formation of the 1:2 complex was evident at very high pH (10.4) in the 1:1 solution, while 1:2 complex formation was evident at acidic pH (4.7) and persisted until the highest measured pH (11.3). Similar results were noted for the <sup>31</sup>P NMR titration. Ultimately the NMR titrations were deemed to support the calculated model for the  $\text{La}^{3+}$ -DEDA-(PO) system.

## **6.4 Experimental**

### **6.4.1 Materials and Reagents**

For details regarding synthetic materials or instrumentation, see Section 3.4.1. Nitric acid Optima and high purity hydrogen peroxide for digestion of ICP-MS samples were purchased from Fisher Scientific. Lanthanum and rhodium standards (1000 µg/mL in 2% HCl) for standard curve calibration in ICP-MS were purchased from High Purity Standards.

All animal studies were carried out at the University of Saskatchewan and were approved by that institution's University Animal Care Committee and performed in accordance with the guidelines outlined by the Canadian Council on Animal Care. All rats had free access to food and water throughout the study period. All oral formulations/solutions were administered

through oral gavage. Rat body weights were measured regularly and the oral dose adjusted weekly. Further information regarding animal procedures can be found in references 231 and 244.

#### 6.4.2 Instruments

For details regarding potentiometric titrations, see Section 3.4.5. For details regarding synthetic instrumentation, see Section 3.4.1. ICP-MS was run using an Agilent 7700x quadrupole machine equipped with an auto-sampler (PCIGR, Earth and Ocean Sciences, UBC). All glassware, vials, Eppendorf tubes, pipette tips etc. were prewashed by soaking overnight in HNO<sub>3</sub> (2%) and thoroughly rinsed with MQ water.

#### 6.4.3 Synthesis and Characterization

*DEDA-(PO)-HCl* (**17**) was prepared according to the literature preparation with appropriate characteristic spectra.<sup>230</sup> Briefly, *N,N'*-ethylenediaminediacetic acid (3.5 g, 20 mmol) and hypophosphorous acid (50% w/w, 2.2 mL, 20 mmol) were dissolved in 6 M HCl (20 mL) and heated to reflux. Formaldehyde (37% w/w, 6.4 mL, 80 mmol) was added dropwise over 1 h. After 4 h, a white precipitate evolved from the reaction mixture. The solid was filtered using a sintered glass funnel, washed several times with 2–3 mL portions of cold methanol, followed by cold acetone. *In vacuo* drying overnight yielded H<sub>3</sub>DEDA-(PO)-HCl as a fluffy white solid (2.84 g, 9.4 mmol, 47% yield).

*Dimethyl 6,6'-(((2-(diethoxyphosphoryl)ethyl)azanediyl)bis(methylene))dipicolinate* (**19**): Diethyl vinylphosphonate (1.00 g, 6.1 mmol) was dissolved in distilled water (25 mL) and

added to a dropping funnel. The phosphonate solution was then added dropwise to a 100 mL round bottom flask containing 28% aqueous  $\text{NH}_4\text{OH}$  (25 mL) at  $0^\circ\text{C}$ . The reaction mixture was allowed to stir for 12 hours. Solvent was evaporated to yield crude product (**18**), which was added to a suspension of  $\text{K}_2\text{CO}_3$  (1.6 g, 11.6 mmol) and ACN (100mL) in a 250 mL round bottom flask. (**4**) (2.4 g, 10.5 mmol) was added to reaction mixture and stirred at  $60^\circ\text{C}$  for 48 hr. The solution was quenched with distilled water, extracted with dichloromethane (3 x 100 mL), the organic phases combined and dried over anhydrous  $\text{MgSO}_4$ . After filtration, the crude product was adsorbed to silica and purified by silica chromatography (CombiFlash Rf automated column system 40 g HP silica; solid (pause) preparation; A: DCM, B: MeOH, 100% A to 20% B, to yield the pure product (yield over 2 steps 54%, 1.57 g).  $^1\text{H}$  NMR (400 MHz,  $\text{D}_2\text{O}$ ,  $25^\circ\text{C}$ ): 8.02 (m, 4H), 7.84 (m, 2H), 4.01 (m, 4H), 2.95 (m, 2H), 2.05 (m, 2H), 1.25 (t, 6H). LR-ESI-MS: calcd for  $[\text{C}_{22}\text{H}_{30}\text{N}_3\text{O}_7\text{P} + \text{Na}]^+ = 502.2$ ; found  $[\text{M} + \text{Na}]^+ = 502.1$ .

*H<sub>4</sub>dppa* (**20**): Compound **19** (1.57 g, 3.3 mmol) was dissolved in *conc.* HCl (20 mL) in a 50 mL round bottom flask and was stirred and heated to reflux for 24h. Evaporation of solvent yielded pure product as HCl salt (85%, 1.10 g).  $^1\text{H}$  NMR (400 MHz,  $\text{D}_2\text{O}$ ,  $25^\circ\text{C}$ ):  $\delta$  7.99 (d, 2H), 7.94 (t, 2H), 7.59 (d, 2H), 4.78 (s, 4H), 3.97 (m, 2H), 2.35 (m, 2H).  $^{31}\text{C}\{^1\text{H}\}$  NMR (400 MHz,  $\text{D}_2\text{O}$ ,  $25^\circ\text{C}$ ):  $\delta$  167.1; 149.7; 146.5; 139.7; 128.1; 125.2; 58.3; 52.7; 23.5, 22.2 (d).  $^{31}\text{P}\{^1\text{H}\}$  NMR (400 MHz,  $\text{D}_2\text{O}$ ,  $25^\circ\text{C}$ ):  $\delta$  16.6. LR-ESI-MS: calcd for  $[\text{C}_{16}\text{H}_{18}\text{N}_3\text{O}_7\text{P} + \text{H}]^+ = 396.1$ ; found  $[\text{M}+\text{H}]^+ = 396$ . Elemental analysis: calcd % for  $\text{C}_{16}\text{H}_{18}\text{N}_3\text{O}_7\text{P}\cdot\text{HCl}$ : C 44.51, H 4.44, N 9.73; found: C 44.28, H 4.64, N 9.40.

$H_5XT$  (**21**) was prepared in large scale (54 g iminodiacetic acid used) according to the literature preparation with appropriate characteristic spectra.<sup>232</sup>

$K_2[La(XT)] \cdot xH_2O$  (**22**) was prepared in several batches using  $H_5XT$  (34.0 g, 95.5 mmol) and  $La(NO_3)_3 \cdot 6H_2O$  (41.4 g, 95.5 mmol) per batch, according to the literature preparation with appropriate characteristic spectra.<sup>232</sup>

#### **6.4.4 $^1H$ and $^{31}P\{^1H\}$ NMR Titrations of $H_4dppa$ , DEDA-(PO) and Their $La^{3+}$**

##### **Complexes**

Protonation constants for the  $dppa$  ligand were determined by  $^1H$  and  $^{31}P\{^1H\}$  NMR titrations using the HypNMR2008 program.<sup>149</sup> Solutions of the ligand (10 mM) in  $D_2O$  were prepared at different pD levels, adjusting with dilute NaOD or DCl. The pD values were measured via an electrode (Mettler Toledo) and corrected to pH for the deuterium isotopic effect by the relation  $pD = pH + 0.4$ .<sup>238</sup> The  $pK_a$  was calculated using the HypNMR2008 program.<sup>149</sup> Complex formation constants of  $[La(dppa)]$  were determined by  $^1H$  NMR titrations. Spectra of 15 mM lanthanum-ligand solutions were collected in approximately a 1:1.5 ratio in  $D_2O$  at 298 K at various pD levels, and the concentrations of  $La^{3+}$  ions were achieved by using a stock deuterated aqueous acidic solution of  $LaCl_3$ .

The NMR spectra of DEDA-(PO) and the  $La^{3+}$ -L solutions ( $[DEDA-(PO)] = 0.008$  M and La:L ratios 1:1 and 1:2) were recorded at variable pH values. The pD was adjusted by adding DCl or NaOD, and the pH was calculated as  $pD = pH + 0.4$ .<sup>238</sup>

## Chapter 7. Ongoing Work and Future Studies

### 7.1 Ongoing Work

A number of improvements to the established  $^{120\text{m}}\text{Sb}$  separation and radiolabeling procedures are ongoing. While the liquid-liquid extraction method is relatively robust, as discussed in Section 2.2.3, a chromatography-based method would be preferable to reduce waste and activity handling times. While the reported cation-exchange chromatography method was successful, elution with NaOH (1 M) is non-optimal. Moreover, the scales performed thus far have been on the order of 1 mL (of a 12 mL) target solution. Work is currently being undertaken to improve both of these shortcomings. While elution of  $^{120\text{m}}\text{Sb}$  as antimonate with NaOH (1 M) is effective in terms of radiochemical separation, further use of the hydrolyzed species has not yet been successful. Since formation of an anionic complex is a necessity for elution, current efforts are underway to induce elution via chelation. While common chelators, such as EDTA, may be satisfactory, the ideal scenario is one in which the chelator is also a reducing agent, as it would remove a step in subsequent radiolabeling steps. While preliminary experiments have been conducted, significant solid-phase retention of  $^{120\text{m}}\text{Sb}$  remains a challenge.

Radiolabeling results reported in Section 2.2.4 could also be improved. I believe that the major obstacle to achieving rapid quantitative radiolabeling with the existing method is the 0.1 M citrate present in  $^{120\text{m}}\text{Sb}$  solutions used for labeling. Having mercaptoacetate in solution instead of citrate would drastically accelerate the radiolabeling process by removing interfering chelating agents, as well as eliminate the need for the multi-hour reduction step. This is being investigated as described above, as well as by using mercaptoacetate in back-extractions,



## 7.2 Future Studies

The contents of Chapter 2 are largely radiochemistry-based, and could benefit from cold chemistry to support explanations of phenomenon. The most pressing matter is characterization of the antimony(III)-trithiol complex, ideally by XRD, but also by NMR spectroscopy. It is postulated that the complex closely resembles that of the arsenic(III)-trithiol complex,<sup>123</sup> with trigonal pyramidal geometry capped by a lone electron pair; however, structural evidence is mandatory to make this assertion. Radiolabeling studies in Chapter 2 are limited to the trithiol ligand that was found to successfully radiolabel. While conditions of this system should be tuned to achieve optimal RCY and molar activity, other ligands may also yield fruitful results. Indeed, no successful [<sup>120m</sup>Sb]Sb<sup>5+</sup> radiolabeling was observed with a variety of hard ligands; however, few chelators were tested for radiolabeling with [<sup>120m</sup>Sb]Sb<sup>3+</sup>. In comparison, the trivalent species is far softer than the pentavalent, but overall still relatively high charge. A broader range of ligands should be tested to determine the ideal antimony chelator, since no such work has ever been conducted in the literature.

Chapters 3 and 4 focus on chelators bearing both phosphonate and picolinic acid moieties. While all four chelators are capable of thermodynamically stable complexes, it appears that the combination of phosphonate coordination on acyclic ligands introduces too much lability into a system that requires robustness. To combat the inherent kinetic inertness of these ligands, introduction of a cyclohexyl backbone would likely induce some degree of inertness (Chart 7.2). Perhaps more promising would be incorporation of both functional groups on a macrocycle to ensure kinetic inertness, while maintaining relatively fast radiolabeling conditions thanks to the rapid binding kinetics of phosphonates. Another interesting alteration would be combining phosphonates with oxinates. The “ox” family has

recently become an exciting topic of interest in our group due to the inherent rigidity and increased basicity of 8-hydroxyquinoline over picolinic acid.<sup>245</sup> Unfortunately, these aromatic systems suffer from poor solubility in aqueous solution. The incorporation of replacement of carboxylic acids with phosphonate groups in H<sub>4</sub>octox<sup>199</sup> (for example) would greatly increase ligand and resultant metal complex solubilities because of the additional anionic charge, which would be left free for solvation during complexation. A foreseeable challenge of this endeavor would be synthesis, as performing a Mannich reaction on H<sub>2</sub>hox<sup>245</sup> is challenging due to poor HCl solubility. Synthesis of ethylenediamine di(methylene phosphonic acid) *via* protection/deprotection would likely first be necessary prior to addition of 8-hydroxyquinoline groups.

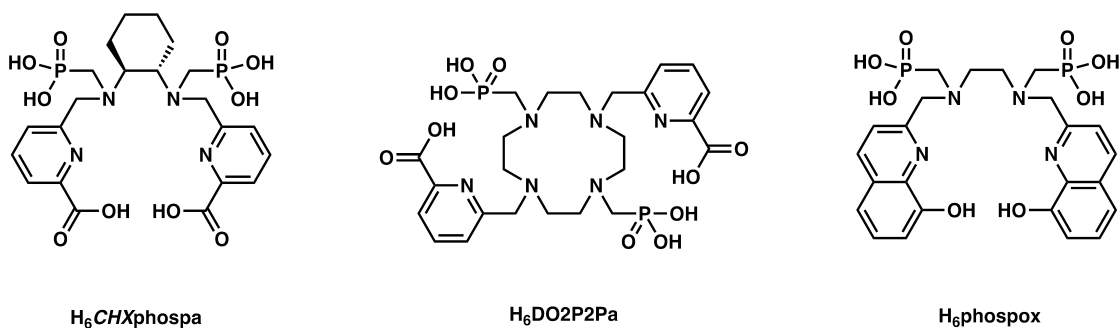


**Chart 7.2** Phosphonate-bearing ligand of potential future interest.

Of the ligands explored in Chapters 3 and 4, radiolabeling was only studied with [<sup>111</sup>In]In<sup>3+</sup> and H<sub>6</sub>dappa. Although it has not yet been studied in recent literature to any significant degree, the hard nature of Sc<sup>3+</sup> may be a natural pair with phosphonates. Radiolabeling studies with H<sub>6</sub>phospa, H<sub>6</sub>dipedpa, H<sub>6</sub>eppy and H<sub>6</sub>dappa would yield interesting radiolabeling results with [<sup>44/47</sup>Sc]Sc<sup>3+</sup>. Interestingly, it has also been demonstrated that phosphonate-bearing macrocycles exhibit favourable radiolabeling with [<sup>213</sup>Bi]Bi<sup>3+</sup>.<sup>246</sup> Given

this unlikely comparison, there is also a compelling case for study of the aforementioned ligands with  $[^{213}\text{Bi}]\text{Bi}^{3+}$  to ascertain any previously improbable compatibility.

The major significance of the research outlined in this thesis is threefold. The separation radiochemistry outlined in Chapter 2 is a stepping stone for future radionuclide production, purification and radiolabeling, and will help further the eventual study of  $^{119}\text{Sb}$  *in vivo*, so the efficacy of top candidate Auger electron emitters can be realized. Several chelators designed for radiopharmaceuticals are outlined in Chapters 3–5. These studies contribute knowledge to the rational design of bifunctional chelators and outline how to both emulate desirable traits and avoid characteristics that lead to non-ideal behaviour. In both cases, this work has added to the wealth of knowledge geared towards making new and better bifunctional chelators. Lastly, the crux of this research revolves around coordination chemistry. The work outlined in Chapters 3–6 explore chelators with a wide variety of properties (e.g., denticities, functional groups, geometries) and their coordination with an array of metal ions. From structural information to thermodynamics of their complexes, this research broadly contributes to a core interest of inorganic chemistry, the fundamental relationship between ligand structure and metal ion coordination.

## References

- (1) Boros, E.; Marquez, B. V.; Ikotun, O. F.; Lapi, S. E.; Ferreira, C. L. Coordination Chemistry and Ligand Design in the Development of Metal Based Radiopharmaceuticals. In *Ligand Design in Medicinal Inorganic Chemistry*; Storr, T., Ed.; John Wiley & Sons: Chichester, UK, 2014; pp 47–79.
- (2) Kostelnik, T. I.; Orvig, C. Radioactive Main Group and Rare Earth Metals for Imaging and Therapy. *Chem. Rev.* **2019**, *119*, 902–956.
- (3) Qaim, S. M. Nuclear Data for Production and Medical Application of Radionuclides: Present Status and Future Needs. *Nucl. Med. Biol.* **2017**, *44*, 31–49.
- (4) Price, E. W.; Orvig, C. Matching Chelators to Radiometals for Radiopharmaceuticals. *Chem. Soc. Rev.* **2014**, *43*, 260–290.
- (5) Blower, P. J. A Nuclear Chocolate Box: The Periodic Table of Nuclear Medicine. *Dalton Trans.* **2015**, *44*, 4819–4844.
- (6) Braad, P. E. N.; Hansen, S. B.; Thisgaard, H.; Høilund-Carlsen, P. F. PET Imaging with the Non-Pure Positron Emitters:  $^{55}\text{Co}$ ,  $^{86}\text{Y}$  and  $^{124}\text{I}$ . *Phys. Med. Biol.* **2015**, *60*, 3479–3497.
- (7) Bernhardt, P.; Forssell-Aronsson, E.; Jacobsson, L.; Skarnemark, G. Low-Energy Electron Emitters for Targeted Radiotherapy of Small Tumours. *Acta Oncol.* **2001**, *40*, 602–608.
- (8) Müller, C.; Zhernosekov, K.; Köster, U.; Johnston, K.; Dorrer, H.; Hohn, A.; Van der Walt, N. T.; Türler, A.; Schibli, R. A Unique Matched Quadruplet of Terbium Radioisotopes for PET and SPECT and for  $\alpha$ - and  $\beta$ -Radionuclide Therapy: An in Vivo Proof-of-Concept Study with a New Receptor-Targeted Folate Derivative. *J. Nucl. Med.* **2012**, *53*, 1951–1959.
- (9) Amoroso, A. J.; Fallis, I. A.; Pope, S. J. A. Chelating Agents for Radiolanthanides: Applications to Imaging and Therapy. *Coord. Chem. Rev.* **2017**, *340*, 198–219.

- (10) Mulford, D. A.; Scheinberg, D. A.; Jurcic, J. G. The Promise of Targeted Alpha-Particle Therapy. *J. Nucl. Med.* **2005**, *46*, 199S-204S.
- (11) Cutler, C. S.; Hennkens, H. M.; Sisay, N.; Huclier-Markai, S.; Jurisson, S. S. Radiometals for Combined Imaging and Therapy. *Chem. Rev.* **2013**, *113*, 858–883.
- (12) Aluicio-Sarduy, E.; Ellison, P. A.; Barnhart, T. E.; Cai, W.; Nickles, R. J.; Engle, J. W. PET Radiometals for Antibody Labeling. *J. Label. Compd. Radiopharm.* **2018**, 1–16.
- (13) McDevitt, M. R.; Sgouros, G.; Sofou, S. Targeted and Nontargeted  $\alpha$ -Particle Therapies. *Annu. Rev. Biomed. Eng.* **2018**, *20*, 73–93.
- (14) Valdovinos, H. F. Production, Labeling and in Vivo Studies with the Theranostic Positron-Emitting Radiometals  $^{44}\text{Sc}$ ,  $^{55/58\text{m}/58\text{g}}\text{Co}$ ,  $^{61/64}\text{Cu}$ ,  $^{86}\text{Y}$  and  $^{69}\text{Ge}$  Ph.D. Thesis, University of Wisconsin - Madison, 2017.
- (15) Ramogida, C. F.; Orvig, C. Tumour Targeting with Radiometals for Diagnosis and Therapy. *Chem. Commun.* **2013**, *49*, 4720–4739.
- (16) Livechart - Table of Nuclides - Nuclear Structure and Decay Data <https://www-nds.iaea.org/relnsd/vcharthtml/VChartHTML.html> (accessed Sep 25, 2020).
- (17) Chu, S. Y. F.; Ekstrom, L. P.; Firestone, R. B. WWW table of radioactive isotopes, database version 2/28/1999 <http://nucleardata.nuclear.lu.se/toi/> (accessed Apr 1, 2018).
- (18) O'Donoghue, J. A.; Wheldon, T. E. Targeted Radiotherapy Using Auger Electron Emitters. *Phys. Med. Biol.* **1996**, *41*, 1973–1992.
- (19) Howell, R. W. Radiation Spectra for Auger-Electron Emitting Radionuclides: Report No. 2 of AAPM Nuclear Medicine Task Group No. 6. *Med. Phys.* **1992**, *19*, 1371–1383.
- (20) Haller, S.; Pellegrini, G.; Vermeulen, C.; Van der Meulen, N. P.; Köster, U.; Bernhardt, P.;

- Schibli, R.; Müller, C. Contribution of Auger/Conversion Electrons to Renal Side Effects after Radionuclide Therapy: Preclinical Comparison of  $^{161}\text{Tb}$ -Folate and  $^{177}\text{Lu}$ -Folate. *EJNMMI Res.* **2016**, *6*, 1–11.
- (21) Seidl, C. Radioimmunotherapy with  $\alpha$ -Particle-Emitting Radionuclides. *Immunotherapy* **2014**, *6*, 431–458.
- (22) Orsini, F.; Lorenzoni, A.; Puta, E.; Mariani, G. Positron-Emitting Radiopharmaceuticals for Diagnostic Applications. In *Nuclear Oncology*; Springer: Cham, 2017; pp 85–98.
- (23) Cherry, S. R.; Dahlbom, M. PET: Physics, Instrumentation, and Scanners. In *PET*; Phelps, M. E., Ed.; Springer: New York, 2004.
- (24) Alauddin, M. M. Positron Emission Tomography (PET) Imaging with  $^{18}\text{F}$ -Based Radiotracers. *Am. J. Nucl. Med. Mol. Imaging* **2012**, *2*, 55–76.
- (25) Sorenson, J. A.; Phelps, M. E. The Anger Camera: Performance Characteristics. In *Physics in Nuclear Medicine*; Grune & Stratton: Orlando, 1987; pp 331–345.
- (26) Rahmim, A.; Zaidi, H. PET versus SPECT: Strengths, Limitations and Challenges. *Nucl. Med. Commun.* **2008**, *29*, 193–207.
- (27) Van der Wall, E. E. Cost Analysis Favours SPECT over PET and CTA for Evaluation of Coronary Artery Disease: The SPARC Study. *Neth. Hear. J.* **2014**, *22*, 257–258.
- (28) Fornell, D. SPECT Scanner vs. PET, Which is Best? <https://www.dicardiology.com/article/spect-scanner-vs-pet-which-best> (accessed Apr 1, 2018).
- (29) Nonnekens, J.; Chatalic, K. L.; Molkenboer-Kuenen, J. D.; Beerens, C. E.; Bruchertseifer, F.; Morgenstern, A.; Veldhoven-Zweistra, J.; Schottelius, M.; Wester, H.-J.; van Gent, D. C.; et al.  $^{213}\text{Bi}$ -Labeled Prostate-Specific Membrane Antigen-Targeting Agents Induce DNA Double-Strand Breaks in Prostate Cancer Xenografts. *Cancer Biother. Radiopharm.* **2017**, *32*, 67–73.

- (30) Saha, G. B. *Fundamentals of Nuclear Pharmacy*; Springer-Verlag: New York, 2018; pp 58–66.
- (31) Kassis, A. I. Therapeutic Radionuclides: Biophysical and Radiobiologic Principles. *Semin. Nucl. Med.* **2008**, *38*, 358–366.
- (32) Behr, T. M.; Béhé, M.; Stabin, M. G.; Wehrmann, E.; Apostolidis, C.; Molinet, R.; Strutz, F.; Fayyazi, A.; Wieland, E.; Gratz, S.; et al. High-Linear Energy Transfer (LET)  $\alpha$  versus Low-LET  $\beta$  Emitters in Radioimmunotherapy of Solid Tumors: Therapeutic Efficacy and Dose-Limiting Toxicity of  $^{213}\text{Bi}$ - versus  $^{90}\text{Y}$ -Labeled CO17-1A Fab' Fragments in a Human Colonic Cancer Model. *Cancer Res.* **1999**, *59*, 2635–2643.
- (33) Zalutsky, M. R.; Pozzi, O. R. Radioimmunotherapy with  $\alpha$ -Particle Emitting Radionuclides. *Q. J. Nucl. Med. Mol. Imaging* **2004**, *48*, 289–296.
- (34) Romer, A.; Seiler, D.; Marincek, N.; Brunner, P.; Koller, M. T.; Ng, Q. K. T.; Maecke, H. R.; Müller-Brand, J.; Rochlitz, C.; Briel, M.; et al. Somatostatin-Based Radiopeptide Therapy with [ $^{177}\text{Lu}$ -DOTA]-TOC versus [ $^{90}\text{Y}$ -DOTA]-TOC in Neuroendocrine Tumours. *Eur. J. Nucl. Med. Mol. Imaging* **2014**, *41*, 214–222.
- (35) Kassis, A. I. Therapeutic Ratios or Targeted Radionuclides. In *Targeted Radionuclide Therapy*; Lippincott Williams & Wilkins, 2012; pp 249–257.
- (36) Srivastava, S. C. Paving the Way to Personalized Medicine: Production of Some Promising Theragnostic Radionuclides at Brookhaven National Laboratory. *Semin. Nucl. Med.* **2012**, *42*, 151–163.
- (37) Synowiecki, M. A.; Perk, L. R.; Nijssen, J. F. W. Production of Novel Diagnostic Radionuclides in Small Medical Cyclotrons. *EJNMMI Radiopharm. Chem.* **2018**, *3*, 1–25.
- (38) Qaim, S. M. The Present and Future of Medical Radionuclide Production. *Radiochim. Acta* **2012**, *100*, 635–651.

- (39) Starovoitova, V. N.; Tchelidze, L.; Wells, D. P. Production of Medical Radioisotopes with Linear Accelerators. *Appl. Radiat. Isot.* **2014**, *85*, 39–44.
- (40) Carzaniga, T. S.; Auger, M.; Braccini, S.; Bunka, M.; Ereditato, A.; Nesteruk, K. P.; Scampoli, P.; Türler, A.; Van der Meulen, N. Measurement of  $^{43}\text{Sc}$  and  $^{44}\text{Sc}$  Production Cross-Section with an 18 MeV Medical PET Cyclotron. *Appl. Radiat. Isot.* **2017**, *129*, 96–102.
- (41) Banerjee, S.; Pillai, M. R. A.; Knapp, F. F. Lutetium-177 Therapeutic Radiopharmaceuticals: Linking Chemistry, Radiochemistry, and Practical Applications. *Chem. Rev.* **2015**, *115*, 2934–2974.
- (42) Ermolaev, S. V.; Zhuikov, B. L.; Kokhanyuk, V. M.; Matushko, V. L.; Kalmykov, S. N.; Aliev, R. A.; Tananaev, I. G.; Myasoedov, B. F. Production of Actinium, Thorium and Radium Isotopes from Natural Thorium Irradiated with Protons up to 141 MeV. *Radiochim. Acta* **2012**, *100*, 223–229.
- (43) Bartoś, B.; Majkowska, A.; Krajewski, S.; Bilewicz, A. New Separation Method of No-Carrier-Added  $^{47}\text{Sc}$  from Titanium Targets. *Radiochim. Acta* **2012**, *100*, 457–461.
- (44) Coenen, H. H.; Gee, A. D.; Adam, M.; Antoni, G.; Cutler, C. S.; Fujibayashi, Y.; Jeong, J. M.; Mach, R. H.; Mindt, T. L.; Pike, V. W.; et al. Consensus Nomenclature Rules for Radiopharmaceutical Chemistry — Setting the Record Straight. *Nucl. Med. Biol.* **2017**, *55*, v–xi.
- (45) Pandey, M. K.; Byrne, J. F.; Jiang, H.; Packard, A. B.; DeGrado, T. R. Cyclotron Production of  $^{68}\text{Ga}$  via the  $^{68}\text{Zn}(p,n)^{68}\text{Ga}$  Reaction in Aqueous Solution. *Am. J. Nucl. Med. Mol. Imaging* **2014**, *4*, 303–310.
- (46) Gansow, O. A. Newer Approaches to the Radiolabeling of Monoclonal Antibodies by Use of Metal Chelates. *Nucl. Med. Biol.* **1991**, *18*, 369–381.
- (47) Ruble, G.; Wu, C.; Squire, R. A.; Gansow, O. A.; Strand, M. The Use of  $^{212}\text{Pb}$ -Labeled

- Monoclonal Antibody in the Treatment of Murine Erythroleukemia. *Int. J. Radiat. Oncol. Biol. Phys.* **1996**, *34*, 609–616.
- (48) Horak, E.; Hartmann, F.; Garmestani, K.; Wu, C.; Brechbiel, M.; Gansow, O. A.; Landolfi, N. F.; Waldmann, T. A. Radioimmunotherapy Targeting of HER2/Neu Oncoprotein on Ovarian Tumor Using Lead-212-DOTA-AE1. *J. Nucl. Med.* **1997**, *38*, 1944–1950.
- (49) Rizvi, S. N. F.; Visser, O. J.; Vosjan, M. J. W. D.; van Lingem, A.; Hoekstra, O. S.; Zijlstra, J. M.; Huijgens, P. C.; van Dongen, G. A. M. S.; Lubberink, M. Biodistribution, Radiation Dosimetry and Scouting of  $^{90}\text{Y}$ -Ibritumomab Tiuxetan Therapy in Patients with Relapsed B-Cell Non-Hodgkin's Lymphoma Using  $^{89}\text{Zr}$ -Ibritumomab Tiuxetan and PET. *Eur. J. Nucl. Med. Mol. Imaging* **2012**, *39*, 512–520.
- (50) Rolleman, E. J.; Krenning, E. P.; Bernard, B. F.; de Visser, M.; Bijster, M.; Visser, T. J.; Vermeij, M.; Lindemans, J.; de Jong, M. Long-Term Toxicity of [ $^{177}\text{Lu}$ -DOTA $^0$ ,Tyr $^3$ ]Octreotate in Rats. *Eur. J. Nucl. Med. Mol. Imaging* **2007**, *34*, 219–227.
- (51) Pearson, R. G. Hard and Soft Acids and Bases, HSAB, Part I: Fundamental Principles. *J. Chem. Educ.* **1968**, *45*, 581–587.
- (52) Martell, A. E.; Hancock, R. D. *Metal Complexes in Aqueous Solutions*; Fackler, J. P., Ed.; Plenum Press: New York, 1996.
- (53) Pearson, R. G. Hard and Soft Acids and Bases, HSAB, Part II: Underlying Theories. *J. Chem. Educ.* **1968**, *45*, 643–648.
- (54) Martell, A. E. The Chelate Effect. In *Advances in Chemistry Series*; Gould, R. F., Ed.; 1967; pp 272–294.
- (55) Frausto da Silva, J. J. R. The Chelate Effect Redefined. *J. Chem. Educ.* **1983**, *60*, 390–392.
- (56) Hancock, R. D. Chelate Ring Size and Metal Ion Selection. The Basis of Selectivity for Metal Ions

- in Open-Chain Ligands and Macrocycles. *J. Chem. Educ.* **1992**, *69*, 615–621.
- (57) Ionescu, R. M.; Vlasak, J.; Price, C.; Kirchmeier, M. Contribution of Variable Domains to the Stability of Humanized IgG1 Monoclonal Antibodies. *J. Pharm. Sci.* **2008**, *97*, 1414–1426.
- (58) Vermeer, A. W. P.; Norde, W. The Thermal Stability of Immunoglobulin: Unfolding and Aggregation of a Multi-Domain Protein. *Biophys. J.* **2000**, *78*, 394–404.
- (59) Tirscó, G.; Kovács, Z.; Sherry, A. D. Equilibrium and Formation/Dissociation Kinetics of Some Ln<sup>III</sup>PCTA Complexes. *Inorg. Chem.* **2006**, *45*, 9269–9280.
- (60) Dadwal, M.; Kang, C. S.; Song, H. A.; Sun, X.; Dai, A.; Baidoo, K. E.; Brechbiel, M. W.; Chong, H. S. Synthesis and Evaluation of a Bifunctional Chelate for Development of Bi(III)-Labeled Radioimmunoconjugates. *Bioorg. Med. Chem. Lett.* **2011**, *21*, 7513–7515.
- (61) Griffiths, G. L.; Govindan, S. V.; Sharkey, R. M.; Fisher, D. R.; Goldenberg, D. M. <sup>90</sup>Y-DOTA-HLL2: An Agent for Radioimmunotherapy of Non-Hodgkin's Lymphoma. *J. Nucl. Med.* **2003**, *44*, 77–84.
- (62) McDevitt, M. R.; Finn, R. D.; Sgouros, G.; Ma, D.; Scheinberg, D. A. An <sup>225</sup>Ac/<sup>213</sup>Bi Generator System for Therapeutic Clinical Applications: Construction and Operation. *Appl. Radiat. Isot.* **1999**, *50*, 895–904.
- (63) Nayak, T. K.; Regino, C. A. S.; Wong, K. J.; Milenic, D. E.; Garmestani, K.; Baidoo, K. E.; Szajek, L. P.; Brechbiel, M. W. PET Imaging of HER1-Expressing Xenografts in Mice with <sup>86</sup>Y-CHX-A"-DTPA-Cetuximab. *Eur. J. Nucl. Med. Mol. Imaging* **2010**, *37*, 1368–1376.
- (64) Liu, B.; Dong, L.; Yu, Q.; Li, X.; Wu, F.; Tan, Z.; Luo, S. Thermodynamic Study on the Protonation Reactions of Glyphosate in Aqueous Solution: Potentiometry, Calorimetry and NMR Spectroscopy. *J. Phys. Chem. B* **2016**, *120*, 2132–2137.
- (65) Vaiana, L.; Esteban-Gómez, D.; Mato-Iglesias, M.; Platas-Iglesias, C.; de Blas, A.; Rodríguez-

- Blas, T. Anion Coordination Effect on the Nuclearity of Co<sup>II</sup>, Ni<sup>II</sup>, Cu<sup>II</sup>, and Zn<sup>II</sup> Complexes with a Benzimidazole Pendant-Armed Crown. *Eur. J. Inorg. Chem.* **2009**, 400–411.
- (66) Harris, W. R.; Carrano, C. J.; Raymond, K. N. Spectrophotometric Determination of the Proton-Dependent Stability Constant of Ferric Enterobactin. *J. Am. Chem. Soc.* **1979**, *101*, 2213–2214.
- (67) Liu, Z. D.; Khodr, H. H.; Liu, D. Y.; Lu, S. L.; Hider, R. C. Synthesis, Physicochemical Characterization, and Biological Evaluation of 2-(1'-Hydroxyalkyl)-3-Hydroxypyridin-4-Ones: Novel Iron Chelators with Enhanced pFe<sup>3+</sup> Values. *J. Med. Chem.* **1999**, *42*, 4814–4823.
- (68) Aaseth, J.; Criponi, G.; Andersen, O. Chelating Agents as Therapeutic Compounds—Basic Principles. In *Chelation Therapy in the Treatment of Metal Intoxication*; Academic Press: Boston, 2016; pp 36-37.
- (69) Wedeking, P.; Kumar, K.; Tweedle, M. F. Dissociation of Gadolinium Chelates in Mice: Relationship to Chemical Characteristics. *Magn. Reson. Imaging* **1992**, *10*, 641–648.
- (70) Graham, P.; Weatherburn, D. Dissociation Kinetics of Metal Complexes in Acid. Copper Complexes of Triazamacrocycles. *Aust. J. Chem.* **1981**, *34*, 291–300.
- (71) Wilson, J. J.; Ferrier, M.; Radchenko, V.; Maassen, J. R.; Engle, J. W.; Batista, E. R.; Martin, R. L.; Nortier, F. M.; Fassbender, M. E.; John, K. D.; et al. Evaluation of Nitrogen-Rich Macrocyclic Ligands for the Chelation of Therapeutic Bismuth Radioisotopes. *Nucl. Med. Biol.* **2015**, *42*, 428–438.
- (72) Comba, P.; Jermilova, U.; Orvig, C.; Patrick, B. O.; Ramogida, C. F.; Rück, K.; Schneider, C.; Starke, M. Octadentate Picolinic Acid-Based Bispidine Ligand for Radiometal Ions. *Chem. Eur. J.* **2017**, *23*, 15945–15956.
- (73) Beykan, S.; Dam, J. S.; Eberlein, U.; Kaufmann, J.; Kjærgaard, B.; Jødal, L.; Bouterfa, H.; Bejot, R.; Lassmann, M.; Jensen, S. B. <sup>177</sup>Lu-OPS201 Targeting Somatostatin Receptors: In Vivo

- Biodistribution and Dosimetry in a Pig Model. *EJNMMI Res.* **2016**, *6*, 1–9.
- (74) Kasten, B. B.; Azure, M. T.; Schoeb, T. R.; Fisher, D. R.; Zinn, K. R. Imaging, Biodistribution, and Toxicology Evaluation of  $^{212}\text{Pb}$ -TCMC-Trastuzumab in Nonhuman Primates. *Nucl. Med. Biol.* **2016**, *43*, 391–396.
- (75) Miederer, M.; Seidl, C.; Beyer, G.-J.; Charlton, D. E.; Vranjes-Duric, S.; Comor, J. J.; Huber, R.; Nikula, T.; Apostolidis, C.; Schuhmacher, C.; et al. Comparison of the Radiotoxicity of Two Alpha-Particle-Emitting Immunoconjugates, Terbium-149 and Bismuth-213, Directed against a Tumor-Specific, Exon 9 Deleted (D9) E-Cadherin Adhesion Protein. *Radiat. Res.* **2003**, *159*, 612–620.
- (76) Sephton, R. G.; Hodgson, G. S.; De Abrew, S.; Harris, A. W. Ga-67 and Fe-59 Distributions in Mice. *J. Nucl. Med.* **1978**, *19*, 930–935.
- (77) Abou, D. S.; Ku, T.; Smith-Jones, P. M. In Vivo Biodistribution and Accumulation of  $^{89}\text{Zr}$  in Mice. *Nucl. Med. Biol.* **2011**, *38*, 675–681.
- (78) Nikula, T. K.; McDevitt, M. R.; Finn, R. D.; Wu, C.; Kozak, R. W.; Garmestani, K.; Brechbiel, M. W.; Curcio, M. J.; Pippin, C. G.; Tiffany-Jones, L.; et al. Alpha-Emitting Bismuth Cyclohexylbenzyl DTPA Constructs of Recombinant Humanized Anti-CD33 Antibodies: Pharmacokinetics, Bioactivity, Toxicity and Chemistry. *J. Nucl. Med.* **1999**, *40*, 166–176.
- (79) Pandey, U.; Gamre, N.; Kumar, Y.; Shetty, P.; Sarma, H. D.; Dash, A. A Systematic Evaluation of the Potential of PCTA-NCS Ligand as a Bifunctional Chelating Agent for Design of  $^{177}\text{Lu}$  Radiopharmaceuticals. *J. Radioanal. Nucl. Chem.* **2016**, *307*, 187–194.
- (80) Lee, S.; Hong, Y.; Kim, H.; Choi, S. Synthesis and Application of a Novel Cysteine-Based DTPA-NCS for Targeted Radioimmunotherapy. *Nucl. Med. Biol.* **2013**, *40*, 424–429.
- (81) Boros, E.; Ferreira, C. L.; Cawthray, J. F.; Price, E. W.; Patrick, B. O.; Wester, D. W.; Adam, M.

- J.; Orvig, C. Acyclic Chelate with Ideal Properties for  $^{68}\text{Ga}$  PET Imaging Agent Elaboration. *J. Am. Chem. Soc.* **2010**, *132*, 15726–15733.
- (82) Kumar, K.; Tweedle, M. F. Macrocyclic Polyaminocarboxylate Complexes of Lanthanides as Magnetic Resonance Imaging Contrast Agents. *Pure Appl. Chem.* **1993**, *65*, 515–520.
- (83) Tircsó, G.; Benyó, E. T.; Suh, E. H.; Jurek, P.; Kiefer, G. E.; Sherry, A. D.; Kovács, Z. (S)-5-(p-Nitrobenzyl)-PCTA, a Promising Bifunctional Ligand with Advantageous Metal Ion Complexation Kinetics. *Bioconjugate Chem.* **2009**, *20*, 565–575.
- (84) Csajbók, É.; Baranyai, Z.; Bányai, I.; Brücher, E.; Király, R.; Müller-Fahrnow, A.; Platzek, J.; Radüchel, B.; Schäfer, M. Equilibrium,  $^1\text{H}$  and  $^{13}\text{C}$  NMR Spectroscopy, and X-Ray Diffraction Studies on the Complexes  $\text{Bi}(\text{DOTA})^-$  and  $\text{Bi}(\text{DO3A-Bu})$ . *Inorg. Chem.* **2003**, *42*, 2342–2349.
- (85) Lattuada, L.; Barge, A.; Cravotto, G.; Giovenzana, G. B.; Tei, L. The Synthesis and Application of Polyamino Polycarboxylic Bifunctional Chelating Agents. *Chem. Soc. Rev.* **2011**, *40*, 3019–3049.
- (86) Spreckelmeyer, S.; Ramogida, C. F.; Rousseau, J.; Arane, K.; Bratanovic, I.; Colpo, N.; Jermilova, U.; Dias, G. M.; Dude, I.; Jaraquemada-Peláez, M. de G.; et al. P- $\text{NO}_2$ -Bn- $\text{H}_4\text{Neunpa}$  and  $\text{H}_4\text{Neunpa}$ -Trastuzumab: Bifunctional Chelator for Radiometal pharmaceuticals and  $^{111}\text{In}$  Immuno-Single Photon Emission Computed Tomography Imaging. *Bioconjugate Chem.* **2017**, *28*, 2145–2159.
- (87) Price, E. W.; Zeglis, B. M.; Cawthray, J. F.; Ramogida, C. F.; Ramos, N.; Lewis, J. S.; Adam, M. J.; Orvig, C.  $\text{H}_4\text{Octapa}$ -Trastuzumab: Versatile Acyclic Chelate System for  $^{111}\text{In}$  and  $^{177}\text{Lu}$  Imaging and Therapy. *J. Am. Chem. Soc.* **2013**, *135*, 12707–12721.
- (88) Brechbiel, M. W.; Gansow, O. A. Backbone-Substituted DTPA Ligands for  $^{90}\text{Y}$  Radioimmunotherapy. *Bioconjugate Chem.* **1991**, *2*, 187–194.
- (89) Liu, S.; Edwards, D. S. Bifunctional Chelators for Therapeutic Lanthanide Radiopharmaceuticals.

- Bioconjugate Chem.* **2001**, *12*, 7–34.
- (90) Ruzza, P.; Calderan, A. Radiolabeled Peptide-Receptor Ligands in Tumor Imaging. *Expert Opin. Med. Diagn.* **2011**, *5*, 411–424.
- (91) Benešová, M.; Bauder-Wüst, U.; Schäfer, M.; Klika, K. D.; Mier, W.; Haberkorn, U.; Kopka, K.; Eder, M. Linker Modification Strategies To Control the Prostate-Specific Membrane Antigen (PSMA)-Targeting and Pharmacokinetic Properties of DOTA-Conjugated PSMA Inhibitors. *J. Med. Chem.* **2016**, *59*, 1761–1775.
- (92) Domnanich, K. A.; Müller, C.; Farkas, R.; Schmid, R. M.; Ponsard, B.; Schibli, R.; Türlér, A.; Van der Meulen, N. P. <sup>44</sup>Sc for Labeling of DOTA- and NODAGA-Functionalized Peptides: Preclinical in Vitro and in Vivo Investigations. *EJNMMI Radiopharm. Chem.* **2016**, *1*, 1–19.
- (93) Müller, C.; Vermeulen, C.; Johnston, K.; Köster, U.; Schmid, R.; Türlér, A.; Van der Meulen, N. P. Preclinical in Vivo Application of <sup>152</sup>Tb-DOTANOC: A Radiolanthanide for PET Imaging. *EJNMMI Res.* **2016**, *6*, 1–10.
- (94) Mijalis, A. J.; Thomas, D. A.; Simon, M. D.; Adamo, A.; Beaumont, R.; Jensen, K. F.; Pentelute, B. L. A Fully Automated Flow-Based Approach for Accelerated Peptide Synthesis. *Nat. Chem. Biol.* **2017**, *13*, 464–466.
- (95) Chari, R. V. J. Targeted Cancer Therapy: Conferring Specificity to Cytotoxic Drugs. *Acc. Chem. Res.* **2008**, *41*, 98–107.
- (96) Boswell, C. A.; Brechbiel, M. W. Development of Radioimmunotherapeutic and Diagnostic Antibodies: An Inside-Out View. *Nucl. Med. Biol.* **2007**, *34*, 757–778.
- (97) Holliger, P.; Hudson, P. J. Engineered Antibody Fragments and the Rise of Single Domains. *Nat. Biotechnol.* **2005**, *23*, 1126–1136.
- (98) Shannon, R. D. Revised Effective Ionic Radii and Systematic Studies of Interatomic Distances in

- Halides and Chalcogenides. *Acta Crystallogr. Sect. A* **1976**, *32*, 751–767.
- (99) Baes, C. F. Jr.; Mesmer, R. E. *The Hydrolysis of Cations*; Wiley-Interscience: New York, 1976.
- (100) Cornelissen, B.; A Vallis, K. Targeting the Nucleus: An Overview of Auger-Electron Radionuclide Therapy. *Curr. Drug Discov. Technol.* **2010**, *7*, 263–279.
- (101) Buchegger, F.; Perillo-Adamer, F.; Dupertuis, Y. M.; Bischof Delaloye, A. Auger Radiation Targeted into DNA: A Therapy Perspective. *Eur. J. Nucl. Med. Mol. Imaging* **2006**, *33*, 1352–1363.
- (102) Makvandi, M.; Dupis, E.; Engle, J. W.; Nortier, F. M.; Fassbender, M. E.; Simon, S.; Birnbaum, E. R.; Atcher, R. W.; John, K. D.; Rixe, O.; et al. Alpha-Emitters and Targeted Alpha Therapy in Oncology: From Basic Science to Clinical Investigations. *Target. Oncol.* **2018**, *13*, 189–203.
- (103) Morgenstern, A.; Abbas, K.; Bruchertseifer, F.; Apostolidis, C. Production of Alpha Emitters for Targeted Alpha Therapy. *Curr. Radiopharm.* **2008**, *1*, 135–143.
- (104) Morgenroth, A.; Dinger, C.; Zlatopolskiy, B. D.; Al-Momani, E.; Glatting, G.; Mottaghy, F. M.; Reske, S. N. Auger Electron Emitter against Multiple Myeloma — Targeted Endo-Radio-Therapy with <sup>125</sup>I-Labeled Thymidine Analogue 5-Iodo-4'-Thio-2'-Deoxyuridine. *Nucl. Med. Biol.* **2011**, *38*, 1067–1077.
- (105) Rosenkranz, A. A.; Slastnikova, T. A.; Khramtsov, Y. V.; Karyagina, T. S.; Georgiev, G. P.; Sobolev, A. S. Antitumor Efficacy of Auger Electron Emitter <sup>111</sup>In Delivered by Modular Nanotransporter into the Nuclei of Cells with Folate Receptor Overexpression. *Dokl. Biochem. Biophys.* **2017**, *473*, 85–87.
- (106) Koumarianou, E.; Slastnikova, T. A.; Pruszynski, M.; Rosenkranz, A. A.; Vaidyanathan, G.; Sobolev, A. S.; Zalutsky, M. R. Radiolabeling and in Vitro Evaluation of <sup>67</sup>Ga-NOTA-Modular Nanotransporter – A Potential Auger Electron Emitting EGFR-Targeted Radiotherapeutic. *Nucl.*

- Med. Biol.* **2014**, *41*, 441–449.
- (107) Balagurumoorthy, P.; Xu, X.; Wang, K.; Adelstein, S. J.; Kassis, A. I. Effect of Distance between Decaying  $^{125}\text{I}$  and DNA on Auger-Electron Induced Double-Strand Break Yield. *Int. J. Radiat. Biol.* **2012**, *88*, 998–1008.
- (108) Tavares, A. A. S.; Tavares, J. M. R. S.  $^{99\text{m}}\text{Tc}$  Auger Electrons for Targeted Tumour Therapy: A Review. *Int. J. Radiat. Biol.* **2010**, *86*, 261–270.
- (109) Sadeghi, M.; Aboudzadeh Rovais, M. R.; Enferadi, M.; Sarabadani, P. Targetry and Radiochemistry for No-Carrier-Added Production of  $^{117,118\text{m},119,120\text{m},112}\text{Sb}$ . *Nukleonika* **2011**, *56*, 9–15.
- (110) Aardaneh, K.; Shirazi, B. Radiochemical Separation of  $^{67}\text{Ga}$  from Zn and Cu Using the Adsorbent Resin Amberlite XAD-7. *J. Radioanal. Nucl. Chem.* **2005**, *265*, 47–51.
- (111) *Cyclotron Produced Radionuclides : Physical Characteristics and Production Methods.*; An International Atomic Energy Agency Publication: Vienna, 2009.
- (112) Sadeghi, M.; Mokhtari, L. Rapid Separation of  $^{67,68}\text{Ga}$  from  $^{68}\text{Zn}$  Target Using Precipitation Technique. *J. Radioanal. Nucl. Chem.* **2010**, *284*, 471–473.
- (113) Dumortier, R.; Weber, M. E.; Vera, J. H. Removal and Recovery of Gallium from Aqueous Solutions by Complexation with Sodium Di-(n-Octyl) Phosphinate. *Hydrometallurgy* **2005**, *76*, 207–215.
- (114) Andrade Martins, P. de; Osso, J. A. Thermal Diffusion of  $^{67}\text{Ga}$  from Irradiated Zn Targets. *Appl. Radiat. Isot.* **2013**, *82*, 279–282.
- (115) Lenher, V.; Merrill, H. B. The Solubility of Silica. *J. Am. Chem. Soc.* **1917**, *39*, 2630–2638.
- (116) Thisgaard, H. Accelerator Based Production of Auger-Electron-Emitting Isotopes for

- Radionuclide Therapy. Ph.D. Dissertation, Technical University of Denmark, 2008.
- (117) Baluev, A. V.; Mityakhina, V. S.; Krasnikov, L. V.; Galkin, B. Y.; Besnosyuk, V. I. Recovery of Antimony-125 from Tin-124 Irradiated by Neutrons. *Czech. J. Phys.* **2003**, *53*, A417–A423.
- (118) Thisgaard, H.; Jensen, M. Production of the Auger Emitter  $^{119}\text{Sb}$  for Targeted Radionuclide Therapy Using a Small PET-Cyclotron. *Appl. Radiat. Isot.* **2009**, *67*, 34–38.
- (119) White, C. E.; Rose, H. J. Separation of Antimony by Solvent Extraction. *Anal. Chem.* **1953**, *25*, 351–353.
- (120) Khorasani, S. S. M. A.; Khundkar, M. H. Solvent Extraction of Antimony(V) with Ethyl Acetate. *Anal. Chim. Acta* **1959**, *21*, 24–28.
- (121) Özer, U. Y.; Bogucki, R. F. Equilibrium Studies of Antimony(III) Chelates in Aqueous Solution. *J. Inorg. Nucl. Chem.* **1971**, *33*, 4143–4153.
- (122) Kraus, K. A.; Michelson, D. C.; Nelson, F. Adsorption of Negatively Charged Complexes by Cation Exchangers 1. *J. Am. Chem. Soc.* **1959**, *81*, 3204–3207.
- (123) DeGraffenreid, A. J.; Feng, Y.; Barnes, C. L.; Ketring, A. R.; Cutler, C. S.; Jurisson, S. S. Trithiols and Their Arsenic Compounds for Potential Use in Diagnostic and Therapeutic Radiopharmaceuticals. *Nucl. Med. Biol.* **2016**, *43*, 288–295.
- (124) Robertson, A. K. H.; McNeil, B. L.; Yang, H.; Gendron, D.; Perron, R.; Radchenko, V.; Zeisler, S.; Causey, P.; Schaffer, P.  $^{232}\text{Th}$ -Spallation-Produced  $^{225}\text{Ac}$  with Reduced  $^{227}\text{Ac}$  Content. *Inorg. Chem.* **2020**, *59*, 12156–12165.
- (125) National Nuclear Data Center, Decay Radiation Search. Version 12/2/2019  
[https://www.nndc.bnl.gov/nudat2/indx\\_dec.jsp](https://www.nndc.bnl.gov/nudat2/indx_dec.jsp).
- (126) Boros, E.; Packard, A. B. Radioactive Transition Metals for Imaging and Therapy. *Chem. Rev.*

**2019**, *119*, 870–901.

- (127) Pinto, S. M.; Tomé, V.; Calvete, M. J. F.; Castro, M. M. C. A.; Tóth, É.; Geraldes, C. F. G. C. Metal-Based Redox-Responsive MRI Contrast Agents. *Coordination Chemistry Reviews*. Elsevier B.V. July 1, 2019, pp 1–31.
- (128) Weekes, D. M.; Orvig, C. Harnessing the Bone-Seeking Ability of Ca(II)-like Metal Ions in the Treatment of Metastatic Cancer and Resorption Disorders. *Chem. Soc. Rev.* **2016**, *45*, 2024–2031.
- (129) Lawson, M. K.; Valko, M.; Cronin, M. T. D.; Jomová, K. Chelators in Iron and Copper Toxicity. *Curr. Pharmacol. Reports* **2016**, *2*, 271–280.
- (130) Bjørklund, G.; Mutter, J.; Aaseth, J. Metal Chelators and Neurotoxicity: Lead, Mercury, and Arsenic. *Arch. Toxicol.* **2017**, *91*, 3787–3797.
- (131) Schubert, J. Chelating Agents in Biological Systems. *Environ. Health Perspect.* **1981**, *40*, 227–232.
- (132) McClung, M.; Harris, S. T.; Miller, P. D.; Bauer, D. C.; Davison, K. S.; Dian, L.; Hanley, D. A.; Kendler, D. L.; Yuen, C. K.; Lewiecki, E. M. Bisphosphonate Therapy for Osteoporosis: Benefits, Risks, and Drug Holiday. *Am. J. Med.* **2013**, *126*, 13–20.
- (133) Kolesnikov-Gauthier, H.; Lemoine, N.; Tresch-Bruneel, E.; Olivier, A.; Oudoux, A.; Penel, N. Efficacy and Safety of <sup>153</sup>Sm-EDTMP as Treatment of Painful Bone Metastasis: A Large Single-Center Study. *Support. Care Cancer* **2018**, *26*, 751–758.
- (134) Agarwal, K. K.; Singla, S.; Arora, G.; Bal, C. <sup>177</sup>Lu-EDTMP for Palliation of Pain from Bone Metastases in Patients with Prostate and Breast Cancer: A Phase II Study. *Eur. J. Nucl. Med. Mol. Imaging* **2015**, *42*, 79–88.
- (135) Ramogida, C. F.; Boros, E.; Patrick, B. O.; Zeisler, S. K.; Kumlin, J.; Adam, M. J.; Schaffer, P.; Orvig, C. Evaluation of H<sub>2</sub>CHXdedpa, H<sub>2</sub>Dedpa- and H<sub>2</sub>CHXdedpa-N,N'-Propyl-2-NI Ligands for

- <sup>64</sup>Cu(II) Radiopharmaceuticals. *Dalton Trans.* **2016**, *45*, 13082–13090.
- (136) Li, L.; Jaraquemada-Peláez, M. de G.; Kuo, H.-T.; Merkens, H.; Choudhary, N.; Gitschtaler, K.; Jermilova, U.; Colpo, N.; Uribe-Munoz, C.; Radchenko, V.; et al. Functionally Versatile and Highly Stable Chelator for <sup>111</sup>In and <sup>177</sup>Lu: Proof-of-Principle Prostate-Specific Membrane Antigen Targeting. *Bioconjugate Chem.* **2019**, *30*, 1539–1553.
- (137) Thiele, N. A.; Brown, V.; Kelly, J. M.; Amor-Coarasa, A.; Jermilova, U.; MacMillan, S. N.; Nikolopoulou, A.; Ponnala, S.; Ramogida, C. F.; Robertson, A. K. H.; et al. An Eighteen-Membered Macrocyclic Ligand for Actinium-225 Targeted Alpha Therapy. *Angew. Chemie Int. Ed.* **2017**, *56*, 14712–14717.
- (138) Balogh, E.; Mato-Iglesias, M.; Platas-Iglesias, C.; Tóth, É.; Djanashvili, K.; Peters, J. A.; de Blas, A.; Rodríguez-Blas, T. Pyridine- and Phosphonate-Containing Ligands for Stable Ln Complexation. Extremely Fast Water Exchange on the Gd III Chelates. *Inorg. Chem.* **2006**, *45*, 8719–8728.
- (139) Price, E. W.; Zeglis, B. M.; Lewis, J. S.; Adam, M. J.; Orvig, C. H<sub>6</sub>Phospa-Trastuzumab: Bifunctional Methylenephosphonate-Based Chelator with <sup>89</sup>Zr, <sup>111</sup>In and <sup>177</sup>Lu. *Dalton Trans.* **2014**, *43*, 119–131.
- (140) Kostelnik, T. I.; Wang, X.; Southcott, L.; Wagner, H. K.; Kubeil, M.; Stephan, H.; Jaraquemada-Peláez, M. de G.; Orvig, C. Rapid Thermodynamically Stable Complex Formation of [<sup>Nat/111</sup>In]In<sup>3+</sup>, [<sup>Nat/90</sup>Y]Y<sup>3+</sup>, and [<sup>Nat/177</sup>Lu]Lu<sup>3+</sup> with H<sub>6</sub>Dappa. *Inorg. Chem.* **2020**, *59*, 7238–7251.
- (141) Jaraquemada-Peláez, M. de G.; Wang, X.; Clough, T. J.; Cao, Y.; Choudhary, N.; Emler, K.; Patrick, B. O.; Orvig, C. H<sub>4</sub>Octapa: Synthesis, Solution Equilibria and Complexes with Useful Radiopharmaceutical Metal Ions. *Dalton Trans.* **2017**, *46*, 14647–14658.
- (142) Abada, S.; Lecointre, A.; Christine, C.; Ehret-Sabatier, L.; Saupe, F.; Orend, G.; Brasse, D.;

- Ouadi, A.; Hussenet, T.; Laquerrière, P.; et al. Phosphonated Chelates for Nuclear Imaging. *Org. Biomol. Chem.* **2014**, *12*, 9601–9620.
- (143) Price, E. W.; Cawthray, J. F.; Bailey, G. A.; Ferreira, C. L.; Boros, E.; Adam, M. J.; Orvig, C. H<sub>4</sub>Octapa: An Acyclic Chelator for <sup>111</sup>In Radiopharmaceuticals. *J. Am. Chem. Soc.* **2012**, *134*, 8670–8683.
- (144) Price, E. W.; Cawthray, J. F.; Adam, M. J.; Orvig, C. Modular Syntheses of H<sub>4</sub>Octapa and H<sub>2</sub>Dedpa, and Yttrium Coordination Chemistry Relevant to <sup>86</sup>Y/<sup>90</sup>Y Radiopharmaceuticals. *Dalton Trans.* **2014**, *43*, 7176–7190.
- (145) Ramogida, C. F.; Cawthray, J. F.; Boros, E.; Ferreira, C. L.; Patrick, B. O.; Adam, M. J.; Orvig, C. H<sub>2</sub>CHXdedpa and H<sub>4</sub>CHX Octapa—Chiral Acyclic Chelating Ligands for <sup>67,68</sup>Ga and <sup>111</sup>In Radiopharmaceuticals. *Inorg. Chem.* **2015**, *54*, 2017–2031.
- (146) Price, E. W.; Zeglis, B. M.; Cawthray, J. F.; Lewis, J. S.; Adam, M. J.; Orvig, C. What a Difference a Carbon Makes: H<sub>4</sub>octapa vs H<sub>4</sub>C<sub>3</sub>octapa, Ligands for In-111 and Lu-177 Radiochemistry. *Inorg. Chem.* **2014**, *53*, 10412–10431.
- (147) Li, L.; Jaraquemada-Peláez, M. de G.; Aluicio-Sarduy, E.; Wang, X.; Jiang, D.; Sakheie, M.; Kuo, H.-T.; Barnhart, T. E.; Cai, W.; Radchenko, V.; et al. [<sup>Nat</sup>44Sc(Pyra)]<sup>−</sup>: Thermodynamic Stability, Radiolabeling, and Biodistribution of a Prostate-Specific-Membrane-Antigen-Targeting Conjugate. *Inorg. Chem.* **2020**, *59*, 1985–1995.
- (148) Gans, P.; Sabatini, A.; Vacca, A. Determination of Equilibrium Constants from Spectrophotometric Data Obtained from Solutions of Known PH: The Program PHab. *Ann. Chim.* **1999**, *89*, 45–49.
- (149) Frassinetti, C.; Ghelli, S.; Gans, P.; Sabatini, A.; Moruzzi, M. S.; Vacca, A. Nuclear Magnetic Resonance as a Tool for Determining Protonation Constants of Natural Polyprotic Bases in Solution. *Anal. Biochem.* **1995**, *231*, 374–382.

- (150) Gans, P.; Sabatini, A.; Vacca, A. Investigation of Equilibria in Solution. Determination of Equilibrium Constants with the HYPERQUAD Suite of Programs. *Talanta* **1996**, *43*, 1739–1753.
- (151) Weekes, D. M.; Ramogida, C. F.; Jaraquemada-Peláez, M. de G.; Patrick, B. O.; Apte, C.; Kostelnik, T. I.; Cawthray, J. F.; Murphy, L.; Orvig, C. Dipicolinate Complexes of Gallium(III) and Lanthanum(III). *Inorg. Chem.* **2016**, *55*, 12544–12558.
- (152) Paúrová, M.; Havlíčková, J.; Pospíšilová, A.; Vetrík, M.; Císařová, I.; Stephan, H.; Pietzsch, H.-J.; Hrubý, M.; Hermann, P.; Kotek, J. Bifunctional Cyclam-Based Ligands with Phosphorus Acid Pendant Moieties for Radiocopper Separation: Thermodynamic and Kinetic Studies. *Chem. - Eur. J.* **2015**, *21*, 4671–4687.
- (153) Alderighi, L.; Gans, P.; Ienco, A.; Peters, D.; Sabatini, A.; Vacca, A. Hyperquad Simulation and Speciation (HySS): A Utility Program for the Investigation of Equilibria Involving Soluble and Partially Soluble Species. *Coord. Chem. Rev.* **1999**, *184*, 311–318.
- (154) Zeng, X.; Coquière, D.; Alenda, A.; Garrier, E.; Prangé, T.; Li, Y.; Reinaud, O.; Jabin, I. Efficient Synthesis of Calix[6]Tmpa: A New Calix[6]Azacryptand with Unique Conformational and Host–Guest Properties. *Chem. - Eur. J.* **2006**, *12*, 6393–6402.
- (155) Sheldrick, G. M. Crystal Structure Refinement with SHELXL. *Acta Crystallogr. Sect. C Struct. Chem.* **2015**, *71*, 3–8.
- (156) Dolomanov, O. V.; Bourhis, L. J.; Gildea, R. J.; Howard, J. A. K.; Puschmann, H. OLEX2 : A Complete Structure Solution, Refinement and Analysis Program. *J. Appl. Crystallogr.* **2009**, *42*, 339–341.
- (157) Gran, G. Determination of the Equivalence Point in Potentiometric Titrations. Part II. *Analyst* **1952**, *77*, 661–671.
- (158) Paul, M. A.; Long, F. A. H<sub>0</sub> And Related Indicator Acidity Function. *Chem. Rev.* **1957**, *57*, 1–45.

- (159) Frisch, M. J.; Trucks, G. W.; Schlegel, H. B.; Scuseria, G. E.; Robb, M. A.; Cheeseman, J. R.; Scalmani, G.; Barone, V.; Petersson, G. A.; Nakatsuji, H.; et al. Gaussian 16, Revision C.01., Gaussian, Inc., Wallingford CT, Gaussian 16, Revision C.01. 2016.
- (160) Li, X.; Frisch, M. J. Energy-Represented Direct Inversion in the Iterative Subspace within a Hybrid Geometry Optimization Method. *J. Chem. Theory Comput.* **2006**, *2*, 835–839.
- (161) Adamo, C.; Barone, V. Toward Reliable Density Functional Methods without Adjustable Parameters: The PBE0 Model. *J. Chem. Phys.* **1999**, *110*, 6158–6170.
- (162) Grimme, S.; Ehrlich, S.; Goerigk, L. Effect of the Damping Function in Dispersion Corrected Density Functional Theory. *J. Comput. Chem.* **2011**, *32*, 1456–1465.
- (163) Grimme, S.; Antony, J.; Ehrlich, S.; Krieg, H. A Consistent and Accurate Ab Initio Parametrization of Density Functional Dispersion Correction (DFT-D) for the 94 Elements H-Pu. *J. Chem. Phys.* **2010**, *132*, 154104.
- (164) Smith, D. G. A.; Burns, L. A.; Patkowski, K.; Sherrill, C. D. Revised Damping Parameters for the D3 Dispersion Correction to Density Functional Theory. *J. Phys. Chem. Lett.* **2016**, *7*, 2197–2203.
- (165) Weigend, F.; Ahlrichs, R. Balanced Basis Sets of Split Valence, Triple Zeta Valence and Quadruple Zeta Valence Quality for H to Rn: Design and Assessment of Accuracy. *Phys. Chem. Chem. Phys.* **2005**, *7*, 3297–3305.
- (166) Martin, J. M. L.; Sundermann, A. Correlation Consistent Valence Basis Sets for Use with the Stuttgart-Dresden-Bonn Relativistic Effective Core Potentials: The Atoms Ga-Kr and In-Xe. *J. Chem. Phys.* **2001**, *114*, 3408–3420.
- (167) Dolg, M.; Wedig, U.; Stoll, H.; Preuss, H. Energy-adjusted Ab Initio Pseudopotentials for the First Row Transition Elements. *J. Chem. Phys.* **1987**, *86*, 866–872.
- (168) Cao, X.; Dolg, M. Valence Basis Sets for Relativistic Energy-Consistent Small-Core Lanthanide

- Pseudopotentials. *J. Chem. Phys.* **2001**, *115*, 7348–7355.
- (169) Cao, X.; Dolg, M. Segmented Contraction Scheme for Small-Core Lanthanide Pseudopotential Basis Sets. *J. Mol. Struct. THEOCHEM* **2002**, *581*, 139–147.
- (170) Schuchardt, K. L.; Didier, B. T.; Elsethagen, T.; Sun, L.; Gurumoorthi, V.; Chase, J.; Li, J.; Windus, T. L. Basis Set Exchange: A Community Database for Computational Sciences. *J. Chem. Inf. Model.* **2007**, *47*, 1045–1052.
- (171) Pritchard, B. P.; Altarawy, D.; Didier, B.; Gibson, T. D.; Windus, T. L. New Basis Set Exchange: An Open, Up-to-Date Resource for the Molecular Sciences Community. *J. Chem. Inf. Model.* **2019**, *59*, 4814–4820.
- (172) Feller, D. The Role of Databases in Support of Computational Chemistry Calculations. *J. Comput. Chem.* **1996**, *17*, 1571–1586.
- (173) Vícha, J.; Patzschke, M.; Marek, R. A Relativistic DFT Methodology for Calculating the Structures and NMR Chemical Shifts of Octahedral Platinum and Iridium Complexes. *Phys. Chem. Chem. Phys.* **2013**, *15*, 7740–7754.
- (174) Bühl, M.; Reimann, C.; Pantazis, D. A.; Bredow, T.; Neese, F. Geometries of Third-Row Transition-Metal Complexes from Density-Functional Theory. *J. Chem. Theory Comput.* **2008**, *4*, 1449–1459.
- (175) Vícha, J.; Novotný, J.; Straka, M.; Repisky, M.; Ruud, K.; Komorovsky, S.; Marek, R. Structure, Solvent, and Relativistic Effects on the NMR Chemical Shifts in Square-Planar Transition-Metal Complexes: Assessment of DFT Approaches. *Phys. Chem. Chem. Phys.* **2015**, *17*, 24944–24955.
- (176) Quintal, M. M.; Karton, A.; Iron, M. A.; Daniel Boese, A.; Martin, J. M. L. Benchmark Study of DFT Functionals for Late-Transition-Metal Reactions. *J. Phys. Chem. A* **2006**, *110*, 709–716.
- (177) Dohm, S.; Hansen, A.; Steinmetz, M.; Grimme, S.; Checinski, M. P. Comprehensive

- Thermochemical Benchmark Set of Realistic Closed-Shell Metal Organic Reactions. *J. Chem. Theory Comput.* **2018**, *14*, 2596–2608.
- (178) Kirschner, K. N.; Reith, D.; Heiden, W. The Performance of Dunning, Jensen, and Karlsruhe Basis Sets on Computing Relative Energies and Geometries. *Soft Mater.* **2020**, 1–15.
- (179) Bauzá, A.; Quiñonero, D.; Deyà, P. M.; Frontera, A. Is the Use of Diffuse Functions Essential for the Properly Description of Noncovalent Interactions Involving Anions? *J. Phys. Chem. A* **2013**, *117*, 2651–2655.
- (180) Ernesto G and Martinez, J. M. M. L. and A. R. and B. PACKMOL: A Package for Building Initial Configurations for Molecular Dynamics Simulations. *J. Comput. Chem.* **2009**, *30*, 2157–2164.
- (181) Cheeseman, J. R. A Comparison of Models for Calculating Nuclear Magnetic Resonance Shielding Tensors. *J. Chem. Phys.* **1996**, *104*, 5497–5509.
- (182) Wolinski, K.; Hinton, J. F.; Pulay, P. Efficient Implementation of the Gauge-Independent Atomic Orbital Method for NMR Chemical Shift Calculations. *J. Am. Chem. Soc.* **1990**, *112*, 8251–8260.
- (183) Pawlak, T.; Niedzielska, D.; Vícha, J.; Marek, R.; Pazderski, L. Dimeric Pd(II) and Pt(II) Chloride Organometallics with 2-Phenylpyridine and Their Solvolysis in Dimethylsulfoxide. *J. Organomet. Chem.* **2014**, *759*, 58–66.
- (184) Toomsalu, E.; Burk, P. Critical Test of Some Computational Methods for Prediction of NMR  $^1\text{H}$  and  $^{13}\text{C}$  Chemical Shifts. *J. Mol. Model.* **2015**, *21*, 1–21.
- (185) Krivdin, L. B. Computational  $^1\text{H}$  NMR: Part 1. Theoretical Background. *Magn. Reson. Chem.* **2019**, *57*, 897–914.
- (186) Reid, D. M.; Kobayashi, R.; Collins, M. A. Systematic Study of Locally Dense Basis Sets for NMR Shielding Constants. *J. Chem. Theory Comput.* **2014**, *10*, 146–152.

- (187) Jensen, F. Segmented Contracted Basis Sets Optimized for Nuclear Magnetic Shielding. *J. Chem. Theory Comput.* **2015**, *11*, 132–138.
- (188) Jensen, F. Unifying General and Segmented Contracted Basis Sets. Segmented Polarization Consistent Basis Sets. *J. Chem. Theory Comput.* **2014**, *10*, 1074–1085.
- (189) Dennington, R.; Keith, T. A.; Millam, J. M. GaussView, Version 6.0.16. *Semichem Inc. Shawnee Mission KS* **2016**.
- (190) Hanwell, M. D.; Curtis, D. E.; Lonie, D. C.; Vandermeersch, T.; Zurek, E.; Hutchison, G. R. Avogadro: An Advanced Semantic Chemical Editor, Visualization, and Analysis Platform. *J. Cheminform.* **2012**, *4*, 1–17.
- (191) Opacic, T.; Paefgen, V.; Lammers, T.; Kiessling, F. Status and Trends in the Development of Clinical Diagnostic Agents. *Wiley Interdiscip. Rev. Nanomed. Nanobiotech.* **2017**, *9*, e1441.
- (192) Strosberg, J.; El-Haddad, G.; Wolin, E.; Hendifar, A.; Yao, J.; Chasen, B.; Mitra, E.; Kunz, P. L.; Kulke, M. H.; Jacene, H.; et al. Phase 3 Trial of  $^{177}\text{Lu}$ -Dotatate for Midgut Neuroendocrine Tumors. *N. Engl. J. Med.* **2017**, *376*, 125–135.
- (193) FDA approves lutetium Lu 177 dotatate for treatment of GEP-NETS  
<https://www.fda.gov/Drugs/InformationOnDrugs/ApprovedDrugs/ucm594105.htm> (accessed Feb 1, 2020).
- (194) Herrmann, K.; Lapa, C.; Wester, H.-J.; Schottelius, M.; Schiepers, C.; Eberlein, U.; Bluemel, C.; Keller, U.; Knop, S.; Kropf, S.; et al. Biodistribution and Radiation Dosimetry for the Chemokine Receptor CXCR4-Targeting Probe  $^{68}\text{Ga}$ -Pentixafor. *J. Nucl. Med.* **2015**, *56*, 410–416.
- (195) Nicolas, G. P.; Schreiter, N.; Kaul, F.; Uiters, J.; Bouterfa, H.; Kaufmann, J.; Erlanger, T. E.; Cathomas, R.; Christ, E.; Fani, M.; et al. Comparison of  $^{68}\text{Ga}$ -OPS202 ( $^{68}\text{Ga}$ -NODAGA-JR11) and  $^{68}\text{Ga}$ -DOTATOC ( $^{68}\text{Ga}$ -Edotreotide) PET/CT in Patients with Gastroenteropancreatic

- Neuroendocrine Tumors: Evaluation of Sensitivity in a Prospective Phase II Imaging. *J. Nucl. Med.* **2018**, *59*, 915–921.
- (196) García-Toraño, E.; Peyrés, V.; Roteta, M.; Sánchez-Cabezudo, A. I.; Romero, E.; Martínez Ortega, A. Standardisation and Precise Determination of the Half-Life of  $^{44}\text{Sc}$ . *Appl. Radiat. Isot.* **2016**, *109*, 314–318.
- (197) Domnanich, K. A.; Müller, C.; Benešová, M.; Dressler, R.; Haller, S.; Köster, U.; Ponsard, B.; Schibli, R.; Türlér, A.; Van der Meulen, N. P.  $^{47}\text{Sc}$  as Useful  $\beta^-$  Emitter for the Radiotheragnostic Paradigm: A Comparative Study of Feasible Production Routes. *EJNMMI Radiopharm. Chem.* **2017**, *2*, 1–17.
- (198) Notni, J.; Hermann, P.; Havlíčková, J.; Kotek, J.; Kubíček, V.; Plutnar, J.; Loktionova, N.; Riss, P. J.; Rösch, F.; Lukeš, I. A Triazacyclononane-Based Bifunctional Phosphinate Ligand for the Preparation of Multimeric  $^{68}\text{Ga}$  Tracers for Positron Emission Tomography. *Chem. Eur. J.* **2010**, *16*, 7174–7185.
- (199) Wang, X.; Jaraquemada-Peláez, M. de G.; Rodríguez-Rodríguez, C.; Cao, Y.; Buchwalder, C.; Choudhary, N.; Jermilova, U.; Ramogida, C. F.; Saatchi, K.; Häfeli, U. O.; et al.  $\text{H}_4\text{Octox}$ : Versatile Bimodal Octadentate Acyclic Chelating Ligand for Medicinal Inorganic Chemistry. *J. Am. Chem. Soc.* **2018**, *140*, 15487–15500.
- (200) Safarzadeh, L.; Ghannadi-Maragheh, M.; Anvari, A.; Aghamiri, S. M. R.; Shirvani-Arani, S.; Bahrami-Samani, A. Production, Radiolabeling and Biodistribution Studies of  $^{175}\text{Yb}$ -DOTMP as Bone Pain Palliation. *Iran. J. Pharm. Sci.* **2012**, *8*, 135–141.
- (201) Salek, N.; Vosoghi, S.; Arani, S. S.; Samani, A. B.; Mehrabi, M.; Maraghe, M. G. Preparation and Dosimetry Evaluation of a Carrier-Free  $^{90}\text{Y}$  Labeled DOTMP as a Promising Agent for Bone Marrow Ablation. *Curr. Radiopharm.* **2018**, *11*, 116–122.

- (202) Yousefnia, H.; Zolghadri, S. Human Absorbed Dose Estimation of a New In-111 Imaging Agent Based on Rat Data. *Int. J. Phys. Math. Sci.* **2015**, *9*, 627–631.
- (203) Zolghadri, S.; Yousefnia, H.; Jalilian, A. R.; Ghannadi-Maragheh, M. Production, Biodistribution Assessment and Dosimetric Evaluation of  $^{177}\text{Lu}$ -TTHMP as an Agent for Bone Pain Palliation. *Asia Ocean. J. Nucl. Med. Biol.* **2015**, *3*, 35–42.
- (204) Cotton, S. *Lanthanide and Actinide Chemistry*; John Wiley & Sons, Ltd: Chichester, UK, 2006.
- (205) Dash, A.; Pillai, M. R. A.; Knapp, F. F. Production of  $^{177}\text{Lu}$  for Targeted Radionuclide Therapy: Available Options. *Nucl. Med. Mol. Imaging* **2015**, *49*, 85–107.
- (206) Tao, J.; Perdew, J. P.; Staroverov, V. N.; Scuseria, G. E. Climbing the Density Functional Ladder: Nonempirical Meta-Generalized Gradient Approximation Designed for Molecules and Solids. *Phys. Rev. Lett.* **2003**, *91*, 146401.
- (207) Schäfer, A.; Huber, C.; Ahlrichs, R. Fully Optimized Contracted Gaussian Basis Sets of Triple Zeta Valence Quality for Atoms Li to Kr. *J. Chem. Phys.* **1994**, *100*, 5829–5835.
- (208) Dolg, M.; Stoll, H.; Preuss, H. Energy-adjusted Ab Initio Pseudopotentials for the Rare Earth Elements. *J. Chem. Phys.* **1989**, *90*, 1730–1734.
- (209) Wani, A. L.; Ara, A.; Usmani, J. A. Lead Toxicity: A Review. *Interdiscip. Toxicol.* **2015**, *8*, 55–64.
- (210) Yong, K.; Brechbiel, M. W. Towards Translation of  $^{212}\text{Pb}$  as a Clinical Therapeutic; Getting the Lead In! *Dalton Trans.* **2011**, *40*, 6068–6076.
- (211) dos Santos, J. C.; Schäfer, M.; Bauder-Wüst, U.; Lehnert, W.; Leotta, K.; Morgenstern, A.; Kopka, K.; Haberkorn, U.; Mier, W.; Kratochwil, C. Development and Dosimetry of  $^{203}\text{Pb}/^{212}\text{Pb}$ -Labelled PSMA Ligands: Bringing “the Lead” into PSMA-Targeted Alpha Therapy? *Eur. J. Nucl. Med. Mol. Imaging* **2019**, *46*, 1081–1091.

- (212) Stenberg, V. Y.; Juzeniene, A.; Chen, Q.; Yang, X.; Bruland, Ø. S.; Larsen, R. H. Preparation of the Alpha-Emitting Prostate-Specific Membrane Antigen Targeted Radioligand [ $^{212}\text{Pb}$ ]Pb-NG001 for Prostate Cancer. *J. Label. Compd. Radiopharm.* **2020**, *63*, 129–143.
- (213) Tworowska, I.; Stallons, T.; Amal, S.; Wagh, N.; Rojas-Quijano, F.; Jurek, P.; Kiefer, G.; Delpassand, E.; Torgue, J. Image Guided Therapy of SSTR (+)-Neuroendocrine Tumors (NETs) Using  $^{203}\text{Pb}$ -Labeled Octreotate Analog. *J Nucl Med* **2018**, *59*, 1124.
- (214) Chong, H. S.; Song, H. A.; Ma, X.; E. Milenic, D.; D. Brady, E.; Lim, S.; Lee, H.; Baidoo, K.; Cheng, D.; Brechbiel, M. W. Novel Bimodal Bifunctional Ligands for Radioimmunotherapy and Targeted MRI. *Bioconjugate Chem.* **2008**, *19*, 1439–1447.
- (215) Bartoś, B.; Lyczko, K.; Kasperek, A.; Krajewski, S.; Bilewicz, A. Search of Ligands Suitable for  $^{212}\text{Pb}/^{212}\text{Bi}$  in Vivo Generators. *J. Radioanal. Nucl. Chem.* **2013**, *295*, 205–209.
- (216) Horlock, P. L.; Thakur, M. L.; Watson, I. A. Cyclotron Produced Lead-203. *Postgrad. Med. J.* **1975**, *51*, 751–754.
- (217) Garmestani, K.; Milenic, D. E.; Brady, E. D.; Plascjak, P. S.; Brechbiel, M. W. Purification of Cyclotron-Produced  $^{203}\text{Pb}$  for Labeling Herceptin. *Nucl. Med. Biol.* **2005**, *32*, 301–305.
- (218) Yong, K.; Brechbiel, M. Application of  $^{212}\text{Pb}$  for Targeted  $\alpha$ -Particle Therapy (TAT): Pre-Clinical and Mechanistic Understanding through to Clinical Translation. *AIMS Med. Sci.* **2015**, *2*, 228–245.
- (219) Chappell, L. L.; Dadachova, E.; Milenic, D. E.; Garmestani, K.; Wu, C.; Brechbiel, M. W. Synthesis, Characterization, and Evaluation of a Novel Bifunctional Chelating Agent for the Lead Isotopes  $^{203}\text{Pb}$  and  $^{212}\text{Pb}$ . *Nucl. Med. Biol.* **2000**, *27*, 93–100.
- (220) Burdinski, D.; Lub, J.; Pikkemaat, J. A.; Moreno Jalón, D.; Martial, S.; Del Pozo Ochoa, C. Triethylenetetramine Penta- and Hexa-Acetamide Ligands and Their Ytterbium Complexes as ParaCEST Contrast Agents for MRI. *Dalton Trans.* **2008**, 4138–4151.

- (221) Cuenot, F.; Meyer, M.; Espinosa, E.; Bucaille, A.; Burgat, R.; Guillard, R.; Marichal-Westrich, C. New Insights into the Complexation of Lead(II) by 1,4,7,10-Tetrakis(Carbamoylmethyl)-1,4,7,10-Tetraazacyclododecane (DOTAM): Structural, Thermodynamic, and Kinetic Studies. *Eur. J. Inorg. Chem.* **2008**, 267–283.
- (222) Bulimestru, I. G.; Petrenko, P. A.; Gulea, A. P.; Gdaniec, M.; Simonov, Y. A. Synthesis and Structure of Heterometallic Bi(III) Complex with Diethylenetriaminepentaacetic Acid. *Russ. J. Coord. Chem.* **2005**, 31, 420–428.
- (223) Paul-Roth, C.; Raymond, K. N. Amide Functional Group Contribution to the Stability of Gadolinium(III) Complexes: DTPA Derivatives. *Inorg. Chem.* **1995**, 34, 1408–1412.
- (224) Martell, A. E.; Smith, R. M. *Critical Stability Constants*; Plenum Press, New York, 1989; Vol. 1–6.
- (225) Clapp, L. A.; Siddons, C. J.; Whitehead, J. R.; VanDerveer, D. G.; Rogers, R. D.; Griffin, S. T.; Jones, S. B.; Hancock, R. D. Factors Controlling Metal-Ion Selectivity in the Binding Sites of Calcium-Binding Proteins. The Metal-Binding Properties of Amide Donors. A Crystallographic and Thermodynamic Study. *Inorg. Chem.* **2005**, 44, 8495–8502.
- (226) Pippin, C. G.; McMurry, T. J.; Brechbiel, M. W.; McDonald, M.; Lambrecht, R.; Milenic, D.; Roselli, M.; Colcher, D.; Gansow, O. A. Lead(II) Complexes of 1,4,7,10-Tetraazacyclododecane-N,N',N'',N'''-Tetraacetate: Solution Chemistry and Application to Tumor Localization with <sup>203</sup>Pb Labeled Monoclonal Antibodies. *Inorganica Chim. Acta* **1995**, 239, 43–51.
- (227) Belatik, A.; Hotchandani, S.; Carpentier, R.; Tajmir-Riahi, H.-A. Locating the Binding Sites of Pb(II) Ion with Human and Bovine Serum Albumins. *PLoS One* **2012**, 7, e36723.
- (228) Cawthray, J. F.; Weekes, D. M.; Sivak, O.; Creagh, A. L.; Ibrahim, F.; Iafate, M.; Haynes, C. A.; Wasan, K. M.; Orvig, C. In Vivo Study and Thermodynamic Investigation of Two Lanthanum

- Complexes, La(Dpp)<sub>3</sub> and La(XT), for the Treatment of Bone Resorption Disorders. *Chem. Sci.* **2015**, *6*, 6439–6447.
- (229) Weekes, D. M.; Cawthray, J. F.; Rieder, M.; Syeda, J.; Ali, M.; Wasan, E.; Kostelnik, T. I.; Patrick, B. O.; Panahifar, A.; Al-Dissi, A.; et al. La(iii) Biodistribution Profiles from Intravenous and Oral Dosing of Two Lanthanum Complexes, La(dpp)<sub>3</sub> and La(XT), and Evaluation as Treatments for Bone Resorption Disorders. *Metallomics* **2017**, *9*, 902–909.
- (230) Weekes, D. M.; Jaraquemada-Peláez, M. de G.; Kostelnik, T. I.; Patrick, B. O.; Orvig, C. Di- and Trivalent Metal-Ion Solution Studies with the Phosphinate-Containing Heterocycle DEDA-(PO). *Inorg. Chem.* **2017**, *56*, 10155–10161.
- (231) Maier, L.; Smith, M. J. ORGANISCHE PHOSPHORVERBINDUNGEN 72. *Phosphorus Sulfur Relat. Elem.* **1980**, *8*, 67–71.
- (232) Xu, L.; Rettig, S. J.; Orvig, C. Lanthanide Chemistry with Bis{[Bis(Carboxymethyl)Amino]Methyl}phosphinate: What Does an Extra Phosphinate Group Do to EDTA? *Inorg. Chem.* **2001**, *40*, 3734–3738.
- (233) Barta, C. A.; Sachs-Barrable, K.; Jia, J.; Thompson, K. H.; Wasan, K. M.; Orvig, C. Lanthanide Containing Compounds for Therapeutic Care in Bone Resorption Disorders. *Dalton Trans.* **2007**, 5019–5030.
- (234) Mawani, Y.; Cawthray, J. F.; Chang, S.; Sachs-Barrable, K.; Weekes, D. M.; Wasan, K. M.; Orvig, C. In Vitro Studies of Lanthanide Complexes for the Treatment of Osteoporosis. *Dalton Trans.* **2013**, *42*, 5999–6011.
- (235) Cawthray, J. F.; Creagh, A. L.; Haynes, C. A.; Orvig, C. Ion Exchange in Hydroxyapatite with Lanthanides. *Inorg. Chem.* **2015**, *54*, 1440–1445.
- (236) Song, B.; Storr, T.; Liu, S.; Orvig, C. Synthesis and Solution Studies of the Complexes of

- Trivalent Lanthanides with the Tetraazamacrocycle TETA-(PO)<sub>2</sub>. *Inorg. Chem.* **2002**, *41*, 685–692.
- (237) Kaboudin, B.; Moradi, K.; Faghihi, M. R.; Mohammadi, F. The Fluorescence Spectroscopic Studies on the Interaction of Novel Aminophosphinic Acids with Bovine Serum Albumin. *J. Lumin.* **2013**, *139*, 104–112.
- (238) Covington, A. K.; Paabo, M.; Robinson, R. A.; Bates, R. G. Use of the Glass Electrode in Deuterium Oxide and the Relation between the Standardized PD (PaD) Scale and the Operational PH in Heavy Water. *Anal. Chem.* **1968**, *40*, 700–706.
- (239) Prata, M. I. M.; Santos, A. C.; Geraldés, C. F. G. C.; Lima, J. J. P. d. Characterisation of <sup>67</sup>Ga<sup>3+</sup> Complexes of Triaza Macrocylic Ligands: Biodistribution and Clearance Studies. *Nucl. Med. Biol.* **1999**, *26*, 707–710.
- (240) Prata, M. I. M.; André, J. P.; Kovács, Z.; Takács, A. I.; Tircsó, G.; Tóth, I.; Geraldés, C. F. G. C. Gallium(III) Chelates of Mixed Phosphonate-Carboxylate Triazamacrocylic Ligands Relevant to Nuclear Medicine: Structural, Stability and in Vivo Studies. *J. Inorg. Biochem.* **2017**, *177*, 8–16.
- (241) Bervoets, A. R. J.; Behets, G. J.; Schryvers, D.; Roels, F.; Yang, Z.; Verberckmoes, S. C.; Damment, S. J. P.; Dauwe, S.; Mubiana, V. K.; Blust, R.; et al. Hepatocellular Transport and Gastrointestinal Absorption of Lanthanum in Chronic Renal Failure. *Kidney Int.* **2009**, *75*, 389–398.
- (242) Di, Y.; Wasan, E. K.; Cawthray, J.; Syeda, J.; Ali, M.; Cooper, D. M. L.; Al-Dissi, A.; Ashjaee, N.; Cheng, W.; Johnston, J.; et al. Evaluation of La(XT), a Novel Lanthanide Compound, in an OVX Rat Model of Osteoporosis. *Bone Reports* submitted (08/2020).
- (243) Ekholm, S.; Jonsson, E.; Sandvik, L.; Fagerlund, M.; Holtås, S.; Isberg, B.; Lindell, D.; Lindén, B.; Sjöberg, S.; Thuomas, K.-Å.; et al. Tolerance and Efficacy of Omniscan (Gadodiamide

- Injection) in MR Imaging of the Central Nervous System. *Acta radiol.* **1996**, *37*, 223–228.
- (244) Ramogida, C. F.; Cawthray, J. F.; Boros, E.; Ferreira, C. L.; Patrick, B. O.; Adam, M. J.; Orvig, C. H<sub>2</sub>CHXdedpa and H<sub>4</sub>CHXoctapa—Chiral Acyclic Chelating Ligands for <sup>67/68</sup>Ga and <sup>111</sup>In Radiopharmaceuticals. *Inorg. Chem.* **2015**, *54*, 2017–2031.
- (245) Wang, X.; Jaraquemada-Peláez, M. de G.; Cao, Y.; Pan, J.; Lin, K.-S.; Patrick, B. O.; Orvig, C. H<sub>2</sub>hox: Dual-Channel Oxine-Derived Acyclic Chelating Ligand for <sup>68</sup>Ga Radiopharmaceuticals. *Inorg. Chem.* **2019**, *58*, 2275–2285.
- (246) Šimeček, J.; Hermann, P.; Seidl, C.; Bruchertseifer, F.; Morgenstern, A.; Wester, H.-J.; Notni, J. Efficient Formation of Inert Bi-213 Chelates by Tetracosphorus Acid Analogues of DOTA: Towards Improved Alpha-Therapeutics. *EJNMMI Res.* **2018**, *8*, 1–6.

## Appendices

### Appendix A. Supplementary Data for Chapter 2

**Table A.1** Total activities of  $^{120\text{m}}\text{Sb}$  and  $^{117\text{m}}\text{Sn}$  measured from target solution.<sup>a</sup>

Radionuclide	Target Solution Activity (Bq/mL)	Total Activity (kBq) <sup>b</sup>
$^{120\text{m}}\text{Sb}$	$1.19 \times 10^5$	$1.42 \times 10^3$
$^{117\text{m}}\text{Sn}$	$2.37 \times 10^3$	$2.85 \times 10^1$

<sup>a</sup>Activities decay corrected to EOB <sup>b</sup>Total volume 12 mL.

**Table A.2** Activities following liquid-liquid extraction of tin target.<sup>a</sup>

Solution	$^{120\text{m}}\text{Sb}$ Activity (Bq/mL)	$^{120\text{m}}\text{Sb}$ Activity Error (Bq/mL)	$^{117\text{m}}\text{Sn}$ Activity (Bq/mL)	$^{117\text{m}}\text{Sn}$ Activity Error (Bq/mL)
Target Solution	$1.19 \times 10^5$	$3.71 \times 10^3$	$2.37 \times 10^3$	$3.96 \times 10^2$
Extracted Target Solution	$3.46 \times 10^3$	$2.67 \times 10^2$	$1.99 \times 10^3$	$2.01 \times 10^2$
HCl Wash #1	0	0	0	0
HCl Wash #2	$5.02 \times 10^2$	$1.07 \times 10^2$	0	0
Extracted Ether	$5.12 \times 10^3$	$3.15 \times 10^2$	0	0
Final Citrate Solution	$1.04 \times 10^5$	$3.30 \times 10^3$	0	0

<sup>a</sup>Activities decay corrected to EOB. Activity error reported directly from gamma spectrometer following data collection.

**Table A.3** Activities of  $^{120\text{m}}\text{Sb}$  and  $^{117\text{m}}\text{Sn}$  expressed as a fraction over total target solution activity.<sup>a</sup>

Solution	$^{120\text{m}}\text{Sb}$ Activity (/initial activity)	$^{117\text{m}}\text{Sn}$ Activity (/initial activity)
Extracted Target Solution	$0.04 \pm 0.003$	$1.05 \pm 0.2$
HCl Wash #1	0.00	0.00
HCl Wash #2	$0.01 \pm 0.001$	0.00
Extracted Ether	$0.05 \pm 0.004$	0.00
Final Citrate Solution	$1.09 \pm 0.05^b$	0.00

<sup>a</sup>Values calculated by solution concentration and volume, while correcting for sacrificed volume. Activity then divided by

initial target solution activity. Reported error propagated from experimental data. <sup>b</sup>Inflation likely due to evaporation of ether.

## Appendix B. Supplementary Data for Chapter 3

**Table A.4** Crystallographic information for H<sub>6</sub>phospa and H<sub>6</sub>dipedpa.

Compound	H <sub>6</sub> phospa	H <sub>6</sub> dipedpa
Formula	C <sub>18</sub> H <sub>26</sub> N <sub>4</sub> O <sub>11</sub> P <sub>2</sub>	C <sub>20</sub> H <sub>40</sub> N <sub>4</sub> O <sub>16</sub> P <sub>2</sub>
<i>D</i> <sub>calc.</sub> / g cm <sup>-3</sup>	1.636	1.500
$\mu$ /mm <sup>-1</sup>	0.266	0.231
Formula Weight	536.37	654.50
Colour	white	colorless
Shape	needle	rectangular
Size/mm <sup>3</sup>	0.03×0.01×0.001	0.01×0.01×0.001
<i>T</i> /K	273(2)	296(2)
Crystal System	monoclinic	monoclinic
Space Group	<i>C</i> 2/ <i>c</i>	<i>P</i> 2 <sub>1</sub>
<i>a</i> /Å	9.403(2)	8.5942(10)
<i>b</i> /Å	12.298(3)	18.759(2)
<i>c</i> /Å	18.868(4)	9.1396(11)
$\alpha$ /°	90	90
$\beta$ /°	91.417(5)	100.374(3)
$\gamma$ /°	90	90
<i>V</i> /Å <sup>3</sup>	2181.3(8)	1449.4(3)
<i>Z</i>	4	2
<i>Z</i> '	0.5	1
Wavelength/Å	0.710730	0.71073
Radiation type	MoK $\alpha$	MoK $\alpha$
$\theta$ <sub>min</sub> /°	2.159	2.171
$\theta$ <sub>max</sub> /°	28.345	22.564
Measured Refl.	14594	23927
Independent Refl.	2728	3810
Reflections with <i>I</i> > 2( <i>I</i> )	2197	2753
<i>R</i> <sub>int</sub>	0.0481	0.1439
Parameters	212	402
Restraints	14	480
Largest Peak	0.694	0.269
Deepest Hole	-0.794	-0.308
Goof	1.182	1.001
<i>wR</i> <sub>2</sub> (all data)	0.1378	0.0971
<i>wR</i> <sub>2</sub>	0.1314	0.0847
<i>R</i> <sub>1</sub> (all data)	0.0899	0.0915
<i>R</i> <sub>1</sub>	0.0708	0.0502

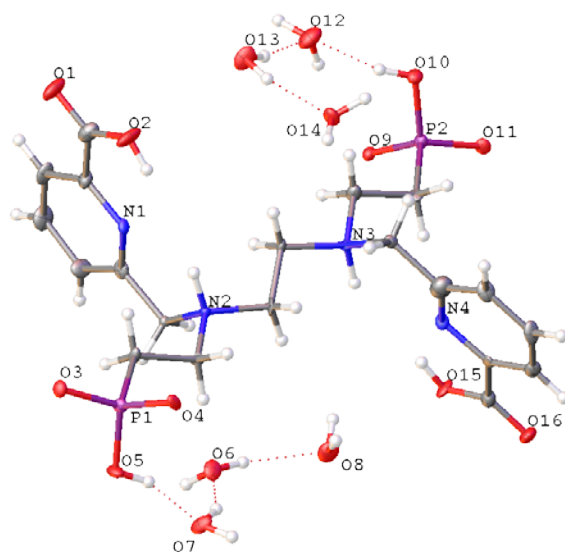


**Figure A.1** ORTEP diagrams of H<sub>6</sub>dipedpa with water H-bonding shown.

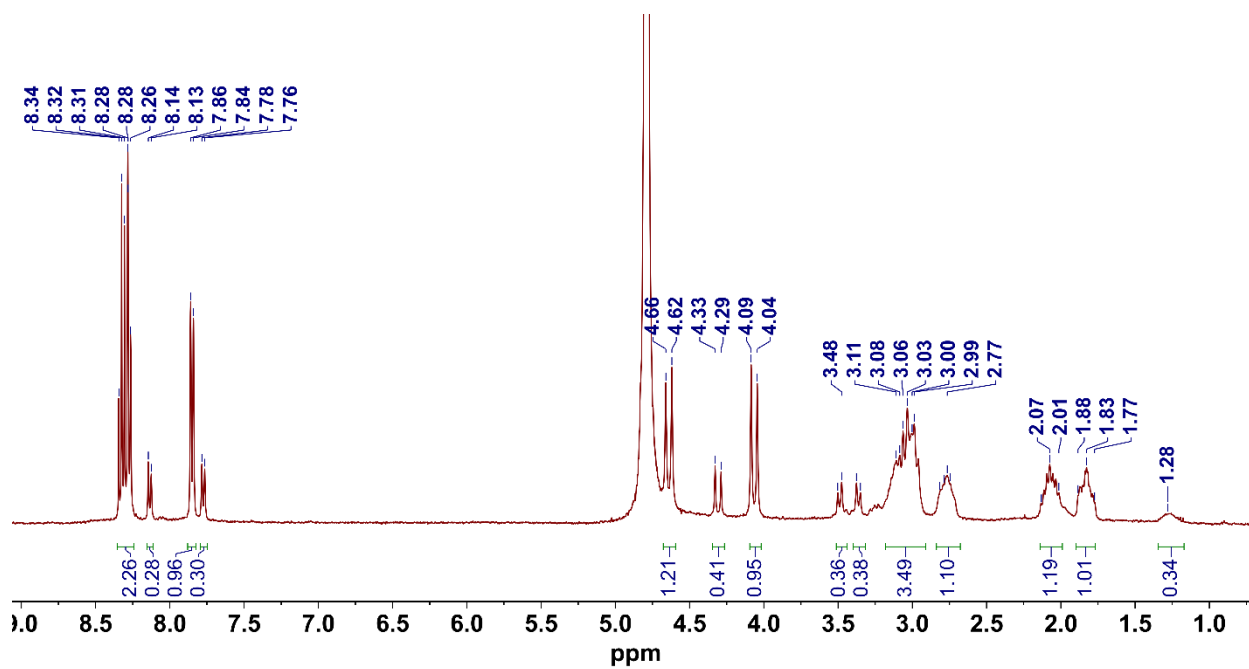


**Figure A.2** <sup>1</sup>H NMR spectrum of the In<sup>3+</sup>-H<sub>6</sub>dipedpa complex (400 MHz, 298 K, D<sub>2</sub>O, pD = 7)

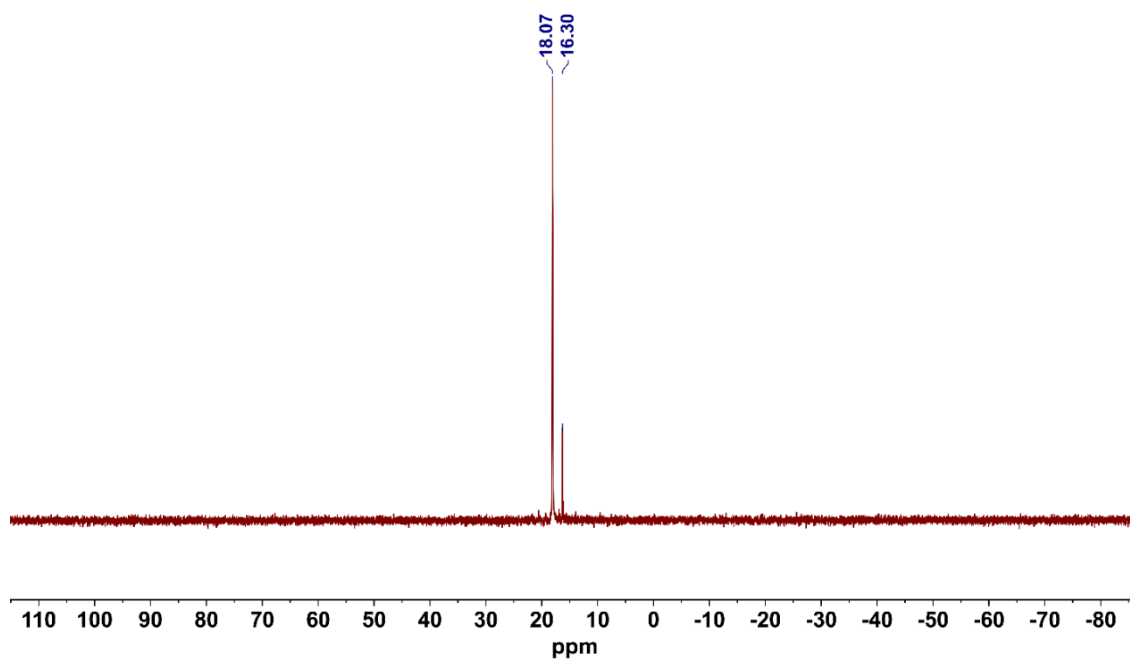


**Figure A.3**  $^{31}\text{P}\{^1\text{H}\}$  NMR spectrum (bottom) of the  $\text{In}^{3+}$ - $\text{H}_6$ dipedpa complex (162 MHz, 298 K,  $\text{D}_2\text{O}$ ,  $\text{pD} = 7$ ).

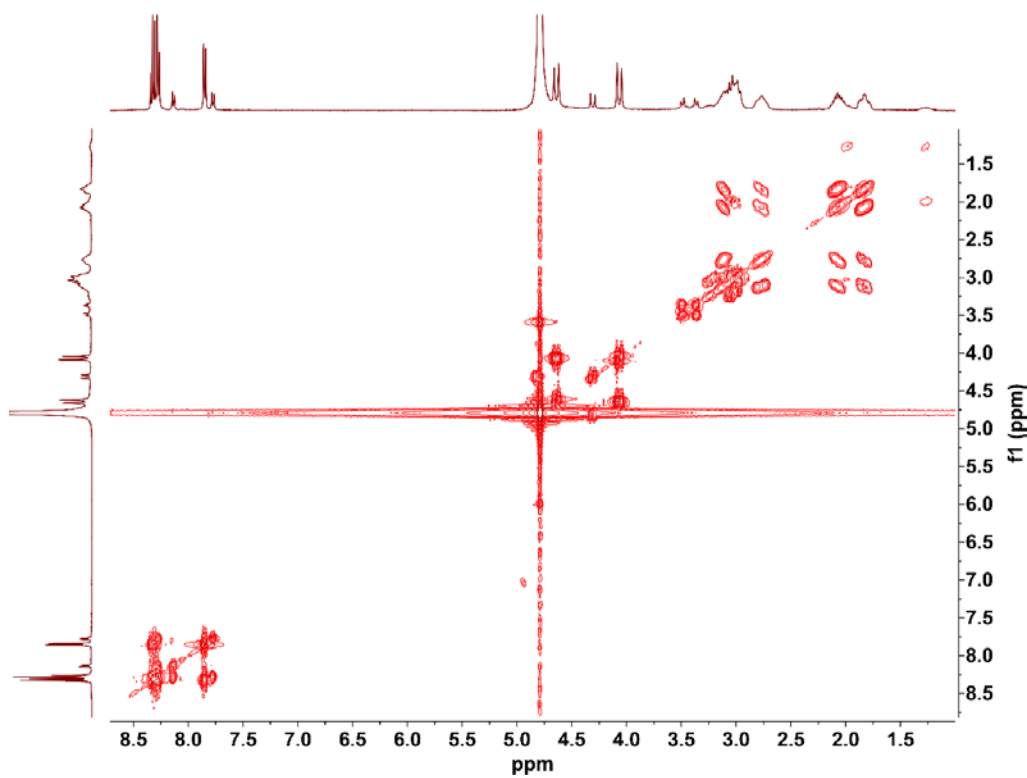


**Figure A.4**  $^1\text{H}$ - $^1\text{H}$  COSY spectrum of the  $\text{In}^{3+}$ - $\text{H}_6$ dipedpa complex (400 MHz, 298 K,  $\text{D}_2\text{O}$ ,  $\text{pD} = 7$ ).

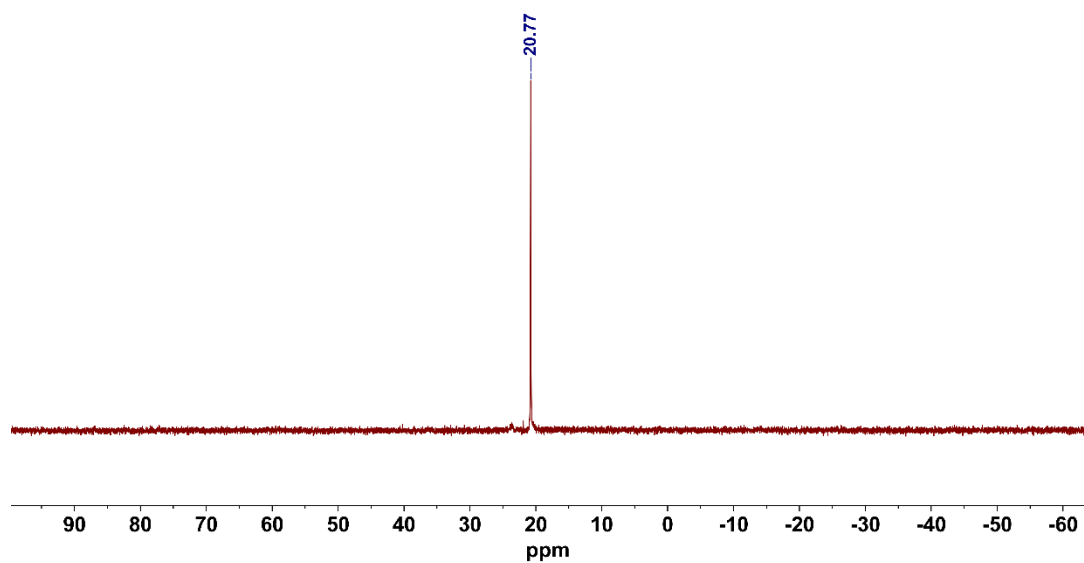


**Figure A.5**  $^{31}\text{P}\{^1\text{H}\}$  NMR spectrum of the  $\text{La}^{3+}$ - $\text{H}_6\text{dipedpa}$  complex (162 MHz, 298 K,  $\text{D}_2\text{O}$ , pD = 7).

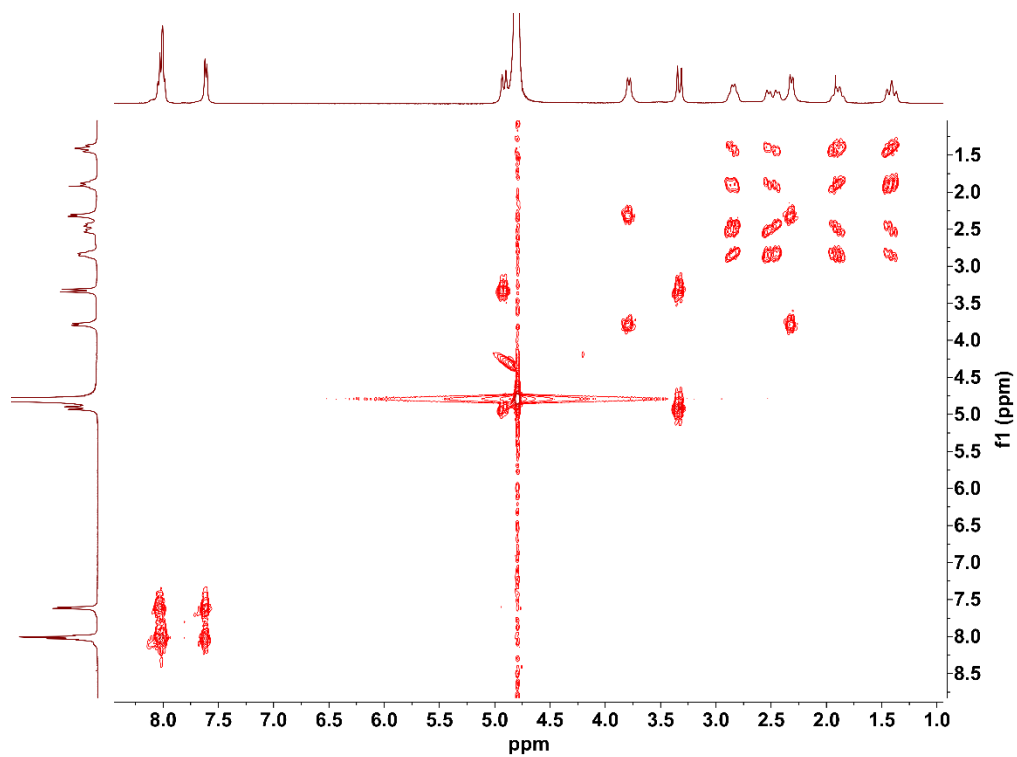


**Figure A.6**  $^1\text{H}$ - $^1\text{H}$  COSY spectrum of the  $\text{La}^{3+}$ - $\text{H}_6\text{dipedpa}$  complex (400 MHz, 298 K,  $\text{D}_2\text{O}$ , pD = 7).

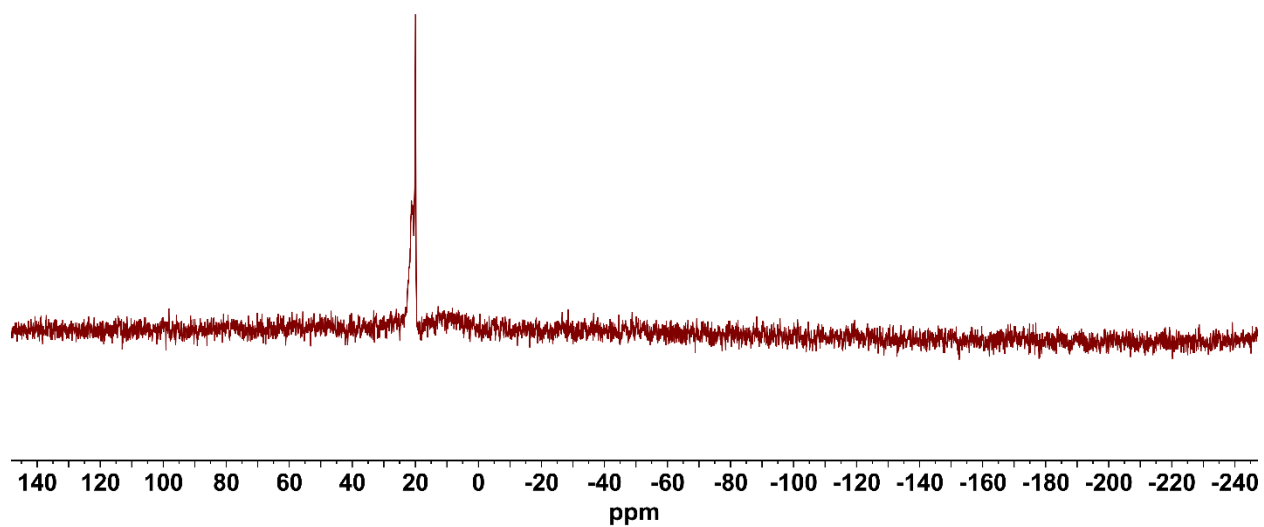


**Figure A.7**  $^{31}\text{P}\{^1\text{H}\}$  NMR spectrum of the  $\text{Sc}^{3+}$ - $\text{H}_6\text{dipedpa}$  complex (162 MHz, 298 K,  $\text{D}_2\text{O}$ , pD = 7).

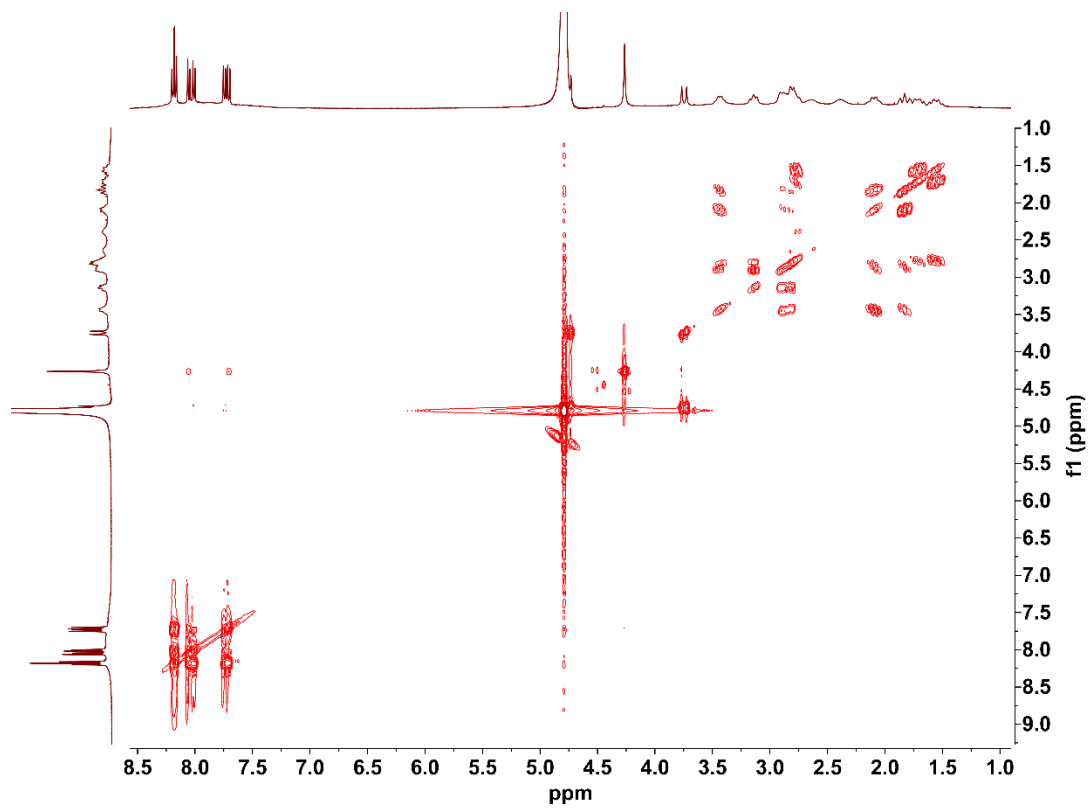


**Figure A.8**  $^1\text{H}$ - $^1\text{H}$  COSY spectrum of the  $\text{Sc}^{3+}$ - $\text{H}_6\text{dipedpa}$  complex (400 MHz, 298 K,  $\text{D}_2\text{O}$ , pD = 7).

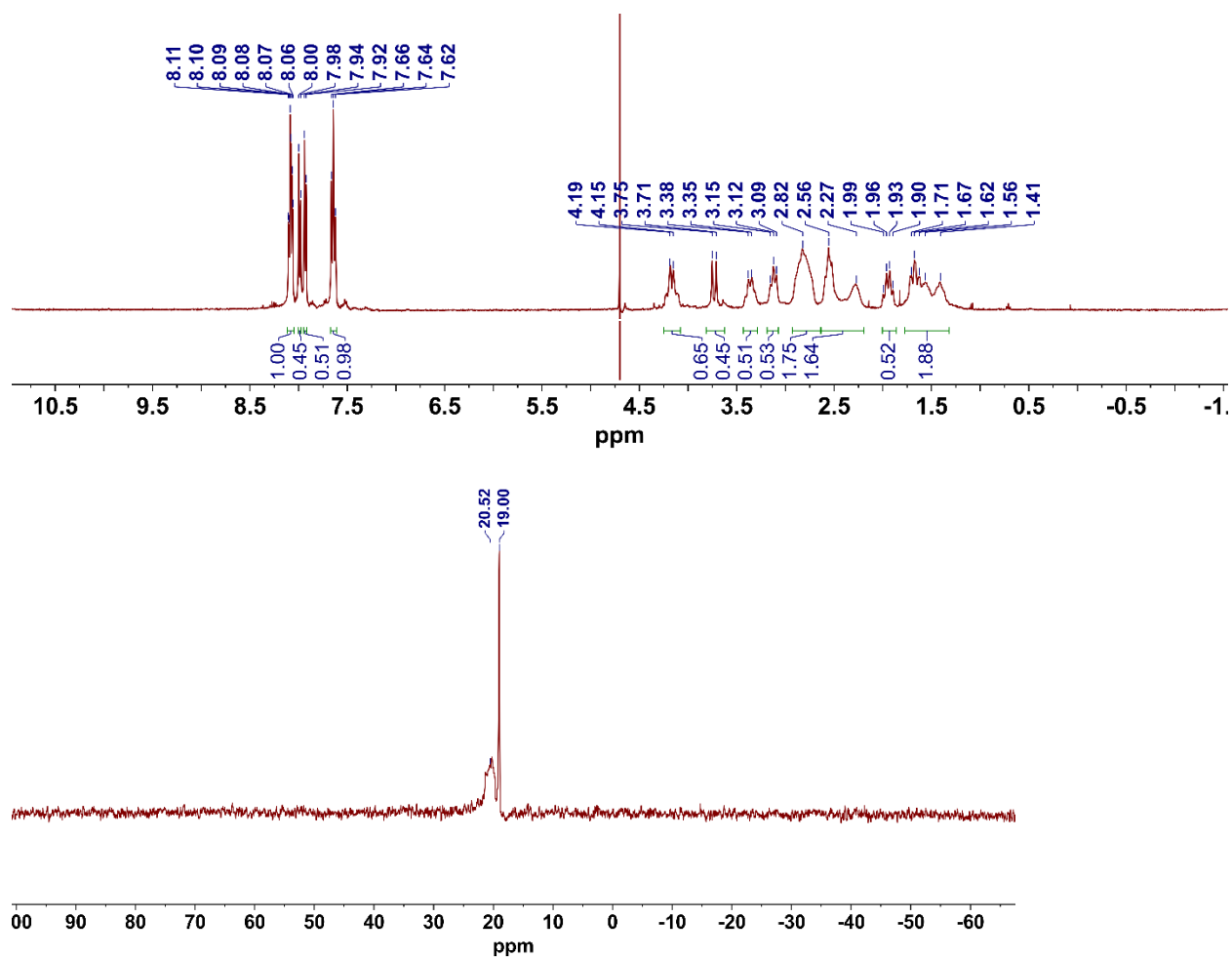


**Figure A.9**  $^1H$  NMR spectrum (top) of the  $Y^{3+}$ - $H_6dipeda$  complex (400 MHz, 298 K,  $D_2O$ , pH = 7);  $^{31}P\{^1H\}$  NMR spectrum (bottom) of the  $Y^{3+}$ - $H_6dipeda$  complex (162 MHz, 298 K,  $D_2O$ , pH = 7).

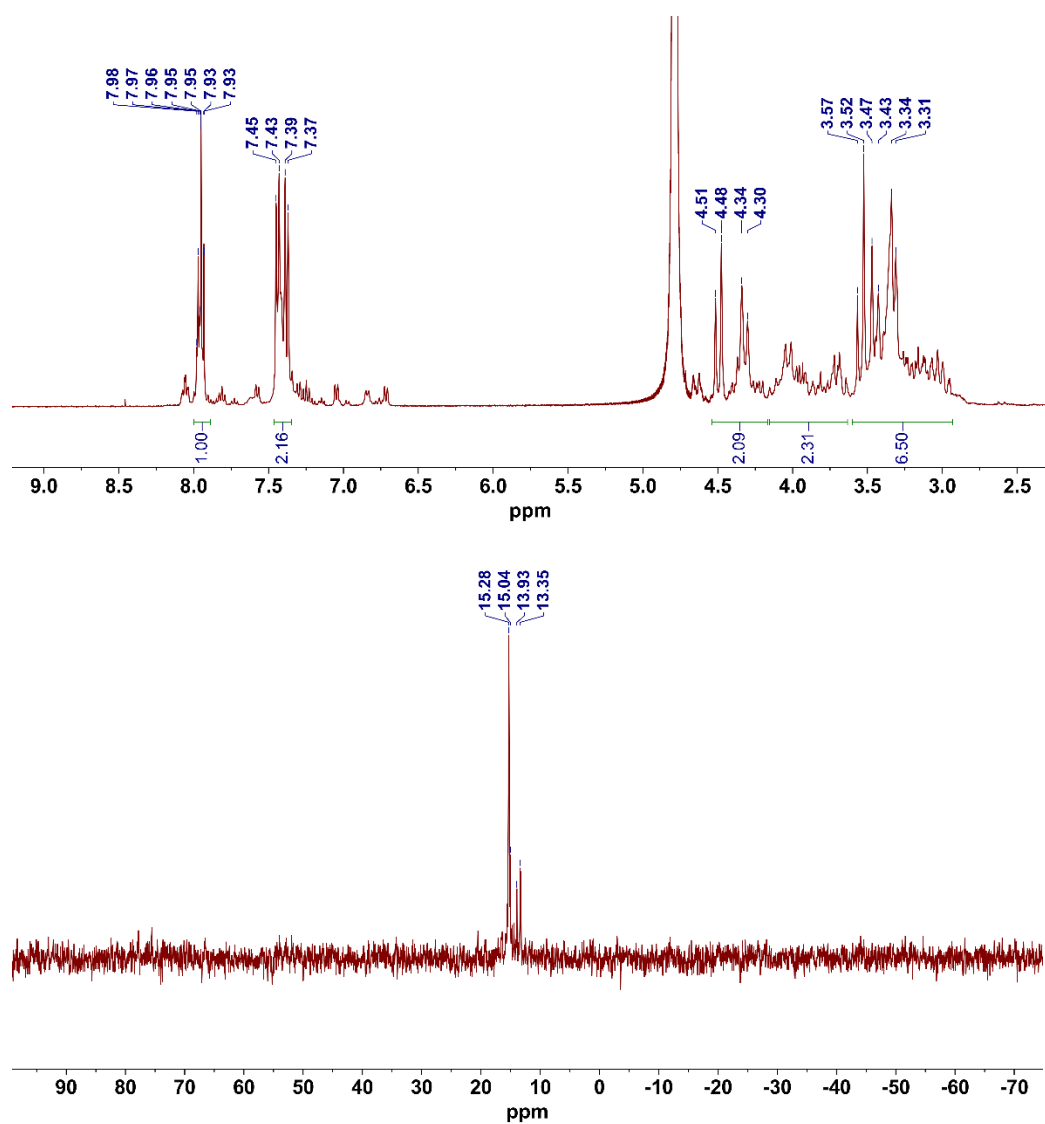


**Figure A.10.**  $^1\text{H}$  NMR spectrum (top) of the  $\text{In}^{3+}$ - $\text{H}_6\text{eppy}$  complex (400 MHz, 298 K,  $\text{D}_2\text{O}$ , pH = 7);  $^{31}\text{P}\{^1\text{H}\}$  NMR spectrum (bottom) of the  $\text{In}^{3+}$ - $\text{H}_6\text{eppy}$  complex (162 MHz, 298 K,  $\text{D}_2\text{O}$ , pH = 7).

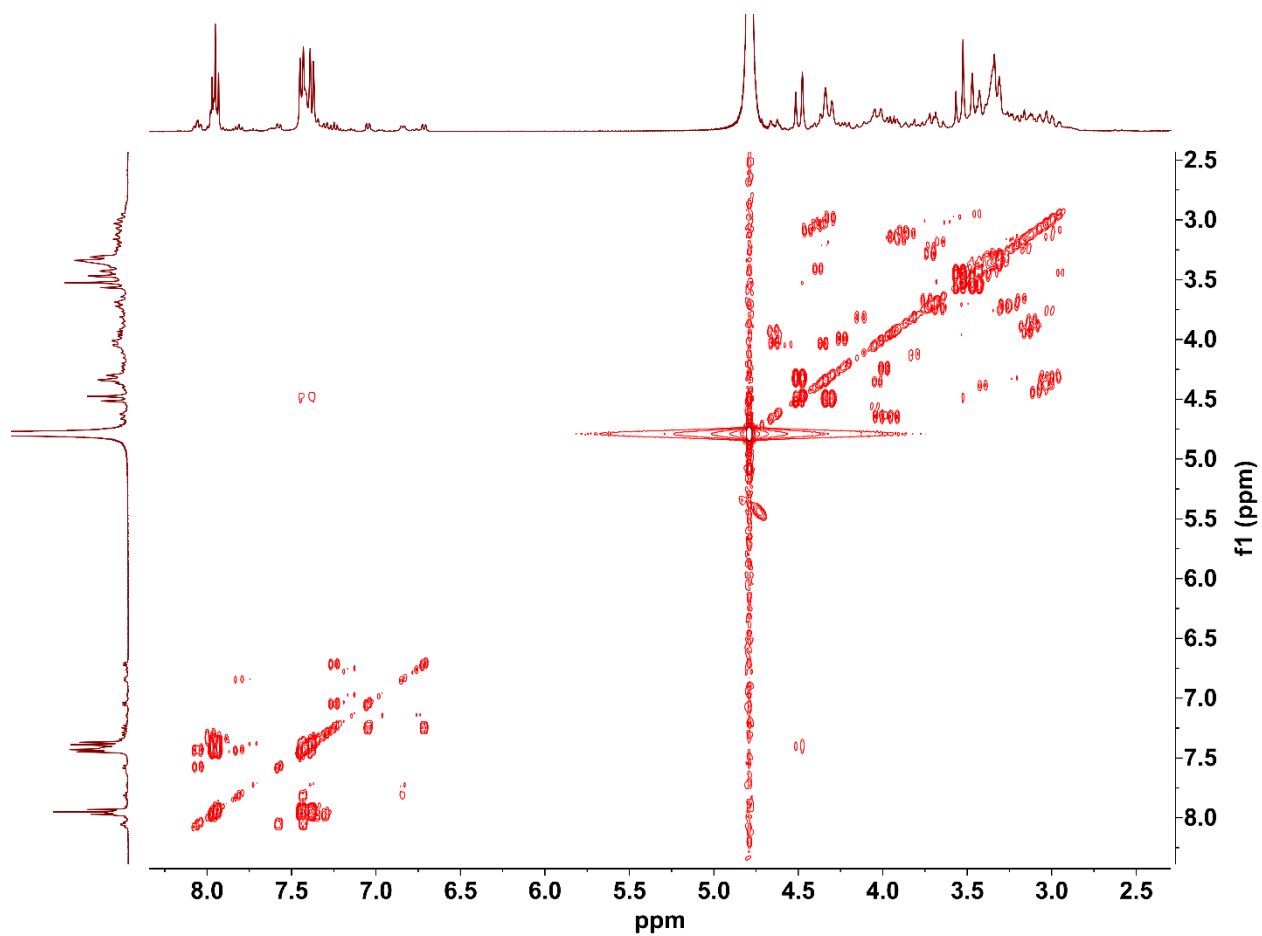


**Figure A.11**  $^1\text{H}$ - $^1\text{H}$  COSY spectrum of the  $\text{In}^{3+}$ - $\text{H}_6\text{eppy}$  complex (400 MHz, 298 K,  $\text{D}_2\text{O}$ ,  $\text{pD} = 7$ ).

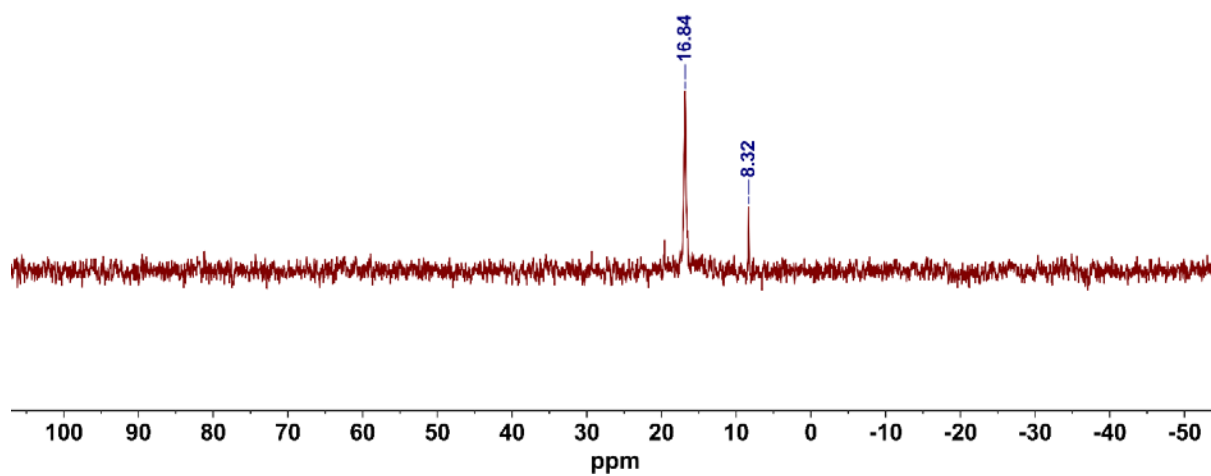


**Figure A.12**  $^{31}\text{P}\{^1\text{H}\}$  NMR spectrum of the  $\text{La}^{3+}$ - $\text{H}_6\text{eppy}$  complex (162 MHz, 298 K,  $\text{D}_2\text{O}$ ,  $\text{pD} = 4$ ).

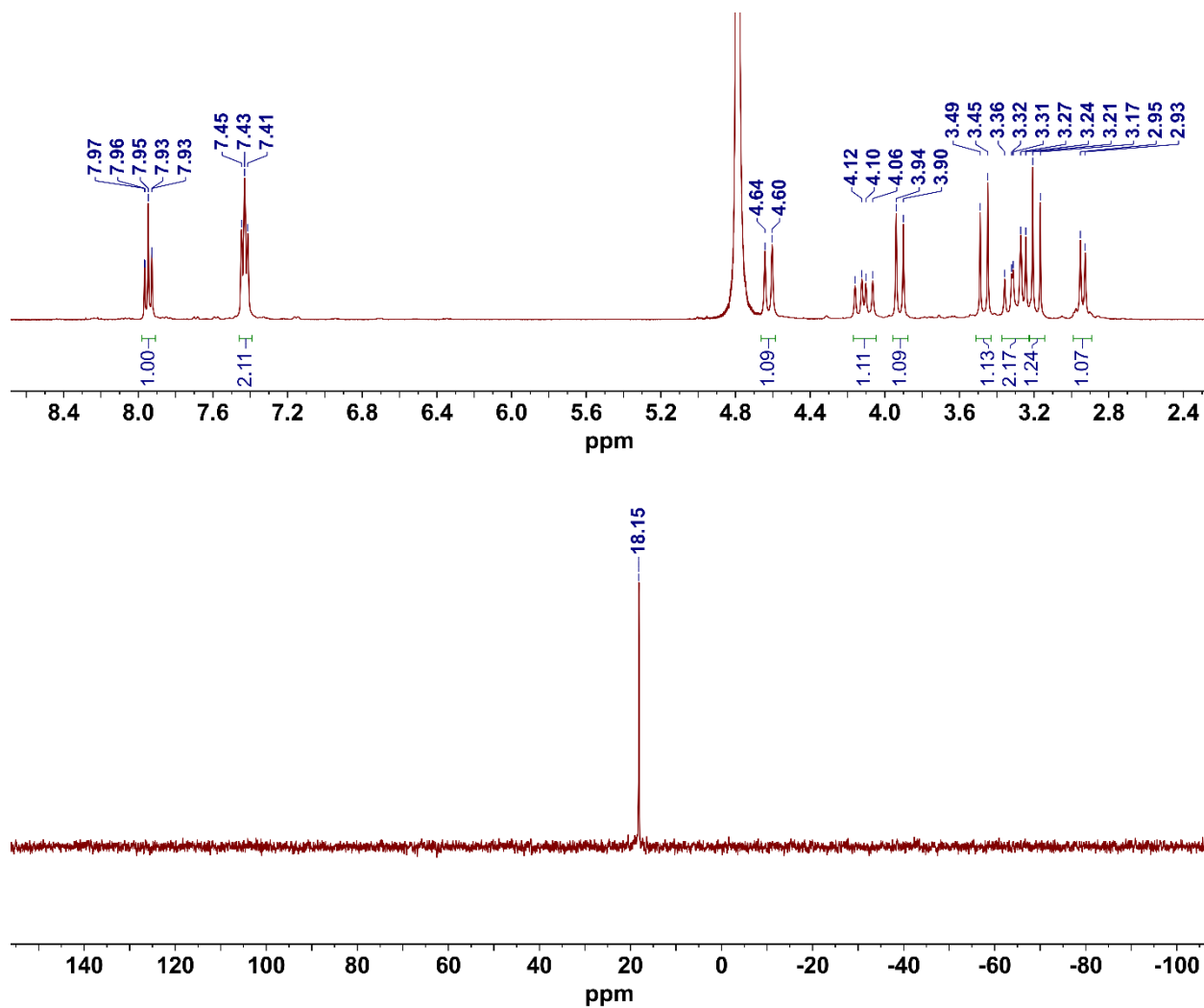


**Figure A.13** <sup>1</sup>H NMR spectrum (top) of the Lu<sup>3+</sup>-H<sub>6</sub>eppy complex (400 MHz, 298 K, D<sub>2</sub>O, pD = 4); <sup>31</sup>P{<sup>1</sup>H} NMR spectrum (bottom) of the Lu<sup>3+</sup>-H<sub>6</sub>eppy complex (162 MHz, 298 K, D<sub>2</sub>O, pD = 4).

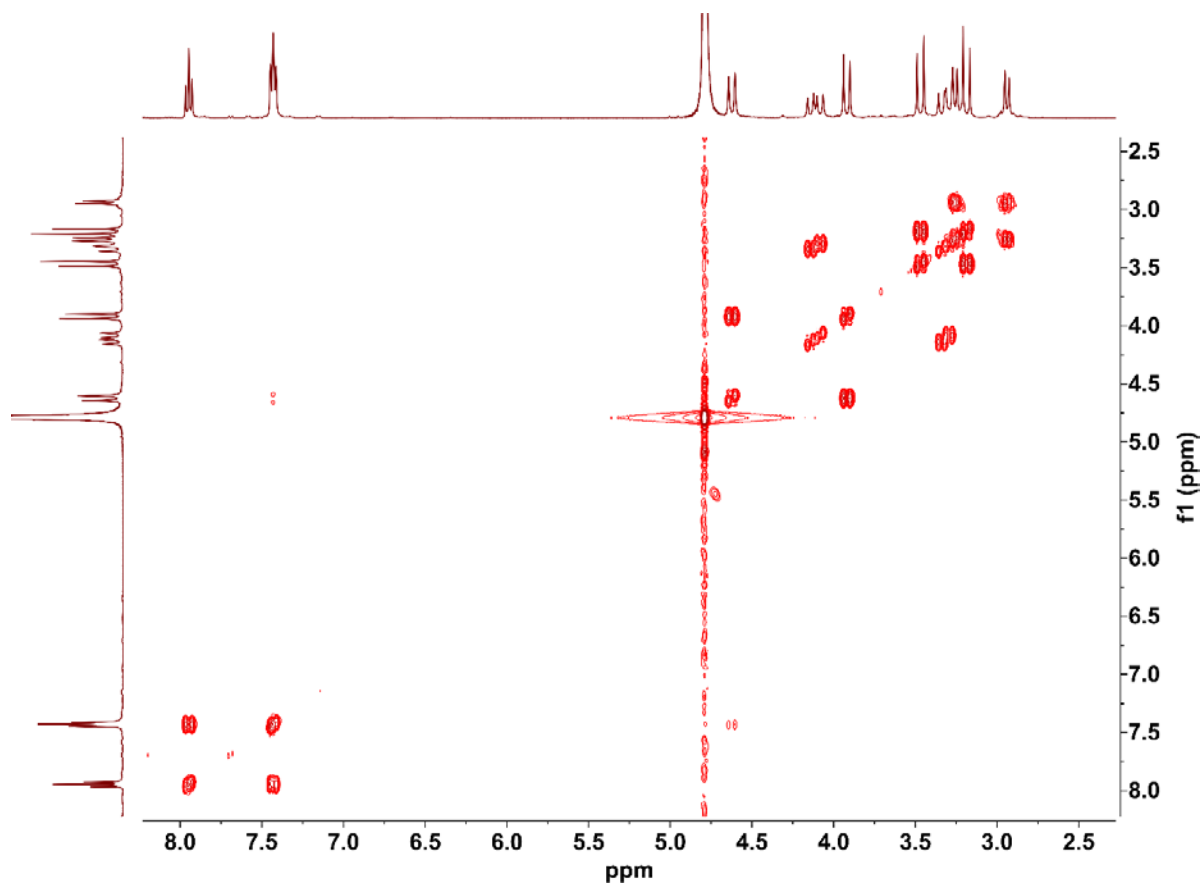


**Figure A.14**  $^1\text{H}$ - $^1\text{H}$  COSY spectrum of the  $\text{Lu}^{3+}$ - $\text{H}_6\text{eppy}$  complex (400 MHz, 298 K,  $\text{D}_2\text{O}$ , pD = 4).

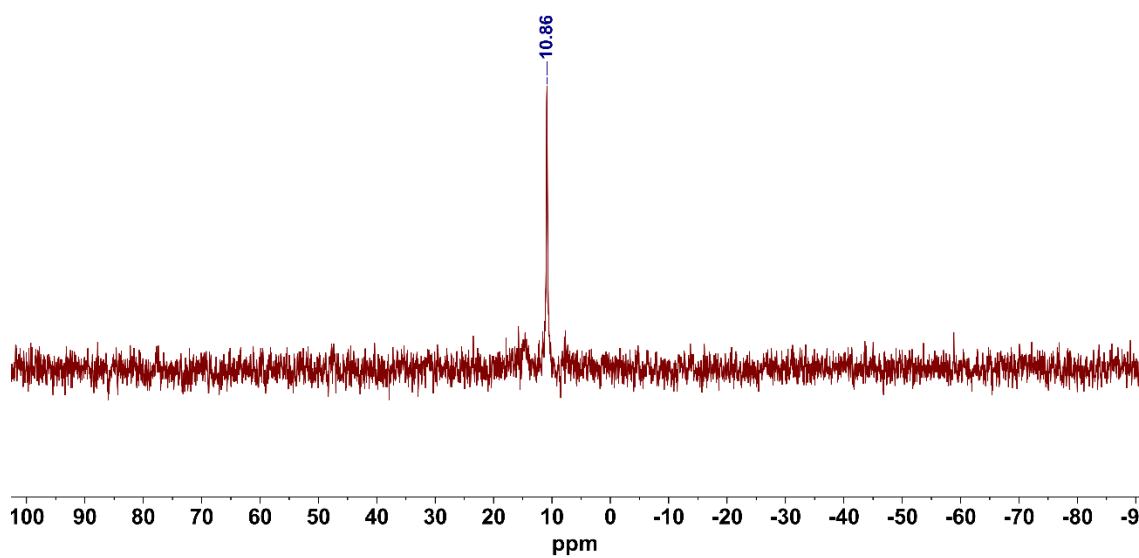


**Figure A.15**  $^{31}\text{P}\{^1\text{H}\}$  NMR spectrum of the  $\text{Sc}^{3+}$ - $\text{H}_6\text{eppy}$  complex (162 MHz, 298 K,  $\text{D}_2\text{O}$ , pD = 4).

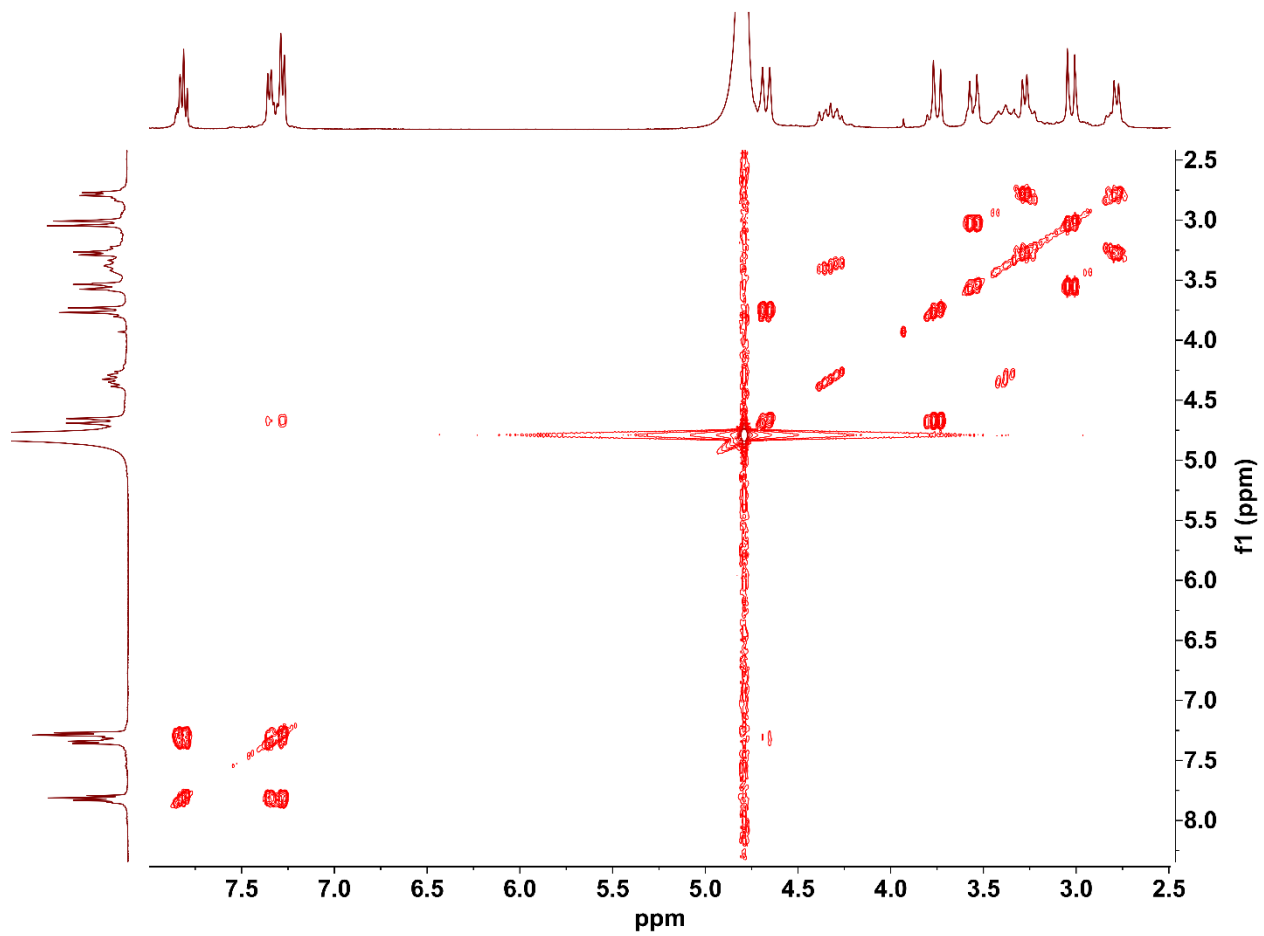


**Figure A.16**  $^1\text{H}$ - $^1\text{H}$  COSY spectrum of the  $\text{Sc}^{3+}$ - $\text{H}_6\text{eppy}$  complex (400 MHz, 298 K,  $\text{D}_2\text{O}$ ,  $\text{pD} = 4$ ).

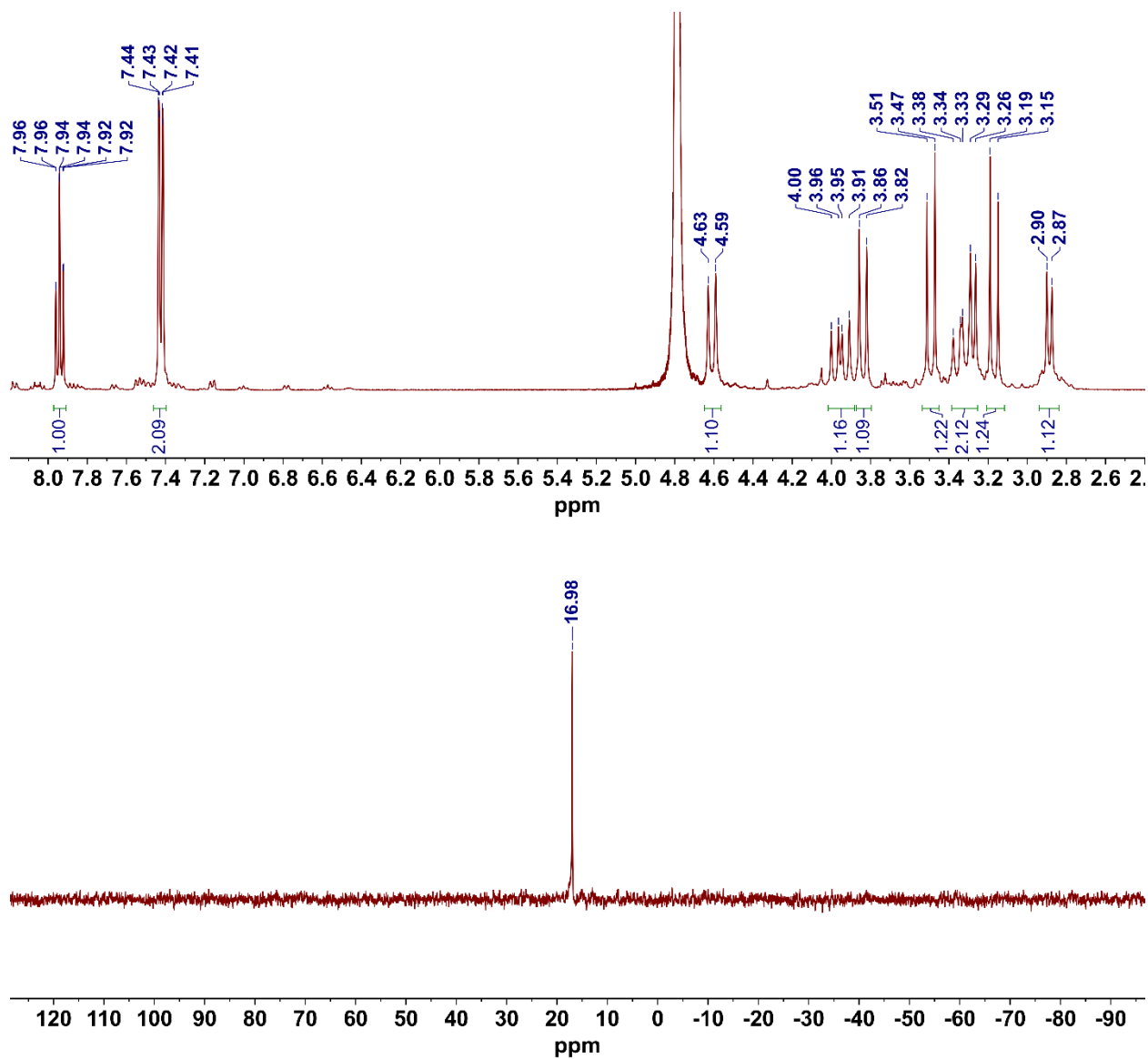


**Figure A.17**  $^1H$  NMR spectrum (top) of the  $Y^{3+}$ - $H_6eppy$  complex (400 MHz, 298 K,  $D_2O$ , pH = 4);  $^{31}P\{^1H\}$  NMR spectrum (bottom) of the  $Y^{3+}$ - $H_6eppy$  complex (162 MHz, 298 K,  $D_2O$ , pH = 4).

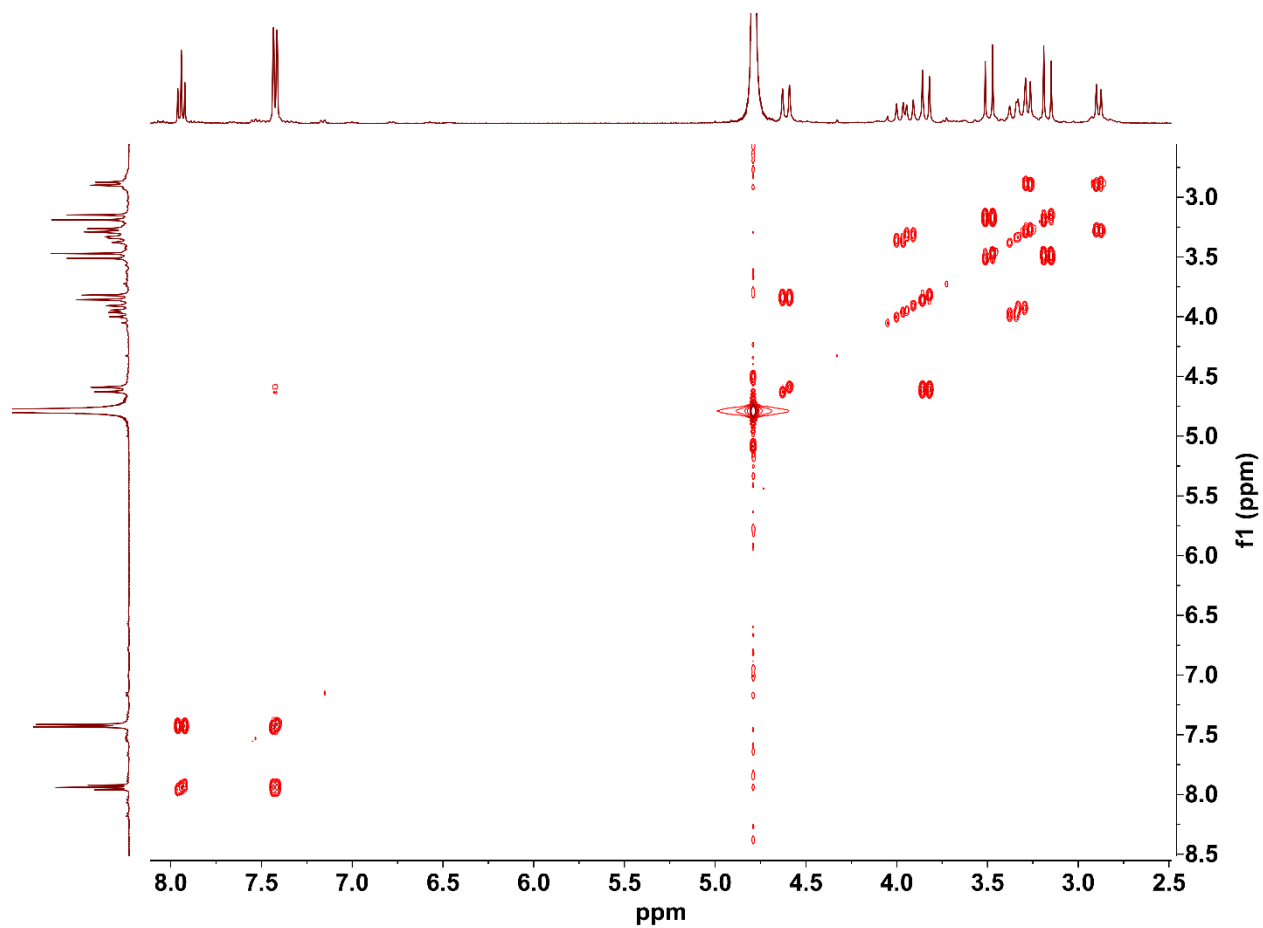


**Figure A.18**  $^1\text{H}$ - $^1\text{H}$  COSY spectrum of the  $\text{Y}^{3+}$ - $\text{H}_6\text{eppy}$  complex (400 MHz, 298 K,  $\text{D}_2\text{O}$ ,  $\text{pD} = 4$ ).

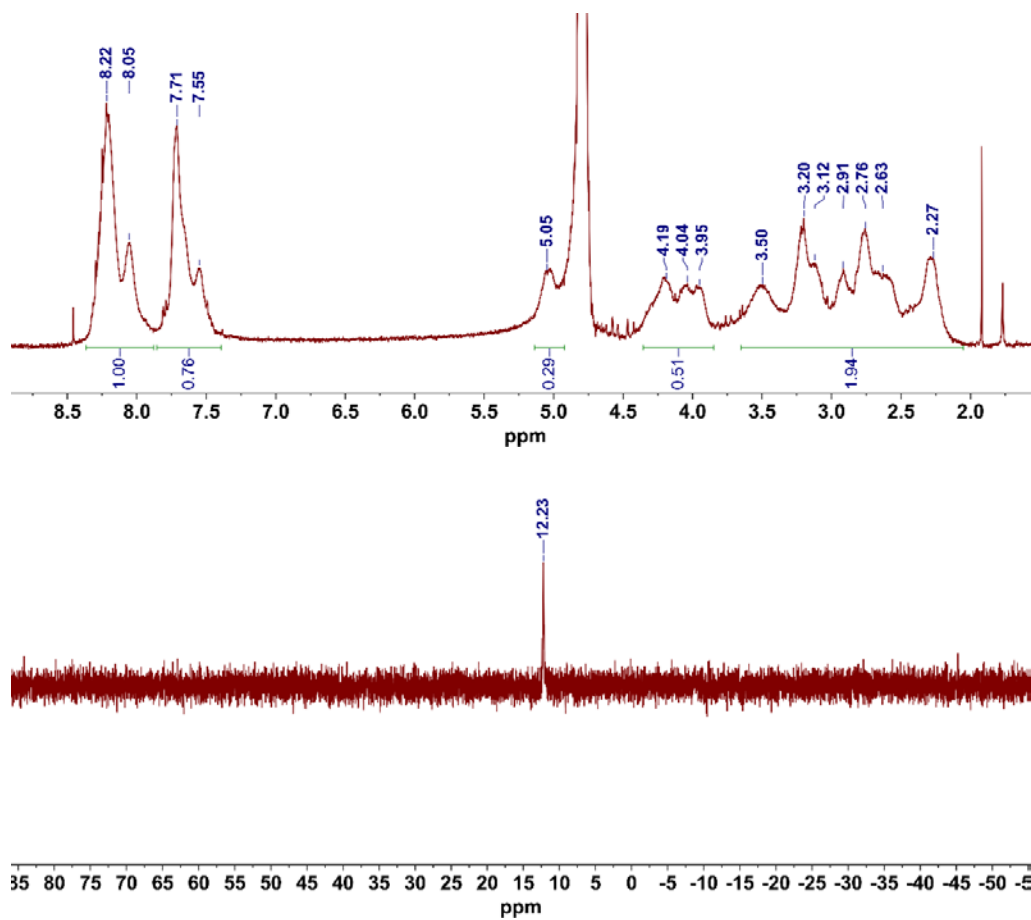


**Figure A.19**  $^1\text{H}$  NMR spectrum (top) of the  $\text{In}^{3+}$ - $\text{H}_6\text{phospa}$  complex (400 MHz, 298 K,  $\text{D}_2\text{O}$ , pH = 7);  $^{31}\text{P}\{^1\text{H}\}$  NMR spectrum (bottom) of the  $\text{In}^{3+}$ - $\text{H}_6\text{phospa}$  complex (162 MHz, 298 K,  $\text{D}_2\text{O}$ , pH = 7).

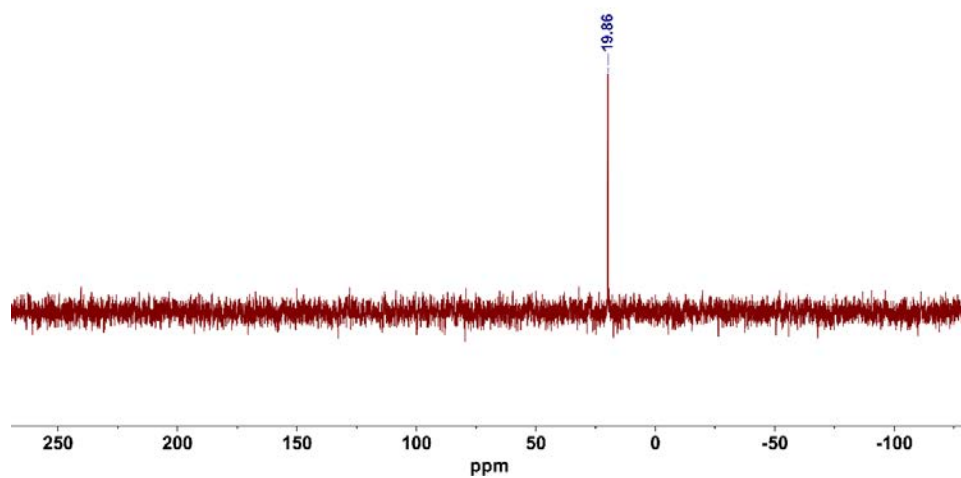


**Figure A.20**  $^{31}\text{P}\{^1\text{H}\}$  NMR spectrum of the  $\text{La}^{3+}$ - $\text{H}_6\text{phospa}$  complex (162 MHz, 298 K,  $\text{D}_2\text{O}$ , pH = 7).

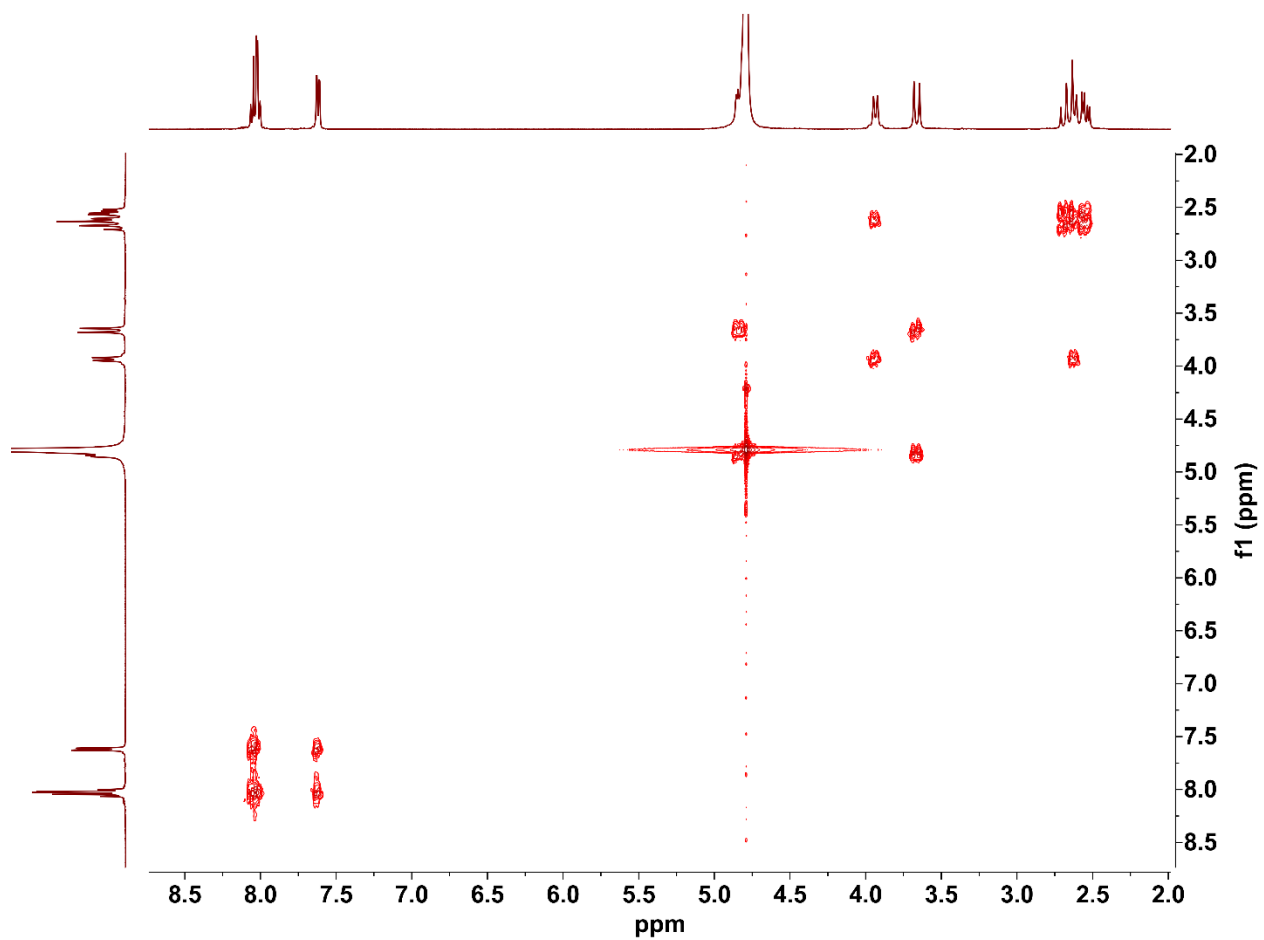


**Figure A.21**  $^1\text{H}$ - $^1\text{H}$  COSY spectrum of the  $\text{La}^{3+}$ - $\text{H}_6\text{phospa}$  complex (400 MHz, 298 K,  $\text{D}_2\text{O}$ ,  $\text{pD} = 7$ ).

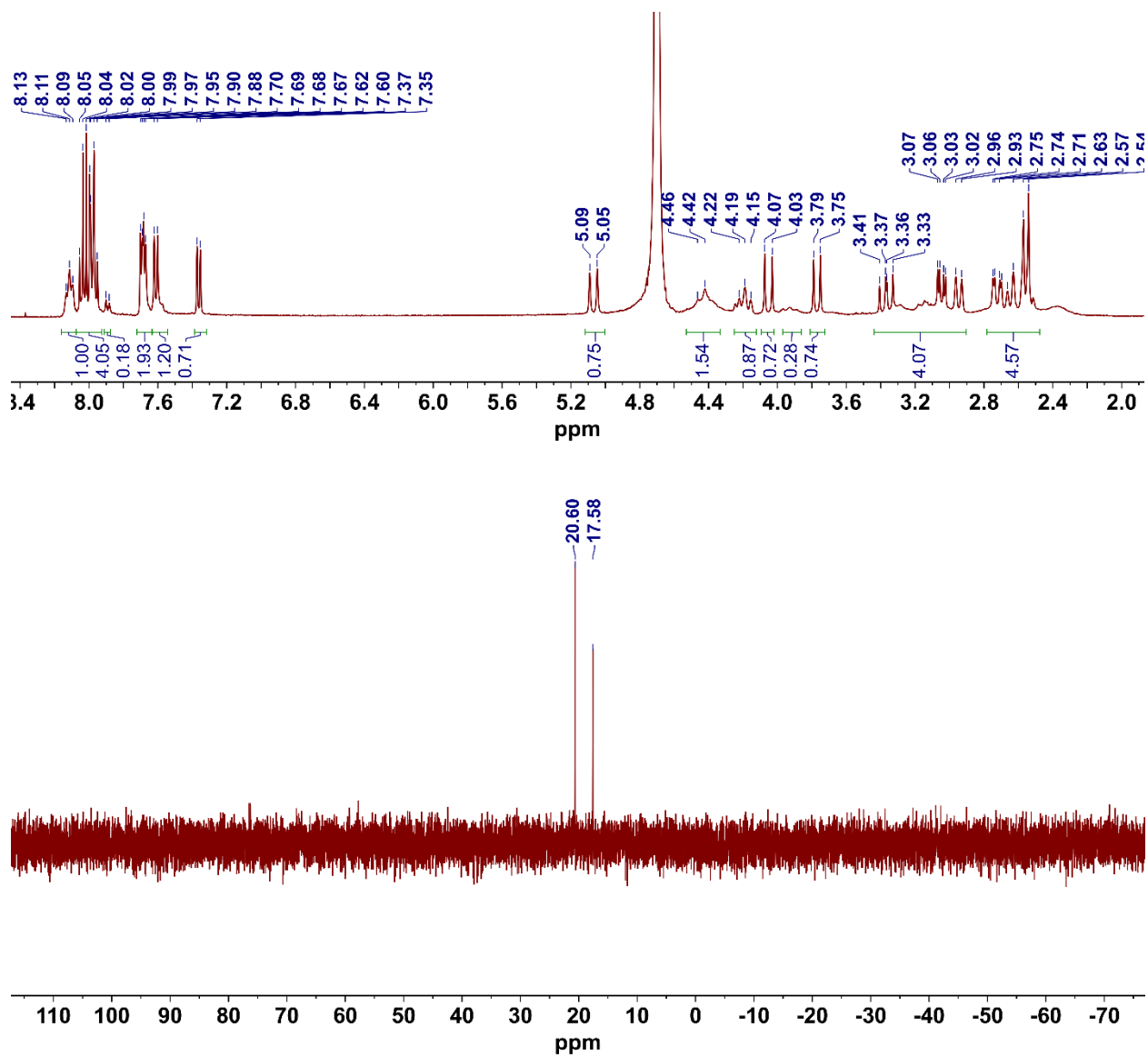


**Figure A.22** <sup>1</sup>H NMR spectrum (top) of the Lu<sup>3+</sup>-H<sub>6</sub>phospa complex (400 MHz, 298 K, D<sub>2</sub>O, pH = 7); <sup>31</sup>P{<sup>1</sup>H} NMR spectrum (bottom) of the Lu<sup>3+</sup>-H<sub>6</sub>phospa complex (162 MHz, 298 K, D<sub>2</sub>O, pH = 7).

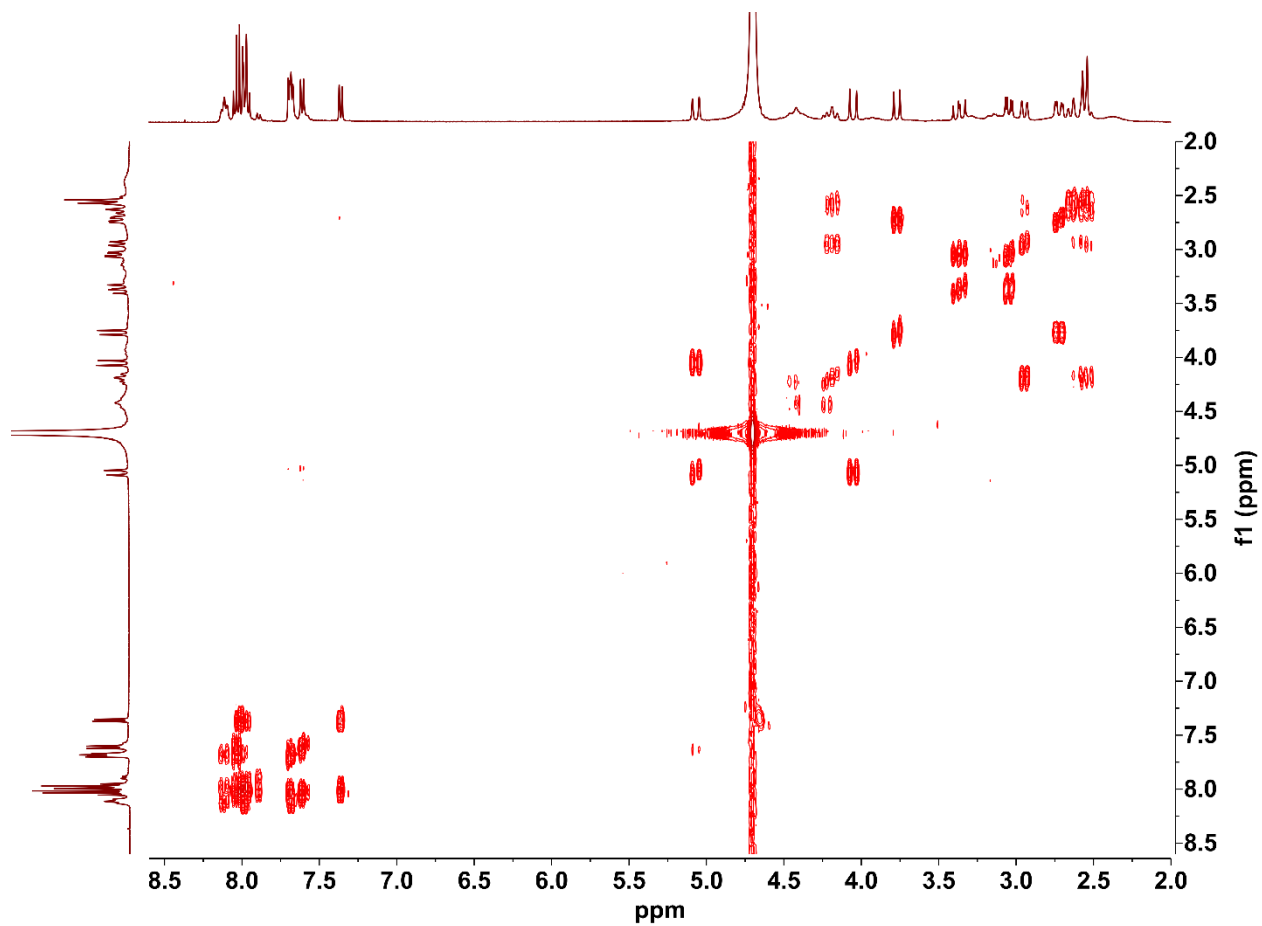


**Figure A.23**  $^1\text{H}$ - $^1\text{H}$  COSY spectrum of the  $\text{Lu}^{3+}$ - $\text{H}_6\text{phospa}$  complex (400 MHz, 298 K,  $\text{D}_2\text{O}$ , pD = 7).

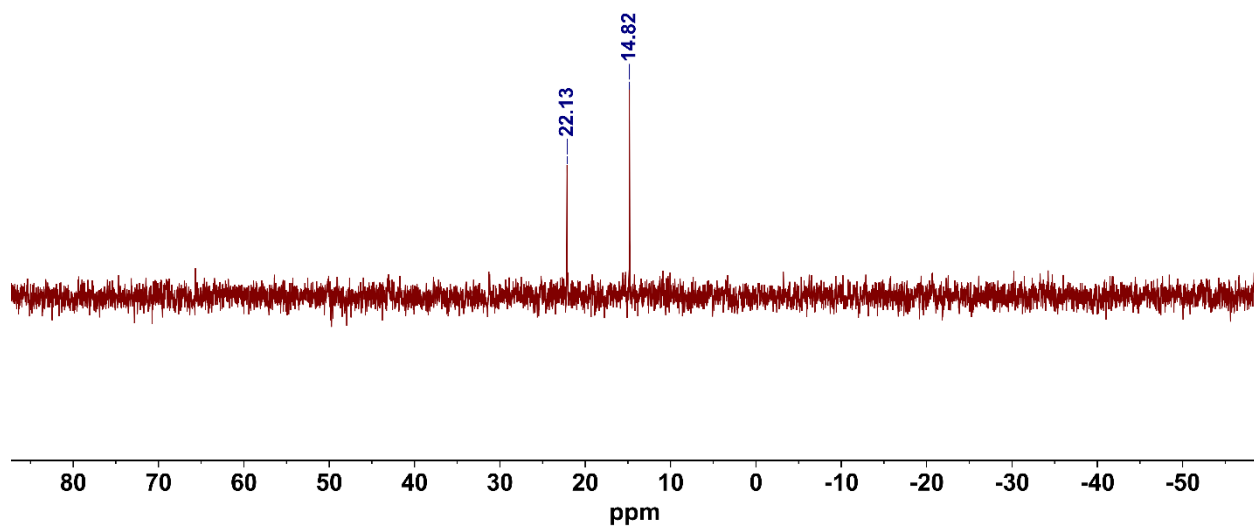


**Figure A.24**  $^{31}\text{P}\{^1\text{H}\}$  NMR spectrum of the  $\text{Sc}^{3+}$ - $\text{H}_6\text{phospa}$  complex (162 MHz, 298 K,  $\text{D}_2\text{O}$ , pD = 4).

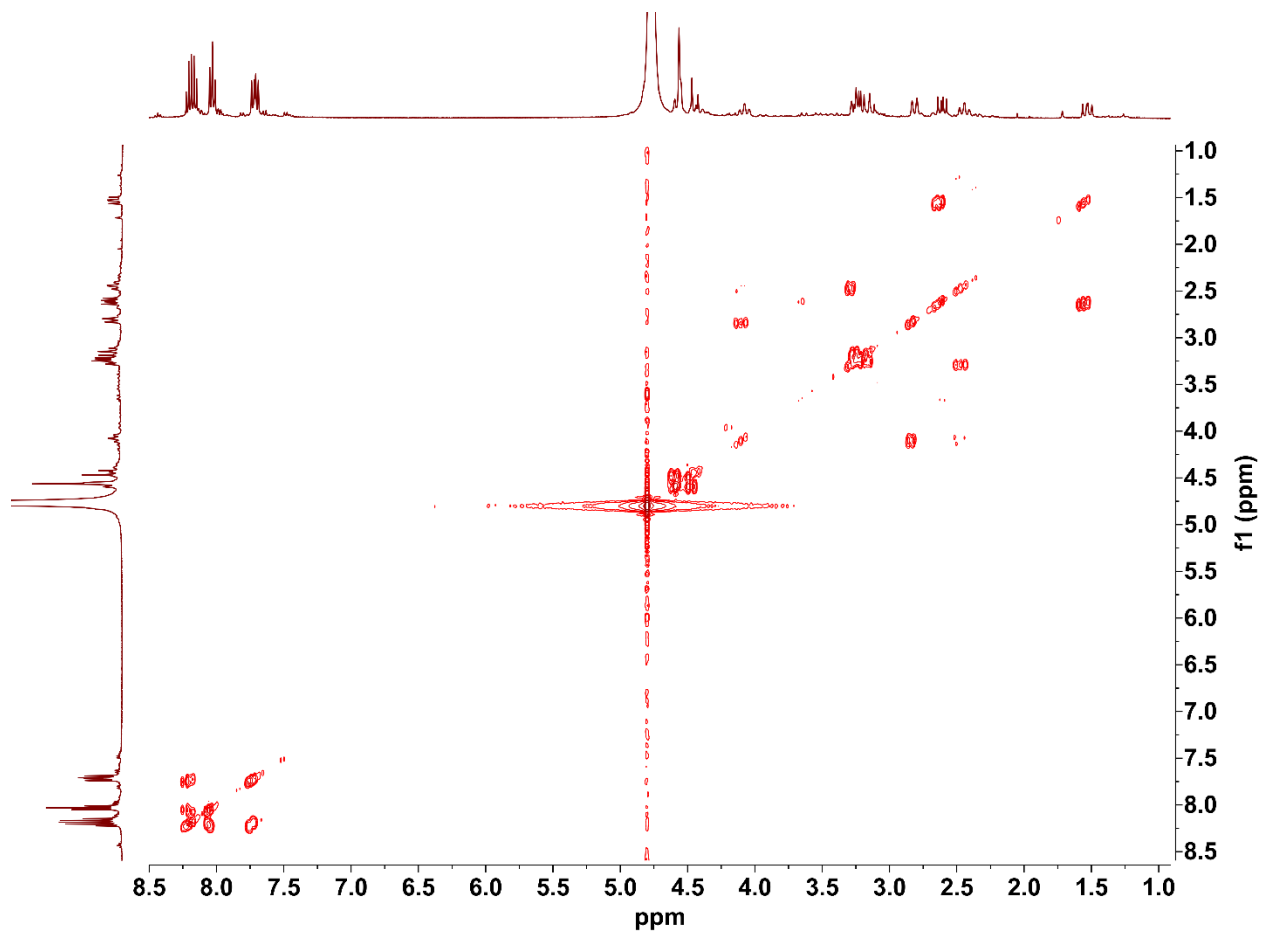


**Figure A.25**  $^1\text{H}$ - $^1\text{H}$  COSY spectrum of the  $\text{Sc}^{3+}$ - $\text{H}_6\text{phospa}$  complex (400 MHz, 298 K,  $\text{D}_2\text{O}$ ,  $\text{pD} = 4$ ).

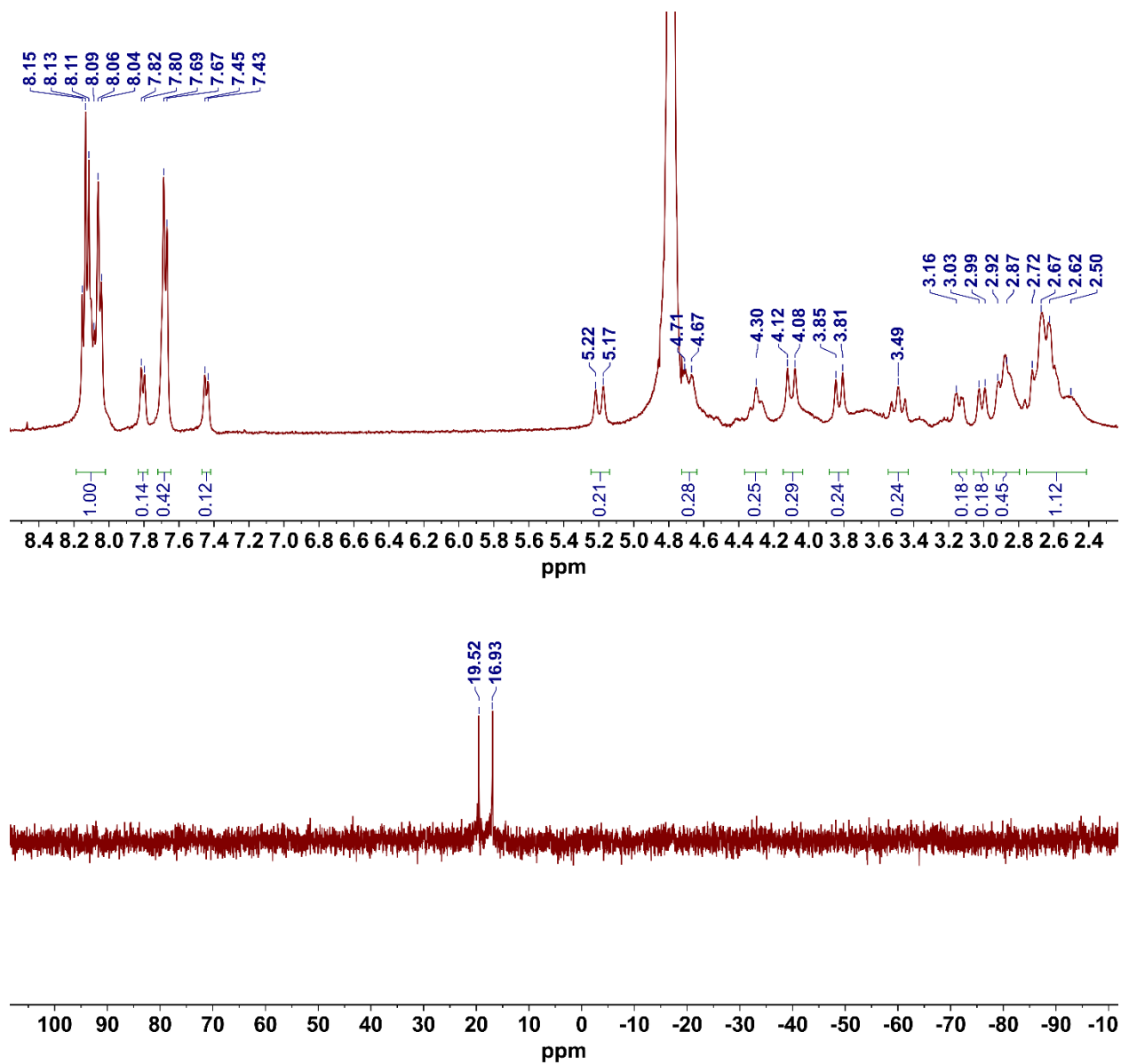
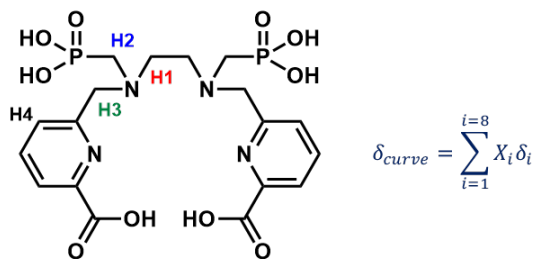


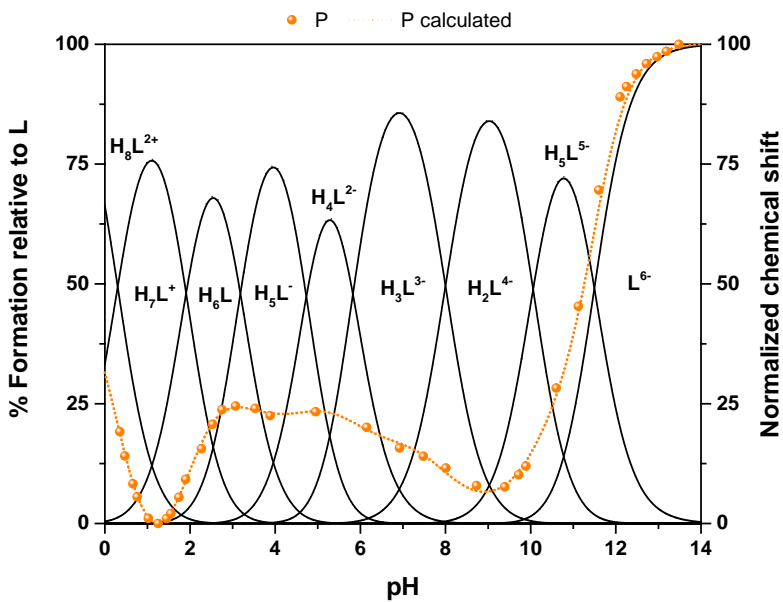
**Figure A.26**  $^1H$  NMR spectrum (top) of the  $Y^{3+}$ - $H_6$ phospa complex (400 MHz, 298 K,  $D_2O$ , pD = 7);  $^{31}P\{^1H\}$  NMR spectrum (bottom) of the  $Y^{3+}$ - $H_6$ phospa complex (162 MHz, 298 K,  $D_2O$ , pD = 7).

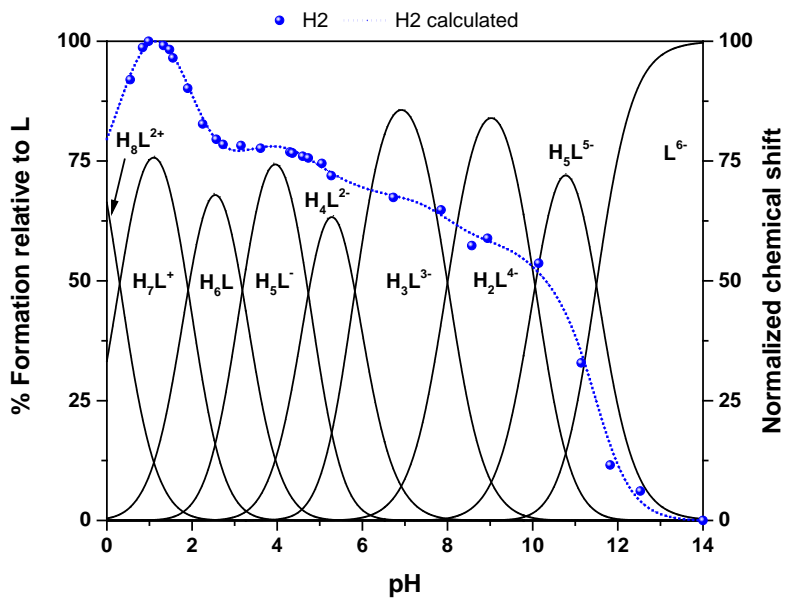
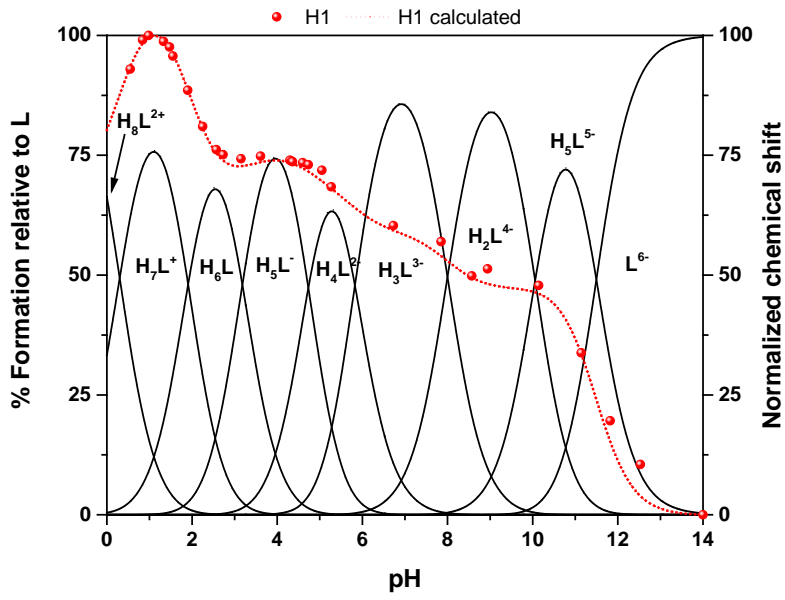
## Ligand protonation constants

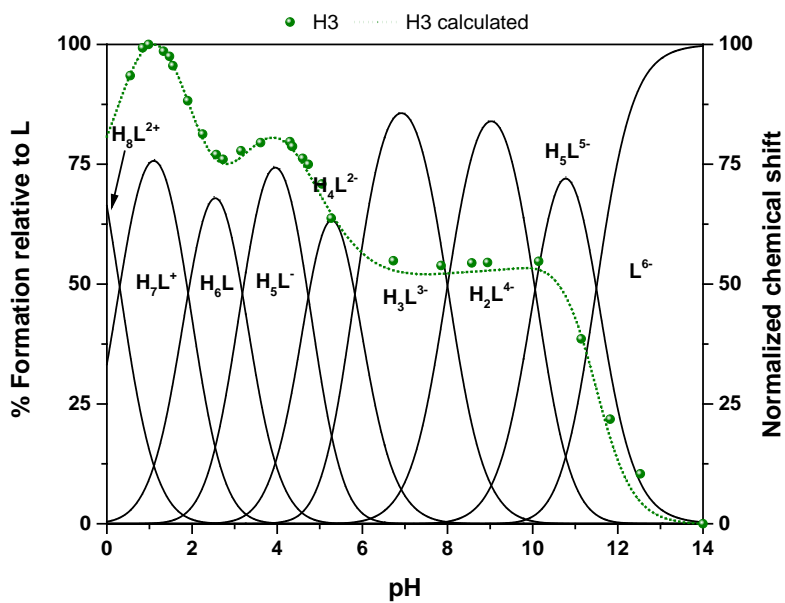
In the graphs below, shown are the experimental chemical shifts for each nucleus (dots) that are overlapped by curves calculated from species concentration (protonation constants from UV-potentiometric titrations), and the intrinsic chemical shifts  $\delta_i$  (calculated with HypNMR).



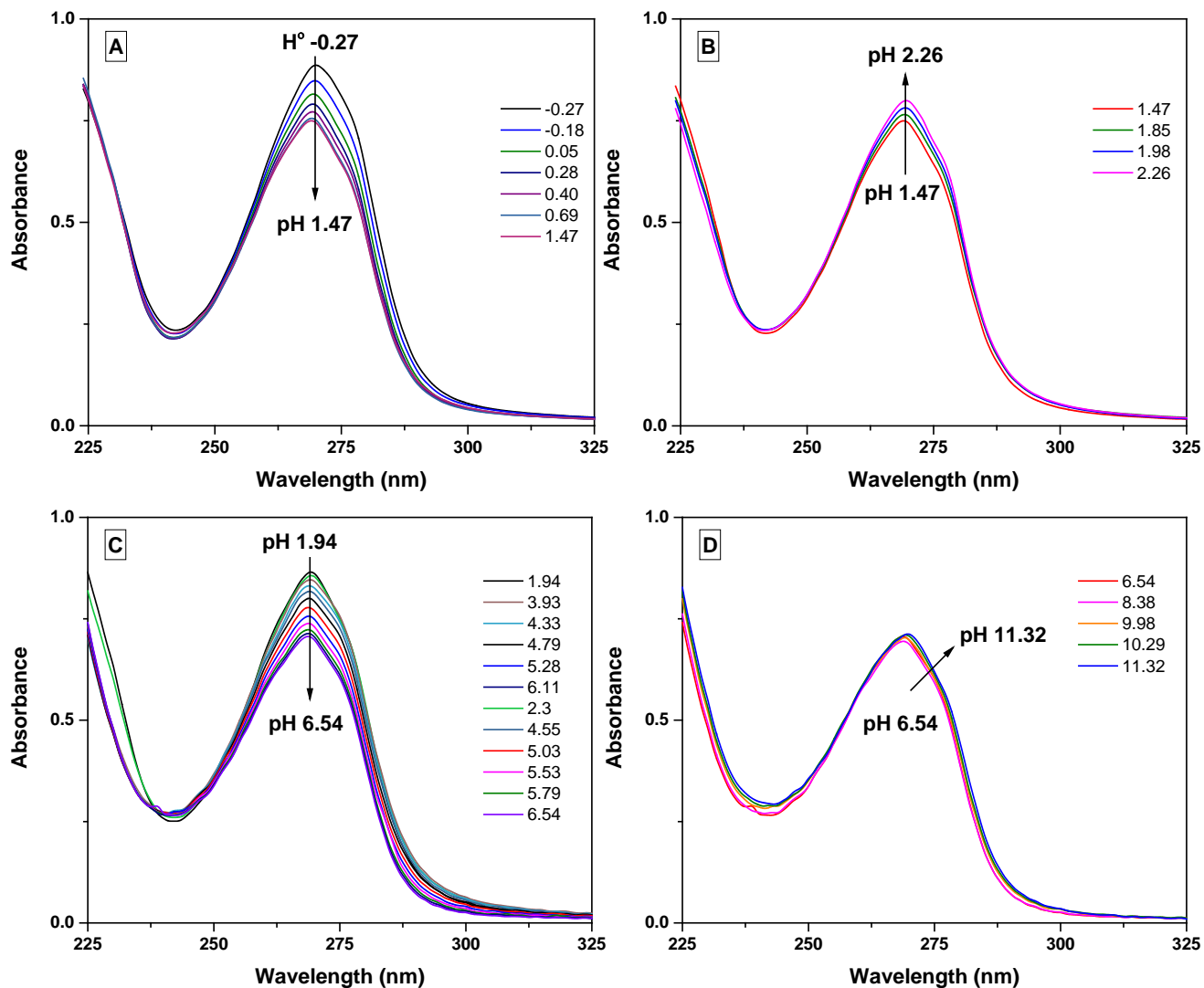
H<sub>6</sub>phospa



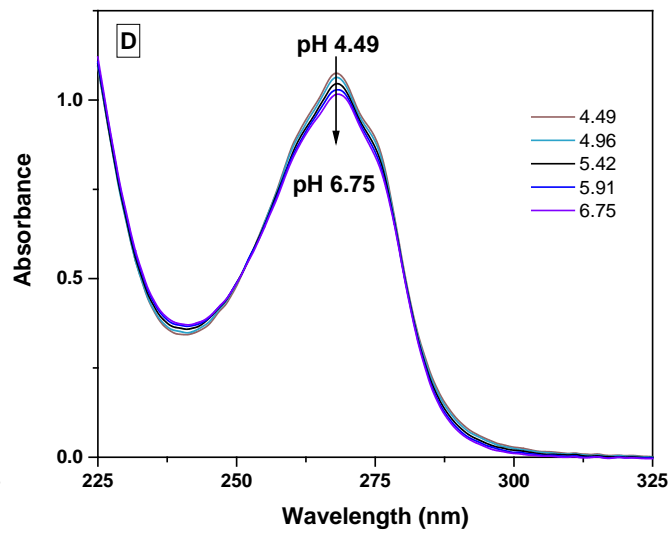
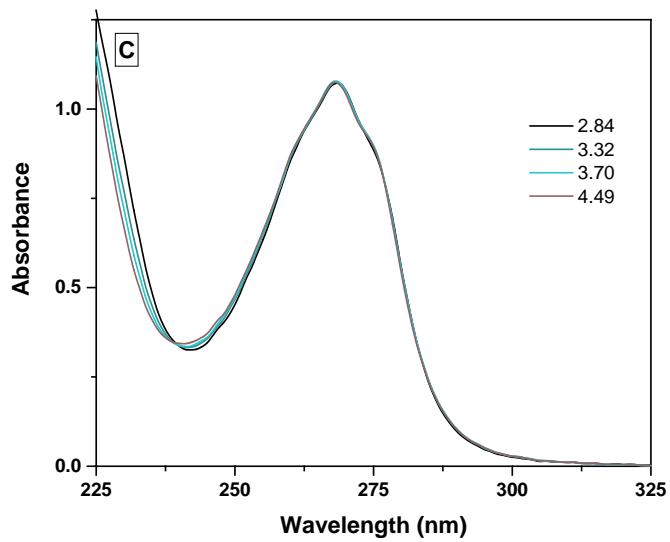
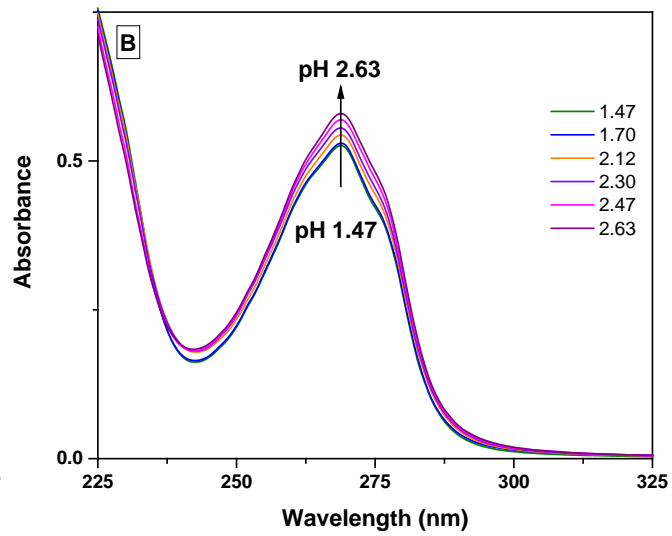
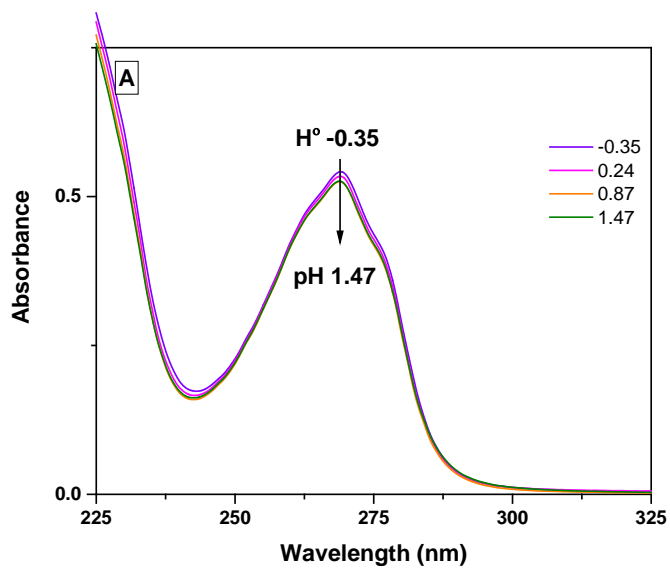


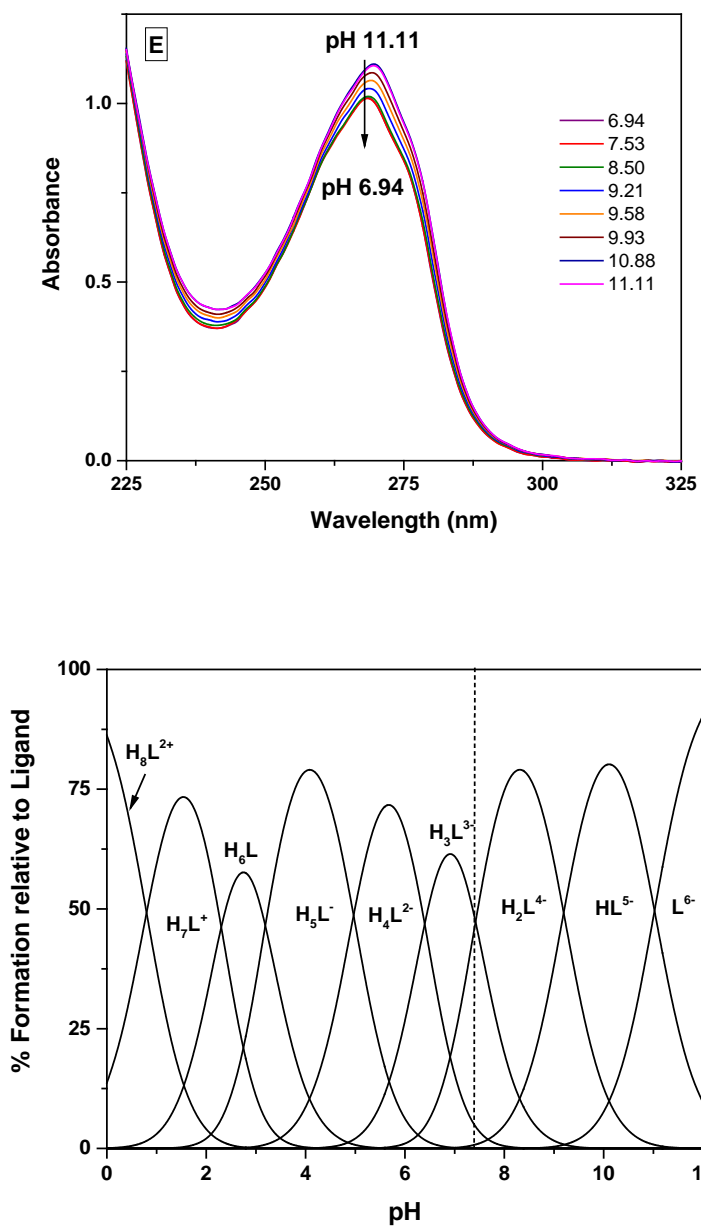


**Figure A.27** Normalized  $^{31}\text{P}\{^1\text{H}\}$  NMR chemical shift dependence on pH overlaid to speciation plot calculated with protonation constants from Table X, a); Normalized  $^1\text{H}$  NMR methylene chemical shift dependence on pH (H1, H2, H3) overlaid to  $\text{H}_6\text{phospa}$  speciation plot, b, c and d).  $[\text{H}_6\text{phospa}] = \text{M}$ ,  $T = 298 \text{ K}$ .

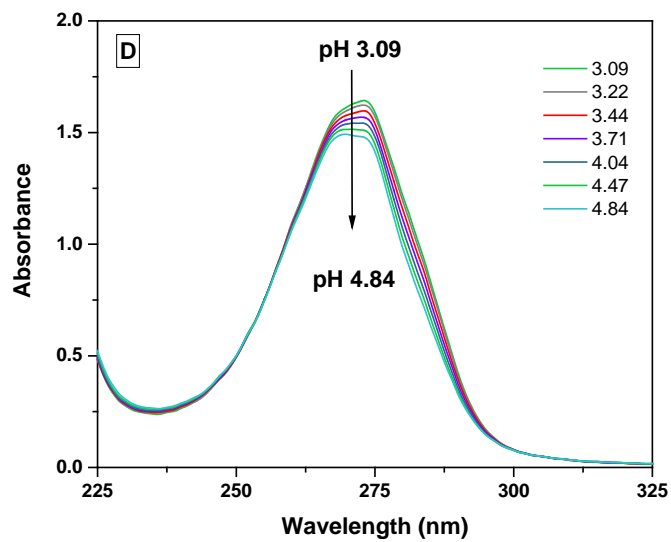
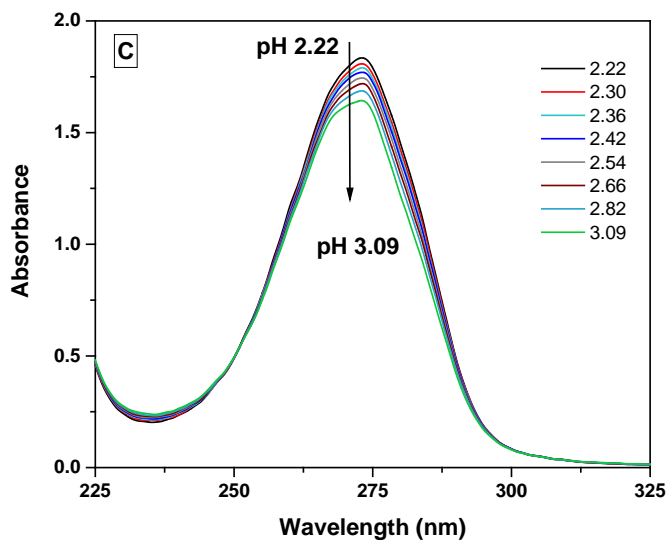
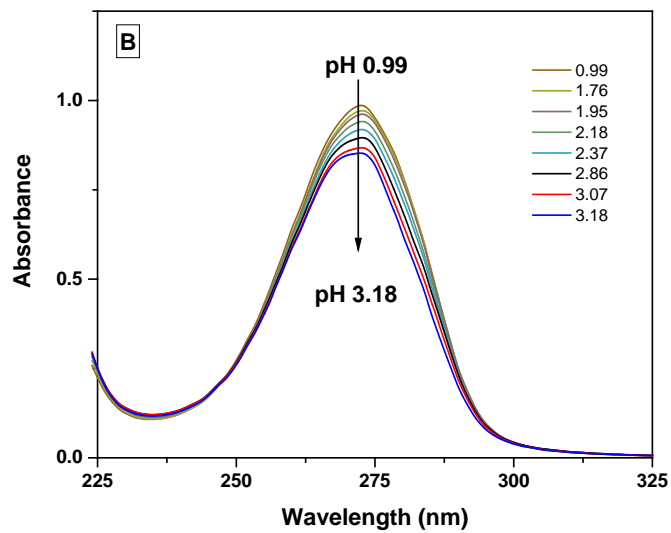
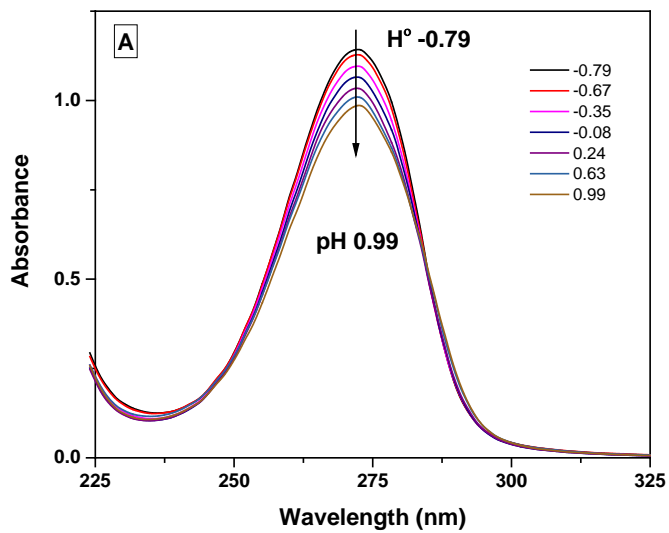


**Figure A.28** Representative spectra of  $H_6\text{phospa}$  during (a/b) acidic in-batch UV spectrophotometric titration  $[L] = 7.77 \times 10^{-5} \text{ M}$ ,  $T = 298 \text{ K}$ ,  $l = 1 \text{ cm}$ ,  $I = 0.16 \text{ M NaCl}$  when possible; (c/d) combined UV-potentiometric titration  $[L] = 4.84 \times 10^{-4} \text{ M}$ ,  $T = 298 \text{ K}$ ,  $l = 0.2 \text{ cm}$ ,  $I = 0.16 \text{ M NaCl}$ .





**Figure A.29** Representative spectra of H<sub>6</sub>dipedpa during (a/b) acidic in-batch UV spectrophotometric titration [L] =  $7.11 \times 10^{-5}$  M, T = 298 K, l = 1 cm, I = 0.16 M NaCl when possible; (c/d) combined UV-potentiometric titration [L] =  $6.76 \times 10^{-4}$  M, T = 298 K, l = 0.2 cm, I = 0.16 M NaCl; (f) speciation plot of H<sub>6</sub>dipedpa calculated with stability constants in Table 3.1, [H<sub>6</sub>dipedpa] = 0.001 M; dashed line indicates pH = 7.4.



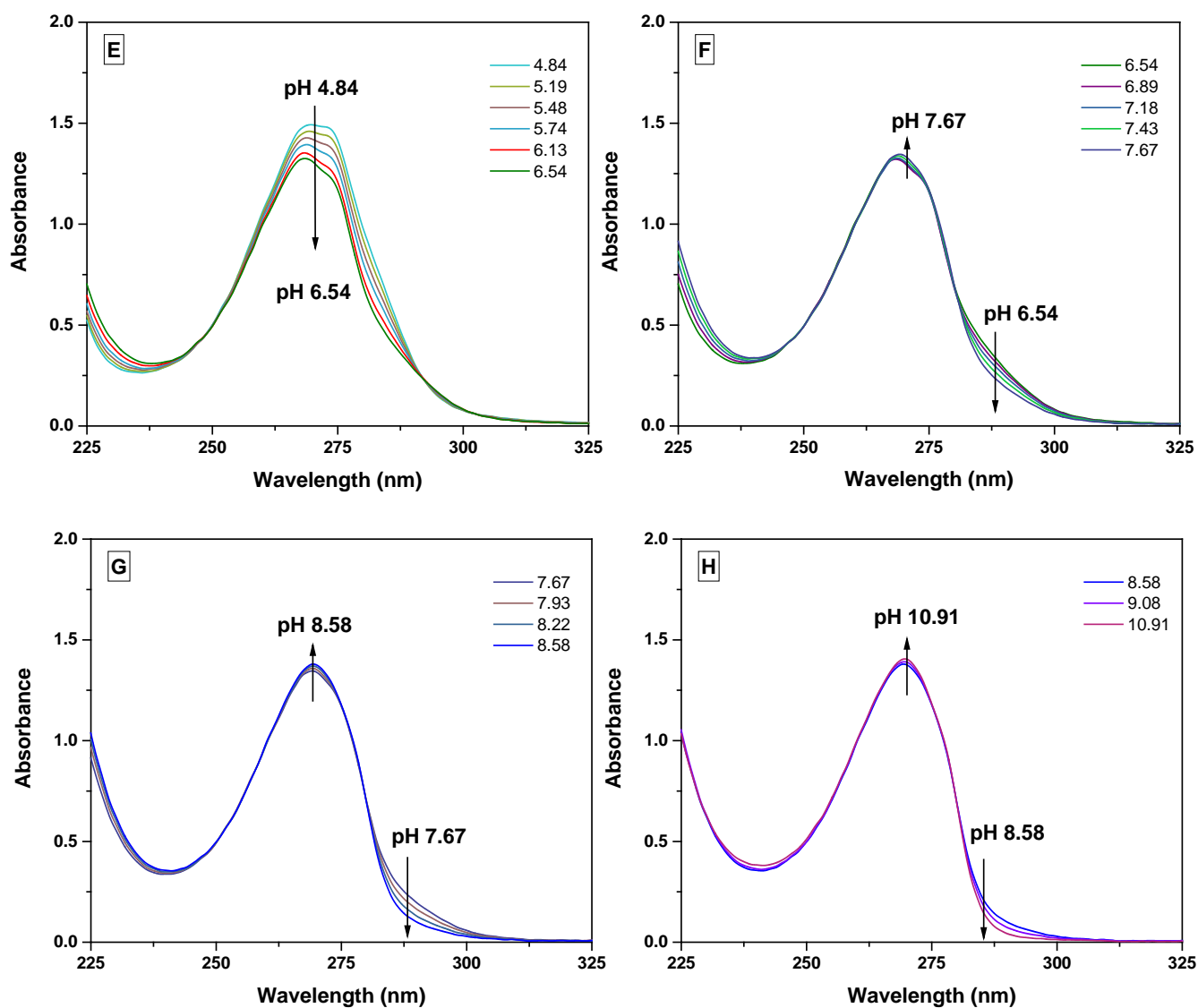


**Figure A.30** Representative spectra of H<sub>6</sub>eppy during (a/b) acidic in-batch UV spectrophotometric titration [L] =  $7.25 \times 10^{-5}$  M, T = 298 K, l = 1 cm, I = 0.16 M NaCl when possible; (c/h) combined UV-potentiometric titration [L] =  $7.15 \times 10^{-4}$  M, T = 298 K, l = 0.2 cm, I = 0.16 M NaCl.

**Table A.5** HR-ESI-MS data for H<sub>6</sub>phospa, H<sub>6</sub>dipedpa and H<sub>6</sub>eppy with In<sup>3+</sup>, Sc<sup>3+</sup>, Lu<sup>3+</sup>, Y<sup>3+</sup>, La<sup>3+</sup>.

Species	Formula	Calcd (m/z)	Found (m/z)
Phospa	C <sub>18</sub> H <sub>24</sub> N <sub>4</sub> O <sub>10</sub> P <sub>2</sub> K	557.0605	557.0601
Phospa-In	C <sub>18</sub> H <sub>20</sub> N <sub>4</sub> O <sub>10</sub> P <sub>2</sub> In	628.9693	628.9691
Phospa-Sc	C <sub>18</sub> H <sub>20</sub> N <sub>4</sub> O <sub>10</sub> P <sub>2</sub> Sc	559.0214	559.0211
Phospa-Lu	C <sub>18</sub> H <sub>20</sub> N <sub>4</sub> O <sub>10</sub> P <sub>2</sub> Lu	689.0063	689.0062
Phospa-Y	C <sub>18</sub> H <sub>22</sub> N <sub>4</sub> O <sub>10</sub> P <sub>2</sub> Y	604.9870	604.9869
Phospa-La	C <sub>18</sub> H <sub>22</sub> N <sub>4</sub> O <sub>10</sub> P <sub>2</sub> La	655.9982	655.9986
Dipedpa	C <sub>20</sub> H <sub>29</sub> N <sub>4</sub> O <sub>10</sub> P <sub>2</sub> K	547.1359	547.1362
Dipedpa-In	C <sub>20</sub> H <sub>25</sub> N <sub>4</sub> O <sub>10</sub> P <sub>2</sub> In	656.0087	656.0087
Dipedpa-Sc	C <sub>20</sub> H <sub>25</sub> N <sub>4</sub> O <sub>10</sub> P <sub>2</sub> Sc	588.0605	588.0600
Dipedpa-Lu	C <sub>20</sub> H <sub>25</sub> N <sub>4</sub> O <sub>10</sub> P <sub>2</sub> Lu	718.0454	718.0453
Dipedpa-Y	C <sub>20</sub> H <sub>25</sub> N <sub>4</sub> O <sub>10</sub> P <sub>2</sub> Y	632.0104	632.0111
Dipedpa-La	C <sub>20</sub> H <sub>25</sub> N <sub>4</sub> O <sub>10</sub> P <sub>2</sub> La	681.0117	681.0122
Eppy	C <sub>20</sub> H <sub>29</sub> N <sub>4</sub> O <sub>10</sub> P <sub>2</sub>	547.1359	547.1360
eppy-In	C <sub>20</sub> H <sub>25</sub> N <sub>4</sub> O <sub>10</sub> P <sub>2</sub> In	656.0087	656.0087
eppy-Sc	C <sub>20</sub> H <sub>25</sub> N <sub>4</sub> O <sub>10</sub> P <sub>2</sub> Sc	588.0605	588.0603
eppy-Lu	C <sub>20</sub> H <sub>25</sub> N <sub>4</sub> O <sub>10</sub> P <sub>2</sub> Lu	718.0454	718.0452
eppy-Y	C <sub>20</sub> H <sub>25</sub> N <sub>4</sub> O <sub>10</sub> P <sub>2</sub> Y	632.0104	632.0108
eppy-La	C <sub>20</sub> H <sub>25</sub> N <sub>4</sub> O <sub>10</sub> P <sub>2</sub> La	681.0117	681.0121

**Table A.6** Selected bond lengths from the crystal structure of H<sub>6</sub>phospa

Atom	Atom	Length (Å)	Atom	Atom	Length (Å)
P1	O3	1.510(18)	N1	C6	1.326(4)
P1	O4	1.231(5)	N2	C7	1.551(3)
P1	O5	1.538(7)	N2	C8	1.516(3)
P1	C9	1.896(6)	N2	C9	1.504(3)
P1A	O3A	1.51(2)	C1	C2	1.494(4)
P1A	O4A	1.551(6)	C2	C3	1.386(4)
P1A	O5A	1.527(7)	C3	C4	1.387(4)
P1A	C9	1.767(7)	C4	C5	1.388(4)
O1	C1	1.332(3)	C5	C6	1.397(4)
O2	C1	1.213(3)	C6	C7	1.503(4)
N1	C2	1.338(3)	C8	C81	1.513(5)

**Table A.7** Selected bond angles from the crystal structure of H<sub>6</sub>phospa

Atoms	Atom	Atom	Angle (°)	Atoms	Atom	Atom	Angle (°)
O3	P1	O4	114.7(6)	O1	C1	C2	115.9(2)
O3	P1	O5	115.4(5)	O2	C1	O1	121.0(3)
O3	P1	C9	107.8(7)	O2	C1	C2	123.1(3)
O4	P1	O5	107.9(4)	N1	C2	C1	114.3(2)
O4	P1	C9	105.7(4)	N1	C2	C3	123.7(3)
O5	P1	C9	104.4(3)	C3	C2	C1	121.9(3)
O3A	P1A	O4A	110.9(8)	C2	C3	C4	117.5(3)
O3A	P1A	O5A	116.5(7)	C3	C4	C5	119.7(3)
O3A	P1A	C9	109.2(8)	C4	C5	C6	118.2(3)
O4A	P1A	C9	107.1(4)	N1	C6	C5	122.7(3)
O5A	P1A	O4A	110.0(5)	N1	C6	C7	114.8(2)
O5A	P1A	C9	102.5(3)	C5	C6	C7	122.4(3)
C6	N1	C2	118.2(2)	C6	C7	N2	111.4(2)
C7	N2	C8	108.0(2)	C81	C8	N2	112.4(2)
C9	N2	C7	111.66(19)	N2	C9	P1	112.9(2)
C9	N2	C8	112.0(2)	N2	C9	P1A	114.7(3)

**Table A.8** Selected bond lengths from the crystal structure of H<sub>6</sub>dipedpa

Atom	Atom	Length (Å)	Atom	Atom	Length (Å)
P1	O3	1.501(6)	N3	C14	1.524(10)
P1	O4	1.527(6)	N4	C15	1.330(10)
P1	O5	1.581(6)	N4	C19	1.358(10)
P1	C9	1.807(8)	C1	C2	1.497(12)
P2	O9	1.516(6)	C2	C3	1.374(12)
P2	O10	1.588(6)	C3	C4	1.369(12)
P2	O11	1.495(6)	C4	C5	1.395(12)
P2	C13	1.816(8)	C5	C6	1.381(12)
O1	C13	1.223(10)	C6	C7	1.510(11)
O2	C13	1.311(10)	C8	C9	1.520(11)
O15	C20	1.326(10)	C10	C11	1.522(10)
O16	C20	1.217(10)	C12	C13	1.529(11)
N1	C20	1.341(10)	C14	C15	1.497(11)
N1	C6	1.321(10)	C15	C16	1.397(11)
N2	C7	1.502(10)	C16	C17	1.375(12)
N2	C8	1.494(10)	C17	C18	1.394(12)
N2	C10	1.497(9)	C18	C19	1.364(12)
N3	C11	1.517(10)	C19	C20	1.506(12)
N3	C12	1.504(10)			

**Table A.9** Selected bond angles from the crystal structure of H<sub>6</sub>dipedpa

Atoms	Atom	Atom	Angle (°)	Atoms	Atom	Atom	Angle (°)
O3	P1	O4	115.8(3)	C4	C3	C2	118.0(9)
O3	P1	O5	108.4(3)	C3	C4	C5	119.7(9)
O3	P1	C9	107.3(4)	C6	C5	C4	117.6(9)
O4	P1	O5	109.8(4)	N1	C6	C5	123.7(9)
O4	P1	C9	108.9(4)	N1	C6	C7	116.1(8)
O5	P1	C9	106.2(4)	C5	C6	C7	120.2(8)
O9	P2	O10	111.2(3)	N2	C7	C6	111.3(7)
O9	P2	C13	108.5(4)	N2	C8	C9	110.5(7)
O10	P2	C13	105.5(4)	C8	C9	P1	115.2(6)
O11	P2	O9	115.5(3)	N2	C10	C11	110.8(6)
O11	P2	O10	107.5(3)	N3	C11	C10	108.9(6)
O11	P2	C13	108.2(4)	N3	C12	C13	111.3(6)
C6	N1	C2	117.4(8)	C12	C13	P2	112.2(6)
C8	N2	C7	112.7(7)	C15	C14	N3	112.2(7)
C8	N2	C10	111.4(6)	N4	C15	C14	117.1(7)
C10	N2	C7	111.9(6)	N4	C15	C16	122.9(8)
C11	N3	C14	112.4(6)	C16	C15	C14	119.9(8)
C12	N3	C11	108.7(6)	C17	C16	C15	118.5(8)
C12	N3	C14	112.0(6)	C16	C17	C18	119.7(9)
C15	N4	C19	117.0(7)	C19	C18	C17	117.5(9)
O1	C1	O2	119.7(9)	N4	C19	C18	124.4(9)
O1	C1	C2	120.6(9)	N4	C19	C20	115.6(8)
O2	C1	C2	119.7(8)	C18	C19	C20	120.0(8)
N1	C2	C1	116.2(8)	O15	C20	C19	117.8(8)
N1	C2	C3	123.7(9)	O16	C20	O15	119.9(8)
C3	C2	C1	120.1(8)	O16	C20	C19	122.3(8)

## Appendix C. Supplementary Data for Chapter 5

**Table A.10** Crystallographic information for [Pb(DTPAm)](NO<sub>3</sub>)<sub>2</sub>.

Formula	C <sub>14</sub> H <sub>28</sub> N <sub>8</sub> O <sub>5</sub> Pb
$D_{calc.}/\text{g cm}^{-3}$	1.455
$\mu/\text{mm}^{-1}$	6.239
Formula Weight	595.63
Colour	colourless
Shape	needle
Size/mm <sup>3</sup>	0.32×0.27×0.07
$T/\text{K}$	296(2)
Crystal System	monoclinic
Space Group	$P2_1/c$
$a/\text{Å}$	8.9884(7)
$b/\text{Å}$	20.3731(16)
$c/\text{Å}$	14.8713(11)
$\alpha/^\circ$	90
$\beta/^\circ$	93.436(2)
$\gamma/^\circ$	90
$V/\text{Å}^3$	2718.4(4)
$Z$	4
$Z'$	1
Wavelength/Å	0.710730
Radiation type	MoK $\alpha$
$\theta_{min}/^\circ$	1.697
$\theta_{max}/^\circ$	30.548
Measured Refl.	50045
Independent Refl.	8315
Reflections with $I > 2(I)$	7492
$R_{int}$	0.0389
Parameters	369
Restraints	0
Largest Peak	0.970
Deepest Hole	-1.015
GooF	1.057
$wR_2$ (all data)	0.0519
$wR_2$	0.0492
$R_1$ (all data)	0.0293
$R_1$	0.0236